A distributed real-time digital control system for a magnetically levitated vehicle

Goble, John M.

Award date:
1988

Awarding institution:
University of Bath

A distributed real-time digital control system for a magnetically levitated vehicle

submitted by John M. Goble
for the degree of PhD
of the University of Bath
1988

ProQuest LLC
789 East Eisenhower Parkway
P.O. Box 1346
Ann Arbor, MI 48106-1346

Summary

A distributed real-time digital control scheme for the control of a quarter scale magnetically levitated vehicle using linear synchronous motors in combined levitative and tractive modes is presented. The design and implementation of the power electronics, the multiprocessor interface hardware, specialised transducer hardware and the controller software are described, with particular attention given to future expansion requirements.

Sample test results from the prototype vehicle are presented and used to assess the performance of two alternative control schemes.

Acknowledgements

The author is indebted to his academic supervisor, Dr. R. T. Lipczynski, and to his industrial supervisor Mr. D. A. Picken, for their help and guidance throughout this work. He would like to thank Professor J. F. Eastham, Head of School, for provision of facilities at the School of Electrical Engineering and also GEC Transmission and Distribution Projects Ltd for the use of their facilities.

Financial support from the Science and Engineering Research Council and from GEC Transmission and Distribution Projects Ltd is gratefully acknowledged.

The author would like to express his appreciation to Mr. A. R. Daniels and to his colleagues at both the University and at GEC for their involvement and interest during this project.

CONTENTS

List of principal symbols

a_0, a_1, a_2	numerator coefficients of the continuous filter transfer function
b_1, b_2	denominator coefficients of the continuous filter transfer function
z	delay operator
δ	modified delay operator
s	Laplace operator
T_s	sample period
T	half sample period
p, q, r	fixed coefficient output multipliers of the digital filter
m_1, m_2	fixed coefficient internal multipliers of the digital filter
P_n, Q_n, R_n	internal variables for the digital filter
X_n, Y_n	input/output variables respectively of the digital filter
x_1, x_2, x_3, x_4	measured air gaps of the linear synchronous motors mounted at corners 1 through 4 respectively
x_5, x_6, x_7, x_8	measured air gaps of the side magnets mounted at corners 1 through 4 respectively
$x_{H,R,P,T,L,Y}$	calculated displacements of the vehicle in heave, roll, pitch, twist (or traction), lateral and yaw modes respectively
$\ddot{x}_1, \ddot{x}_2, \ddot{x}_3, \ddot{x}_4$	measured vertical accelerations of the linear synchronous motors mounted at corners 1 through 4 respectively
$\ddot{x}_H, \ddot{x}_R, \ddot{x}_P, \ddot{x}_T$	calculated accelerations of the vehicle in heave, roll, pitch and twist modes respectively
F_1, F_2, F_3, F_4	lift force contributions from the linear synchronous motors mounted at corners 1 through 4 respectively

F_5, F_6, F_7, F_8	lateral guidance force contributions from the side magnets mounted at corners 1 through 4 respectively
$F_{H,R,P,T,L,Y}$	total control force applied to the vehicle in heave, roll, pitch, twist (or traction), lateral and yaw modes respectively
K_v	velocity damping factor in the twist mode
K_θ	torsional stiffness
P	chopper linearisation pole
τ_L	time constant of the chopper linearisation pole
K_g	overall gain of the combined gap transducer readings
K_a	overall gain of the combined accelerometer readings
K_c	chopper gain
K_m	motor force constant
K_i	inverter/LSM combined gain
K_p	pole position transducer gain
K	forward path gain of the vehicle controllers
h_0, h_1, h_2	feedback constants of the vehicle controllers
A	cross sectional area
B	flux density
M_m	combined mass of a linear synchronous motor/side magnet pair
M_d	distributed mass of the vehicle chassis
I_m	inertia component due to M_m
I_d	inertia component due to M_d

1. Introduction

With the recent introduction of solid state microelectronics, together with recent advances in high power semiconductor devices, research into alternative forms of the conventional railed vehicle has gathered momentum.

Early developments using these comparatively new technologies were based on the use of linear induction motors to provide the propulsion force whilst retaining the wheels for guidance and suspension purposes. This arrangement, for example, was used for an intermediate capacity transit system developed by the Urban Transportation Development Corporation of Canada[1]. In this particular case, however, the linear induction motors were included to overcome traction difficulties when climbing unusually steep gradients. The next major advancement in vehicle development was to dispense with the guidance wheels altogether, instead using separately controlled d.c. lift magnets operated in conjunction with the linear induction motor.

A major advantage of this magnetically levitated vehicle arrangement is the elimination of track wear, giving a consequent reduction in vehicle and track maintainance costs. The absence of wheels also eliminates much of the noise produced by railed vehicles and this is of particular importance where the route passes through densely populated urban areas. A further advantage offered by the magnetically levitated vehicle is that it presents the prospect of very high operational speeds, much higher than those obtainable with propulsion and guidance being provided by flanged wheels.

A current disadvantage of this type of vehicle, however, is that the linear induction motor requires a secondary member, in the form of a reaction rail, to be incorporated into the track in addition to the levitation and guidance rails. This reaction rail is partly comprised of a continuous conducting material, usually aluminium, and can thus significantly add to the overall track material costs. Further, to provide the necessary clearances, the airgap of these motors must be large in comparison to a

conventional design. Consequently the motor will operate at a relatively low power factor, thus requiring a heavy and expensive power supply system.

1.1 The linear synchronous motor

To overcome some of the problems associated with the linear induction motor, recent investigations carried out at the University of Bath have produced a prototype magnetically levitated vehicle using linear synchronous motors to provide both the tractive thrust and the lift forces required. In this application, the magnetic circuits of these motors are arranged so that both the armature and field windings reside on a 'short primary' member attached to the vehicle. The motor secondary is passive and consists of plain steel segments that are built into the track. This arrangement is clearly desirable since the cost per metre of track can be kept to a minimum. A full description of the operation of the linear synchronous motor in combined levitative and tractive modes is given in chapter 2 (section 2.1.1).

1.2 Vehicle control

Whatever type of motor is used to implement a magnetically levitated vehicle, the required control system will invariably have to be very complex in order to provide simultaneous control of lift, tractive thrust and lateral guidance. Further, this control system must also be very robust if the safety of the vehicle and occupants is to be ensured. To achieve this, the prototype vehicle at Bath was to implement a digital controller using an embedded microprocessor-based control system. Once working, such a system would provide an ideal platform for the development of advanced vehicle control schemes. Much of the original work on this system was carried out by Dunn[2].

However, the original digital control system, which was based on a single microprocessor, was shown to be inadequate and only partial control of the vehicle could be achieved. In order to successfully conclude this work, therefore, it would be necessary to first incorporate a more powerful microprocessor system.

1.3 Microprocessor developments

The earliest microprocessors were not very powerful, providing only simple logic sequencing rather than general purpose computing facilities. As fabrication techniques improved and the digital electronics market expanded, the price of these devices fell rapidly whilst yet more powerful devices were introduced. The integration levels of present day microprocessors allow architecture features from mini and main frame computers to be incorporated.

The low cost of microprocessor based computers has allowed them to be dedicated to a range of tasks, particularly where immediate response is more important than a high peak throughput. A good example is the growth in the use of personal computers for word processing and other low level data processing applications. Applications requiring simultaneous access to a database by many users have also been successfully implemented on microprocessor systems using local area networks to couple individual personal computers. Multiple microprocessor systems can also have advantages in reliability by using redundancy and majority voting techniques. Further, by exploiting concurrency in a given control task, these multiprocessor systems can increase controller throughput above that of the individual processing elements.

The present work describes the use of a multiprocessor system in the implementation of a distributed digital control scheme for a magnetically levitated vehicle propelled by four linear synchronous motors. Chapter 2 provides full details of the power electronics, multiprocessor system and specialised transducer hardware. Chapter 3 describes the development of a generalised set of fixed point digital filter algorithms with the aim of simplifying controller implementation and maintainance. A set of linearised mathematical models representing the vehicle dynamics are derived in chapter 4 and chapter 5 presents a preliminary vehicle control scheme implementing full levitation and lateral guidance control. Chapter 6 describes the implementation of a fast acting flux feedback loop around the linear synchronous motors whilst chapter 7

presents the corresponding control system details. Using a purpose designed pole position transducer system described in chapter 8, this control system was then extended in chapter 9 to include a tractive mode position controller, thus providing full control of the vehicle in combined levitative, lateral and tractive modes. General conclusions are drawn in chapter 10.

Finally, with the reliability of the vehicle models and control system established, chapter 11 suggests further work. Subjects include passenger comfort, condition monitoring and multivariable control systems.

2. Vehicle hardware

The levitated vehicle consisted of a box section aluminium chassis (illustrated in figure 2.1) upon which were mounted four linear synchronous motors, four side control magnets, eight gap transducers, four accelerometers, one pole position transducer and the multiple 68000 microprocessor hardware required to implement a real-time digital control scheme for the vehicle. In addition to chassis mounted hardware, two power electronics racks alongside the vehicle track provide the eight current feedback choppers and two 3-phase inverters required to drive the linear synchronous motors and side control magnets. A detailed description of the vehicle hardware will now be given.

2.1 The linear synchronous motors and side control magnets

The vehicle is supported and propelled by four linear synchronous motors (LSM's). A motor is positioned at each corner of the vehicle and two parallel tracks of secondary members are used. Lateral control of the vehicle was provided by simple d.c. side magnets wound on C-cores and mounted on each corner of the vehicle. These react on an additional pair of lateral guidance rails running down each side of the track, which also provide the positional reference for the side controllers.

2.1.1 The linear synchronous motor Figure 2.2 shows a sketch of a transverse flux, homopolar linear synchronous motor[3-6] of the type used on the vehicle. To best illustrate how the LSM provides both levitative and tractive forces consider one primary member of the motor, as illustrated in figure 2.3, together with the associated d.c. and a.c. flux patterns.

Energisation of the d.c. windings produces magnetic poles of one polarity at one end of the secondary track members and poles of the opposite polarity at the other end of these members. This sets up a flux distribution under one primary member of the motor as shown in figure 2.3b. The flux distribution under the other primary member, which is not represented in the diagram, would be of the opposite sign. The three

phase a.c. winding sets up an approximately sinusoidal current distribution along the length of each of the primary members (figure 2.3c), producing a corresponding sinusoidal flux pattern (figure 2.3d) which is phase displaced by 90° from the current distribution. Interaction between this a.c. flux and the d.c. flux produces tractive thrust in the direction indicated. Additionally, the flux linking the primary and secondary members produces a force of attraction which can be utilised to provide support for the vehicle.

In order that maximum thrust is produced by this mechanism the centre line of each secondary track member must be in alignment with the peaks of the a.c. winding current distribution. This corresponds to maintaining the motor at a constant torque angle of $\pm 90°$. It follows, therefore, that the motor will only produce tractive thrust when the primary advances at synchronous speed and in the opposite direction to the primary a.c. current pattern. For variable speed operation it is therefore necessary to use a variable frequency supply capable of operating down to d.c. to provide reliable starting of the motor.

It can be shown that operating the motor at a constant torque angle of $\pm 90°$ also minimises interaction between the levitative and tractive modes[6]. Under these conditions it is both convenient and practical to consider the levitative and tractive modes separately for design purposes.

2.1.2 Tractive effort Once a d.c. flux has been established to levitate the vehicle, and provided the torque angle is maintained at a constant $\pm 90°$, then the tractive effort produced by each LSM is approximately proportional to the product of the d.c. levitation current and the a.c. tractive current.

Details of the positioning of the linear synchronous motors and side magnets are provided in figure 2.4. Principal parameters of the four LSM d.c. windings and four side magnets are provided in appendix A.

2.2 Current feedback choppers

Choppers for setting demand currents in the levitation motors and side control magnets were mounted in two free standing power electronics racks alongside the vehicle track. A general description of chopper operation will now be given followed by specific circuit details.

2.2.1 General description Each chopper was of the regenerative type, employing the circuit configuration shown in figure 2.5a. Although more complex than the simpler single transistor chopper shown in figure 2.5b, the regenerative chopper offered two important advantages.

1. The load current waveform is more symmetrical (similar rise and fall times)
2. Energy is restored to the supply during regeneration

To see how the regenerative chopper achieves this consider the two chopper configurations during transistor off periods.

When transistors T1 and T2 in the regenerative chopper turn off, load current is taken up by diodes D1 and D2 and circulates in the regeneration path as indicated in figure 2.5a. This path includes the chopper source voltage, V_s. It follows that during regeneration the load current falls towards the limiting value of $-V_s/R$ whilst returning energy from the load inductance to the supply via the regeneration current path. The equivalent flywheel path in the single transistor chopper of figure 2.5b does not include the chopper source voltage. Hence when transistor T1 turns off, the load current falls towards a limiting value of zero whilst load energy is dissipated in the load resistance.

During transistor on periods, the load current characteristic for the two choppers is the same, rising towards a limiting value of $+V_s/R$ in each case. Figure 2.6 illustrates typical load current waveforms of both the regenerative chopper and the single transistor chopper during a step response test. This diagram clearly shows the adverse

effect on load current response due to the asymmetrical aiming currents of the single transistor type of chopper.

In any type of chopper, modulation of the transistor on/off times must be employed to maintain the load current at a desired mean level.

2.2.2 Chopper modulation Slitwidth modulation techniques[7] were used to provide closed loop control of the mean load current about a set reference level. With slitwidth modulation, a tolerance band or window is set on the reference demand input. If the measured load current is at or below the lower limit set by this window the chopper power transistors are turned on to start the load current ramping up. When the load current reaches the upper window limit the power transistors are turned off, allowing the load current to fall towards the lower window limit, whereupon the sequence repeats. Figure 2.7 illustrates a typical slitwidth modulated load current following a sinusoidal reference input.

The advantage of slitwidth modulation is that the load current reaches the set demand level in the minimum possible time. When used in linear control applications, however, slitwidth modulation can be a disadvantage because the relationship between the reference demand input and the mean load current is non-linear.

2.2.3 Chopper frequency The chopper frequency is governed by the time taken for the load current to traverse the full width of the window limits. In most slitwidth applications the window limits would typically be set at ±5% of the chopper's full scale output capability. The chopper frequency must then be set independently by modifying the load time constant to limit the rate of change of current across the window.

Figure 2.8 shows a block diagram of the slitwidth modulated chopper implementation used on the levitated vehicle. Specific details of each of the units making up the chopper will now be given.

2.2.4 Chopper control card The chopper control card includes the circuitry for the slitwidth modulator implementation together with additional protection logic to limit the switching frequency of the modulator output. This frequency limit is to prevent high frequency switching of the power transistors which, if permitted, would lead to excessive switching losses in these devices. The following circuit description refers to the chopper control card circuit diagram of figure 2.9. Figure 2.10 provides the corresponding component layout details.

The analogue reference input to the slitwidth modulator is taken from a BNC socket mounted on the front panel of the chopper control card. For test purposes, the reference input can also be derived from the panel mounted potentiometer, VR1. The appropriate reference source is selected by SW1 and buffered by the voltage follower circuit of IC1. Summing amplifier IC2 is then used to generate an error signal by subtracting the output of the load current transducer from the buffered reference signal. This error signal is then amplified by IC3. To provide a degree of chopper frequency control the gain of IC3 can be adjusted using preset resistor PR1. The slitwidth modulator output is then derived from the error signal using the comparator circuit formed using IC4 and associated circuitry. This comparator has symmetrical hysteresis levels (set by preset resistor PR2) to provide the slitwidth window. Minimum on/off times for the modulator output are set by the monostable pair of IC6 and associated circuitry. Finally, the two 50Ω buffered line drivers of IC7 are used to ensure sufficient output drive capability for the opto-isolators on the base drive units.

2.2.5 Base drive unit and Power Darlington stage The signal from the chopper control card is required in the form of a current drive for a discrete power Darlington stage, which is used as the main switching element in the chopper realisation. This current drive was provided by a self contained isolated base drive unit, which also included additional circuitry for protection of the power devices against overcurrent or out of saturation conditions. The following circuit description is made with reference to figures 2.11 and 2.12, which provide the circuit details of the base drive unit and

discrete Darlington connection. Figure 2.13 provides the component layout details of the base drive printed circuit board.

The logical on/off demand signal from the chopper control card is electrically isolated at the input of the base drive unit using opto-isolator OPTO1, and is then directly coupled to a d.c. power amplifier comprised of transistors TR1 through TR5 inclusive and associated components. This amplifier provides the base drive current for the Darlington drive transistor, TR12. In the on state, the amplifier sources approximately 2 A of continuous base drive current to the drive transistor. This level of drive is sufficient to ensure saturation of the output transistor up to the chopper current limit of 80 A. To ensure rapid turn-on of the Darlington pair, approximately 0.5 A of drive is also supplied directly to the base of the Darlington output transistor, TR13, through resistor R18.

To turn off the Darlington pair, the amplifier sinks approximately 4 A continuous from the drive transistor to remove any stored charge from the base region of this device. Further speed up is provided by an additional sink circuit, connected to the base of the output transistor, which is comprised of transistors TR6 through TR9 inclusive and associated components. After a short delay to allow the Darlington drive transistor to turn off, this circuit generates a 20 A sink pulse for 20 μs to remove stored charge directly from the base region of the Darlington output transistor. Note that during the on to off transition it is important that the drive transistor is turned off before the output transistor, otherwise the load current would divert through the smaller drive transistor and probably damage the device. The remainder of the circuitry on the base drive board is concerned with the protection of the power Darlington pair.

Overcurrent protection is provided by monitoring the non-inductive 5 $m\ \Omega$ shunt in the emitter connection of the output transistor. The output from this shunt is connected to differential amplifier IC1, which produces an output voltage signal proportional to the current in the output transistor. This signal is then fed into a

latching level detector circuit formed using half of IC2 and associated components. If the measured current exceeds a nominal value of 80 A (set by preset resistor VR2) the level detector output will change state and inhibit the input opto-coupler, effectively removing the demand signal and forcing the base drive unit into the off state.

To provide out of saturation protection, the collector voltage of the Darlington output transistor is monitored by a second latching level detector circuit formed using half of IC2 and associated components. If the measured collector voltage exceeds a nominal preset level of 2.0 volts (set by VR1) during the on period, the level detector output, which is in wired-OR connection with the overcurrent detector, will change state and inhibit the base drive. During transistor off periods transistor TR10 is turned on, effectively shorting out the voltage sense input and inhibiting the out of saturation protection circuit.

An isolated $\pm$ 9 V supply for the base drive unit is derived from a mains input by transformer TX1, bridge rectifier BR1 and filter capacitors C4, C5, C10 and C11. Supply monitoring is provided by LED 6 and LED 7 mounted on the base drive front panel.

2.2.6 Load current transducer The current feedback signal for the slitwidth modulator is provided by an isolated load current transducer unit. The following circuit description of this unit is made with reference to the transducer unit circuit diagram of figure 2.14. Mechanical details of the circuit board layout and magnetic E-core assembly are provided by figures 2.15 and 2.16 respectively.

Load current circulates through a 4 turn multi-strand coil wound onto the centre pole of an E-core pair. Flux set up by the load current in the centre pole of this magnetic circuit is monitored by a differential pair of linear Hall effect devices, H1 and H2. A differential connection of these devices is required to cancel out common mode temperature drift, which can become a problem if a single device is used. Differential amplifier IC1, which has unity gain, is used to buffer the differential signal from the

Hall effect devices, providing an output voltage which is proportional to the load current . Amplifier IC2 is then used to set the overall gain of the current transducer assembly to a nominal 10 A/V (set by preset resistor PR1). Preset resistor PR2 is used to cancel out any d.c. offset from the first amplifier stage.

2.3 The three-phase inverter

Two three-phase power transistor inverters producing controlled sinusoidal output currents over a wide frequency range were mounted in one of the power electronics racks alongside the vehicle track. These inverters provide the three-phase currents required by the a.c. armature windings of the linear synchronous motors when operated in combined levitative and tractive modes. A general description of inverter operation will now be given, followed by specific circuit details.

2.3.1 General description Each inverter uses the standard three-phase four quadrant bridge circuit shown in figure 2.17. A two level slitwidth modulation technique and class ABD operation[8] are employed to control the red and the yellow phase currents according to two reference sinusoids phase displaced by 120° . Further, by using a three wire star connected load, the uncontrolled blue phase current is defined by the sum of the two controlled phase currents. It is easily shown that this summation produces the negative of the required third phase sinusoid in the standard three-phase set. Hence, by reversing the blue phase load connection, it is possible to generate the required three-phase load currents using just two controlled phases.

2.3.2 Class ABD operation using slitwidth modulation In class ABD operation the controlled phases of the inverter can operate in any of three modes - rectification, flywheel and inversion (sometimes called regeneration). The inversion mode is only used when the reference input of a controlled phase is changing too quickly for the corresponding load current to follow in the flywheel mode.

It follows that to implement a slitwidth modulated 3-phase inverter using class ABD operation it is necessary for the error signal of each controlled phase to use two

symmetrical slitwidth windows, a first level window and a second level window, in which the second level is slightly larger than the first. To see how this arrangement works consider figure 2.18a, which shows the slitwidth modulated load current of a single phase inverter employing class ABD operation to follow a sinusoidal reference input. Figure 2.18b shows the corresponding error signal and illustrates the first and the second level slitwidth windows used to control the three inverter modes.

In normal operation the first level window is used to modulate the load current using alternate rectification/flywheel modes. If, however, a flywheeling load current cannot keep pace with a rapidly changing reference input, then the corresponding error signal will increase beyond the first level and eventually reach the second level, at which point the modulator will reconfigure the inverter for inversion. Assuming that the improved response of the inversion mode can force the load current more quickly than the changing reference, then the error signal will eventually traverse the full width of the second level slitwidth window and the next rectification cycle can commence. Normal operation is then resumed using the first level slitwidth window.

By using alternate rectification/flywheel modes whenever possible, the switching frequency of the power devices is kept to a minimum without compromising the level of output distortion.

2.3.3 Inverter operation It has been suggested that by using a three wire star connected load it is only necessary to control two of the three phase currents. For this to work, the load current in the two controlled phases must always have a return path through the third phase. This provides the criteria for controlling the switching elements in the third phase.

To best describe the method of control, consider the first segment ($0 \rightarrow 60°$) of the required three phase set of sinusoidal waveforms shown in figure 2.19, in which the two controlled phase currents, I_R and I_Y, are positive and the third phase current I_B is negative.

Figure 2.20a illustrates the inverter configuration used when both the red and the yellow phase currents require a rectification path. To achieve this, transistors TR1 and TR3 in the red and the yellow phases respectively are turned on, together with transistor TR6 in the uncontrolled blue phase to provide the return current path. This situation is sustained until either the red or the yellow phase currents (or both) requires a flywheel path to reduce the corresponding load current.

Figure 2.20b illustrates the situation when the yellow phase demands a flywheel path whilst the red phase still requires a rectification path. To achieve this, transistor TR3 is turned off and the corresponding yellow phase current then circulates through diode D4 and transistor TR6. Note that the red phase rectification path through transistors TR1 and TR6 remains undisturbed.

If, however, the flywheel path taken by the yellow phase current does not produce a sufficiently rapid fall in the load current magnitude, then an inversion path must be provided to speed up the rate of decay of this current. To achieve this the common path transistor TR6 would have to be turned off, which in turn would interrupt the rectification path required by the red phase current. Consequently there is a conflict between the requirement for an inversion path in the yellow phase whilst maintaining a rectification path in the red phase. Preference can either be given to the inversion path required by the yellow phase current (inversion preference), in which case the red phase current is directed through a flywheel path, or preference can be given to the rectification path required by the red phase current (rectification preference), in which case the yellow phase current continues in the flywheel path. The inverter used in the present study operates with inversion preference. Figure 2.20c illustrates the inversion preference situation, with the yellow phase current circulating in the inversion path comprised of diodes D4 and D5 whilst the red phase current is diverted through the flywheel path comprised of transistor TR1 and diode D5.

If, however, from figure 2.20a, the red phase demands a flywheel path whilst the yellow phase still requires a rectification path, then the inverter configuration illustrated in figure 2.20d is used. In this situation, transistor TR1 is turned off and the corresponding red phase flywheel current then circulates through diode D2 and transistor TR6. The yellow phase rectification path through transistors TR3 and TR6 remains undisturbed. If the red phase current then requires an inversion path, transistor TR6 is turned off as illustrated in figure 2.20e. In this case the red phase current circulates through the inversion path comprised of diodes D2 and D5 whilst the yellow phase current is forced to flywheel through transistor TR3 and diode D5 (due to the inversion preference of the inverter).

The situation in which both the red and the yellow phase currents of figure 2.20a require a flywheel path is illustrated in figure 2.20f. In this case transistors TR1 and TR3 are turned off such that the red and the yellow phase currents are then taken up by diodes D2 and D4 respectively. Transistor TR6 in the uncontrolled blue phase is held on to provide a common return current path. If both the red and the yellow phase currents then require an inversion path, transistor TR6 is turned off and the common return current is taken up by diode D5. This situation is illustrated in figure 2.20g.

To summarise, the positive switching elements in the red and the yellow controlled phases (transistors TR1 and TR3 respectively) together with the negative switching element of the uncontrolled blue phase (transistor TR6) can be switched to give any one of seven inverter modes over the first sixty degrees of the full three phase cycle illustrated previously in figure 2.19. These seven inverter modes define all of the possible combinations of rectification, flywheel and inversion modes that can be accommodated simultaneously in the two controlled phases. Further, by decoding the required polarity of each of the three phases and modulating the corresponding positive or negative switching elements of the inverter, it is easily shown that the seven

inverter modes can be implemented for the remaining five segments of the full three phase cycle. For example, in the second segment ($60 \rightarrow 120^{o}$), both the red and the blue phase currents are negative whilst the yellow phase current is positive. Hence transistors TR2, TR3 and TR6 are used for modulating the two controlled phases during this second segment.

2.3.4 Inverter control logic In practice then, the inverter control logic must include circuitry to perform the following,

1. Select the switching elements to be used according to the required polarity (positive or negative) of each of the three phase currents.
2. Select one of seven inverter modes according to the modulation request signals fed back from each controlled phase (rectification, flywheel or inversion). As stated earlier, the inverter is not able to accommodate all possible combinations of request, and conflicting requirements for simultaneous rectification and inversion of the two controlled phases are handled according to the inversion preference criteria.

Figure 2.21 shows a block diagram of the 3-phase inverter implementation used on the levitated vehicle. Specific details of each of the units making up the inverter will now be given.

2.3.5 Reference generator board The reference generator board includes the circuitry for generating two accurate sinusoids, phase displaced by 120^{o}, for use as the red and the yellow phase reference inputs. Polarity signals for the red, the yellow and the blue phases are also derived. The following circuit description refers to the reference generator board circuit diagram of figure 2.22. Figure 2.23 provides the corresponding board layout details.

The red and the yellow reference signals are generated using two EPROM based sinewave lookup tables (IC8 and IC11 respectively), which contain eight bit data in an

offset binary format (0-255) as shown in figure 2.24. For completeness, this diagram also shows the required waveform of the uncontrolled blue phase.

Considering the red phase circuitry, the EPROM data from IC8 is presented directly to IC9, which is an eight bit high speed D to A converter device. In this application, IC9, together with the transresistance amplifier configuration formed using op-amp IC10, is configured to convert the eight bit offset binary data from IC8 into a corresponding bipolar voltage signal, R_{ref}, which is in the range $-V_{ref}$ to $+V_{ref}$. V_{ref} is the multiplying reference input to the DAC (nominally in the range 0 to 5 V), and can be set either manually, using a panel mounted potentiometer VR2, or remotely, using the voltage signal from the panel mounted BNC socket J4. The changeover switch SW4b is used to select the appropriate amplitude control signal.

Because an offset binary number system is used, the polarity signals $\overline{RED}$ and $\overline{YELLOW}$ of the reference sinusoids can be obtained directly from the msb of the corresponding DAC data bus. Further, by using phase offsets of $+60^{o}$ and -60^{o} for the red and the yellow phase reference sinusoids respectively, it can be seen from figure 2.24 that the blue phase polarity signal, $\overline{BLUE}$, is represented by the msb of the six bit EPROM address bus.

This address bus, which is common to both the red and the yellow phase EPROMS, determines the current operating position of the inverter ($0 \rightarrow 360^{o}$) along the three-phase sinusoidal waveform. Normally this operating position signal is provided by the output of the pole position transducer system introduced in section 2.4.3, thus providing closed loop torque angle control of the linear synchronous motors. This is achieved by using a tri-state octal buffer, IC6, to interface the common address bus to a 9-way D-type connector, J2, mounted on the front panel of the reference generator board.

For test purposes, the inverter can also be operated in a free running open loop mode

with manual frequency control. This is achieved by using a second tri-state octal buffer, IC5, to interface the common address bus to an eight bit ripple counter, IC4. This device is clocked at a variable frequency ϕ by the oscillator circuit comprised of IC1 and associated components. Manual control of this clock frequency, and hence the free running frequency of the inverter, is provided by potentiometer VR1 mounted on the front panel of the reference generator board. If required, the DIL switch pack SWP1 can be used to select one of two lower clock frequencies ($\phi/8$ or $\phi/16$) derived using the frequency prescaler device, IC2. Further, to provide an inverter run/stop facility, the two input NAND gate of IC3 is used in conjunction with the panel mounted switch SW2 to enable or disable the clock signal into IC4.

The changeover switch SW1, mounted on the front panel of the reference generator board, is used to select the required inverter mode by enabling the appropriate octal buffer device onto the common address bus.

Now it can be seen from figure 2.24 that the polarity of the three-phase output currents can be reversed by inverting the msb of the position signal. Hence polarity control of the inverter was achieved by preceding the msb of the common EPROM address bus with an exclusive-OR gate, IC7, which acts as a selectable inverter/buffer according to a polarity control signal. This signal can be set either manually, using SW3, or remotely, using the voltage signal from the panel mounted BNC socket, J3. The changeover switch SW4a is used to select the appropriate signal source.

2.3.6 Modulator and switching control board The modulator and switching control board includes the two level slitwidth comparator circuitry required for both the red and the yellow phase modulators and also includes an EPROM implementation of the required inverter switching control logic[9] discussed previously in section 2.3.4. The following circuit description refers to the modulator and switching control board circuit diagram of figure 2.25. Figure 2.26 provides the corresponding board layout details.

Considering the red phase circuitry, the sinusoidal reference input R_{ref} from the reference generator board is first buffered and inverted using op-amp IC1. Summing amplifier IC2 is then used to add the inverted reference signal to the corresponding feedback signal from the red phase load current transducer, thus generating the red phase error signal. To provide the first and the second level slitwidth modulator outputs, this error signal is monitored by two comparator circuits formed using op-amps IC3 and IC4 respectively and associated components. The first level comparator generates the red phase flywheel request signal, F_R, whilst the second level comparator generates the red phase inversion request signal, I_R. These two TTL compatible signals provide two of the seven inputs to the inverter switching control logic. Preset resistors PR1 and PR2 set the first and the second level window limits respectively.

The switching control logic for the inverter was implemented using EPROM IC10, which decodes the phase polarity signals from the reference generator board ($\overline{RED}$, $\overline{YELLOW}$ and $\overline{BLUE}$), together with the four slitwidth modulation request signals (F_R, I_R, F_Y and I_Y), to generate the switching control signals for the six power devices. The input signals to the EPROM are strobed on every positive going edge of a 100 kHz clock using octal latch IC9, whilst the six EPROM outputs are strobed one half clock cycle later using hex latch IC11. This half clock period is necessary to allow for the minimum data set up time required by the EPROM.

Now whilst the general procedure for generating the switching functions provided by IC10 has been described previously in section 2.3.3, it is beyond the scope of this thesis to actually set out the full set of switching functions for the inverter.

The six modulator outputs from IC11 are then frequency limited using three monostable circuit pairs, IC14, IC15 and IC16, to provide guaranteed minimum on/off times for the power devices. Finally, the six open collector buffers of IC18 are used to ensure sufficient output drive capability for the opto-isolators on the gate drive units.

2.3.7 Gate drive unit and power transistor stage Each of the open collector signals from the switching control logic discussed above is required in the form of an isolated voltage drive for charging and discharging the gate-source capacitance of a power switching HEXFET[10]. The following circuit description is made with reference to figure 2.27, which provides the circuit diagram of the gate drive unit and power transistor stage. Figure 2.28 provides the corresponding component layout details.

The logical on/off demand signal from the switching control logic is electrically isolated at the input of the gate drive unit using opto-isolator OPTO1, and is then directly coupled to a voltage amplifier comprised of transistors TR1 through TR5 inclusive and associated components. In the on-state, this amplifier provides a gate-source voltage of 12 V for the heatsink mounted HEXFET, TR6. Note that the series resistor R6 in the gate circuit of this device is required to damp out parasitic oscillations, whilst the zener diode ZD1 is necessary to limit the gate-source voltage to a safe level of 12 V. The heatsink assembly also includes the corresponding flywheel diode D2 and associated snubbing network components D3, R7 and C3.

An isolated d.c. supply for the gate drive unit is derived from a mains input using one of six isolated windings on transformer TX1. A full wave bridge comprised of diodes D4 through D7 inclusive is used, together with filter capacitors C4 and C5. Regulated +12 V and +5 V supplies are then derived using voltage regulator devices IC1 and IC2 respectively.

2.3.8 Load current transducer The current feedback signals from the red and the yellow phase load circuits are provided by two isolated load current transducer units. These units are identical to those used in the current feedback choppers described previously except that a more sensitive gain of 1.5 A/V is used. A full description of these units is given in section 2.2.6.

2.4 Vehicle transducers

The present vehicle control software required the measurement of the height and side displacements of each corner of the vehicle, the vertical acceleration of the four linear synchronous motors and, for the tractive mode controller, the position of the vehicle along the track. Outputs from the digital controller were to drive the linear synchronous motors and side control magnets via the current feedback choppers and 3-phase inverters described previously.

2.4.1 The displacement transducers Relative displacements were derived by measuring the phase difference between transmitted and received 40 kHz ultrasonic signals reflected off the tracks from remote transducer units. Functional details of these remote ultrasonic sender/receiver units will be discussed in section 2.6.3 together with the required phase measurement electronics. Figure 2.29 provides details of the positioning of the units on the prototype vehicle.

2.4.2 The accelerometers A Brüel & Kjaer piezoelectric accelerometer type 8306[11] was mounted in the vertical plane at each corner of the vehicle and supplied with 24 V d.c. from a common source. This type of accelerometer has an integral voltage output amplifier calibrated to give a nominal 1000 mV/ms^{-2} output within the accelerometer limits of $\pm 5\ g$. Details of the positioning of the accelerometers are provided in figure 2.29.

2.4.3 The pole position transducer The relative position of the vehicle along the track was derived from the output of a non-contact pole position transducer system specifically designed to provide the position feedback signal required by each 3-phase inverter. The transducer system has a resolution of 5 mm and provides a six bit digital output representing the position of a secondary track member within the 0.2 m pitch of these members. This output rolls through zero and repeats as each track member passes over the sensor array. Details of the design and implementation of the pole position transducer system will be given in chapter 8.

2.5 The multiprocessor system

To achieve the necessary throughput required by the digital controller, a multiprocessor computer system developed at the University of Bath was used as shown in the block diagram of figure 2.30. The complete system was mounted in a single rack on the vehicle chassis.

The MC68000 microprocessor based Single Board Computer (SBC) processing nodes and the four channel bus arbitration card were designed at the University of Bath by Dale[12] as part of a study into the real-time simulation of power system transient behaviour. These two boards form the basis of a multiprocessor system having a closely coupled architecture in which all task address space is globally accessible. This allows data blocks to be passed by reference only, without the need to copy and reconstitute the data on the target processing node.

2.5.1 The Multiprocessor Operating System The multiprocessor operating system[12] used in the development of real-time control programs was developed at the University of Bath from TRIPOS[13-15], a multitasking single processor operating system. By maintaining compatibility with standard TRIPOS, multiprocessor Tripos has all of the standard TRIPOS commands available. These commands include an editor, assemblers, compilers, a linker and various debugging tools, and so provides a very comprehensive software development suite.

Typically this full multiprocessor Tripos would only be loaded onto one of the processing nodes making up the multiprocessor system. This node would then be responsible for all IO handling (terminal, disk etc) and would be used to download programs onto the remaining processors (called Slave or Remote processing nodes). The remote processors are then only required to run a simplified TRIPOS real-time kernel and serving tasks and consequently are able to dedicate more time to the real-time control programs.

A description of the hardware making up the complete multiprocessor system will now be given.

2.5.2 MC68000 processing nodes For the purpose of the real-time control work carried out in this thesis, the multiprocessor system included three of the MC68000 based SBC's. By convention, only one of these SBC's was fully populated with all the IO hardware and multiprocessor Tripos bootstrap EPROMS. The bootstrapping procedure loads the multiprocessor kernel and Tripos superstructure into this IO processor from hard disc. Once the IO processor is running, a system load command can be executed in the initialisation sequence to down load from disc the real-time kernels and serving tasks to each of the remaining processors.

Due to the closely coupled architecture of the multiprocessor system, each of the SBC's has a dual ported memory which may be accessed either locally by the host processor, or externally via the shared bus. In its local memory, a processor has access priority and may run at full speed. To access other memory areas, the processor must request the shared bus and wait for arbitration to allow the access to continue. Once a processor has ownership of the bus, it may address the bus mounted memory and IO cards or the contents of other processors via the dual porting arrangement.

Due to the inevitable time overhead associated with memory access via the shared bus it is common for each processor within the system to be pre-loaded with all the program segments it will require before run time. Hence all further shared bus activity during run time is restricted to inter-processor communication only. By suitable partitioning of the real-time control program, inter-processor communication can be minimised.

2.5.3 System arbiter board The shared bus arbiter was a four channel parallel arbiter with each channel daisy chained by the SBC's. Ideally all SBC's require an equal priority because the task distribution of application programs is unknown. However, because the amount of shared bus bandwidth used by one SBC is small, the

use of a fixed priority arbiter will not cause the exclusion of a low priority SBC for any appreciable time.

2.5.4 Quarter megabyte dynamic RAM memory board with error detection and correction logic[16]. This board provides extra shared memory which is not the local memory of any one processing node. It is used as a communications area between processors running a partitioned real-time controller.

2.5.5 High resolution colour graphics controller board The high resolution colour graphics board[16] is based on the Thomson EF9366 colour graphics controller and features 2 pages or screens of 256 by 512 pixels in 8 colours. Use of this board for the graphical display of test results was made via GKS (Graphics Kernel System), which was implemented on the 68000 machines at Bath by Selwyn and Chandler[17].

2.5.6 MultiLink local area network board MultiLink[18] is a low cost ring type local area network which provides virtual character stream data links between network stations. The MultiLink network provides a file transfer mechanism to other computers and also access to shared printers and graphics pen plotters.

2.5.7 Dedicated IO boards Purpose designed interface boards were built for taking transducer readings and setting chopper demand currents on the vehicle. The following sections cover the design and construction of these circuits.

2.6 Gap measurement board and Remote transducer units

The eight vehicle mounted remote transducer units discussed earlier in section 2.4.1, were interfaced to the multiprocessor system using a purpose designed eight channel phase measurement board based on an original design by Dunn[2]. Each of the eight channels uses a high speed synchronous state machine to implement the phase measurement logic, producing an updated phase reading every 50 μs independently of the system processors. Hence, to read any channel, either of the system processors simply performs a byte access of the appropriate channels output latch.

A general description of the gap measurement technique will now be given, followed by specific functional details of the hardware realisation.

2.6.1 General description Each gap measurement point requires an ultrasonic transmitter/receiver pair, collectively called a remote transducer unit, mounted opposite a static reference surface as shown in figure 2.31. The ultrasonic transmitter is continuously energised with a high stability 40 kHz reference signal derived from a crystal oscillator. The 40 kHz acoustic signal from the transmitter is reflected from the reference surface and then picked up by the ultrasonic receiver, which in turn produces a 40 kHz electrical return signal phase displaced from the 40 kHz reference. Because this phase difference is directly related to the acoustic path length taken by the ultrasonic signal, any change in the measured phase between the transmitted and received signals can be directly related to a corresponding change in measured gap.

2.6.2 Resolution The phase difference between the reference and returned 40 kHz signals is measured by using a high speed counter to time the delay between an edge of the reference signal and the corresponding edge of the return signal. Hence any relative gap displacements can be accurately measured by reading the counter value at the end of each timed interval and comparing these values with a reference counter value obtained at the rest position. The accuracy of this measurement is determined by the resolution of the counter, which can be expressed in terms of gap displacement according to equation 2.1 below,

$$gap\ resolution = \frac{1}{2} \times velocity\ of\ sound \times \frac{1}{\phi} \qquad \text{equation 2.1}$$

where ϕ is the clock frequency of the counter.

The factor of ½ is required because the distance between the remote transducer unit and the reference surface, i.e. the measured gap, is approximately half the acoustic path length.

Note that absolute displacements cannot be determined when using a continuous

ultrasonic signal. This is because it is not possible to associate a received wavefront with its corresponding transmitted wavefront. In practice this does not present a problem because an absolute displacement offset can be introduced into the software used for reading the gap transducers.

Figure 2.32 shows a block diagram of the gap measurement hardware used on the levitated vehicle. Specific details of each of the units making up the gap measurement system will now be given.

2.6.3 Remote transducer units The remote transducer unit contains the ultrasonic transmitter/receiver transducer pair together with additional signal conditioning circuitry to shape the receivers low level output signal into a TTL compatible square wave output. The following circuit description refers to the remote transducer unit circuit diagram of figure 2.33. Figure 2.34 provides the corresponding component layout details.

A 40 kHz signal from a line driver on the gap measurement board is used to drive the resonant 40 kHz ultrasonic transmitter unit, TX1, which generates a high stability ultrasonic signal. This signal is reflected from the reference surface opposite the unit and picked up by the ultrasonic receiver, RX1. The output from RX1 is buffered by the unity gain emitter follower configuration of transistor TR1 and a.c. coupled to comparator IC1 via C8 and R3. At this point the comparator input is in the form of a low level sinusoidal voltage signal with a mean level of 0 V. Hence, by setting the comparator reference input to zero using R4, the comparator output will change state every half cycle of the input sinewave to produce a TTL compatible square wave signal in phase with the received sinusoidal signal. Finally, the parallel combination of the open collector gates of IC2 is used to ensure sufficient output drive capability for the opto-isolated inputs on the gap measurement board.

2.6.4 Gap measurement board The gap measurement board included eight independent phase measurement channels together with the required multiprocessor backplane interfacing circuitry. In addition, the board also provided eight 40 kHz drive signals for the ultrasonic transmitter units. The following circuit description is made with reference to the gap measurement board circuit diagram of figure 2.35. Figure 2.36 provides the corresponding component layout details.

The 40 kHz reference for the phase measurement circuitry and the ultrasonic transmitter units was derived from an accurate base frequency of 10.240 MHz generated by the crystal controlled oscillator circuit formed using IC9. IC11 is then used to divide this base frequency by 256 to produce the required 40 kHz reference signal. Two four-channel line drivers, IC13 and IC14, are used to ensure sufficient drive capability for the 40 kHz ultrasonic transmitters contained within each of the eight remote transducer units.

Return signals from the remote transducer units are taken from two 25-way D-type connectors, J1 and J2, mounted on the front panel of the gap measurement board. These open collector signals are electrically isolated from the gap measurement electronics using four dual-channel opto-couplers, OPTO1 through OPTO4 inclusive. This isolation was added to reduce the noise level on the return signals, which were found to pick up considerable interference from the 40 kHz electrical drive to the ultrasonic transmitters. Without the improved noise immunity offered by this isolation technique, earlier versions of the gap measurement board had exhibited high levels of noise on the phase readings.

Considering channel one only, the isolated 40 kHz return signal from OPTO1 is first divided by two, using one half of IC15, to produce a 20 kHz return signal having an equal mark-space ratio. Similarly the 40 kHz reference signal is also divided by two using one half of IC12. To understand why 20 kHz reference and return signals are used, recall that the phase difference between these two signals is measured by using a

high speed digital counter to time the delay between an edge of the reference signal and the corresponding edge of the return signal. Since either edge of the reference signal can be used to start the timing interval, it follows that an unequal mark-space ratio in either the reference or returned signals would give rise to an uncertainty in the final count value, which in turn would lead to a phase reading jitter.

The 20 kHz reference and return signals provide the two inputs to the phase measurement circuit, which was implemented as a high speed synchronous state machine using an 8-bit latch, IC101, and a bipolar PROM, IC102. The state machine controls the clear input of an 8-bit counter, IC103, to time the delay between an edge of the reference signal and the next edge of the return signal. A full description of the phase measurement state machine is given in appendix B.

Using a clock frequency of 10.240 MHz the corresponding gap measurement resolution represented by the lsb of the counter can be calculated using equation 2.1 reproduced below,

$$\begin{aligned} gap\ resolution &= \frac{1}{2} \times velocity\ of\ sound \times \frac{1}{\phi} \\ &= \frac{1}{2} \times 331.45 \times \frac{1}{10.240 \times 10^6} \\ &= 16\mu m \end{aligned} \qquad \text{equation 2.2}$$

At the end of each timed interval a tri-state octal latch, IC104, is used to store the final count value. This is achieved by strobing the current counter value into the latch using the rising edge of the counter clear signal, which is taken high at the end of the timed interval. Because the latch has zero set up time, there is no danger of the count value being cleared before the data can be transferred. The octal output from the latch is connected to an eight bit data bus together with the outputs from the other seven channels. This internal data bus is interfaced to the lower eight bits of the backplane data bus using octal buffer, IC8. Hence by strobing the output enable of one of the eight latches, together with the output enable of the backplane buffer, the final count

value of the selected channel will be transferred to the backplane data bus.

The remainder of the gap measurement board circuitry is concerned with the backplane interface, providing the mechanism by which the output latch of each phase measurement channel can be interrogated by either of the system processors. The following description of the backplane interface circuitry is made with reference to the timing diagram of figure 2.37, which shows a typical off board read cycle for one of the 68000 single board computers. Figure 2.38 shows the corresponding flowchart, which divides the read cycle between the gap measurement board and the 68000 single board computer in order to illustrate the backplane handshaking protocol. Backplane signal assignments are shown in table 2.1.

Backplane address lines A_1 to A_{11} inclusive, together with the IO address strobe ($\overline{IOPAGE}$) and upper and lower data strobes ($\overline{UDS}$ and $\overline{LDS}$ respectively), are brought onto the gap measurement board via two octal buffers, IC1 and IC2. An eight bit equal-to comparator, IC3, is then used to compare the upper eight address lines, A_4 to A_{11} inclusive, with the preset board address set up on the DIL switch pack, SWP1. Once a matching address is found the address strobe $\overline{IOPAGE}$ enables the comparator output which in turn asserts* the board select signal, $\overline{BS}$. Once selected, the gap measurement board is required to maintain the 68000 handshake protocol by placing the requested data onto the backplane data bus and asserting the $\overline{DTACK}$ backplane handshake signal.

An on board data strobe, $\overline{DS}$, was derived using IC5 to produce a negative logic OR combination of the 68000 upper and lower data strobe signals. The negative logic AND gate of IC7 combines this data strobe with the board select signal, thus ensuring that

* The terms *assertion* and *negation* will be used extensively throughout this thesis. This is done to avoid confusion when dealing with a mixture of active-low and active-high signals. The term assert or assertion is used to indicate that the signal is active or true independent of whether that voltage is low or high. The term negate or negation is used to indicate that a signal is inactive or false.

the data strobe is only asserted during an access of the gap measurement board. The gated data strobe, $\overline{GDS}$, performs the following three functions,

1. Enables the 3-to-8 line decoder, IC4, to select one of the eight output latches according to the address set up on the lower three address lines A_1, A_2 and A_3.
2. Enables the backplane data buffer, IC8.
3. Asserts the $\overline{DTACK}$ backplane handshake signal via the open collector buffer of IC6.

Data from the selected output latch remains on the backplane data bus until it is latched by the requesting processor, which then negates the address and data strobe signals. This in turn causes the gap measurement board to release the backplane data bus and negate the $\overline{DTACK}$ signal, thus terminating the 68000 read cycle.

The gap measurement software, which interprets the phase readings to provide absolute gap displacement data for each of the eight measurement points, is described in detail in chapter 5. Table 2.2 below provides the backplane address of each of the eight channels on the gap measurement board. To read a given channel, either of the system processors simply performs a byte read of the appropriate address.

Channel	Gap transducer	Address (hex)
channel 1	corner 1 height	8404F1
channel 2	corner 2 height	8404F3
channel 3	corner 3 height	8404F5
channel 4	corner 4 height	8404F7
channel 5	corner 1 side	8404F9
channel 6	corner 2 side	8404FB
channel 7	corner 3 side	8404FD
channel 8	corner 4 side	8404FF

TABLE 2.2. Gap transducer addressing

2.7 Analogue to digital converter board

The four vehicle mounted accelerometers were interfaced to the multiprocessor system using a purpose designed 8-bit analogue to digital converter board. Although only four

channels were required, eight channels were implemented on the board to allow for possible future expansion. An on board clock and associated control circuitry are used to allow each of the eight channels to function at maximum speed independently of the system processors, with all channels producing an updated result every 14 μs. Hence to read any channel either of the system processors simply performs a byte read of the appropriate output latch. This is in contrast to simpler analogue to digital converter circuit designs which require a start conversion pulse from the processor, with the processor then having to wait for the duration of the conversion time before the result is available.

The following circuit description is made with reference to the analogue to digital converter board circuit diagram of figure 2.39. Figure 2.40 provides the corresponding component layout details.

Each of the eight analogue inputs is taken from one of eight corresponding BNC sockets mounted on the front panel of the analogue to digital converter board. Considering channel one, the input is first attenuated by the potential divider combination of resistors R101 and R102 and is then buffered by the unity gain voltage follower op-amp configuration formed using half of IC101. The level of signal attenuation at the output of this stage is given by equation 2.3 below,

$$d.c.gain = \frac{R_{102}}{R_{101} + R_{102}}$$

$$= \frac{1K}{15K + 1K}$$

$$= \frac{1}{16} \qquad \text{equation 2.3}$$

To avoid aliasing problems the attenuated signal is frequency limited by the second order low pass Butterworth filter configuration formed using the second half of IC101 and associated components. The overall transfer function for the combined attenuator and Butterworth filter sections is then given by equation 2.4 below,

$$T(s) = \frac{1}{16} \times \frac{2}{(sRC)^2 + sRC + 1} \qquad \text{equation 2.4}$$

where $R = 33K$ and $C = 10nF$

Consider the standard form of transfer function for a second order low pass Butterworth filter section[19] given by equation 2.5 below.

$$T(s) = \frac{a_0}{\frac{s^2}{\omega_0^2} + \frac{s}{\omega_0} + 1} \qquad \text{equation 2.5}$$

where ω_0 is the 3 dB roll off frequency and a_0 is the d.c. gain.

Comparing equation 2.4 with the standard form the following values for ω_0 and a_0 were determined.

$$\omega_0 = \frac{1}{RC}$$

$$= \frac{1}{33\times10^3 \times 10\times10^{-9}}$$

$$= 3030\ rad.s^{-1}$$

or

$$f_0 = \frac{3030}{2\pi}$$

$$= 480\ Hz$$

The corresponding d.c. gain, a_0, is 0.125

The filter output is connected to IC102, which is an 8-bit successive approximation A/D converter device. In this application IC102 is configured to accept a unipolar input signal in the range 0 to V_{refin}, where V_{refin} is nominally 2.55 volts as governed by an on-chip reference source. Thus the overall resolution of each conversion channel when combined with the 1000 mV/ms^{-2} gain of the accelerometers is given by equation 2.6 below.

$$resolution = \frac{2.55}{0.125} \times \frac{1}{256} \times 1.0$$

$= 0.08\ ms^{-2}/lsb$ equation 2.6

To perform an analogue to digital conversion, IC102 requires a clock signal and an appropriate negative going pulse on the start conversion input, $\overline{SC}$. Nine clock cycles after the start conversion pulse, the end of conversion output (EOC) is taken high to indicate that valid 8-bit data has been latched onto the devices tri-state bus. This data can then be read by asserting the output enable line, OE.

The analogue to digital converter board included additional circuitry to implement the above described signal protocol autonomously (i.e. independent of either of the system processors) at the maximum speed supported by the A/D devices. The following description of this circuitry is made with reference to the control signal timing diagram of figure 2.41.

A 640 kHz clock was derived from an accurate base frequency of 10.240 MHz generated by the crystal controlled oscillator circuit formed using IC9. IC10 is then used to divide this base frequency by 16 to produce the required 640 kHz. The negative going $\overline{SC}$ pulses were derived from the EOC output of the A/D device using a positive edge triggered D-type latch, IC11. The latch was required to stretch and invert the EOC output over one period of the 640 kHz clock, thus providing a guaranteed minimum width for the $\overline{SC}$ pulse.

At the end of each conversion a tri-state octal latch, IC103, is used to store the data output from the A/D converter. This is achieved by strobing the converter data into the latch using the rising edge of the EOC signal. The octal output from the latch is connected to a common eight bit data bus together with the outputs from the other seven channels. This internal data bus is interfaced to the lower eight bits of the backplane data bus using octal buffer, IC8. Hence by strobing the output enable of one of the eight latches, together with the output enable of the backplane buffer, the data from the selected A/D channel is transferred to the backplane data bus.

The remainder of the analogue to digital converter board circuitry is concerned with the backplane interface, providing the mechanism by which the output latch of each A/D channel can be interrogated by either of the system processors. This circuitry, which is comprised of IC's 1 through 8 inclusive, is identical to that used on the gap measurement board described previously, and is fully explained in section 2.6.4. Table 2.3 below provides the backplane address of each of the eight converter channels on the analogue to digital converter board. To read a given channel, either of the system processors simply performs a byte read of the appropriate address.

Channel	Accelerometer	Address (hex)
channel 1	corner 1	8405F1
channel 2	corner 2	8405F3
channel 3	corner 3	8405F5
channel 4	corner 4	8405F7
channel 5	spare	8405F9
channel 6	spare	8405FB
channel 7	spare	8405FD
channel 8	spare	8405FF

TABLE 2.3. Accelerometer addressing

2.8 Digital to analogue converter board

The eight current feedback chopper units described in section 2.2 were interfaced to the multiprocessor system using a purpose designed eight channel digital to analogue converter board. Hence either of the system processors is able to set chopper demand currents for the LSM d.c. windings and side control magnets by writing bytes of data to the appropriate D to A channels. The following circuit description is made with reference to the digital to analogue converter board circuit diagram of figure 2.42. Figure 2.43 provides the corresponding component layout details.

Incoming data from the multiprocessor backplane is directed to the appropriate D to A channel by the backplane interface circuit comprised of IC's 1 through 8 inclusive. This circuitry is identical to the interface circuitry used on the gap measurement and A to D boards, and is fully described in section 2.6.4. Note however that the direction of the

data buffer, IC8, is reversed to accept data coming in from the backplane.

Considering D to A channel one, the data received from the backplane interface circuit is first latched using octal latch, IC101. The latched data is then presented to IC102, which is an 8-bit high speed current output D to A converter device. In this application, IC102 is configured to convert the eight bit data from IC101 into a corresponding unipolar current signal, I_{out}, which is in the range 0 to $-I_{fs}$. I_{fs} is the full scale output current set by resistor R101.

$$-I_{fs} = \frac{V_{cc}}{R_{101}}$$

$$= \frac{12}{6200}$$

$$= 1.935\ mA$$

Finally an inverting transresistance amplifier configuration formed using IC103 was used to convert the output current from IC102 into an equivalent voltage signal, V_{out}. This signal was then made available as the D to A channel output via the BNC socket mounted on the front panel of the digital to analogue converter board. The full scale output voltage, V_{fs}, from this final stage is governed by gain setting resistor R103,

$$V_{fs} = -I_{fs} \times R_{103}$$

$$= 1.935 \times 10^{-3} \times 2700$$

$$= 5.2\ V$$

Note that capacitor C102 was included across R103 to prevent ringing during transitions of the output voltage.

When connected to one of the vehicles current feedback choppers, the overall resolution of the D to A channel and chopper combination would be given by equation 2.7 below (recall that the nominal chopper gain is 10 A/V).

$$resolution = \frac{5.2}{256}\ V/lsb \times 10\ A/V$$

$= 0.2\ A\ /lsb$ equation 2.7

Table 2.4 below provides the backplane address of each of the eight channels on the digital to analogue converter board together with the corresponding chopper assignment.

Channel	Chopper	Address (hex)
channel 1	corner 1 height	8406F1
channel 2	corner 2 height	8406F3
channel 3	corner 3 height	8406F5
channel 4	corner 4 height	8406F7
channel 5	corner 1 side	8406F9
channel 6	corner 2 side	8406FB
channel 7	corner 3 side	8406FD
channel 8	corner 4 side	8406FF

TABLE 2.4. Chopper addressing

2.9 Inverter interface board

The two 3-phase inverter units described in section 2.3, together with the pole position transducer system introduced in section 2.4, were interfaced to the multiprocessor system using a purpose designed inverter interface board. This board includes the following circuitry.

1. A single digital to analogue converter channel. This is used to set the rms current demand to the two 3-phase inverters.
2. An open collector latched output port for setting the output polarity of the two 3-phase inverters.
3. An eight bit parallel input port for reading the output of the pole position transducer system.

The following circuit description is made with reference to the inverter interface board circuit diagram of figure 2.44. Figure 2.45 provides the corresponding board layout details.

2.9.1 Backplane interface Backplane data flow to and from the inverter interface board is controlled by the backplane interface circuit comprised of IC's 1 through 8 inclusive. This circuitry is identical to the interface circuitry used on the gap measurement, A to D and D to A boards, and is fully described in section 2.6.4. Note however that in this application the data buffer IC8 is a bidirectional device which makes use of the backplane control signal $R/\overline{W}$ to control the direction of data flow.

2.9.2 Digital to analogue converter channel The digital to analogue converter channel implemented on the inverter interface board is comprised of an octal latch IC9, an eight bit high speed current output D to A converter device IC10 and an inverting transresistance amplifier configuration formed using IC11 and associated components. This conversion circuitry is identical to that used on the digital to analogue converter board described previously, and is fully explained in section 2.8. The output signal from IC11 is made available as the D to A channel output via the BNC socket J3 mounted on the front panel of the inverter interface board.

The overall gain of the digital to analogue converter channel is reproduced in equation 2.8 below (recall that the nominal full scale output voltage V_{fs} is 5.2 V),

$$resolution = \frac{5.2}{256}$$

$$= 0.02\ V/lsb \qquad \text{equation 2.8}$$

2.9.3 Latched output port The latched output port is based on the first stage (data latch) of the digital to analogue converter circuit discussed above, and uses octal latch IC12 to latch the data from the backplane interface circuit. The least significant output bit from this latch, D_0, is buffered using a series combination of two open collector inverters from IC6. The buffered output signal is then presented to BNC socket J4 mounted on the front panel of the inverter interface board.

2.9.4 Parallel input port The eight bit parallel input port is comprised of a tri-state octal buffer device, IC13, connected to the 9-way D-type connector, J5, mounted on the

front panel of the inverter interface board. To avoid possible problems with floating inputs, the input bus from J5 is also pulled low using resistor pack RP2.

Table 2.5 below provides the backplane address of each of the IO channels on the inverter interface board.

Channel	Function	Address (hex)
channel 1	D to A	8404E1
channel 2	output port	8404E3
channel 3	input port	8404E5

TABLE 2.5. Inverter interface addressing

Pin No.	Edge connector J1		Edge connector J2	
	Row a	Row c	Row a	Row c
32	+5 V	+5 V	+5 V	+5 V
31	-5 V	-5 V	+15 V	-15 V
30	D14	D15	FC0	DLY1
29	D12	D13	FC1	DLY2
28	D10	D11	FC2	DLY3
27	D8	D9	FC3	DLY4
26	D6	D7	$\overline{IAKOC}$	DLY5
25	D4	D5	$\overline{POR}$	DLY6
24	D2	D3		DLY7
23	D0	D1	$\overline{IRQ\,7}$	DLY8
22	$\overline{ASOLD}$		$\overline{IRQ\,6}$	$\overline{IOPAGE}$
21	EOLD		$\overline{IRQ\,5}$	$\overline{68PG}$
20	$\overline{RESET}$	$\overline{BR\,0}$	$\overline{IRQ\,4}$	
19	$\overline{R/W}$	$\overline{DTACK}$	$\overline{IRQ\,3}$	$\overline{BR\,3}$
18	$\overline{VMA}$	$\overline{VPA}$	$\overline{IRQ\,2}$	$\overline{BR\,2}$
17	$\overline{BERR}$	$\overline{BGACK}$	$\overline{IRQ\,1}$	$\overline{BR\,1}$
16	$\overline{UDS}$	$\overline{LDS}$	$\overline{BGOUT\,0}$	$\overline{BGIN\,0}$
15	CLK	A20	$\overline{IAOUT}$	$\overline{IAIN}$
14	A18	A19	$\overline{BGOUT\,3}$	$\overline{BGIN\,3}$
13	A16	A17	$\overline{BGOUT\,2}$	$\overline{BGIN\,2}$
12	A14	A15	$\overline{BGOUT\,1}$	$\overline{BGIN\,1}$
11	A12	A13	$\overline{AS}$	ECLK
10	A10	A11		
09	A8	A9	PCL3	
08	A6	A7	PCL2	$\overline{HIBYTE}$
07	A4	A5	PCL1	$\overline{DTC}$
06	A2	A3	PCL0	$\overline{DONE}$
05	A21	A1	$\overline{DREQ\,3}$	$\overline{DACK\,3}$
04	A22	A23	$\overline{DREQ\,2}$	$\overline{DACK\,2}$
03	-12 V	-12 V	$\overline{DREQ\,1}$	$\overline{DACK\,1}$
02	+12 V	+12 V	$\overline{DREQ\,0}$	$\overline{DACK\,0}$
01	0 V	0 V	0 V	0 V

TABLE 2.1. Backplane signal assignments

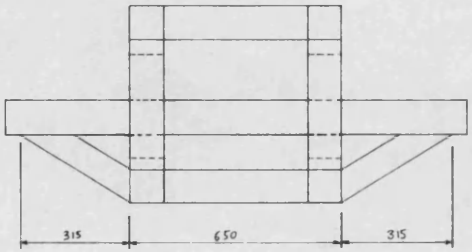

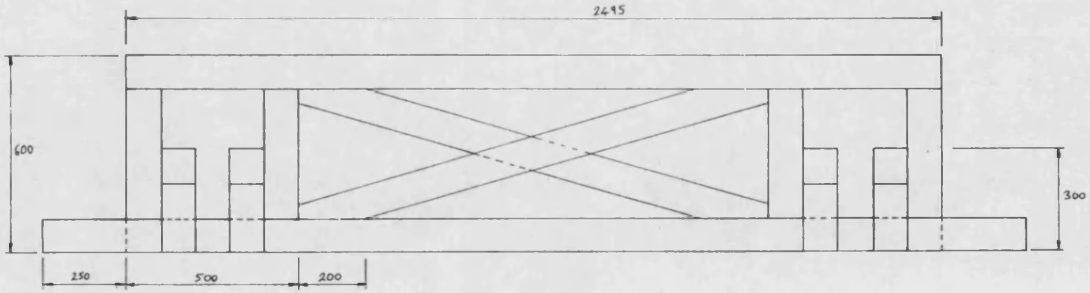

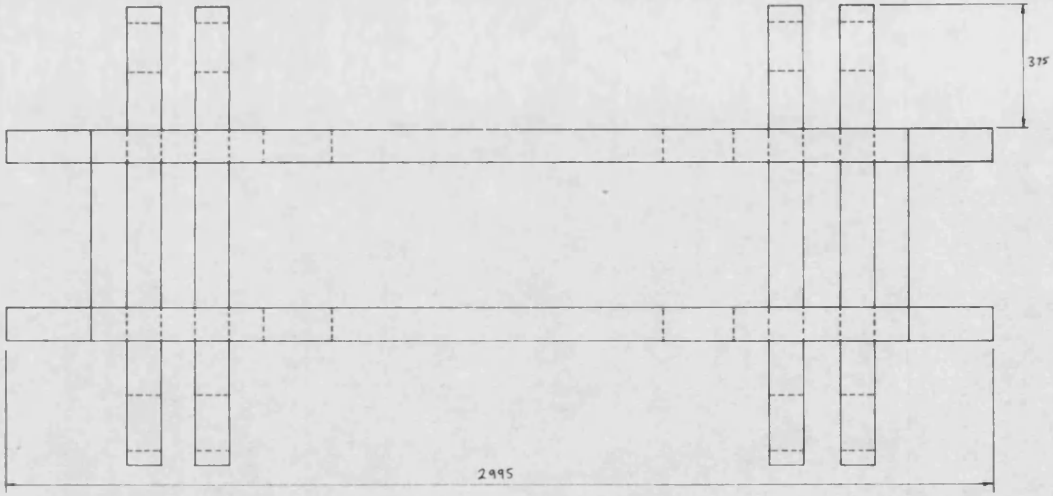

Dimensions in mm

Box section aluminium chassis Figure 2.1

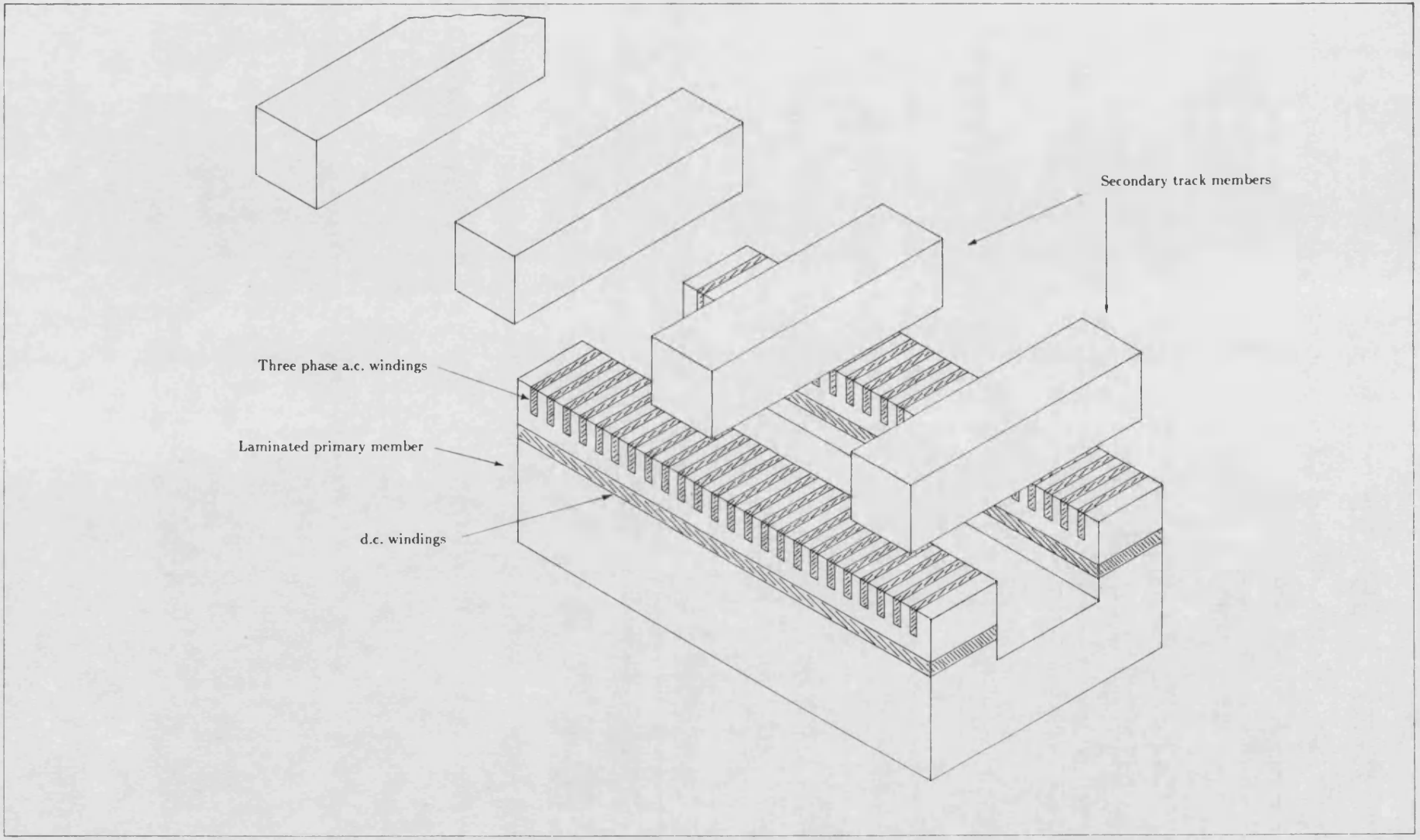

Figure 2.2 Transverse flux homopolar linear synchronous motor (LSM)

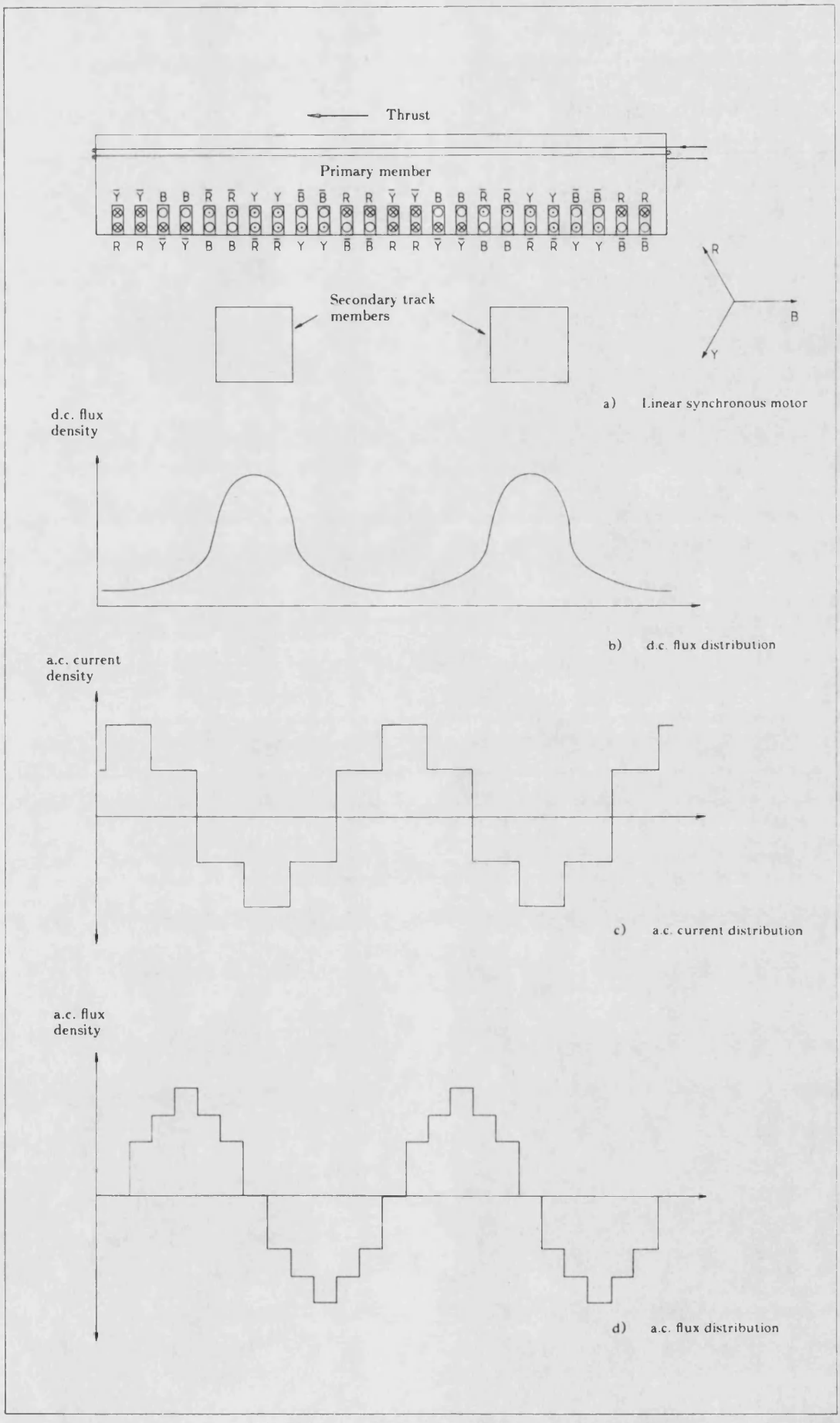

LSM primary member current and flux distributions Figure 2.3

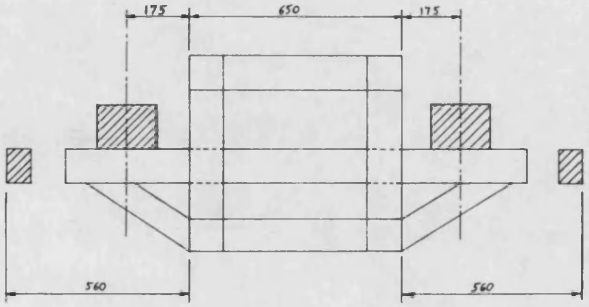

Dimensions in mm

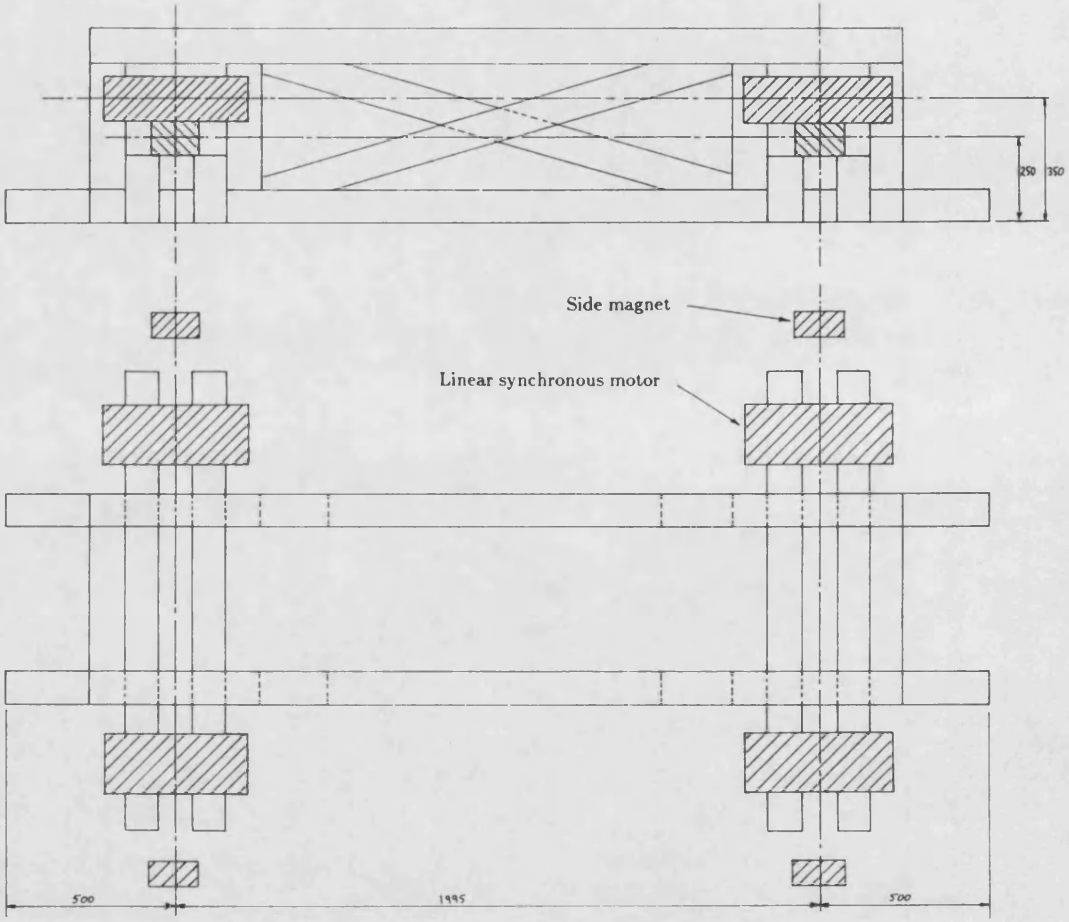

Positioning of the linear synchronous motors and side magnets

Figure 2.4

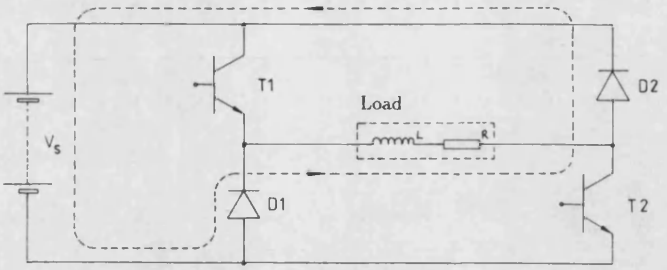

a) Two transistor regenerative chopper showing regeneration current path

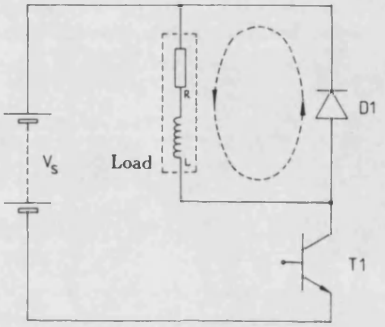

b) Single transistor chopper showing flywheel current path

Chopper configurations Figure 2.5

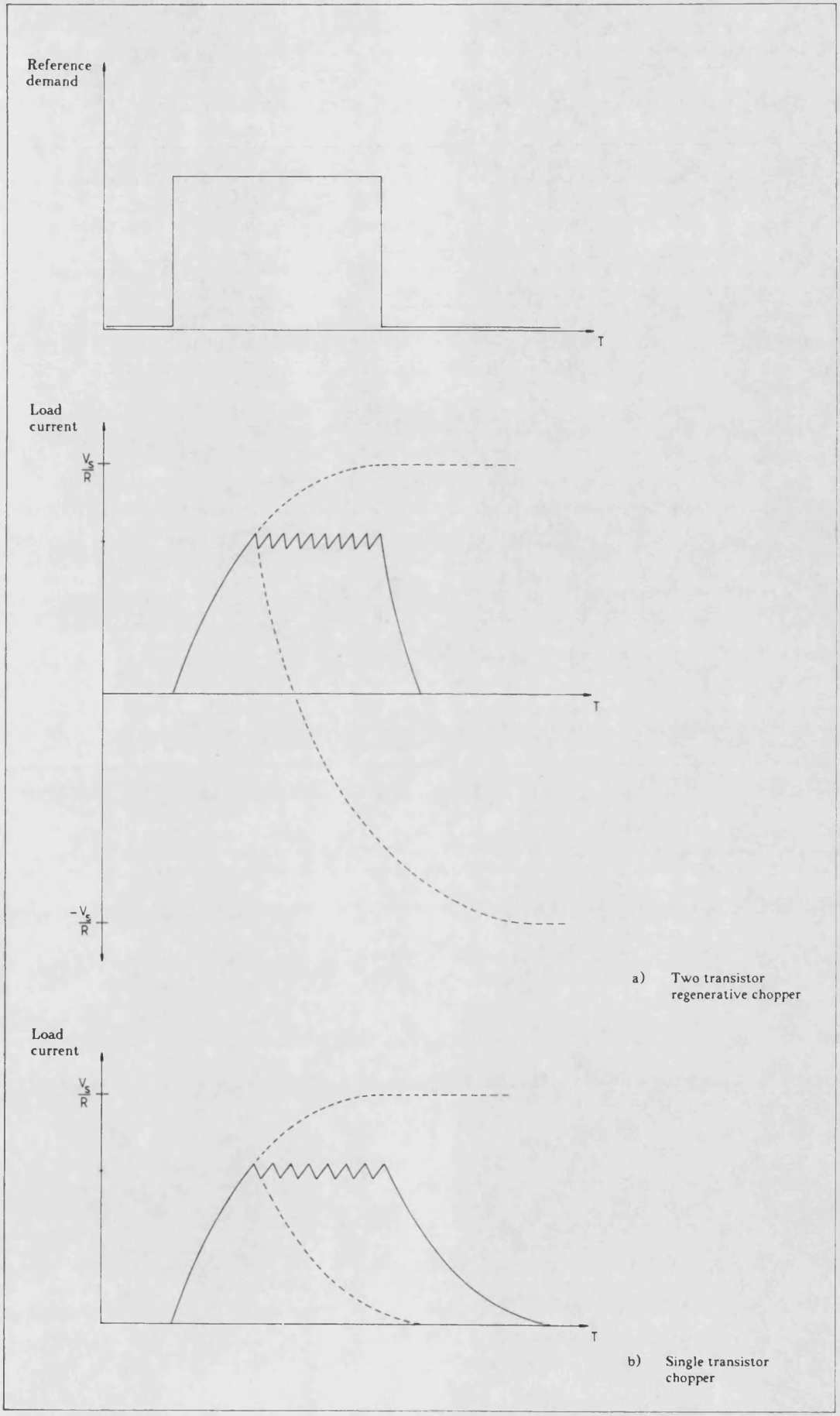

Chopper step response waveforms Figure 2.6

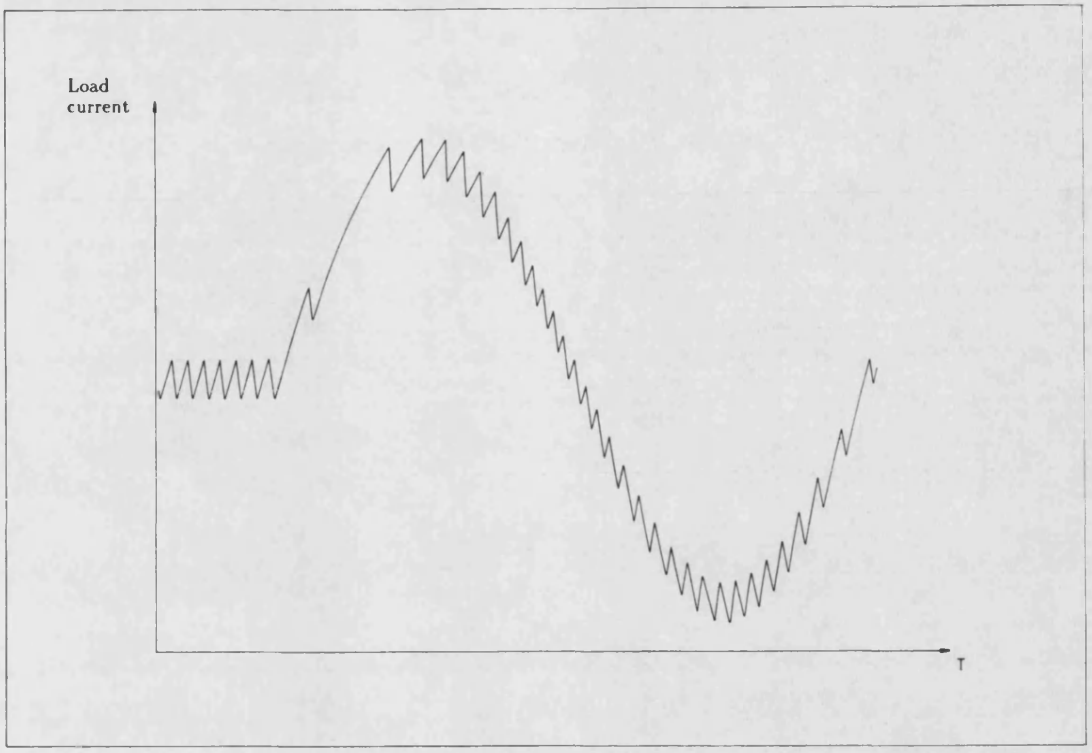

Slitwidth modulated chopper load current following a sinusoidal reference input — Figure 2.7

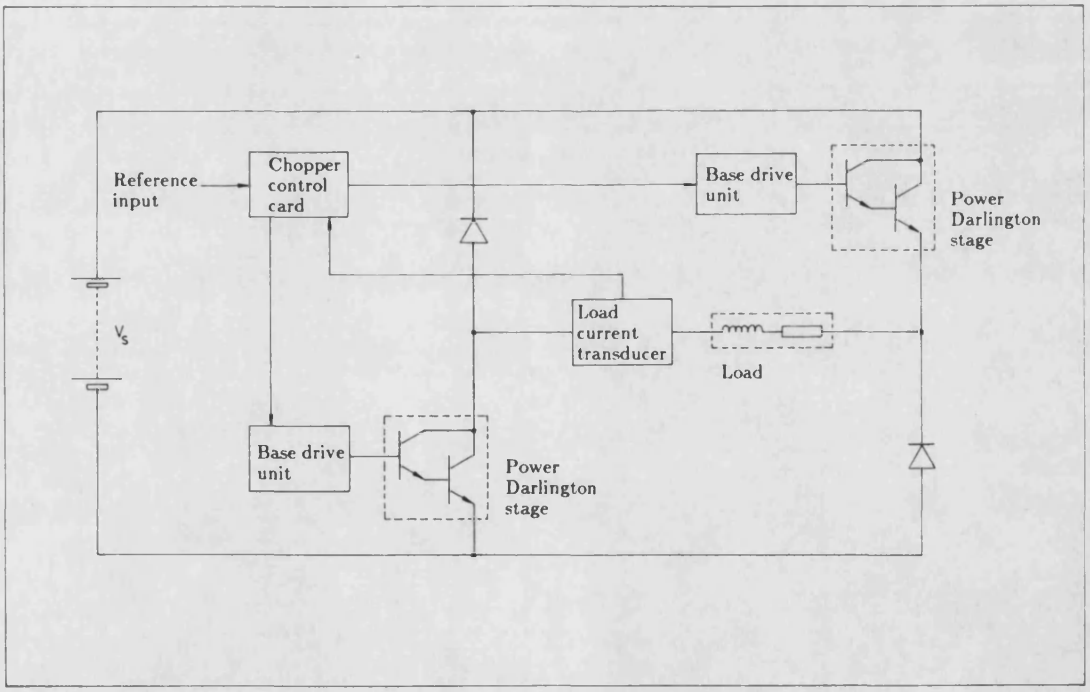

Block diagram of a slitwidth modulated chopper — Figure 2.8

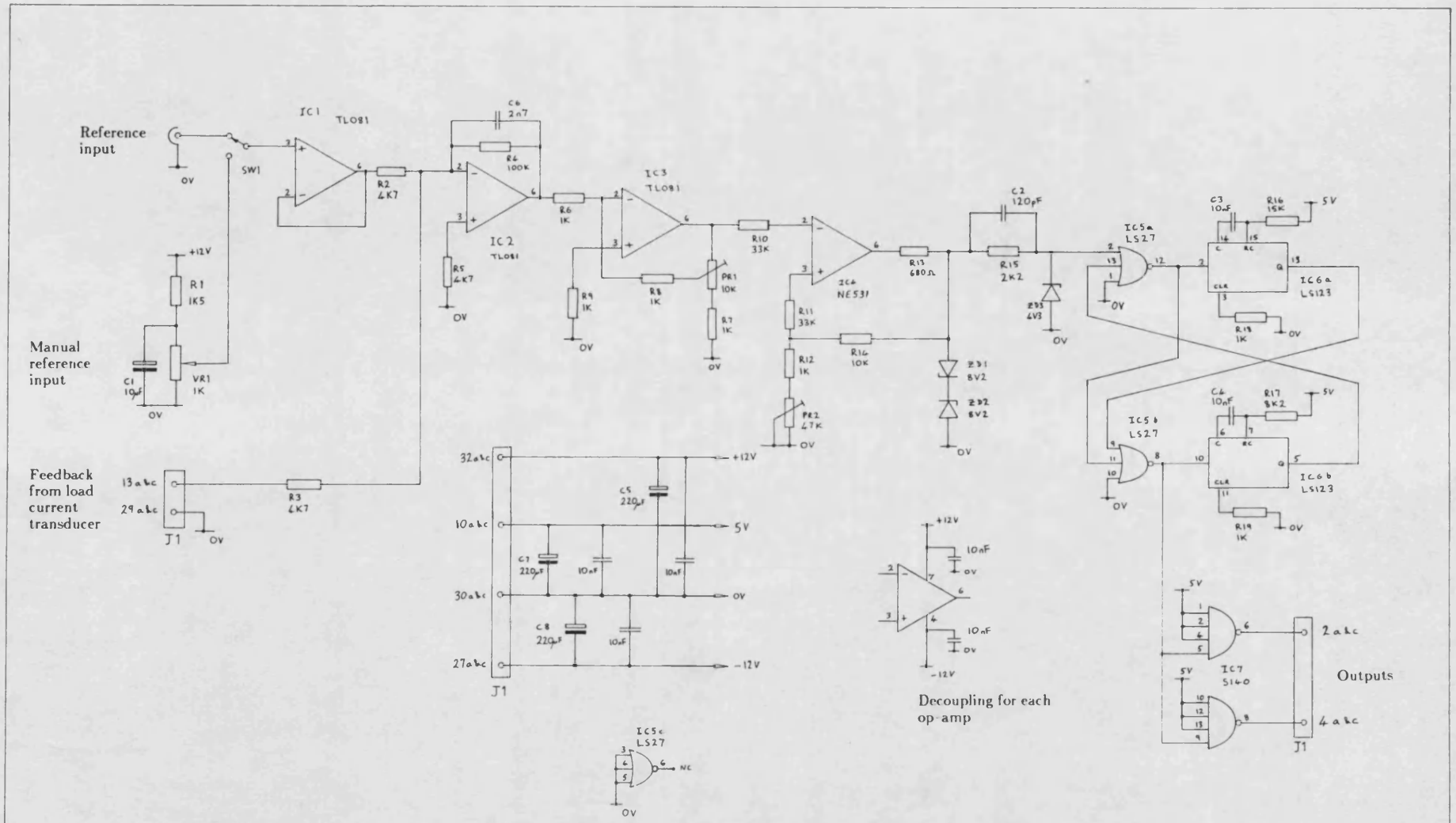

Chopper control card circuit diagram Figure 2.9

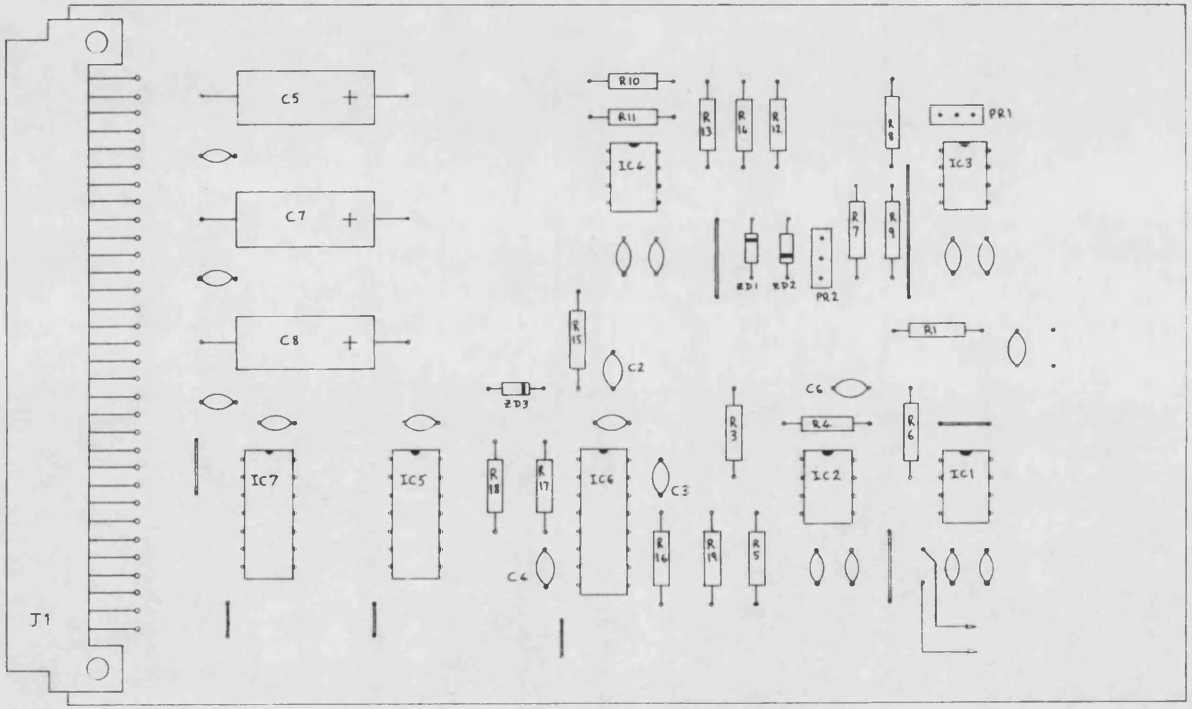

Chopper control card component layout Figure 2.10

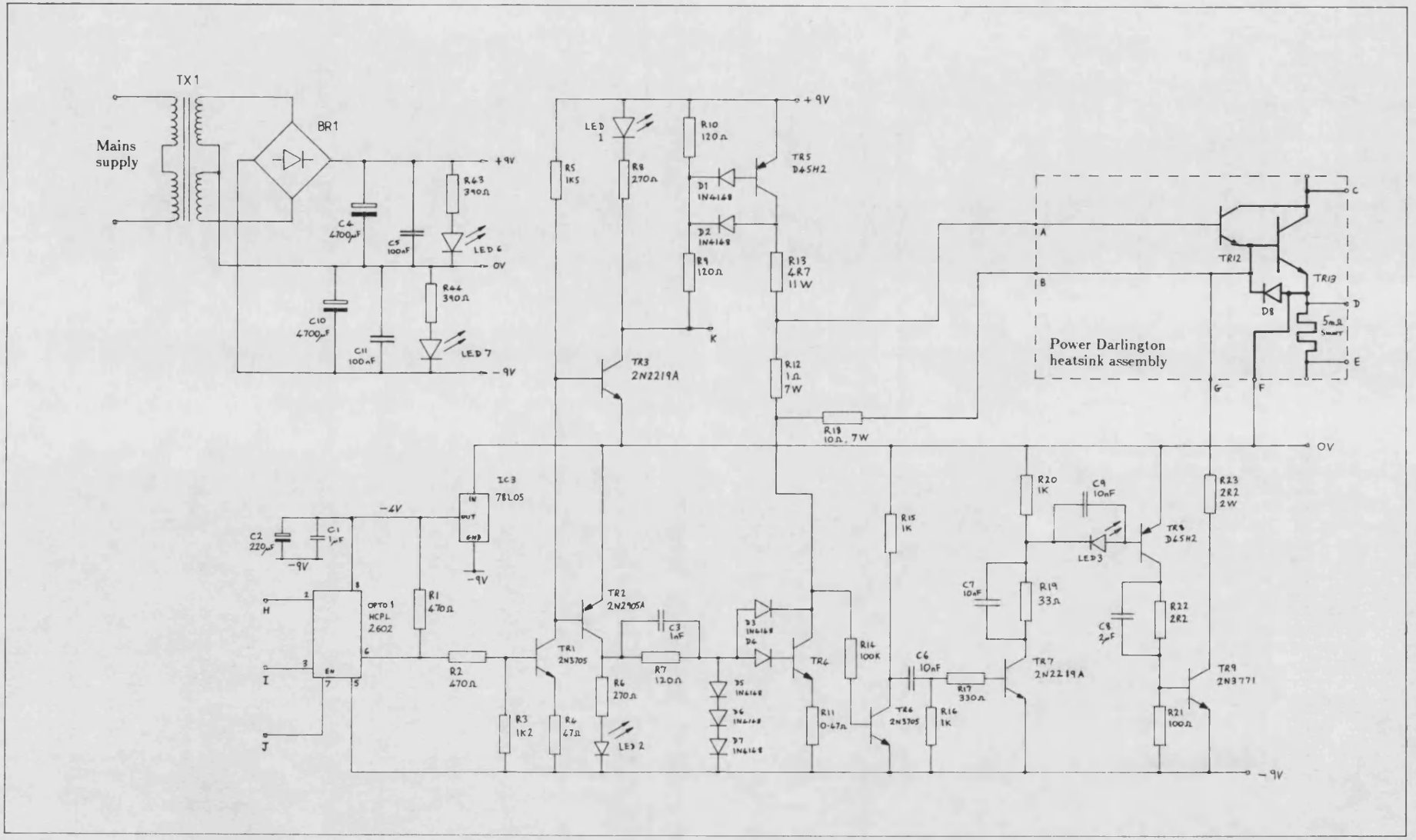

Base drive unit and power Darlington stage circuit diagram (sheet 1) Figure 2.11

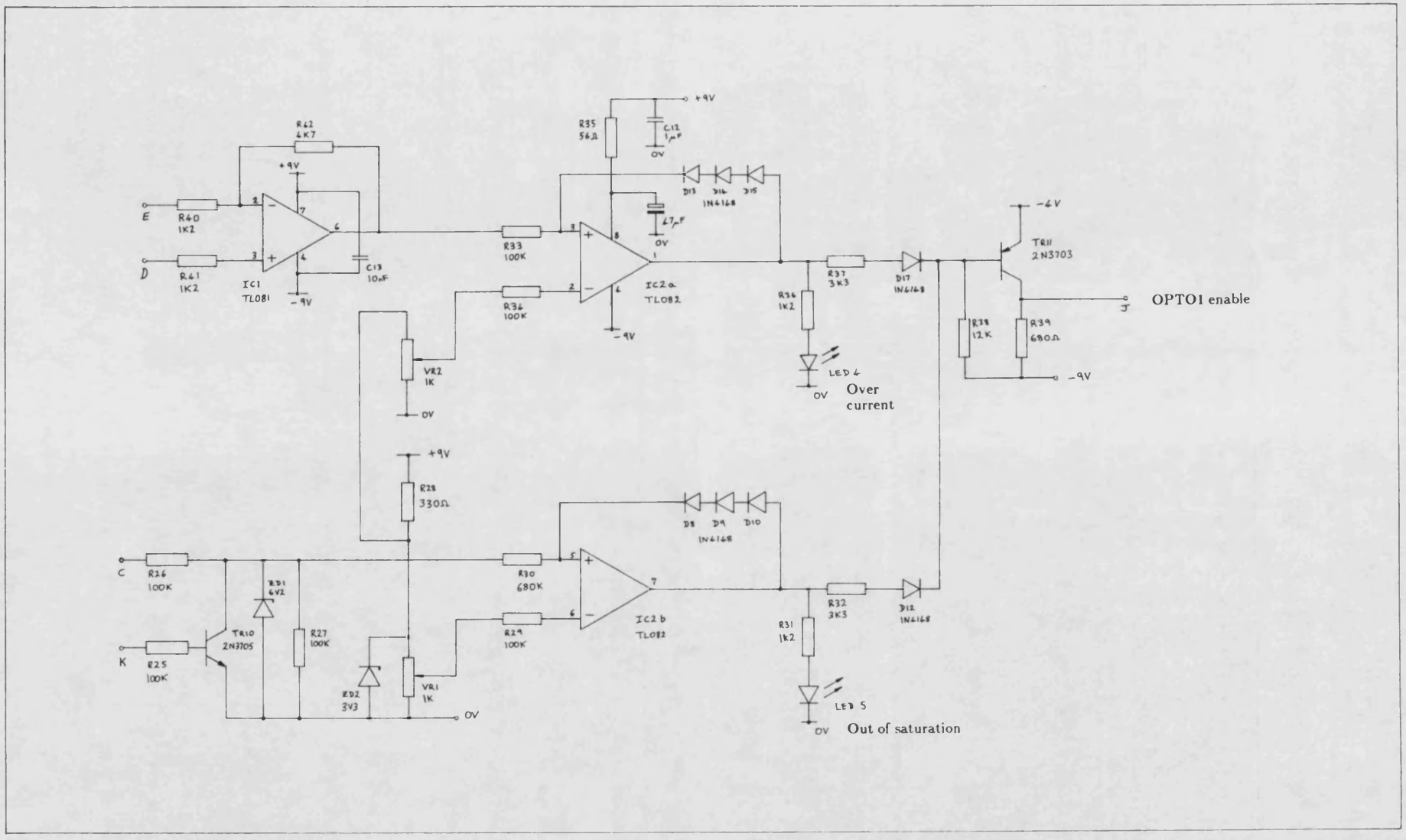

Base drive unit and power Darlington stage circuit diagram (sheet 2) Figure 2.12

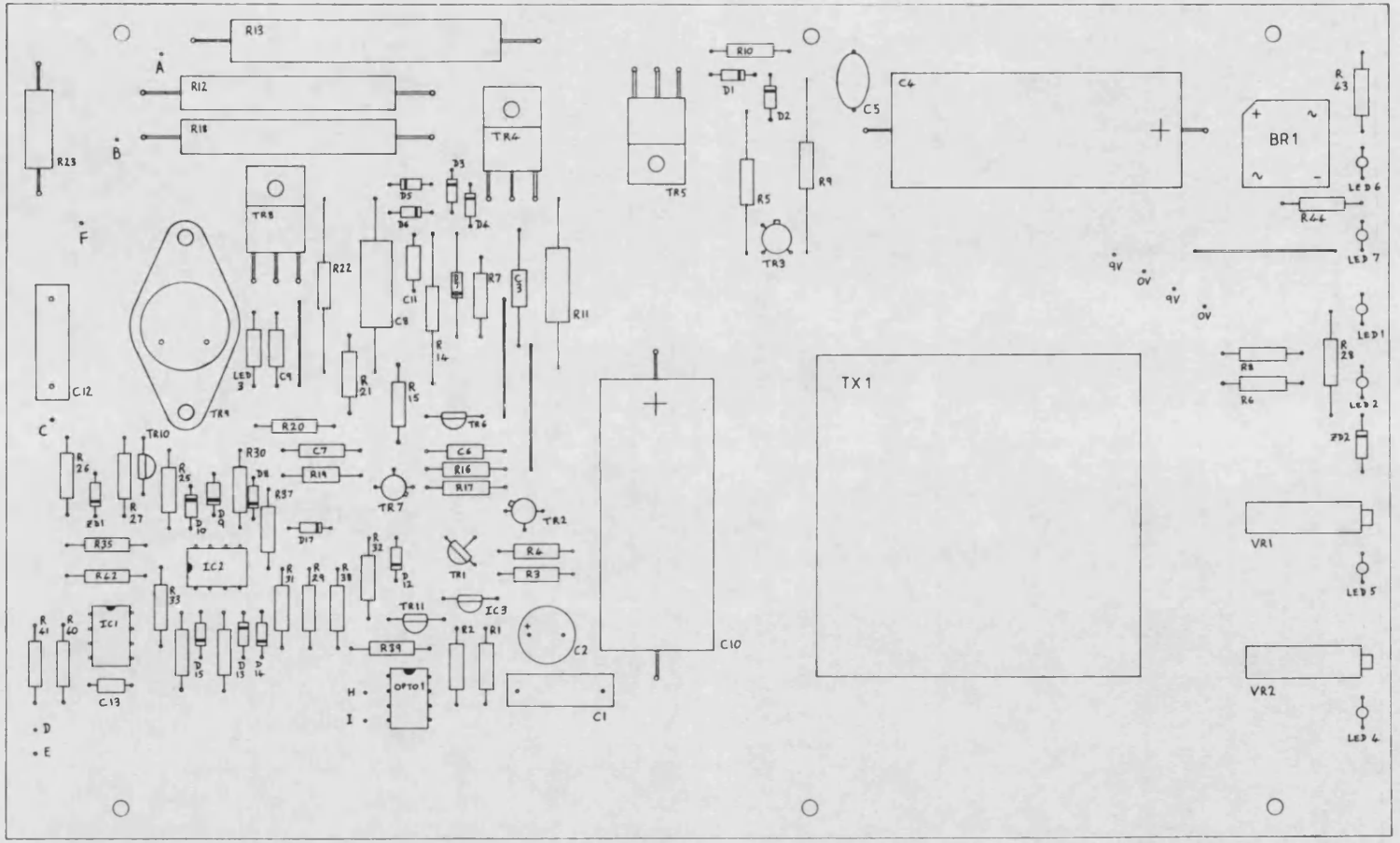

Base drive unit component layout Figure 2.13

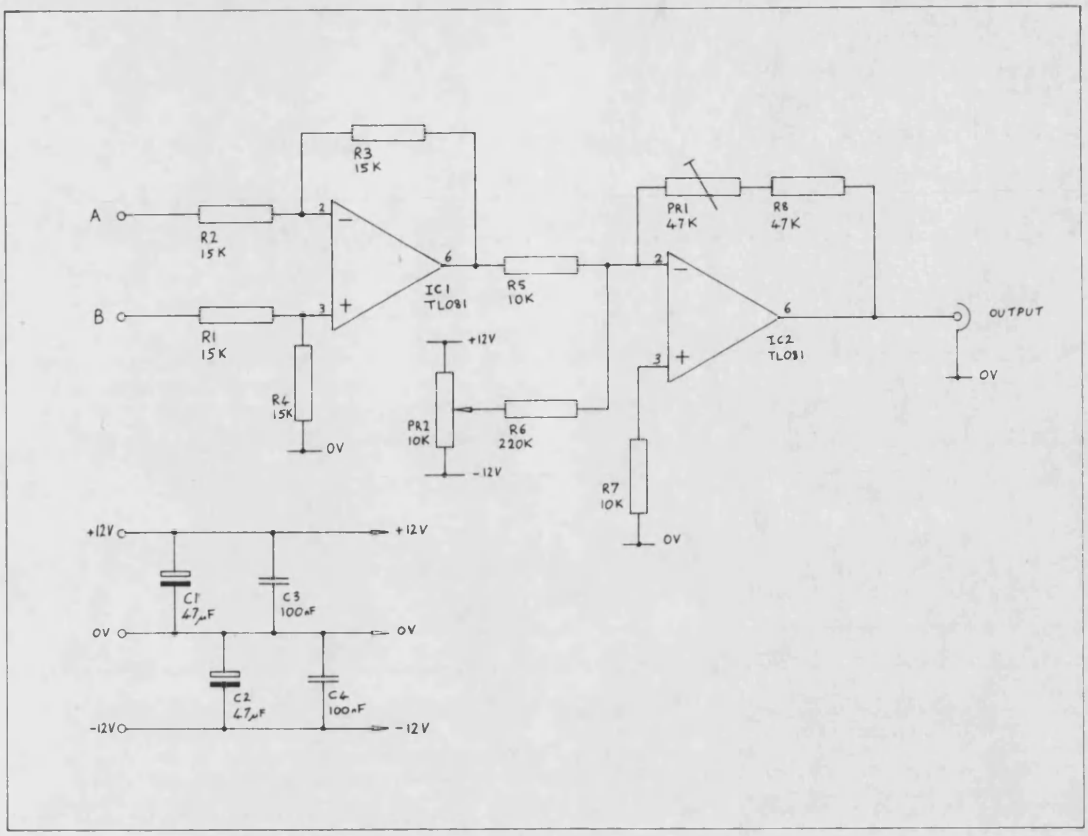

Load current transducer unit circuit diagram Figure 2.14

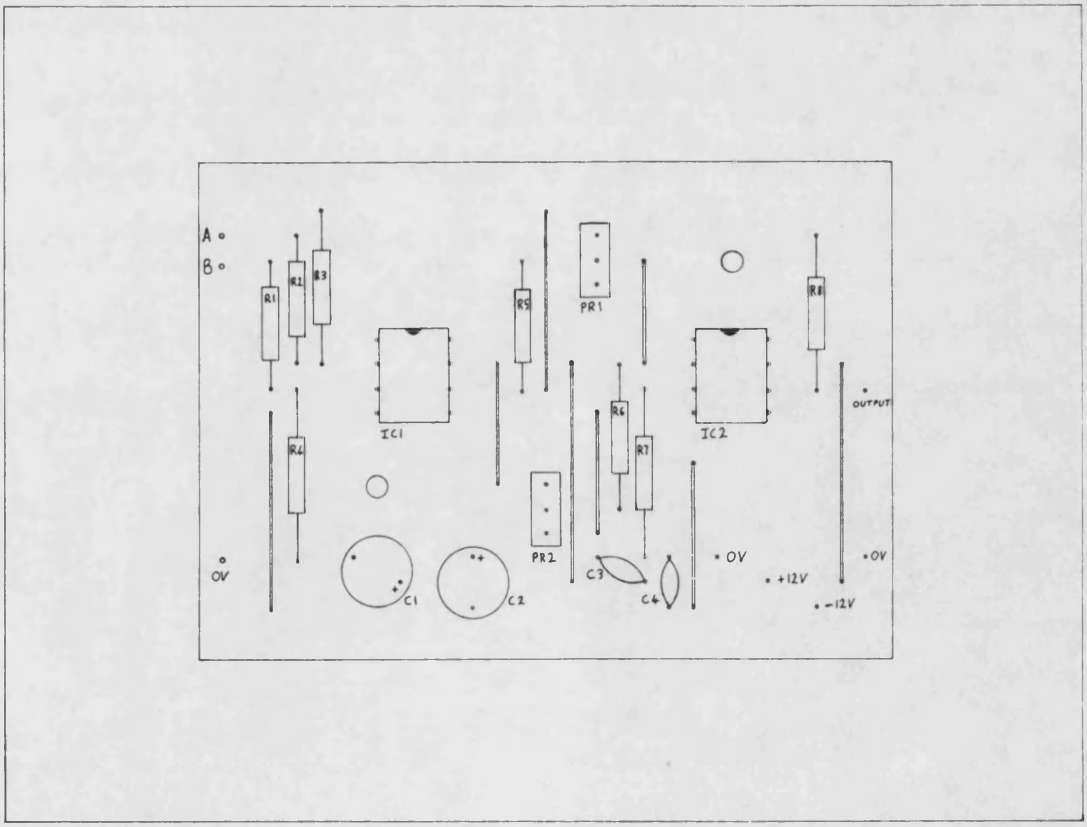

Load current transducer unit component layout Figure 2.15

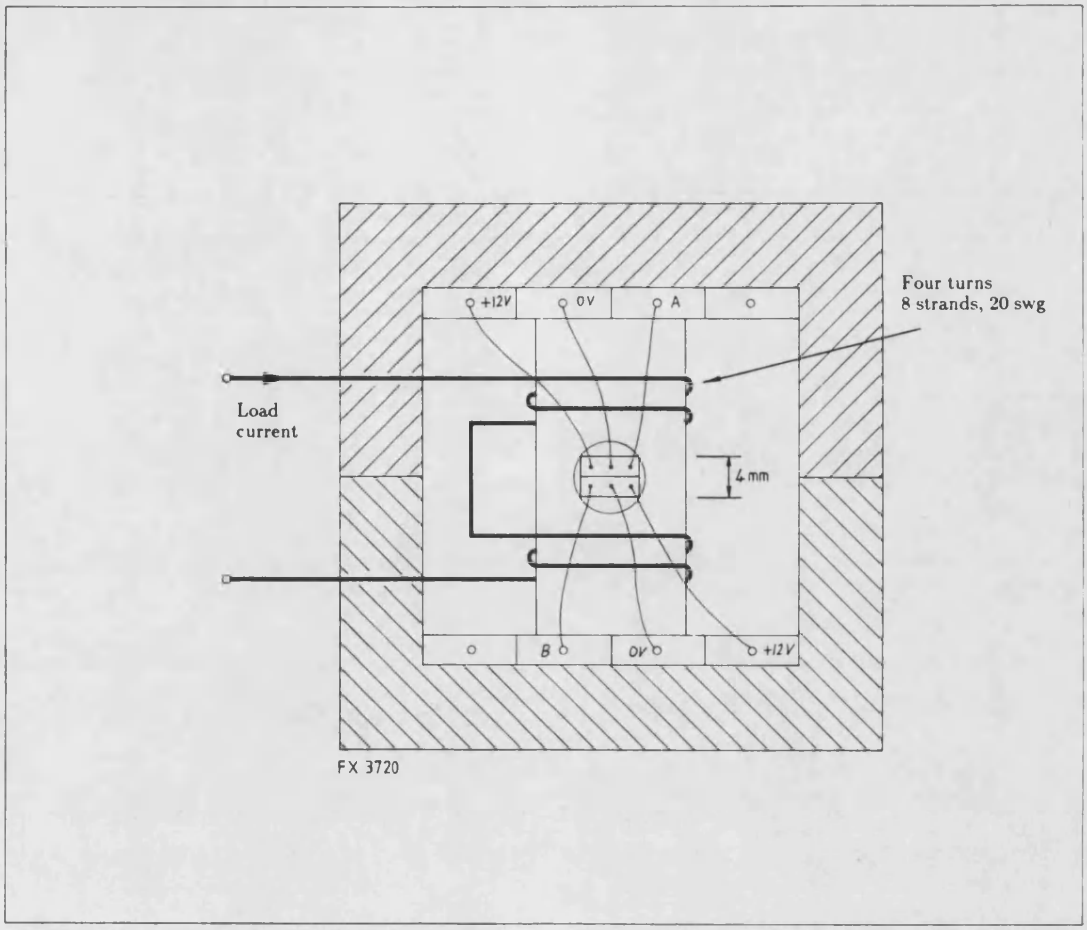

Magnetic E-core assembly Figure 2.16

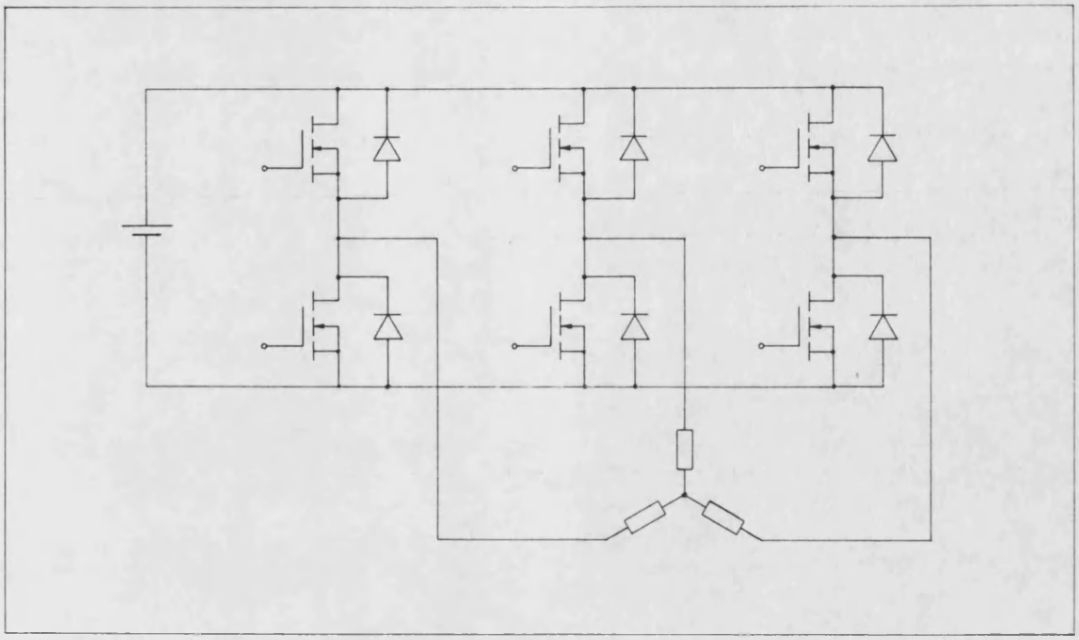

Standard 3-phase four quadrant bridge circuit Figure 2.17

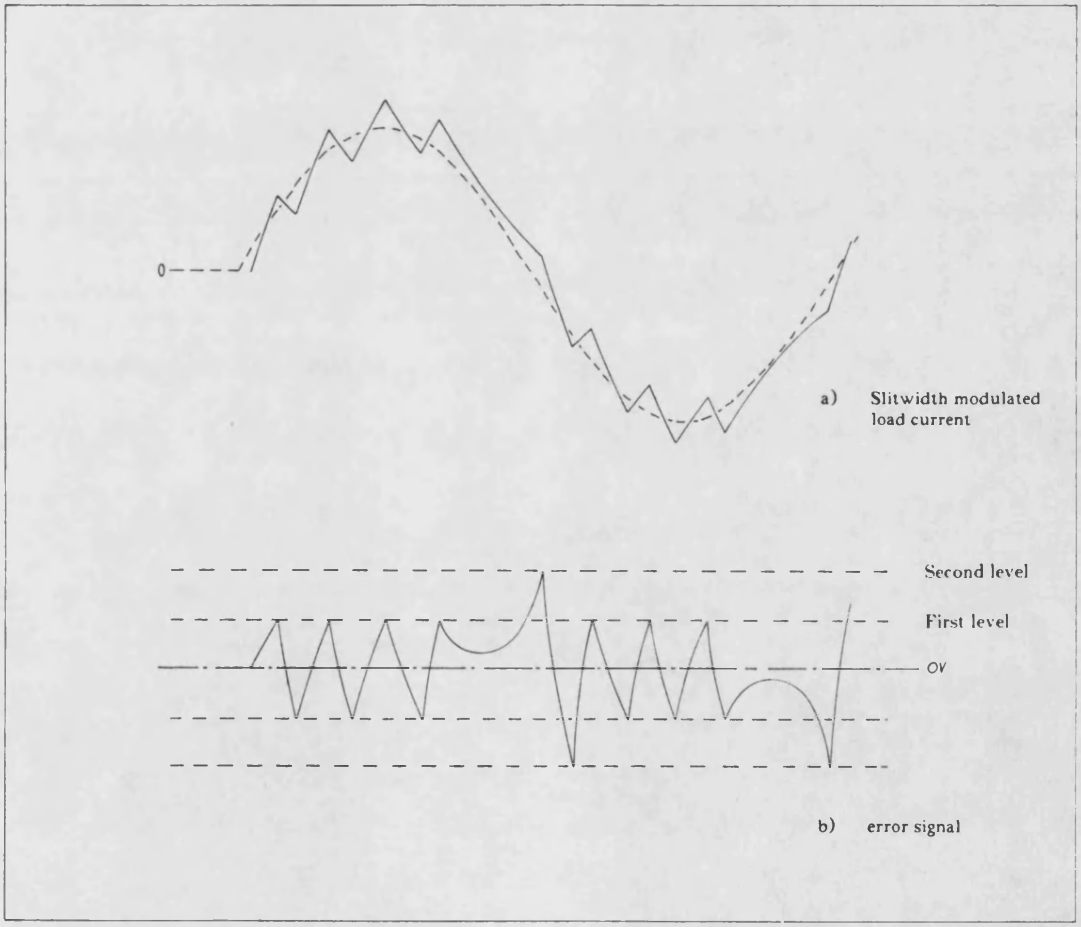

Slitwidth modulator waveforms using class ABD operation Figure 2.18

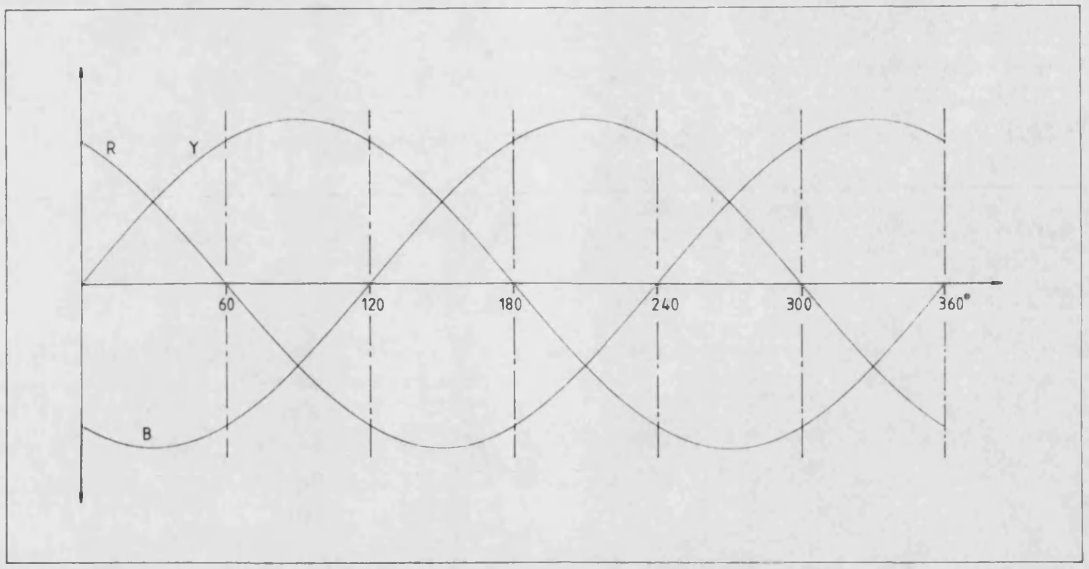

The 3-phase set of sinusoidal waveforms Figure 2.19

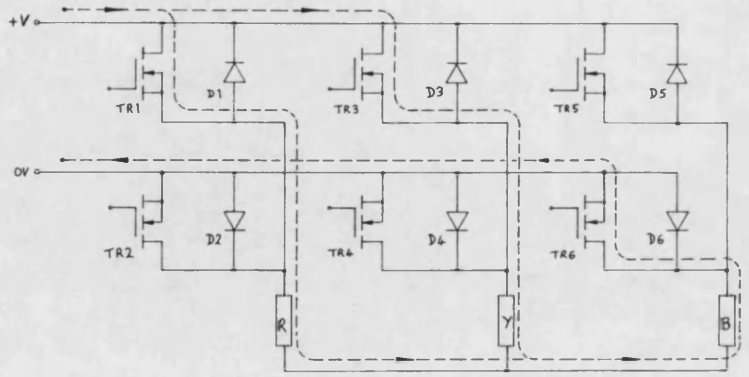

a) Red phase rectification
Yellow phase rectification

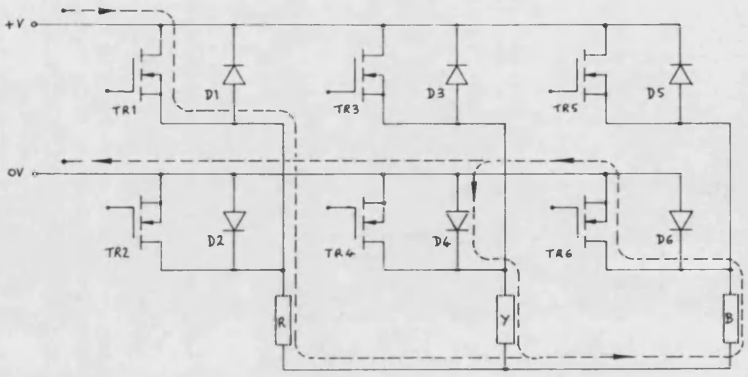

b) Red phase rectification
Yellow phase flywheel

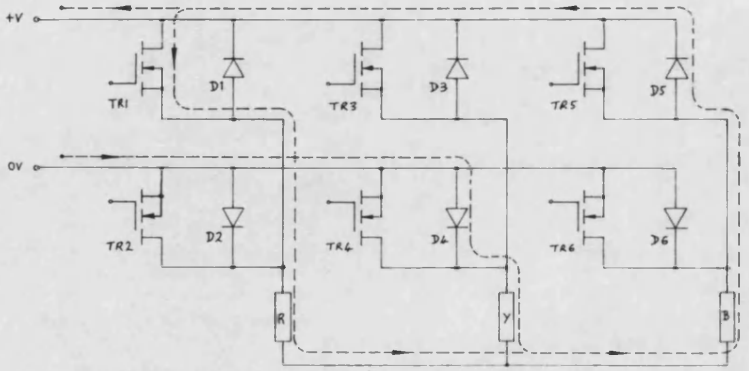

c) Red phase flywheel
Yellow phase inversion

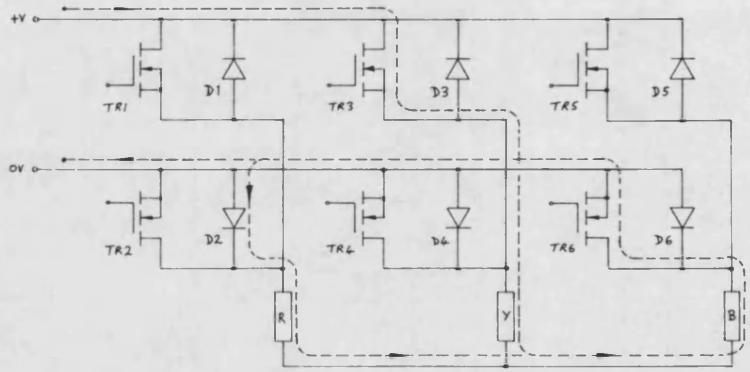

d) Red phase flywheel
Yellow phase rectification

Inverter operating modes (sheet 1) Figure 2.20

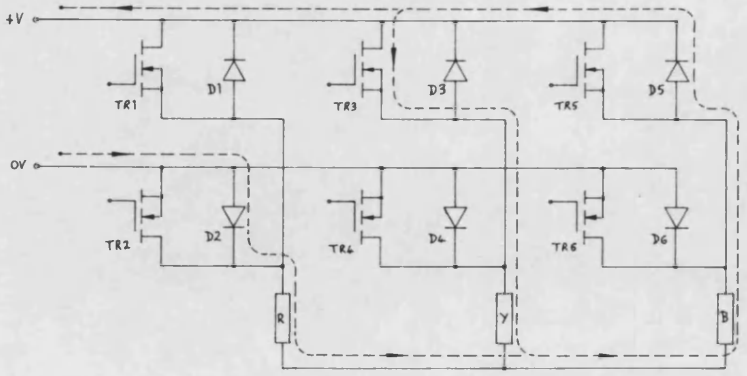

e) Red phase inversion
Yellow phase flywheel

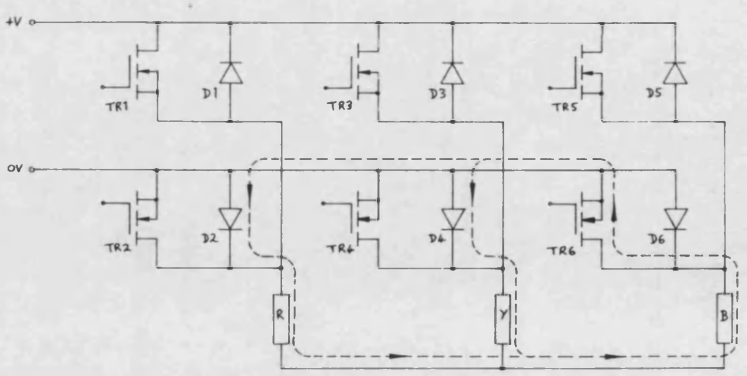

f) Red phase flywheel
Yellow phase flywheel

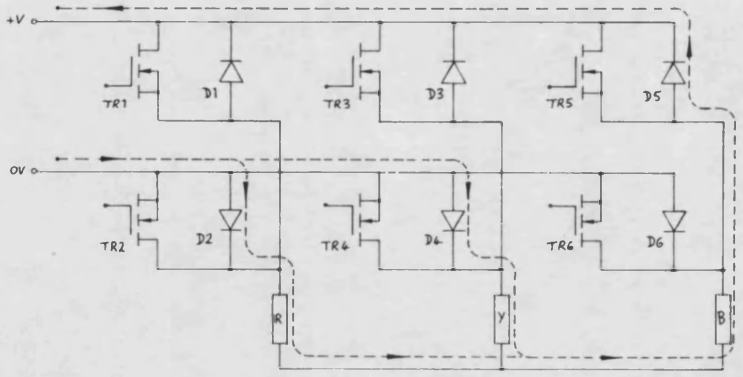

g) Red phase inversion
Yellow phase inversion

Inverter operating modes (sheet 2) Figure 2.20

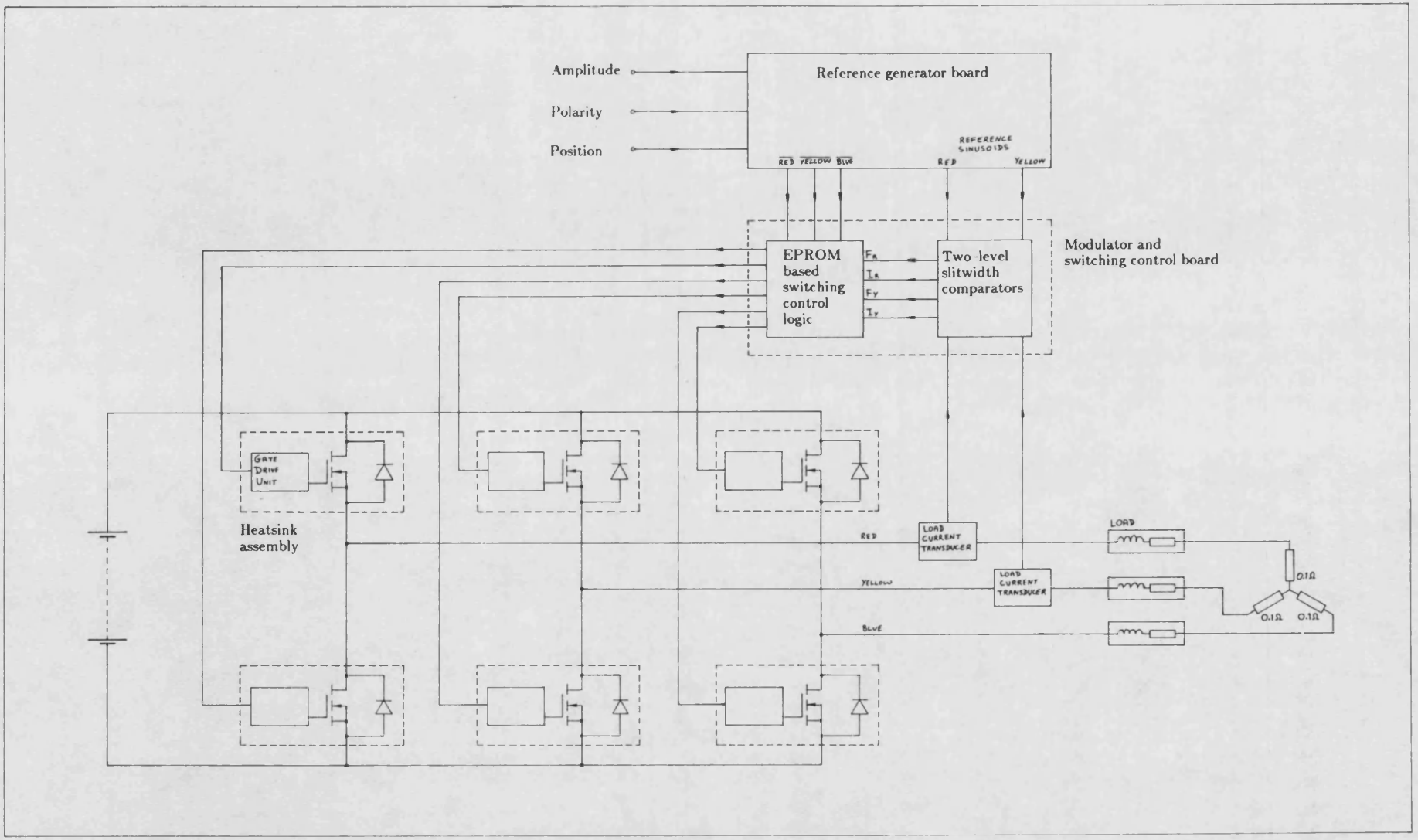

Block diagram of the 3-phase inverter Figure 2.21

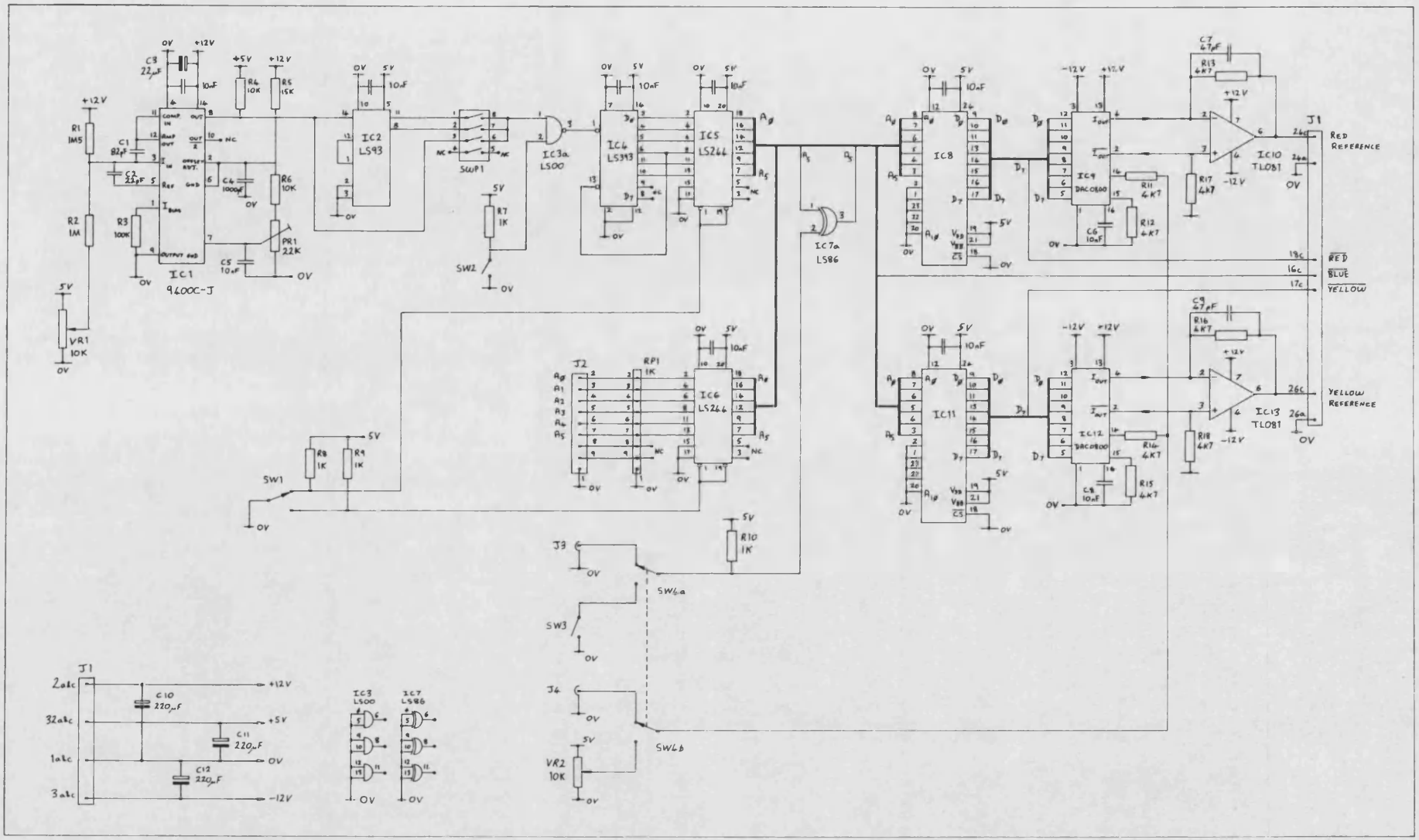

Reference generator board circuit diagram Figure 2.22

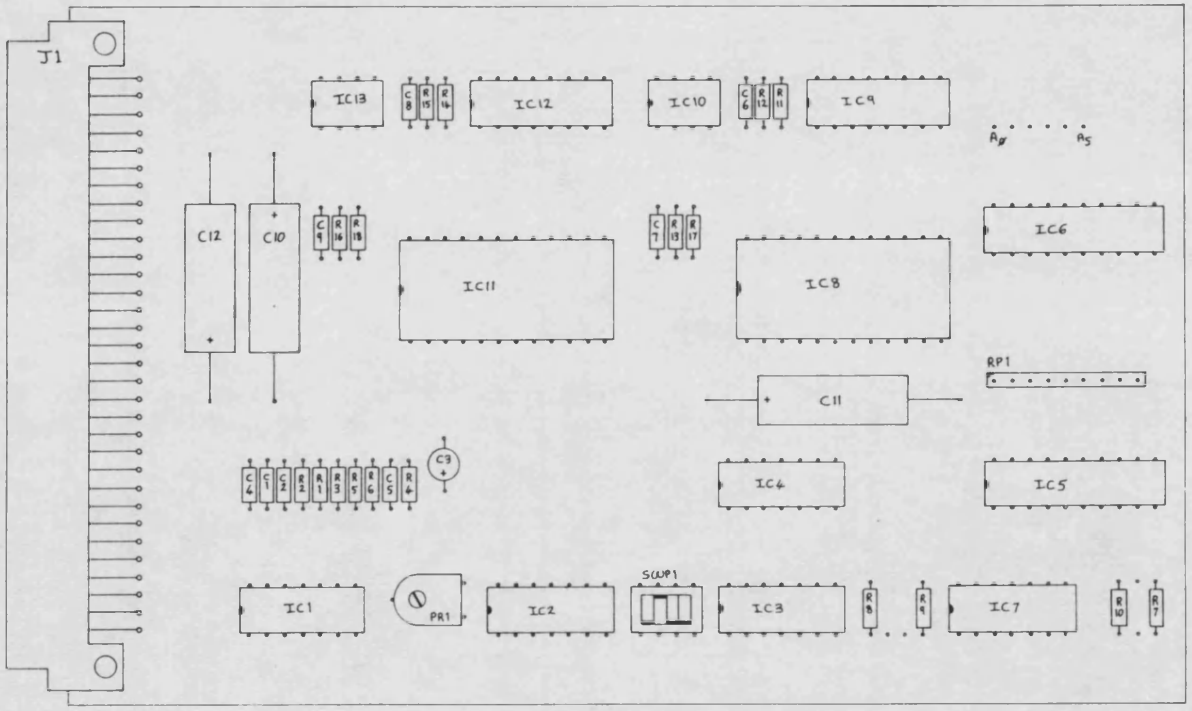

Reference generator board component layout Figure 2.23

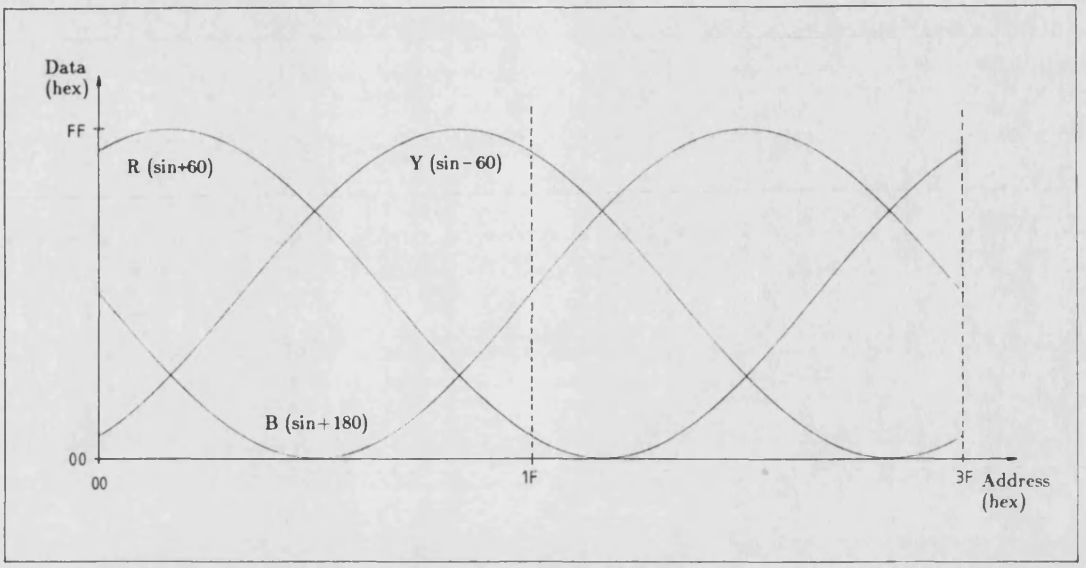

EPROM based reference sinusoids Figure 2.24

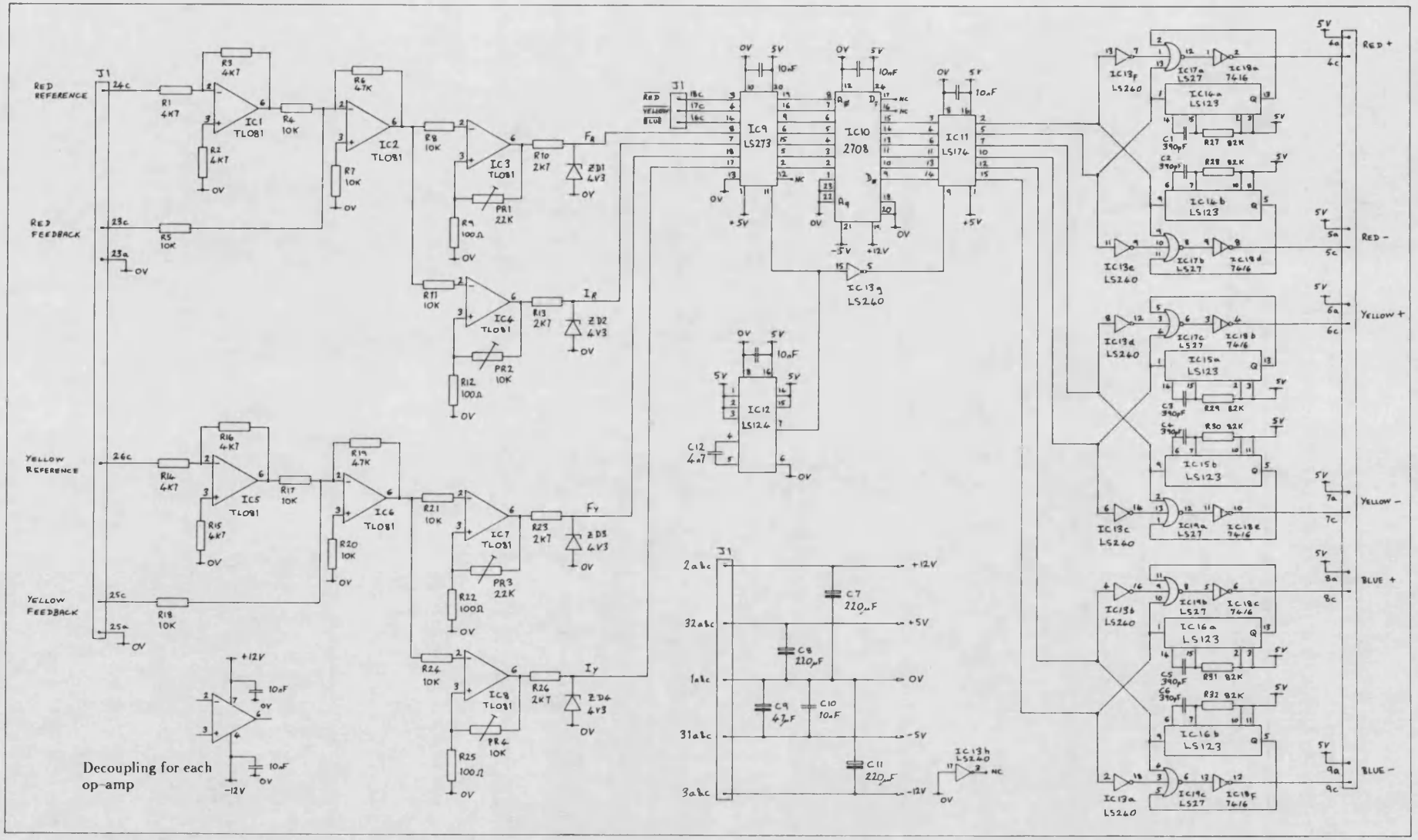

Modulator and switching control board circuit diagram

Figure 2.25

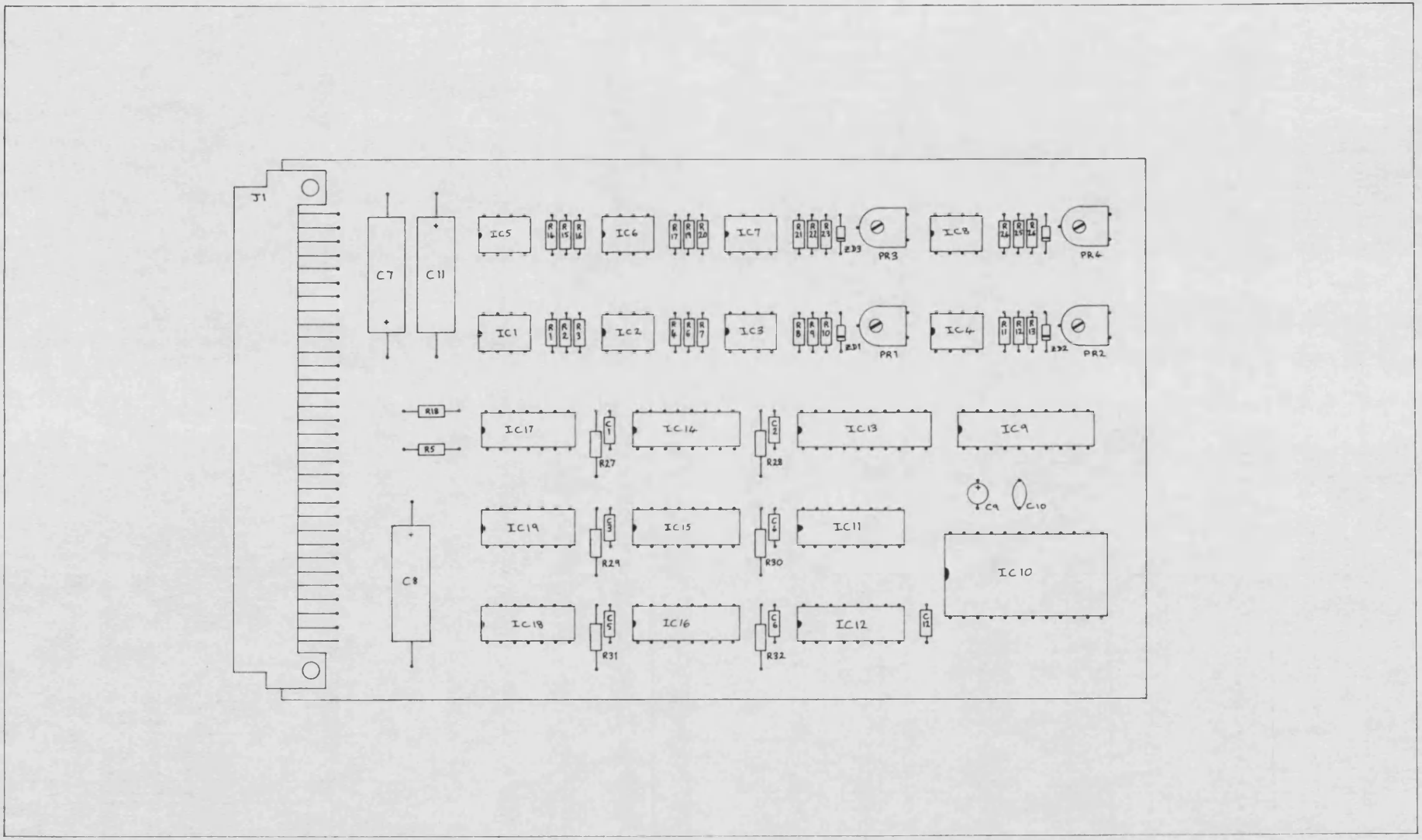

Modulator and switching control board component layout — Figure 2.26

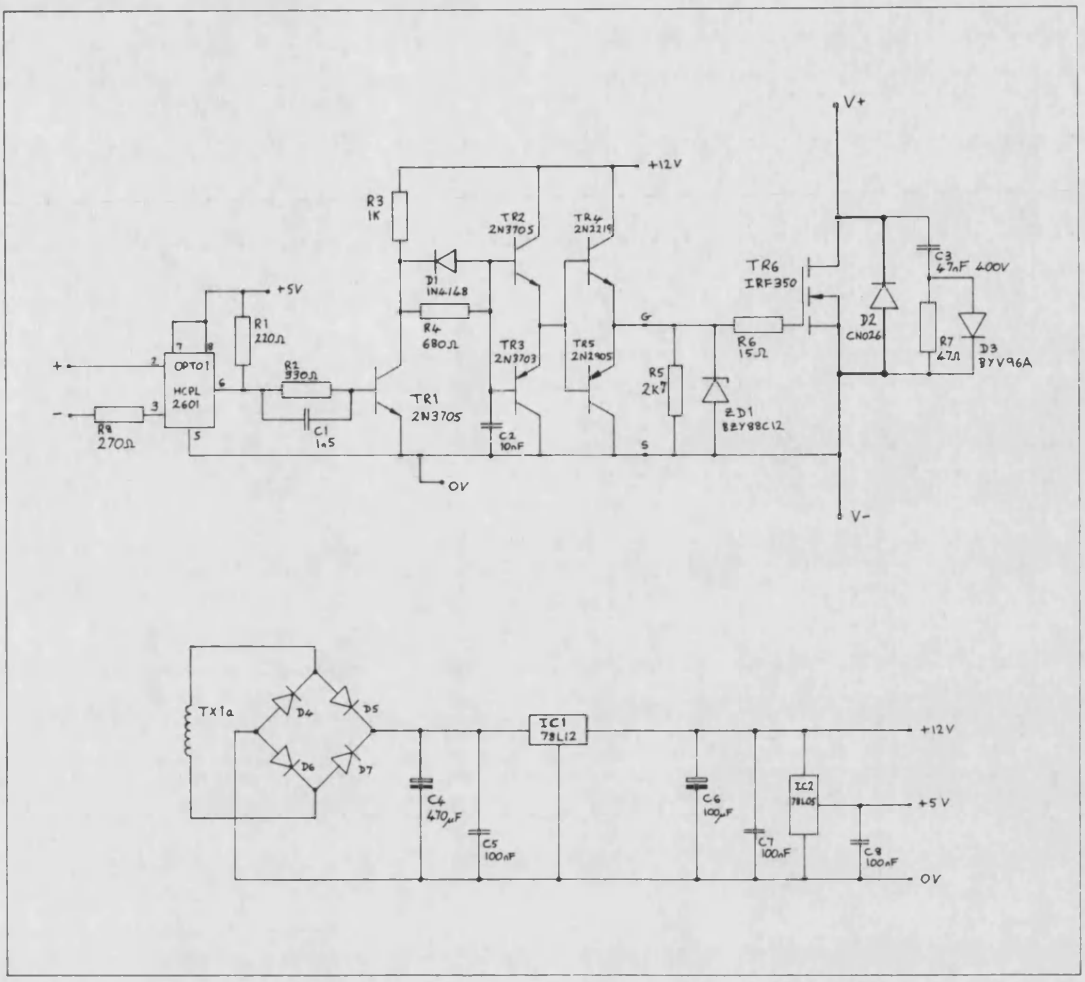

Gate drive unit and power transistor stage circuit diagram Figure 2.27

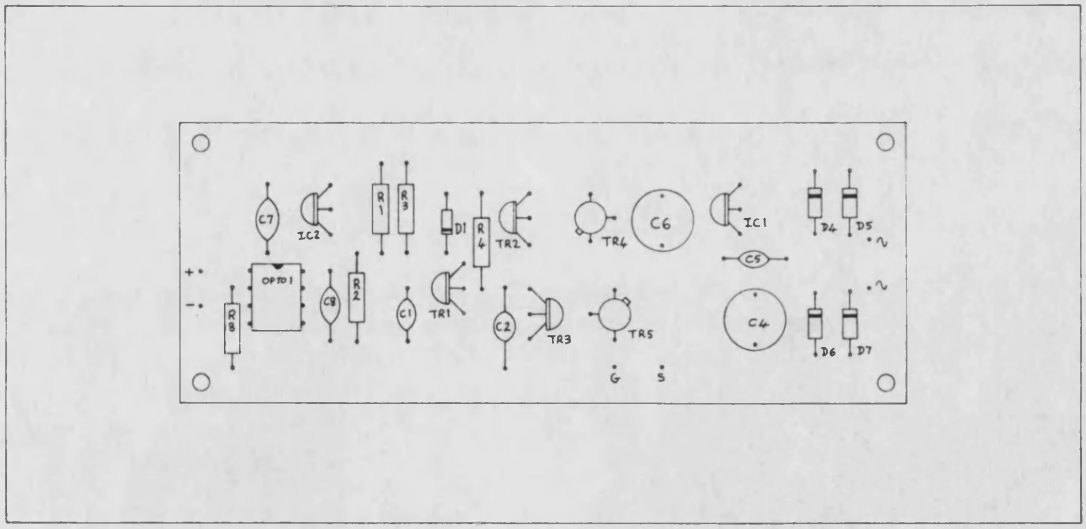

Gate drive unit component layout Figure 2.28

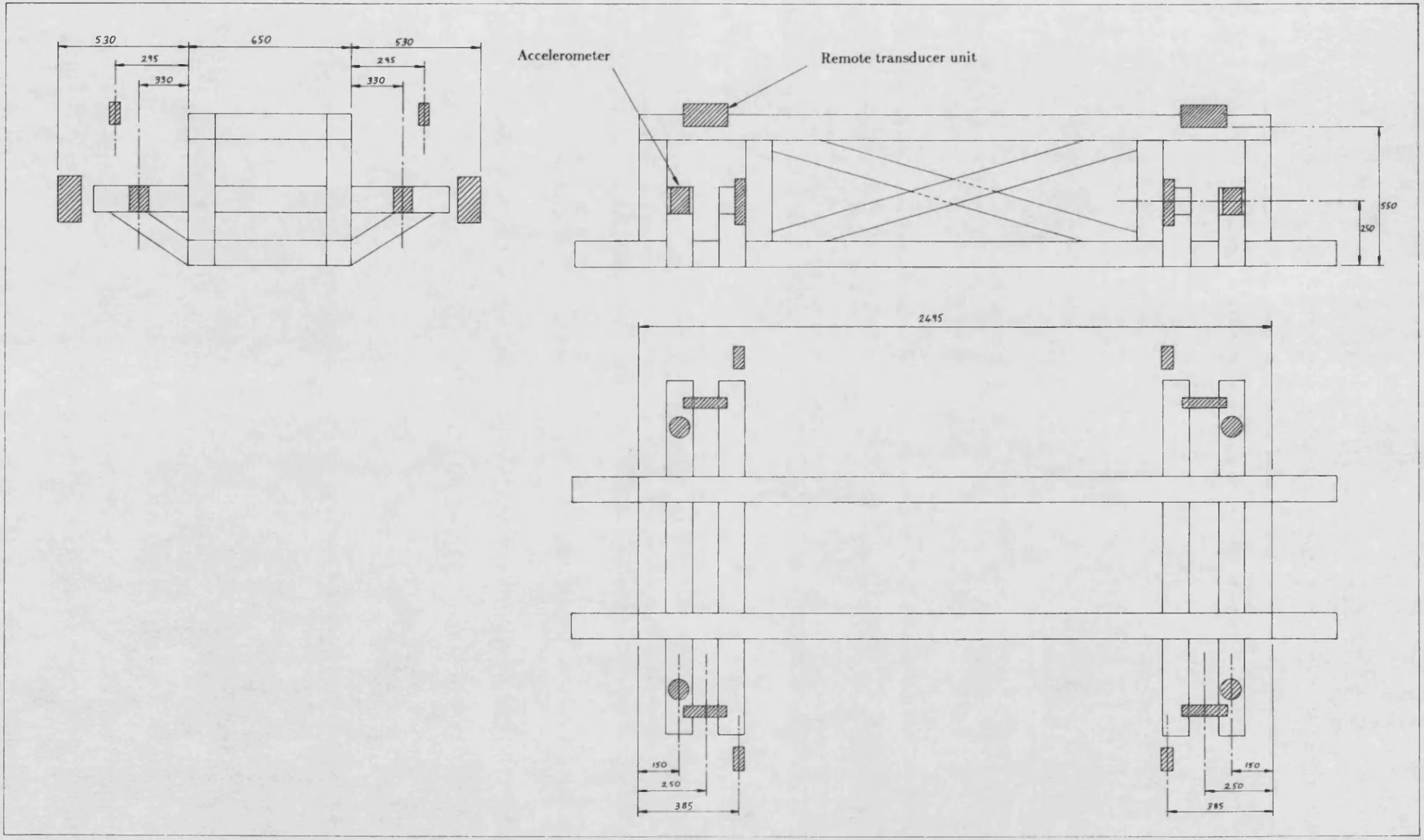

Remote transducer unit and accelerometer positioning

Figure 2.29

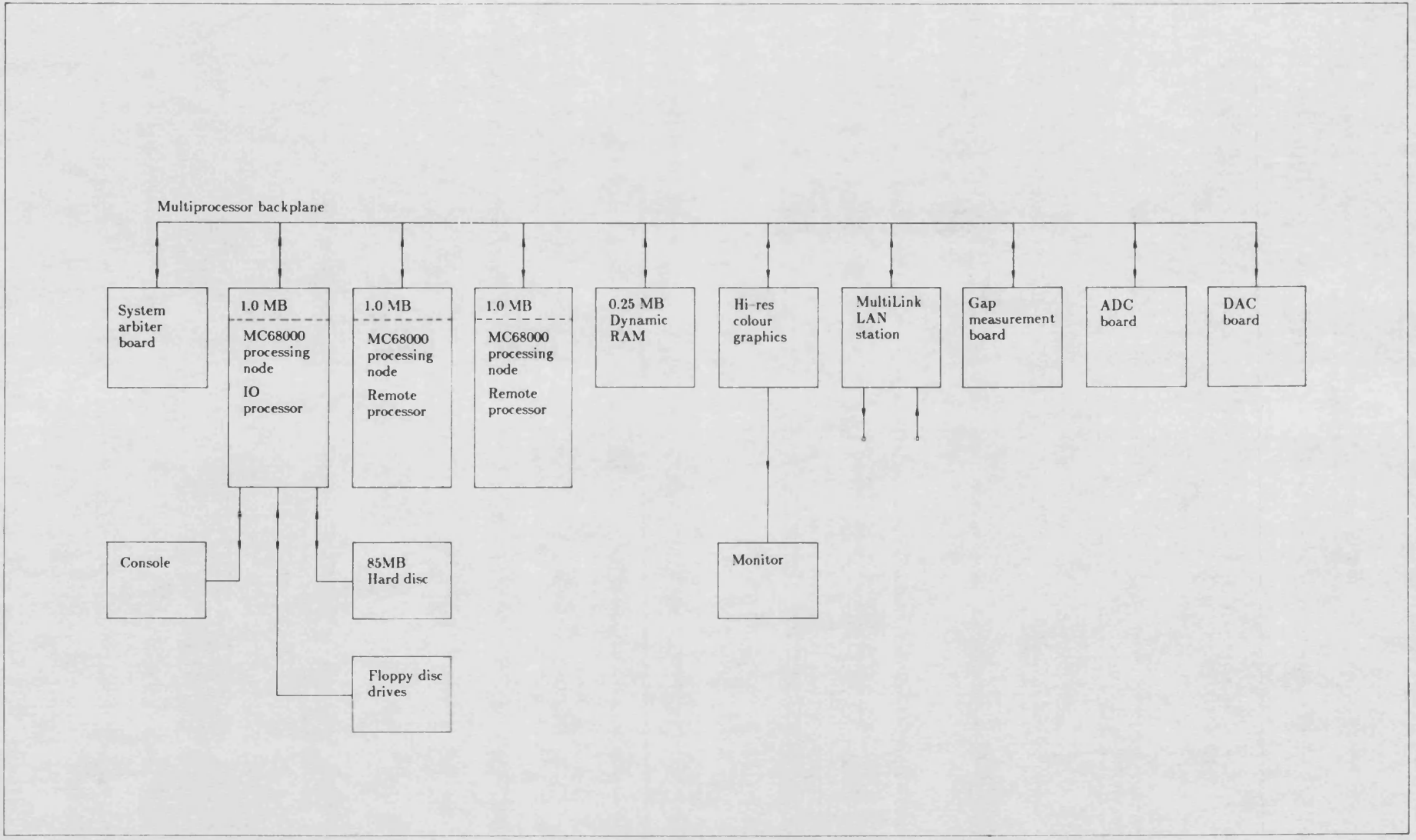

Multiprocessor computer system block diagram Figure 2.30

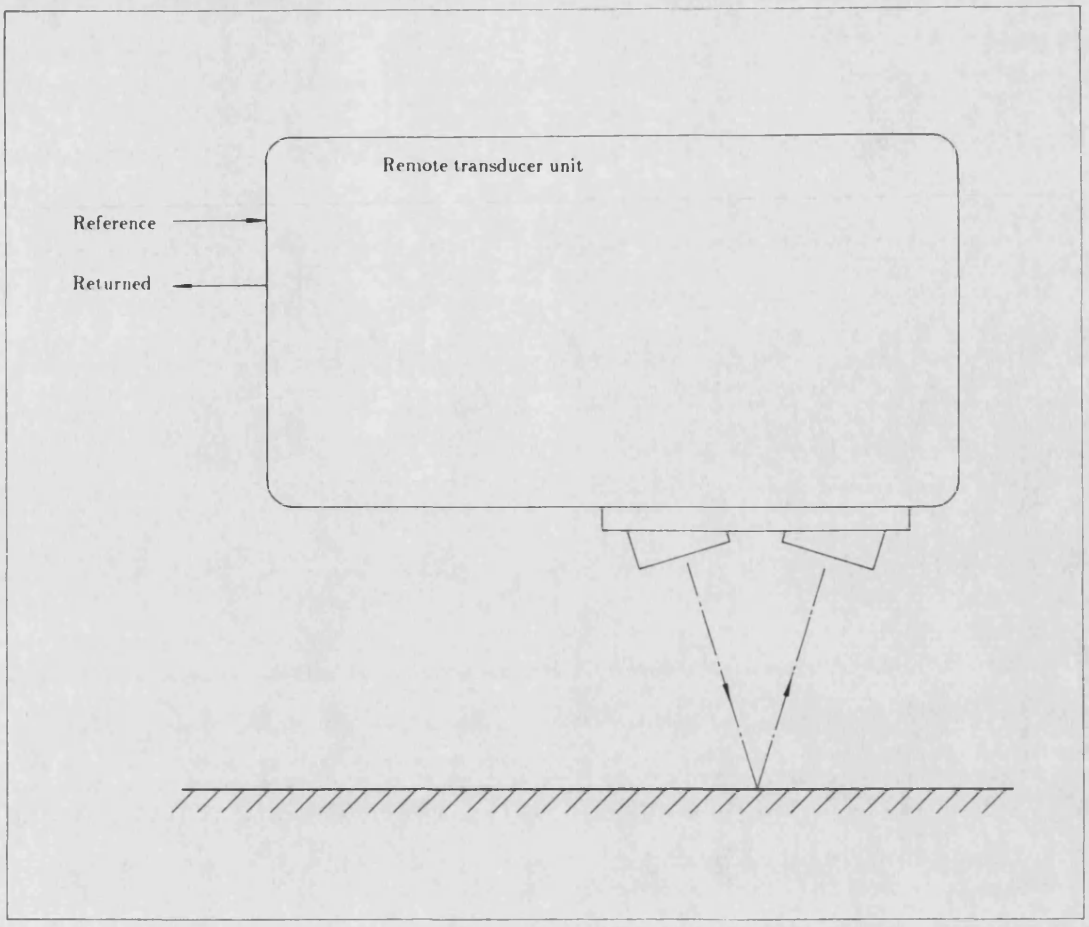

A remote transducer unit mounted opposite a reference surface

Figure 2.31

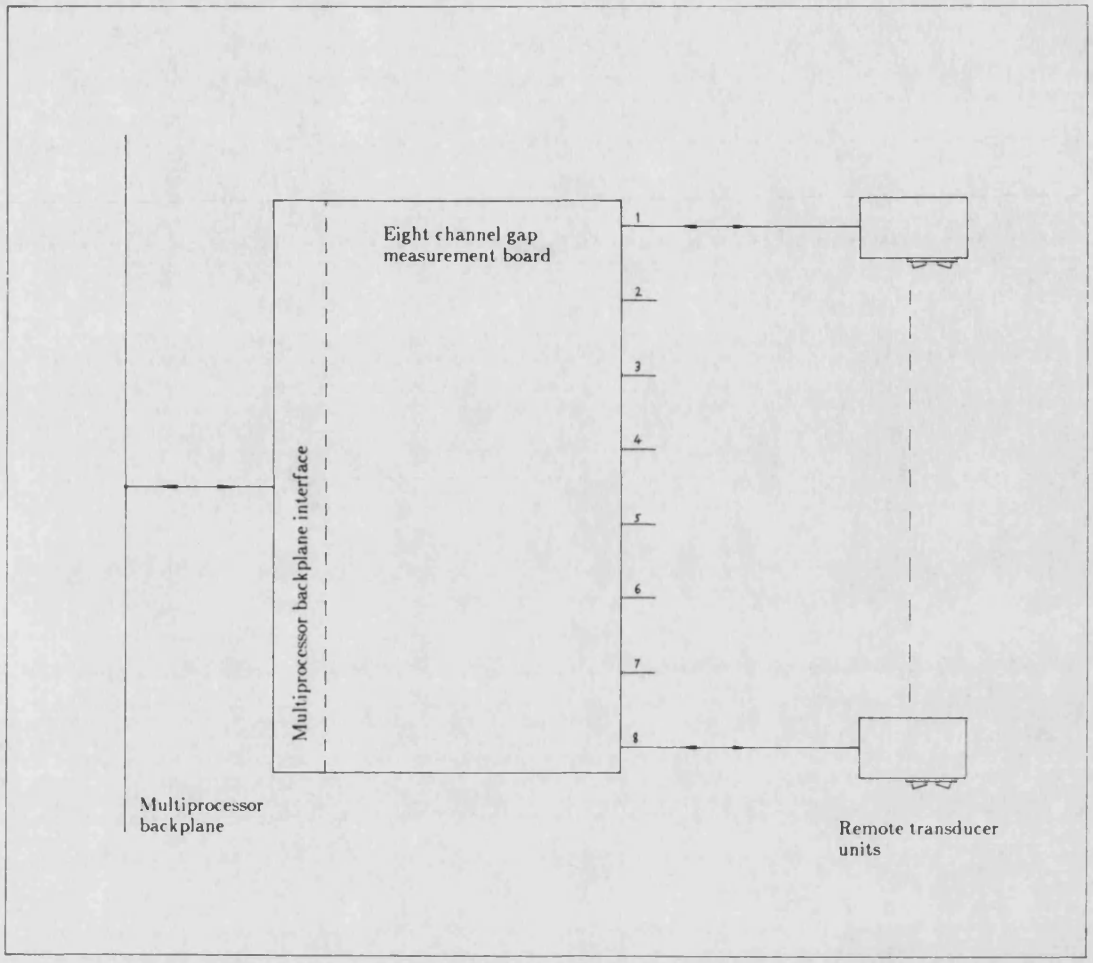

Block diagram of the gap measurement hardware Figure 2.32

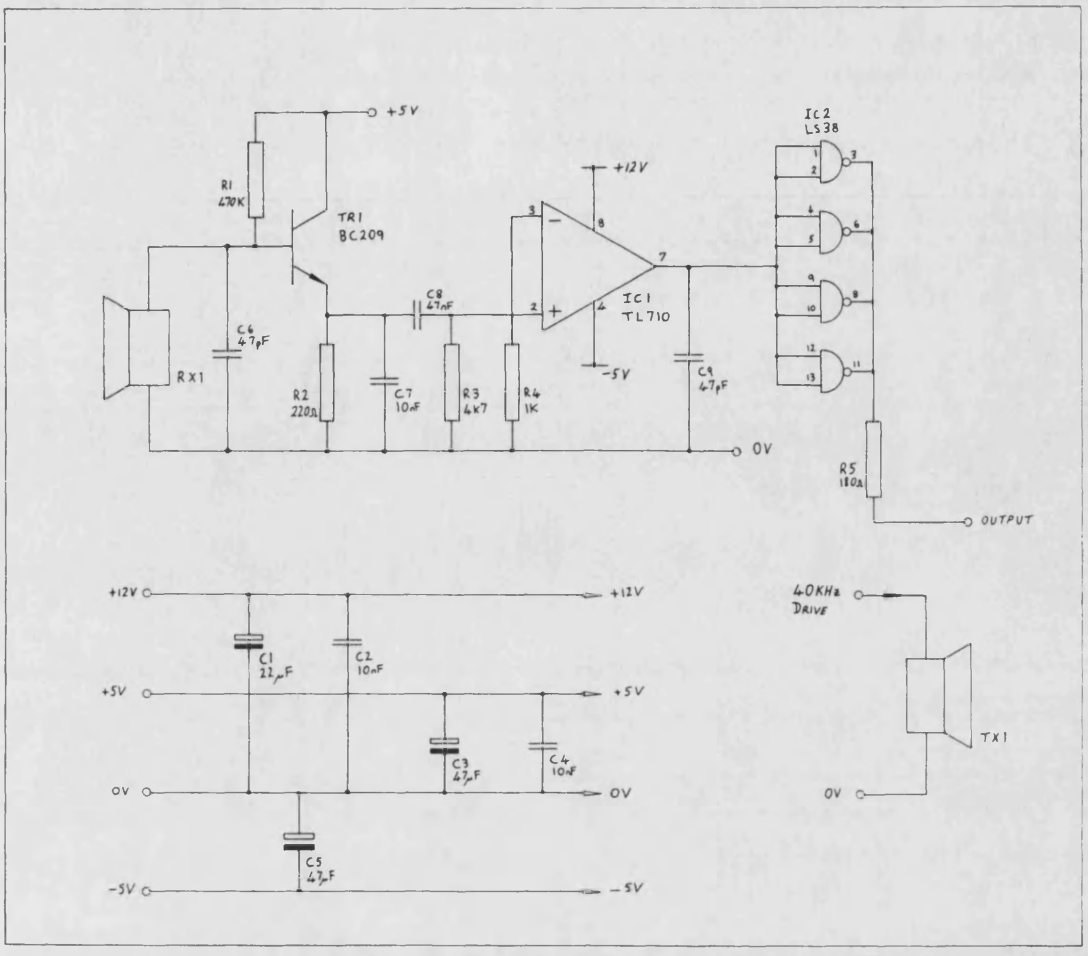

Remote transducer unit circuit diagram Figure 2.33

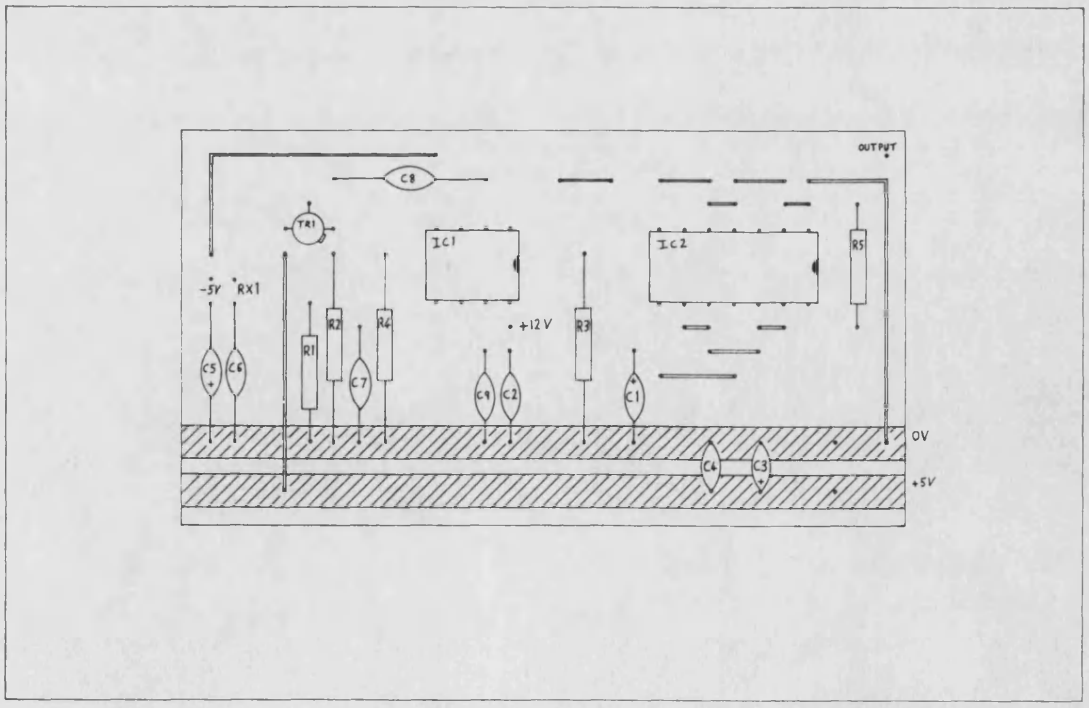

Remote transducer unit component layout Figure 2.34

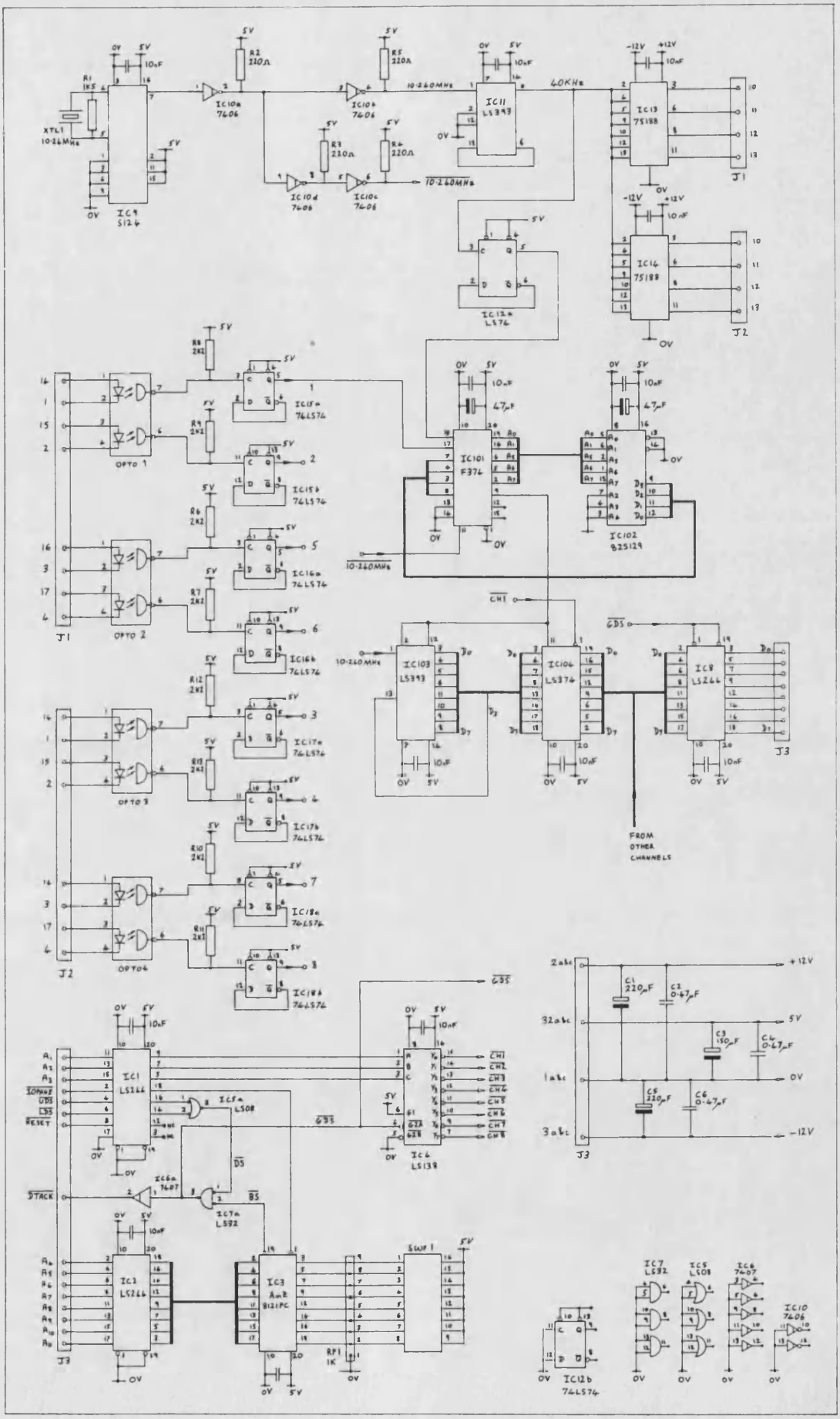

Gap measurement board circuit diagram Figure 2.35

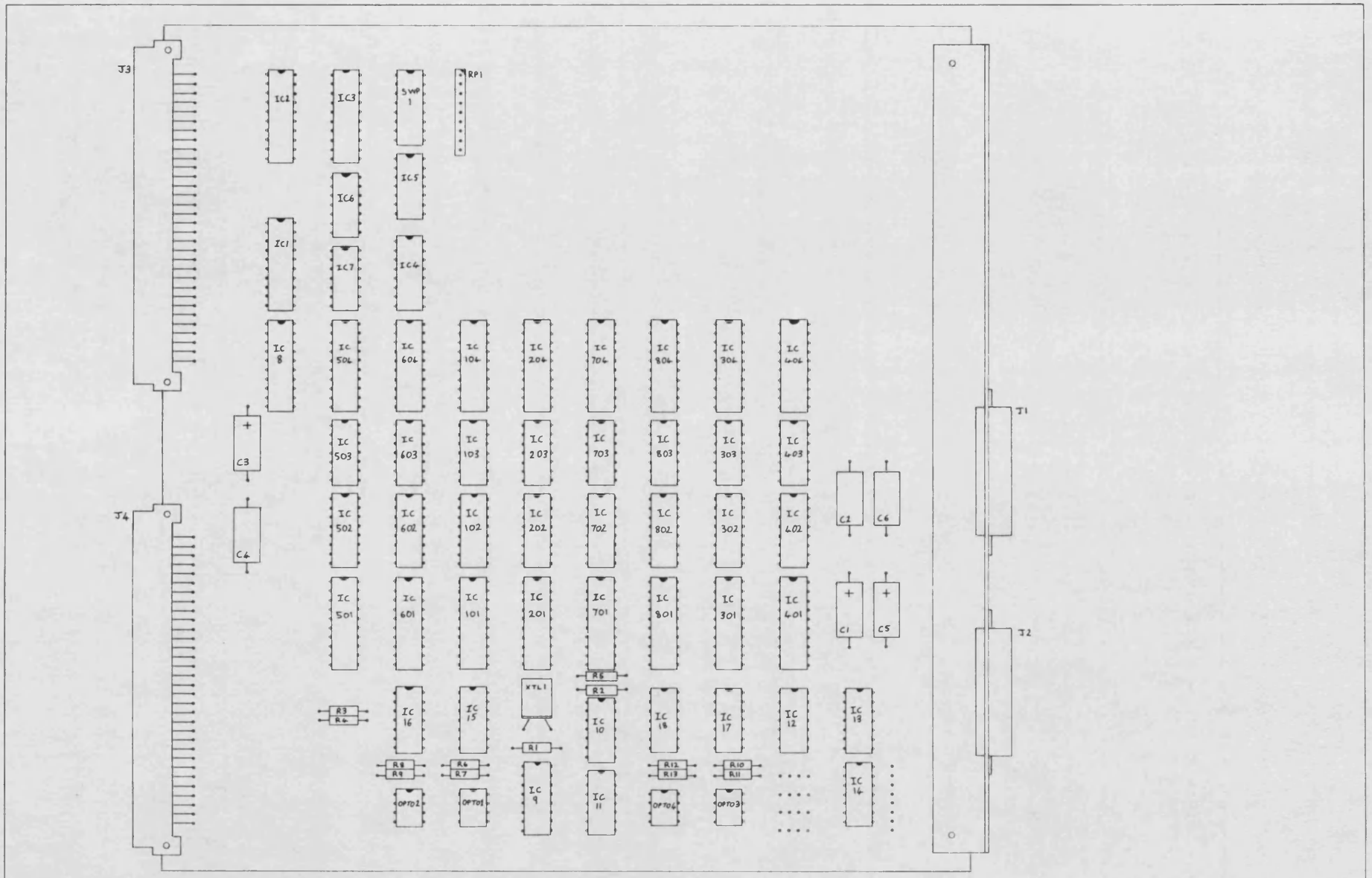

Gap measurement board component layout Figure 2.36

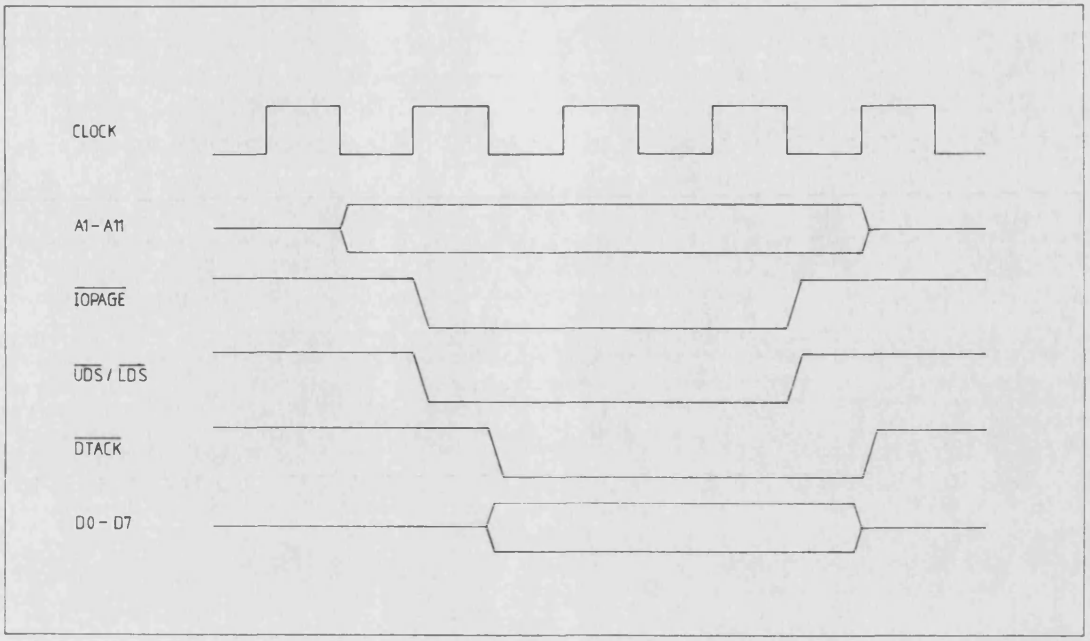

68000 SBC off board read cycle timing diagram Figure 2.37

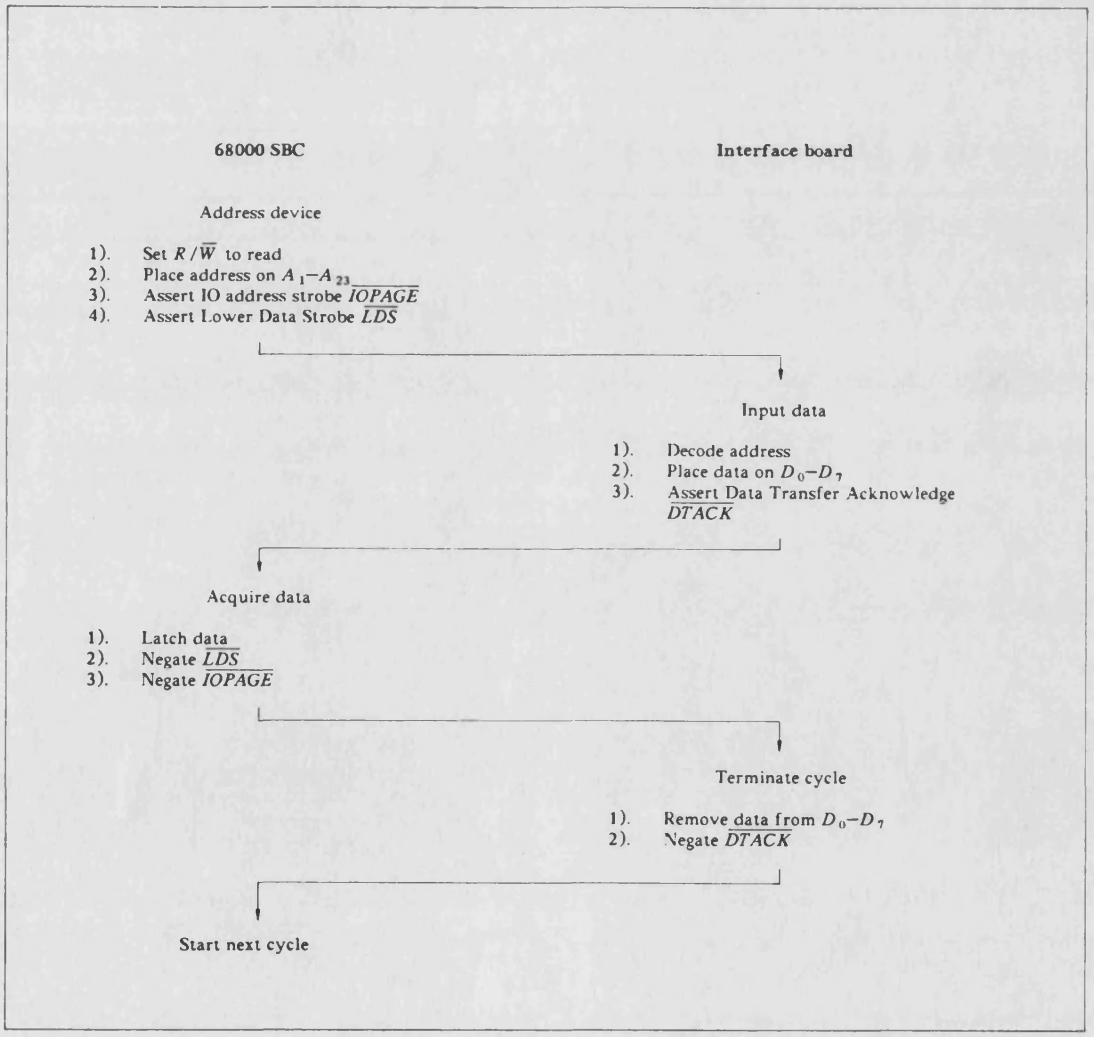

68000 SBC off board read cycle flowchart showing backplane handshake protocol Figure 2.38

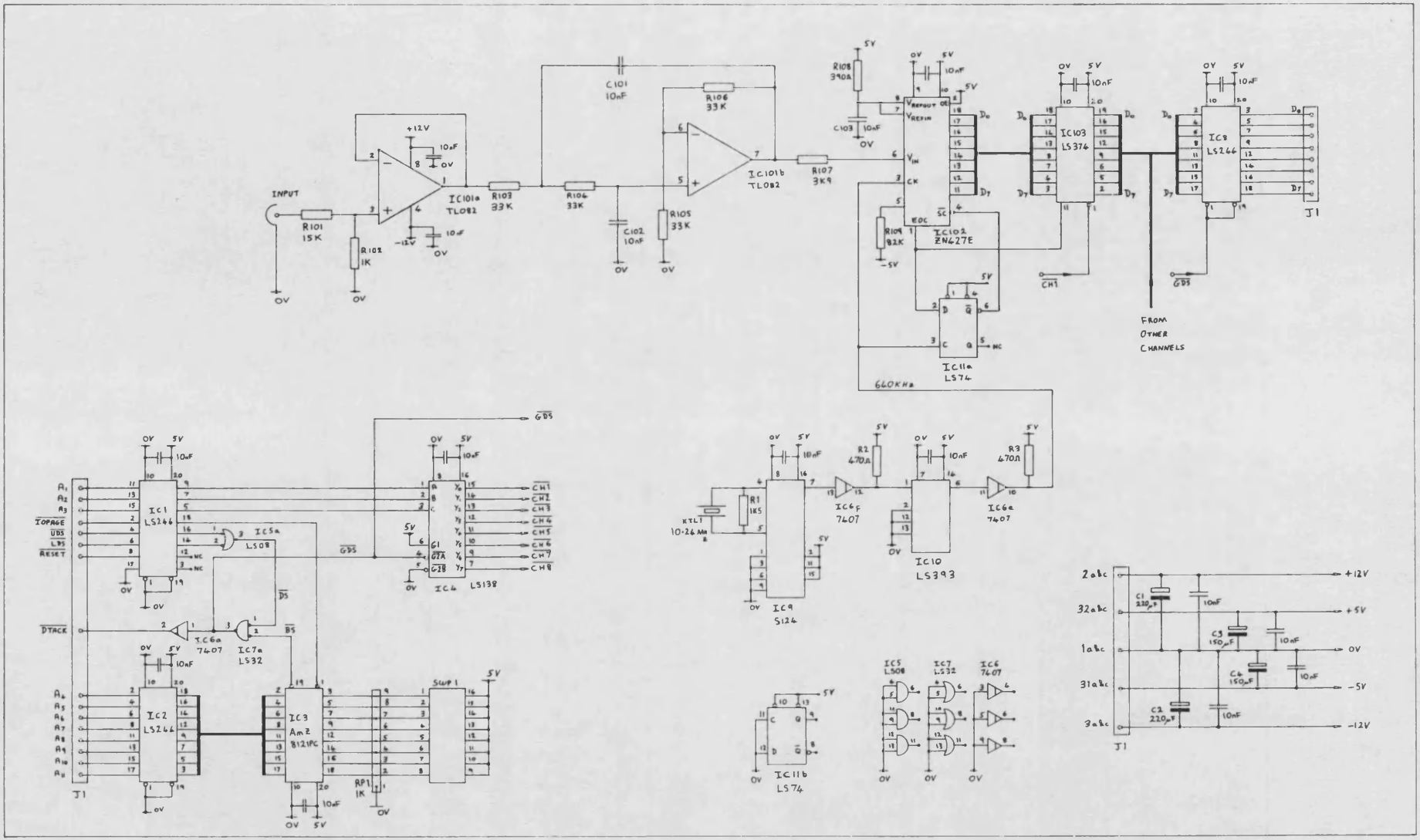

Analogue to digital converter board circuit diagram — Figure 2.39

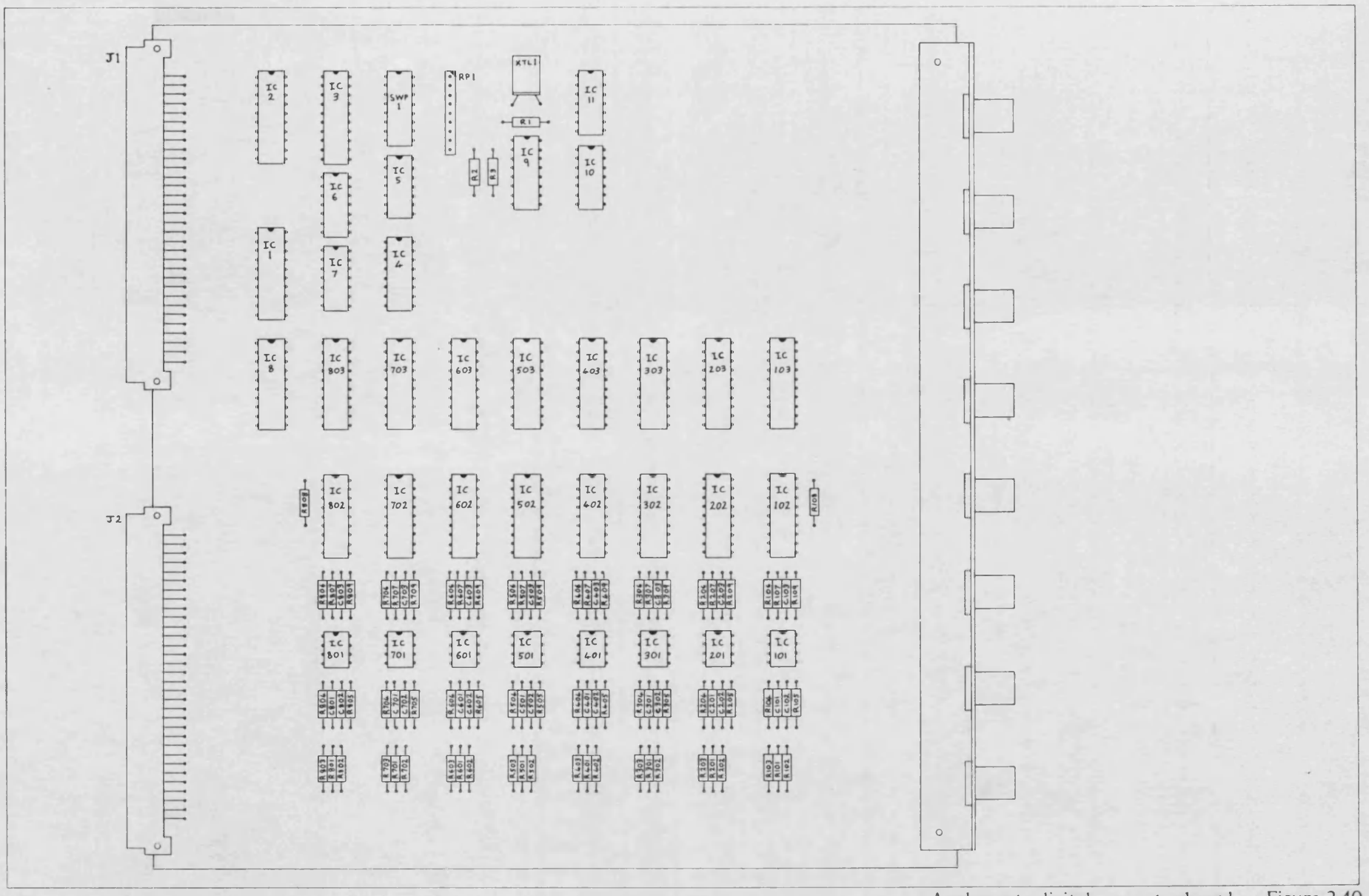

Analogue to digital converter board component layout

Figure 2.40

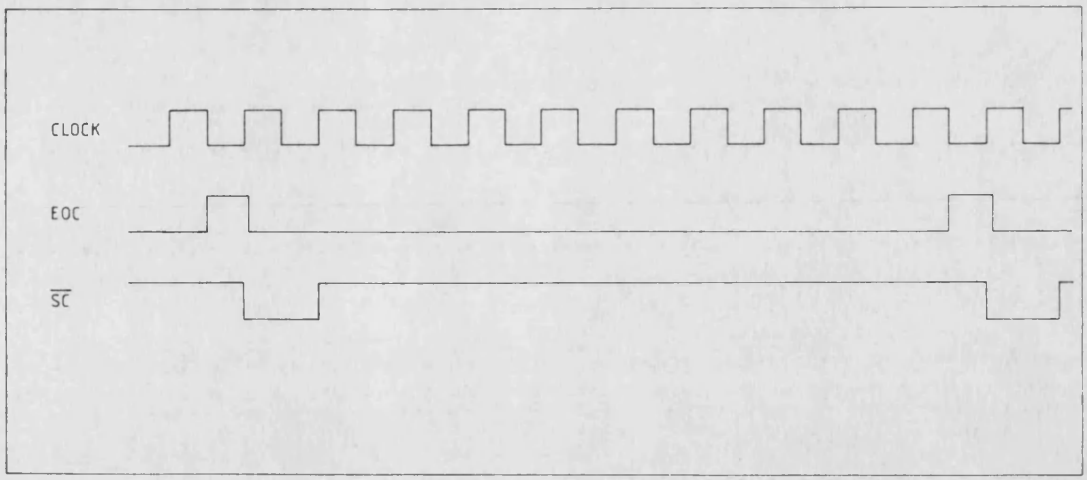

Analogue to digital converter control signal timing diagram Figure 2.41

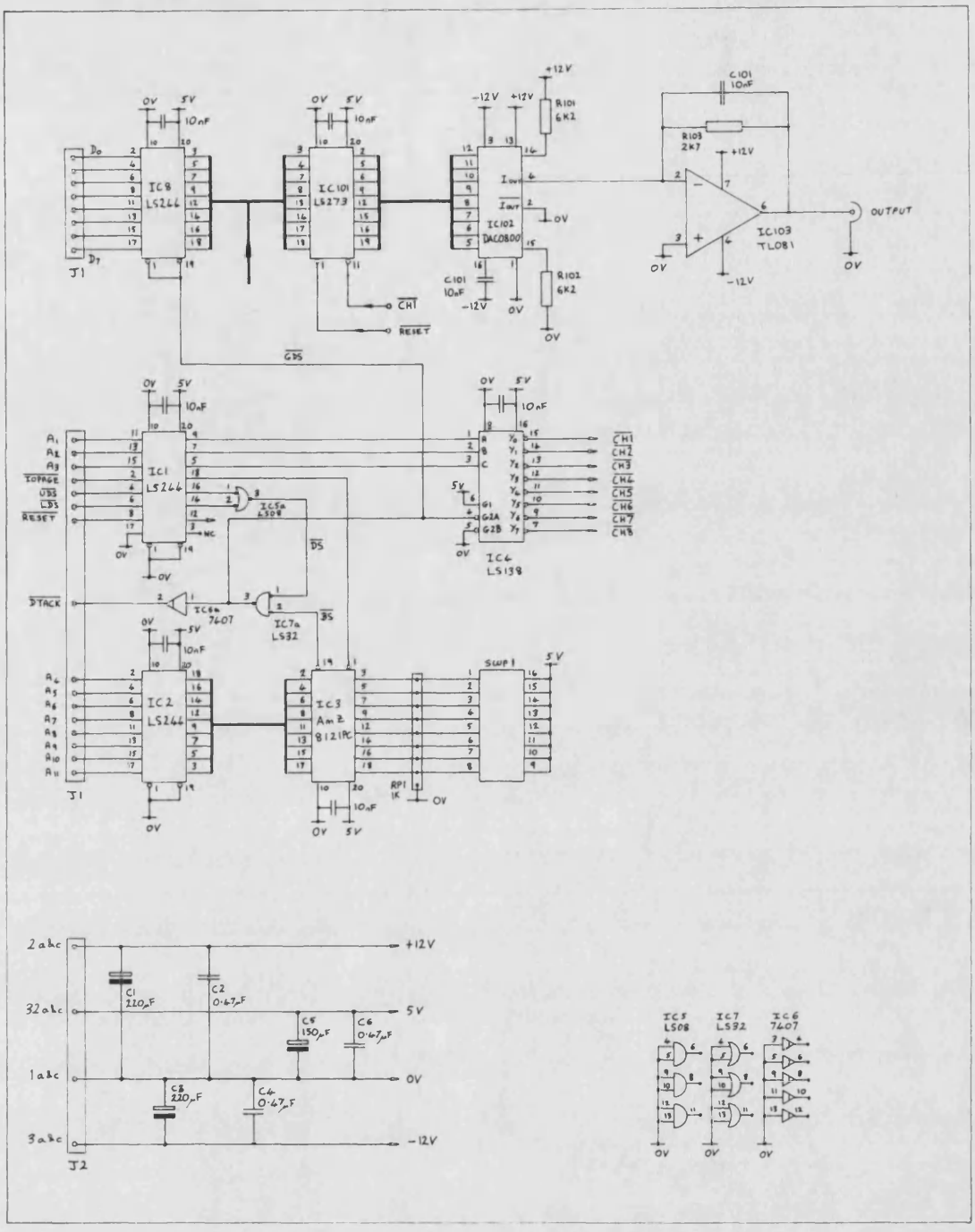

Digital to analogue converter board circuit diagram

Figure 2.42

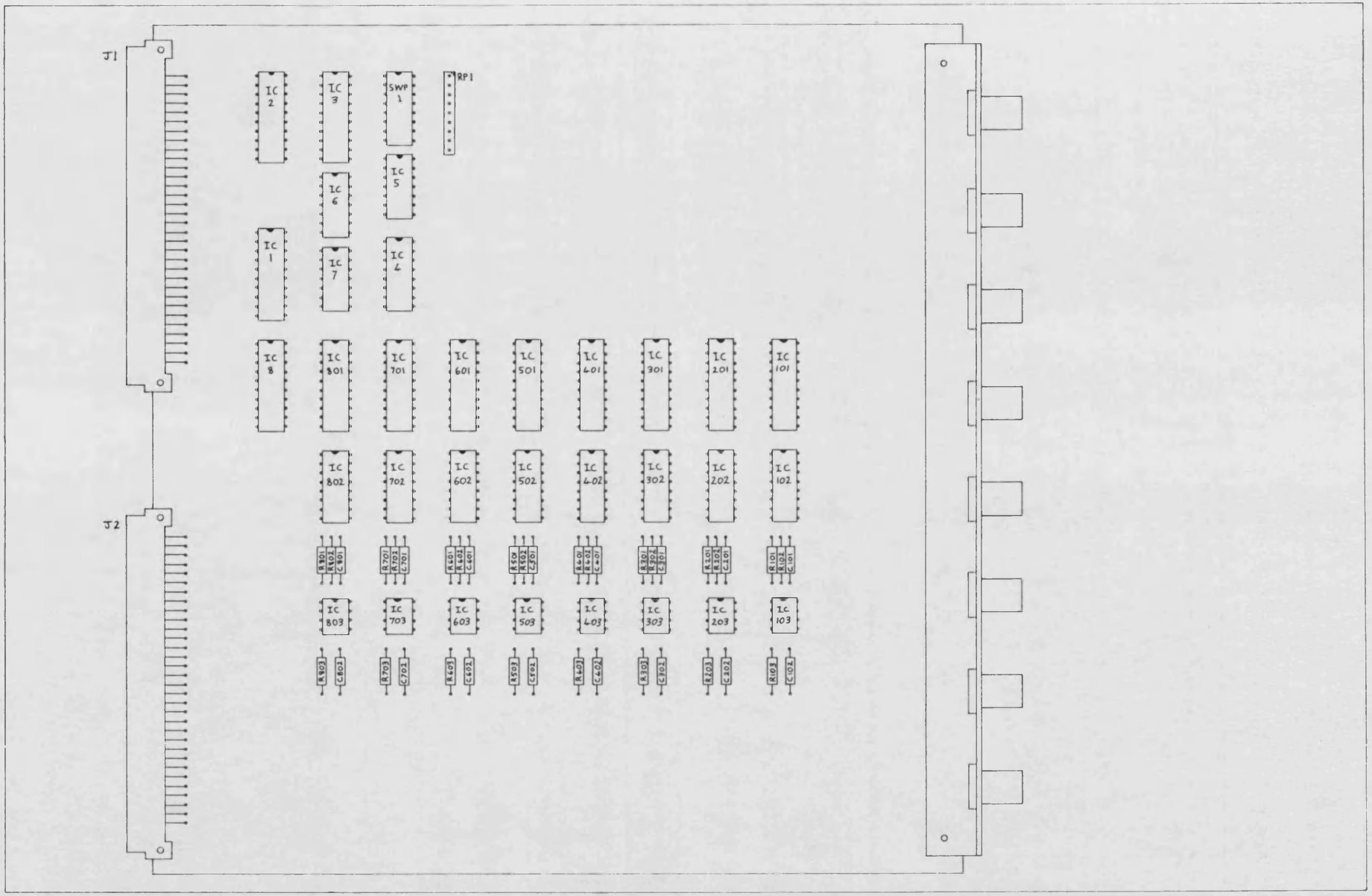

Digital to analogue converter board component layout — Figure 2.43

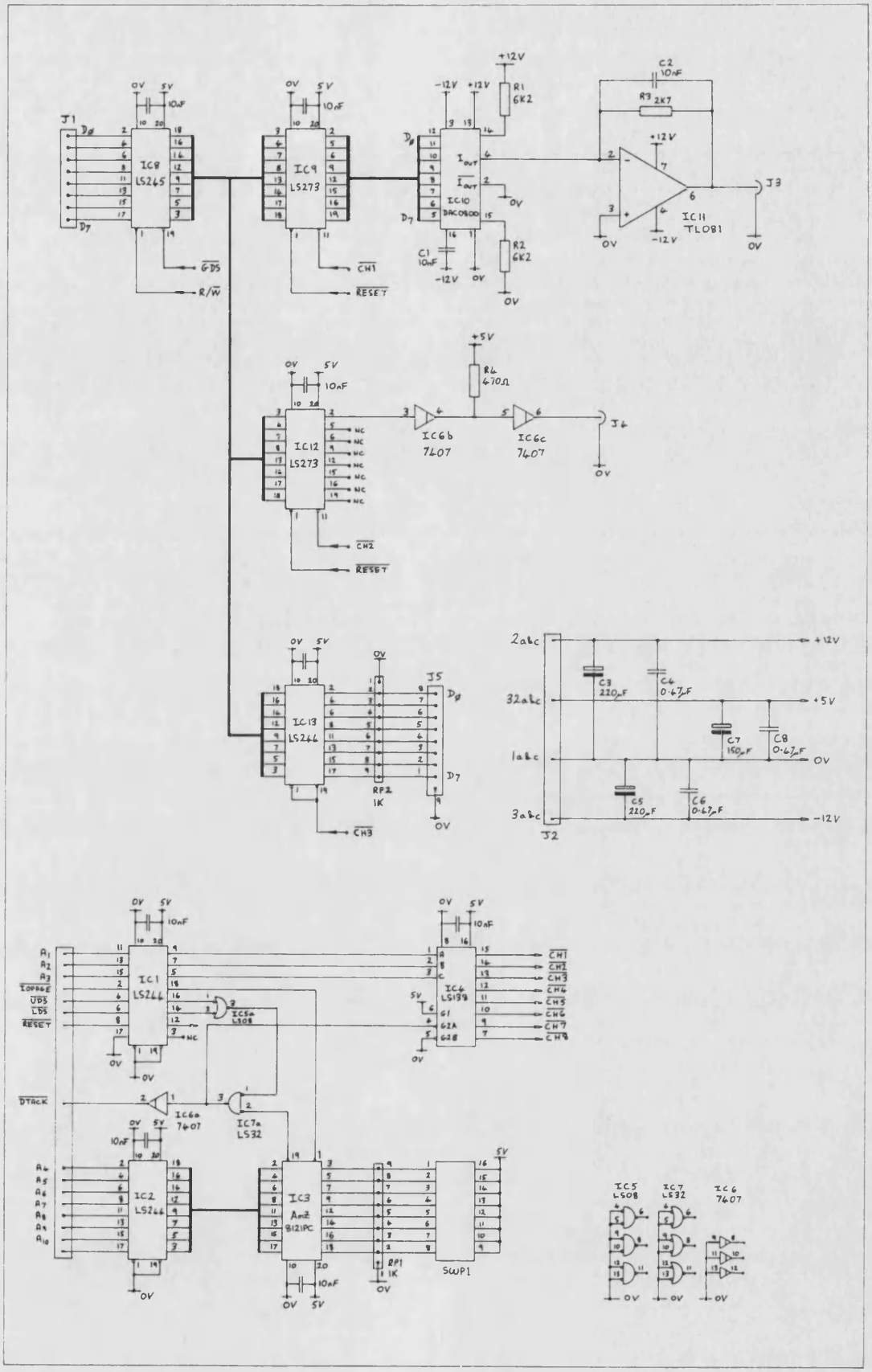

Inverter interface board circuit diagram Figure 2.44

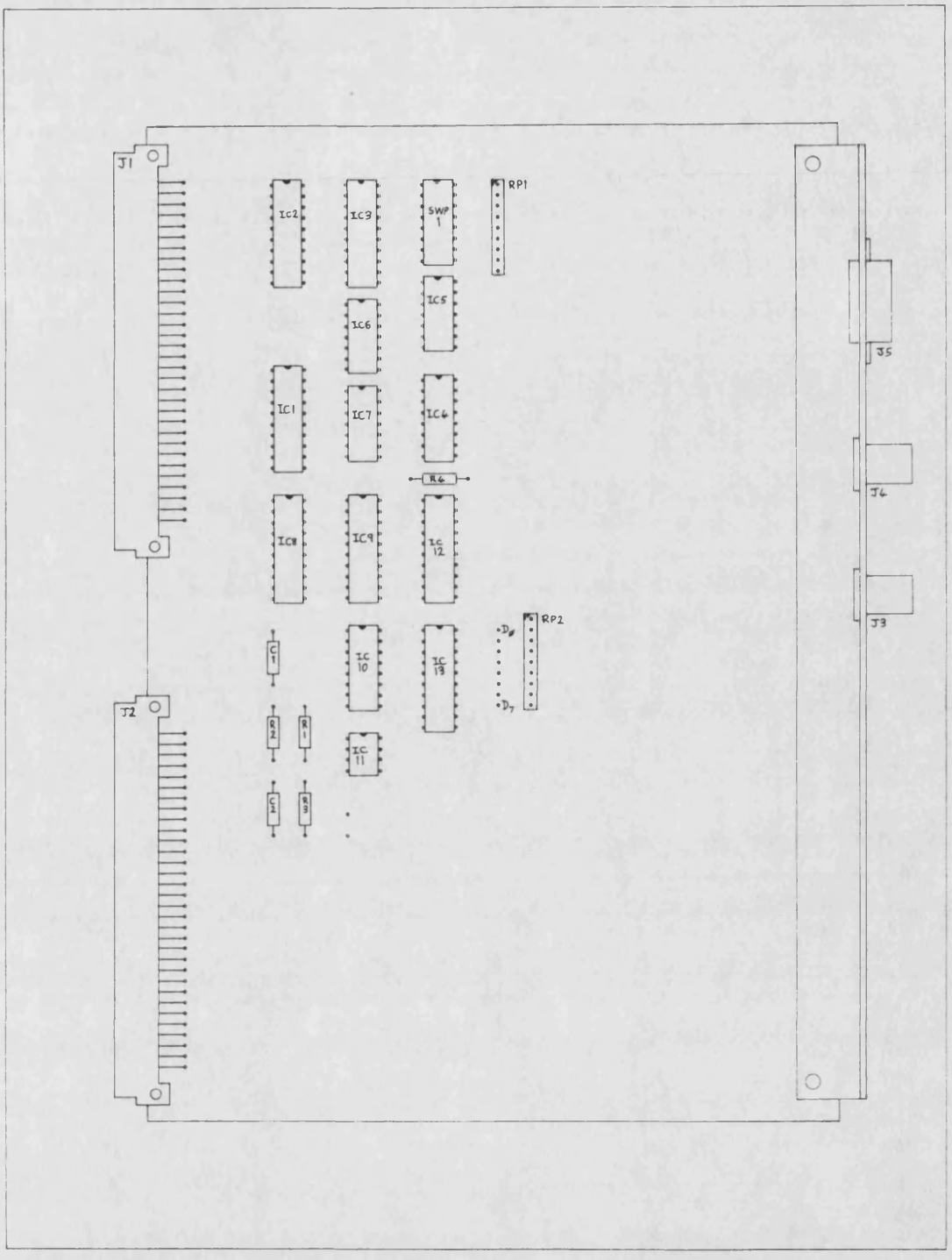

Inverter interface board component layout Figure 2.45

3. High speed digital filter implementation

Because the vehicle controller was to be fully digital, it was decided to develop a generalised set of high performance digital filter structures[20] which would enable any controller transfer function to be realised. By using this pre-defined filter block approach, the control programs could be kept highly structured, making debugging and modification very much simpler than perhaps a purpose designed controller might achieve. The cost for this readability is met by an inevitable reduction in speed, although by careful use of a conditional assembler the filter speed can be kept very close to optimum.

The filters developed probably represent close to the maximum performance which can be obtained from a standard sixteen bit microprocessor within which all arithmetic computations are carried out by the processor itself.

3.1 The digital filter structure

3.1.1 The delay operator The more usual method of designing a digital filter is to use the delay operator z to derive the linear difference equations of the filter function. However, for reasonably fast filters[21], the difference between samples can be very small resulting in a potentially high sensitivity of the filter performance to changes in filter coefficients. To overcome this sensitivity, a different operator is often used which is equal to $z - 1$ and will hereafter be referred to as δ[22].

$$\delta = z - 1 \qquad \text{equation 3.1}$$

3.1.2 The transform The Bilinear transform was used to convert a continuous filter, expressed in terms of the linear Laplace operator s, to the equivalent discrete filter representation using the above δ operator. Expressed in terms of z, the Bilinear transform was written down as follows,

$$s = \frac{z - 1}{T(z + 1)} \qquad \text{equation 3.2}$$

where T is half the sample period.

This can be expressed in terms of δ as shown in equation 3.3 below.

$$s = \frac{\delta}{T(\delta + 2)} \qquad \text{equation 3.3}$$

This has the advantage of being a simple algebraic substitution, and is therefore very straightforward to use.

Having defined the operator for expressing the discrete filter functions, the filter structure will now be developed so as to minimise the number and complexity of multiplications carried out within the filter. By way of example, the following three basic filter blocks will be derived in discrete form.

1. First order filter
2. Second order filter
3. Integrator

By careful design of these three basic filter functions, any desired filter or controller transfer function could be realised with minimal difficulty simply by combining pre-tested routines.

3.1.3 The first order filter Consider the general form of the first order filter given below.

$$T(s) = \frac{a_0 + a_1 s}{1 + b_1 s} \qquad \text{equation 3.4}$$

Applying the Bilinear transform of equation 3.3,

$$T(\delta) = \frac{a_0 + \dfrac{a_1 \delta}{T(\delta + 2)}}{1 + \dfrac{b_1 \delta}{T(\delta + 2)}}$$

$$= \frac{\delta(Ta_0 + a_1) + 2a_0 T}{\delta(T + b_1) + 2T}$$

$$= \frac{p + qm_1\delta^{-1}}{1 + m_1\delta^{-1}} \qquad \text{equation 3.5}$$

where

$$p = \frac{Ta_0 + a_1}{T + b_1} \qquad \text{equation 3.6}$$

$$q = a_0 \qquad \text{equation 3.7}$$

$$m_1 = \frac{2T}{T + b_1} \qquad \text{equation 3.8}$$

The discrete transfer function of equation 3.5 may be implemented by recognising the standard first order state feedback transfer function of equation 3.9 below,

$$\frac{m_1\delta^{-1}}{1 + m_1\delta^{-1}} \qquad \text{equation 3.9}$$

This equation is derived from the standard first order feedback structure illustrated in the block diagram of figure 3.1a. It follows that the full implementation of equation 3.5 may then be represented by the block diagram of figure 3.1b, from which the linear difference equations of the first order filter can be written down as follows,

$$P_n = X_n - Q_n \qquad \text{equation 3.10}$$

$$Y_n = qQ_n + pP_n \qquad \text{equation 3.11}$$

$$Q_n = m_1\delta^{-1}P_n \qquad \text{equation 3.12}$$

The P_n and Q_n values are internal to the digital filter and are used to form the Y_n result. After Y_n has been calculated as the filter output, the next Q_n value, Q_{n+1}, must be calculated. Using equation 3.1 in equation 3.12 it follows that,

$$Q_n = \frac{m_1P_n}{z - 1}$$

giving

$$Q_{n+1} = m_1P_n + Q_n \qquad \text{equation 3.13}$$

3.1.4 The second order filter Consider the general form of the second order filter given below.

$$T(s) = \frac{a_0 + a_1 s + a_2 s^2}{1 + b_1 s + b_2 s^2} \qquad \text{equation 3.14}$$

Applying the Bilinear transform of equation 3.3, it can be shown that the equivalent discrete transfer function is given by,

$$T(\delta) = \frac{p + q m_1 \delta^{-1} + r m_1 m_2 \delta^{-2}}{1 + m_1 \delta^{-1} + m_1 m_2 \delta^{-2}} \qquad \text{equation 3.15}$$

where

$$p = \frac{T^2 a_0 + T a_1 + a_2}{T^2 + b_1 T + b_2} \qquad \text{equation 3.16}$$

$$q = \frac{2T a_0 + a_1}{2T + b_1} \qquad \text{equation 3.17}$$

$$r = a_0 \qquad \text{equation 3.18}$$

$$m_1 = \frac{4T^2 + 2b_1 T}{T^2 + b_1 T + b_2} \qquad \text{equation 3.19}$$

$$m_2 = \frac{2T}{2T + b_1} \qquad \text{equation 3.20}$$

The discrete transfer function of equation 3.15 may be implemented by recognising the standard second order full state feedback transfer function of equation 3.21 below,

$$\frac{m_1 m_2 \delta^{-2}}{1 + m_1 \delta^{-1} + m_1 m_2 \delta^{-2}} \qquad \text{equation 3.21}$$

This equation is derived from the standard second order full state feedback structure illustrated in the block diagram of figure 3.2a. It follows that the full implementation of equation 3.15 may then be represented by the block diagram of figure 3.2b, from which the linear difference equations of the second order filter can be written down as follows,

$$P_n = X_n - R_n - Q_n \qquad \text{equation 3.22}$$

$$Y_n = pP_n + qQ_n + rR_n \qquad \text{equation 3.23}$$

$$R_{n+1} = m_2 Q_n + R_n \qquad \text{equation 3.24}$$

$$Q_{n+1} = m_1 P_n + Q_n \qquad \text{equation 3.25}$$

As with the first order filter, after the value Y_n has been calculated and output, the

internal filter variables Q_n and R_n are updated.

3.1.5 The integrator Consider the generalised integrator transfer function given by equation 3.26 below,

$$T(s) = \frac{a_0}{s} \qquad \text{equation 3.26}$$

Applying the transform of equation 3.3 the equivalent discrete transfer function was derived as follows,

$$T(\delta) = a_0 T\left\{\frac{\delta + 2}{\delta}\right\}$$

$$= a_0 T(1 + 2\delta^{-1})$$

$$= p + m_1\delta^{-1} \qquad \text{equation 3.27}$$

where

$$p = a_0 T \qquad \text{equation 3.28}$$

$$m_1 = 2a_0 T \qquad \text{equation 3.29}$$

The discrete transfer function of equation 3.27 was implemented as shown in the block diagram of figure 3.3. Note that the integrator function has a similar structure to that of the first order filter but does not make use of negative feedback. With reference to figure 3.3, the linear difference equations of the integrator function were written down as follows,

$$P_n = X_n \qquad \text{equation 3.30}$$

$$Y_n = pP_n + Q_n \qquad \text{equation 3.31}$$

$$Q_{n+1} = m_1 P_n + Q_n \qquad \text{equation 3.32}$$

As with the first and second order filters, after the value Y_n has been calculated and output, the internal variable Q_n is updated.

3.2 The number format

Digital filter implementations are notorious for using combinations of obscure number

systems which have been 'designed' for extracting the greatest possible speed from a given microprocessor. Such filters are difficult to maintain and debug, with any modifications sometimes requiring a complete redesign. Not least, the mechanism of these filters can be very hard to explain, leading to awkward documentation. With the aim of avoiding these difficulties a fixed point number system was adopted based on work originated by Goodall and Brown[20].

To be able to use a fixed point number system universally throughout the filter, all input, output and internal variables must be of similar order.

3.2.1 Filter variables For both the input and output variables of the filter, a twelve bit integer format was used. This would directly represent an input or output from the processor using, for example, the purpose built IO boards described in the previous chapter.

The first internal variable P_n is formed from a difference equation with X_n, and hence must have the same resolution as X_n. The remaining internal variables Q_n and R_n, however, are formed by accumulating fractional numbers (the filter coefficients m_1 and m_2 are always less than unity) and hence require fractional bits to achieve the higher resolution. To decide upon the number of fractional bits required, the filter step response to a one lsb change in input (and hence P_n) is considered with respect to the equation for Q_{n+1} (equation 3.13) reproduced below,

$$Q_{n+1} = m_1 P_n + Q_n$$

So if Q_{n+1} is to respond to the one lsb change in P_n, then Q_n must have a resolution of m_1 or better.

The number system finally adopted was designed to fit into a field width of 32 bits as shown in figure 3.4. This would achieve the required number resolution and also suit the 32-bit arithmetic instruction set provided by the MC68000 microprocessor. The upper sixteen bits represent integer values (twelve bits plus four overflow) and the

lower sixteen bits represent the fractional bits required by the internal variables Q_n and R_n. Note that when performing input or output of eight or twelve bit values, care must be taken to duplicate the sign as represented by bit 31.

3.3 Fixed coefficient multiplication

Having standardised the number format for the filter variables all that remained was a requirement for a multiplication routine which would multiply these variables by fixed coefficients, specifically p, q, r, m_1 and m_2, which would always be small integers or fractional. To cope with these fractional numbers a floating point format was adopted, again as first suggested by Goodall and Brown. The coefficient thus represented is then given by equation 3.33 below,

$$coefficient = mantissa \times 2^{-exponent} \qquad \text{equation 3.33}$$

Using this format a filter variable is multiplied by the required coefficient value in two stages,

1. The filter variable is first multiplied by the mantissa part of the coefficient using a conventional binary multiplication algorithm (shift, add etc).

2. Providing the exponent part of the coefficient is non-zero, the multiplication result is then shifted n bits to the right, where n is the exponent value.

A mantissa width of four bits was specified to ensure good multiplication speed whilst maintaining adequate resolution for representing a given filter coefficient to an accuracy of better than 10%.

By defining the multiply routine as an assembler macro containing conditional assembly statements, an optimised four bit multiply could be derived at assembly time for any given coefficient. For example, to multiply a filter variable by the integer value of eight, the optimised multiplication routine would be comprised of three left shift instructions.

All filter coefficients were converted to the above floating point format using the program *bcpl.format* (included as listing 3.1), which calculates and prints the mantissa and exponent values required to represent a given filter coefficient.

3.3.1 Format program operation The format program is required to represent an integer or fractional coefficient as a four bit mantissa with negative exponent as shown previously in equation 3.33. Now to obtain maximum resolution all four mantissa bits should be used, which provides the criterion for fixing the initial exponent value as follows.

$$exponent = \log_2 \left\{ \frac{mantissa.max}{coefficient} \right\} \qquad \text{equation 3.34}$$

where $mantissa.max = 15$ using four bits.

The exponent is then truncated to an integer value which is substituted back into equation 3.33 to obtain the required mantissa value. The mantissa value is then rounded up or down according to which gives the least error.

3.4 Filter software

3.4.1 Standard macro definitions To maintain ease of use and good readability of the filter software, the various filter components together with the fixed coefficient multiplication routine were defined as macros which could be invoked via the assembler to achieve any given filter or controller transfer function. Listing 3.2 includes the full set of filter macro definitions used throughout this study and appendix C summarises their function and usage. The argument list for each macro includes storage offset and coefficient information so that any number of separate filters can be defined using the same macros.

In order to be able to use the filter software, a filter timebase was required which would effectively call a user defined filter combination once every sample period.

3.4.2 Generating the filter timebase To obtain a periodic filter timebase, a series of three programs (included as listing 3.3) were written in 68000 assembly language to gain control of the Tripos interrupt driven clock. A description of the operation and use of each of these programs is given below.

init() The initialisation program speeds up the Tripos clock* to generate an accurate 1 ms periodic interrupt for use as a filter timebase. The program then arranges to intercept these interrupts by replacing the Tripos clock interrupt vector with a new vector pointing to the filter service routine. The remainder of the program performs initialisation of the filter variables as required.

service() The service routine is where the user defined filter programs would reside. Additionally this routine includes a globally defined counter which is incremented every filter cycle to provide a bcpl supervisory program with a filter duration parameter. To maintain the 20 ms Tripos clock a local timer is maintained so that the Tripos clock service routine can be called at these intervals.

uninit() The uninitialisation routine terminates the filter program and restores the original Tripos clock interrupt vector and clock period.

Note that the init() and uninit() programs were written as bcpl callable routines** such that a high level supervisory program written in bcpl could call these programs as required. An example of the supervisor program, called bcpl.runtimer, is included as listing 3.4.

---

* The Tripos clock period is normally 20 ms

** The rules for writing bcpl callable assembly language routines are given in the Tripos Programming Guide[14].

3.4.3 Data logging A reasonably sophisticated multi-channel 'moving window' data logging algorithm was developed for generalised use with the filter software. This type of logger has the important advantage of being able to record continuously using a finite length FIFO buffer. Essentially the buffer can record up to T seconds of data, after which the buffer is said to *roll over* and any new data overwrites old data from the previous T seconds. The advantage here is that any event may be recorded by stopping the logger after the event, rather than starting the logger before the event. Operation of the data logger is described below.

An initialisation routine (illustrated by the flowchart of figure 3.5) finds the base address of the buffer space allocated by the bcpl supervisory program, which is then stored locally as the buffer start address. The buffer pointer variable points to the next buffer location to be used, and hence has an initial value equal to the buffer start address. A third variable, called buffer position, counts the number of entries in the buffer from the base address, and is used to control buffer rollover. When the number of entries reaches the length of the buffer, the rollover flag is permanently set and the buffer pointer is reset to the buffer start address. The rollover flag is used to warn the bcpl supervisory program that the buffer start is no longer necessarily at the buffer base address.

The data logging routine itself is described by the flowchart of figure 3.6. Note that channel one must always contain the interrupt cycle count, and is used by the bcpl supervisory program to derive the timebase for the other channels.

Once the filter program has finished and the filter interrupts have been disabled, the bcpl supervisory program separates and scales each of the buffer channels and writes out the data to the hard disc.

3.5 Filter testing

The following three filters were implemented in digital form to check the validity of

the filter software thus far developed.

$$T(s) = \frac{10}{s + 10} \qquad \text{Filter1}$$

$$T(s) = \frac{\omega_n^2}{s^2 + 2\zeta\omega_n s + \omega_n^2} \qquad \text{Filter2}$$

$$T(s) = \frac{3.0}{s} \qquad \text{Filter3}$$

where $\omega_n = 30$ and $\zeta = 0.5$

A listing of the filter assembly program is given in listing 3.5 (asm.filter), which shows how the integrator, the first and the second order filter macros were invoked and how the filter coefficients are passed in the macro argument list. The supervisory program which loads and runs the filter software is included as listing 3.6 (bcpl.supervisor). Note that the filter software makes use of two header files, namely asm.filterhdr and bcpl.filterhdr (listings 3.7 and 3.8 respectively), which specify the manifest constants and the global variables.

3.5.1 Filter reference inputs One of the more familiar filter characteristics is the step response, and hence it was decided to provide the filters with a step input from 0 to 255, which would be applied after 100 ms. Timing of the reference inputs was provided by using a local software counter to maintain an interrupt cycle count. A second run was then made using a step input from 0 to 1 to check the filter response to an input change of one lsb.

3.5.2 Filter simulation The first and second order filter responses were calculated using a fourth order Runge-Kutta based simulator routine[23]. Using a time increment of 1 ms the simulated results would be highly accurate and could be used to assess the digital filter performance. The integrator response to a step input is simply a ramp with a slope given by the step magnitude multiplied by the integrator gain, a_0. Hence a simulated result of the integrator response was not required.

3.6 Results

Graphs 3.1a and 3.1b illustrate the outputs of the first and second order digital filters respectively during the first test, in which a reference input from 0 to 255 is applied 100 ms into the filter run. Graphs 3.1c and 3.1d provide the corresponding simulation results.

Graphs 3.2a and 3.2b illustrate the first and second order digital filter outputs during the second test, in which a reference input from 0 to 1 is applied to test the filter responses to a one lsb change in the reference input. The digital integrator responses during the first and second tests are illustrated by graphs 3.3a and 3.3b respectively.

The high degree of correlation between the digital filter responses and the simulated results illustrates the integrity achieved by the digital filter implementation techniques developed in this chapter.

3.6.1 Filter speed Listing 3.9 provides all the timing information of the various filter macros developed in this chapter. Note that because each filter is optimally assembled for a given set of coefficients, the precise filter speed would have to be calculated for each specific application. The overall filter routine servicing time must also include the context switching time on entry to and exit from the routine, which in the worst case is 614 clock cycles of the 8 MHz microprocessor (includes a call to the Tripos clock service routine).

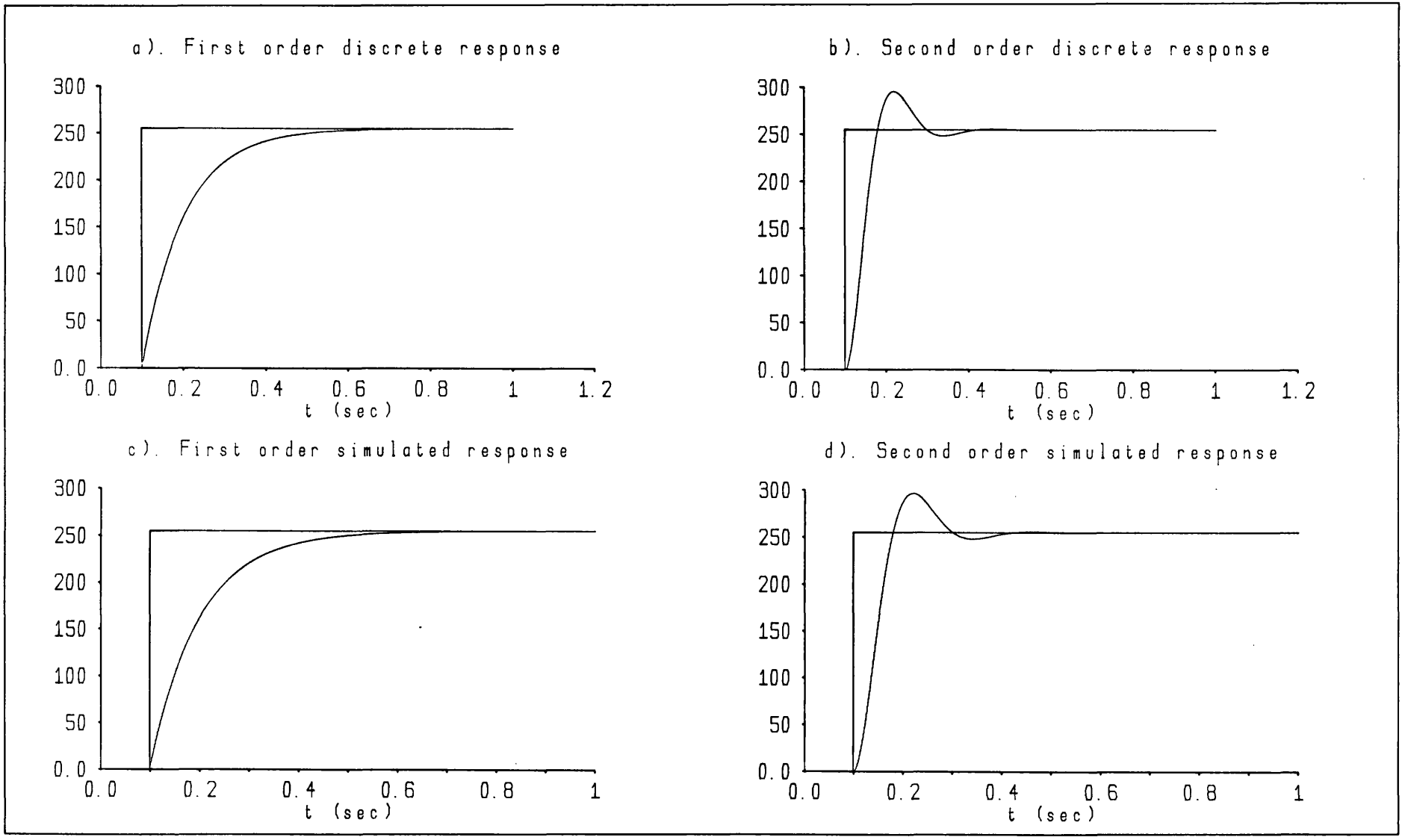

First and second order filter step responses **Graph 3.1**

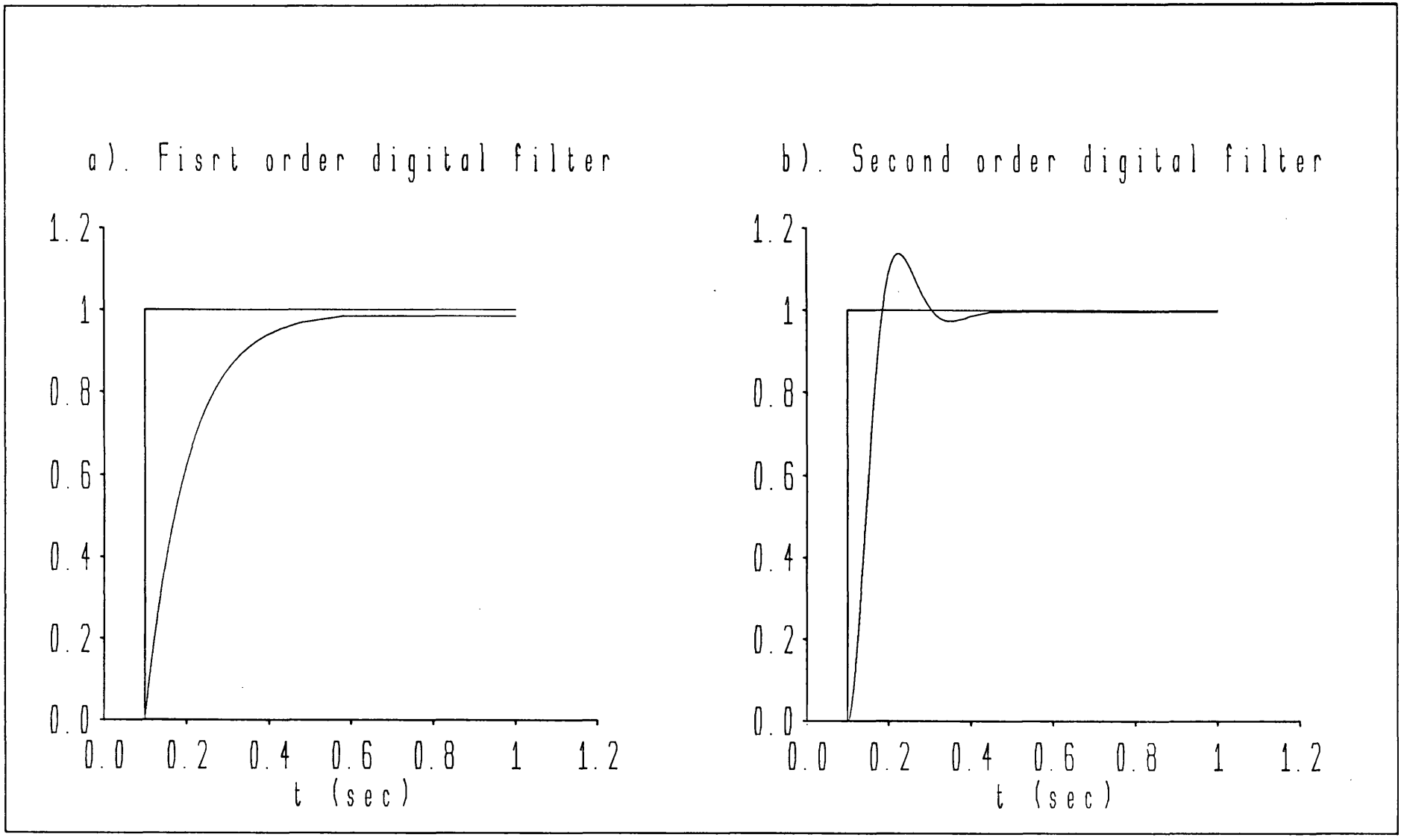

First and second order filter step responses (one lsb) Graph 3.2

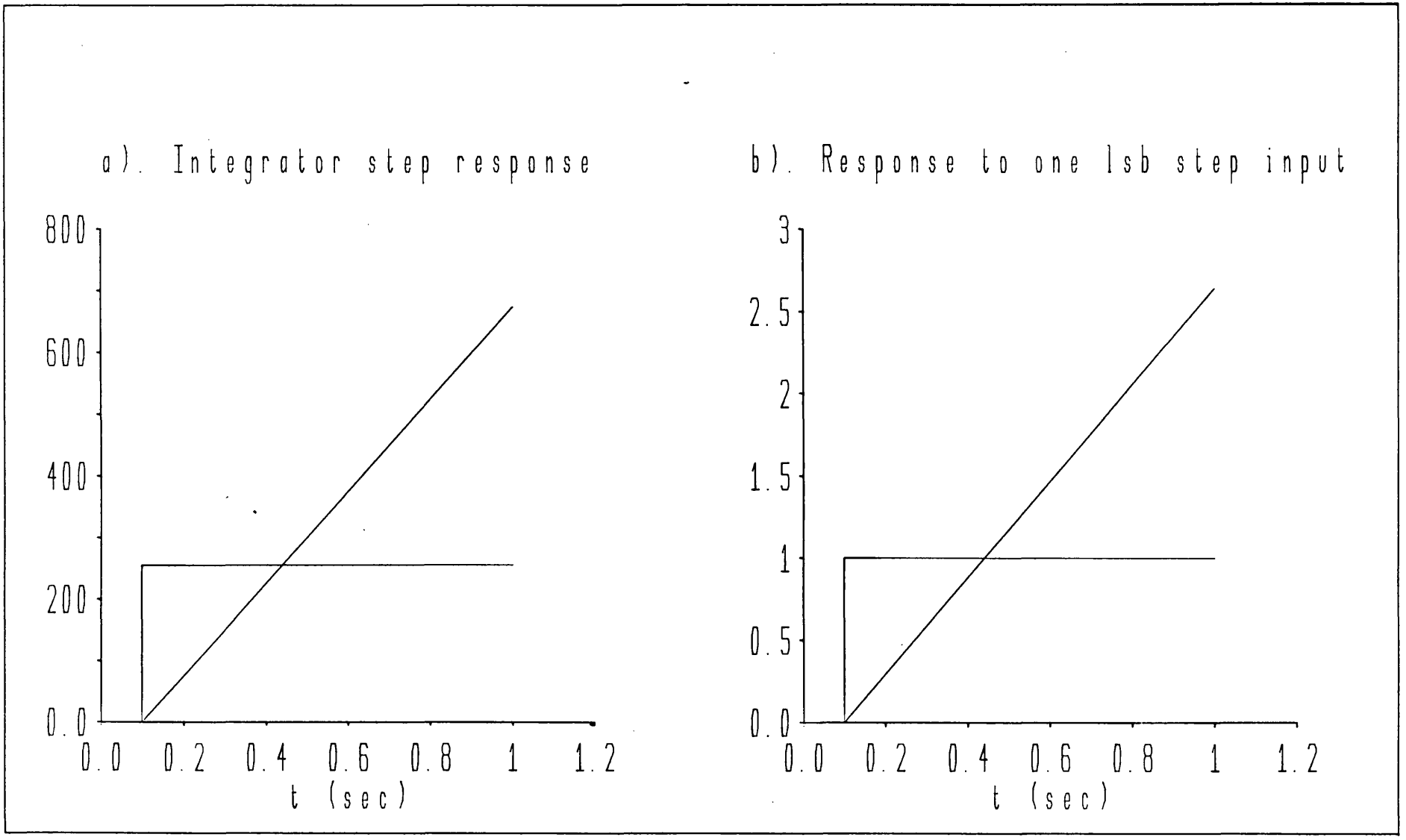

Integrator step responses Graph 3.3

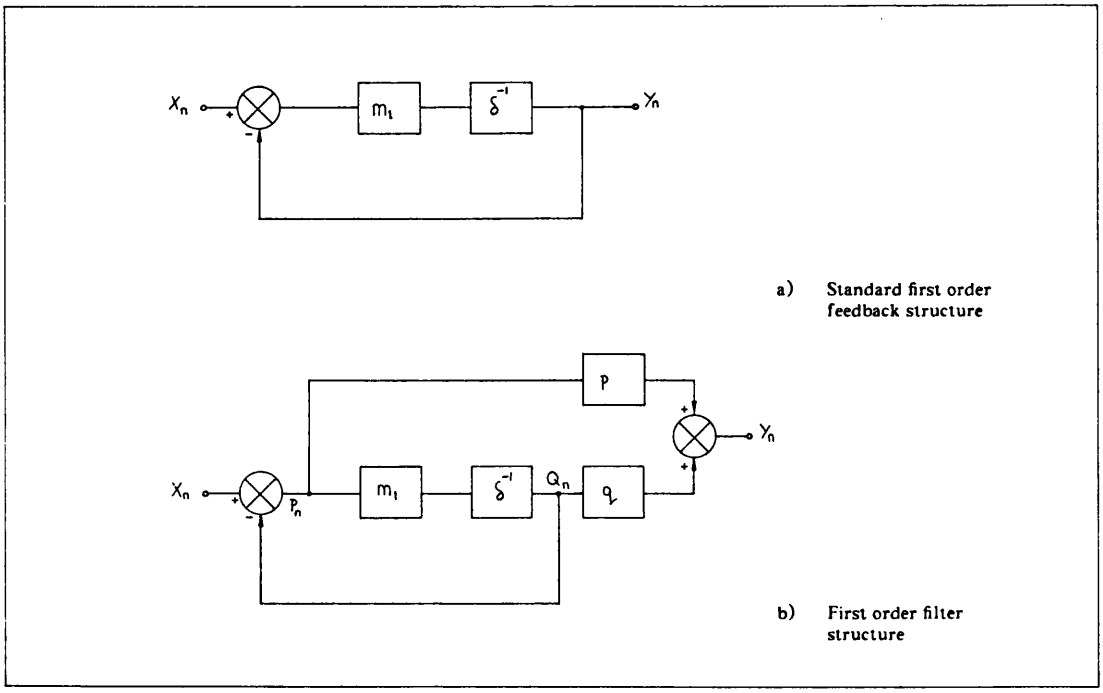

Derivation of the first order filter structure Figure 3.1

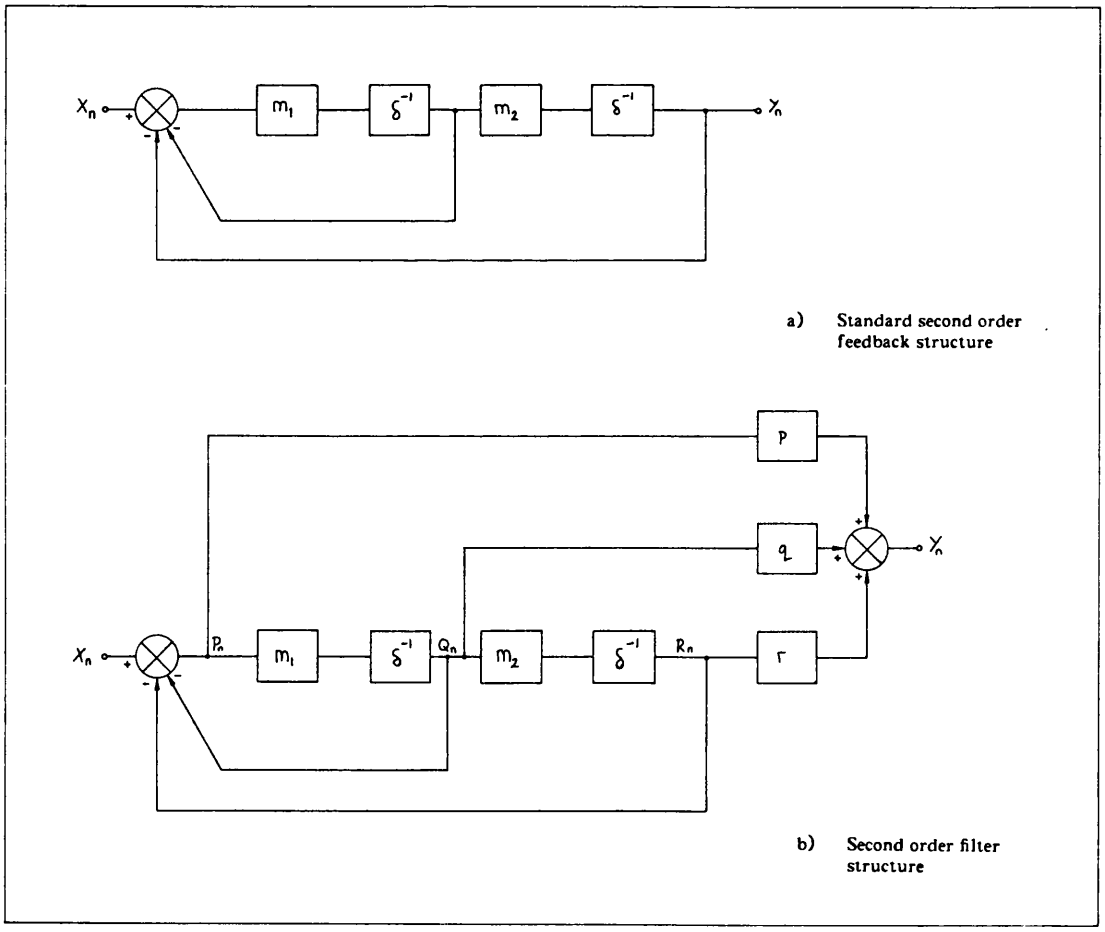

Derivation of the second order filter structure Figure 3.2

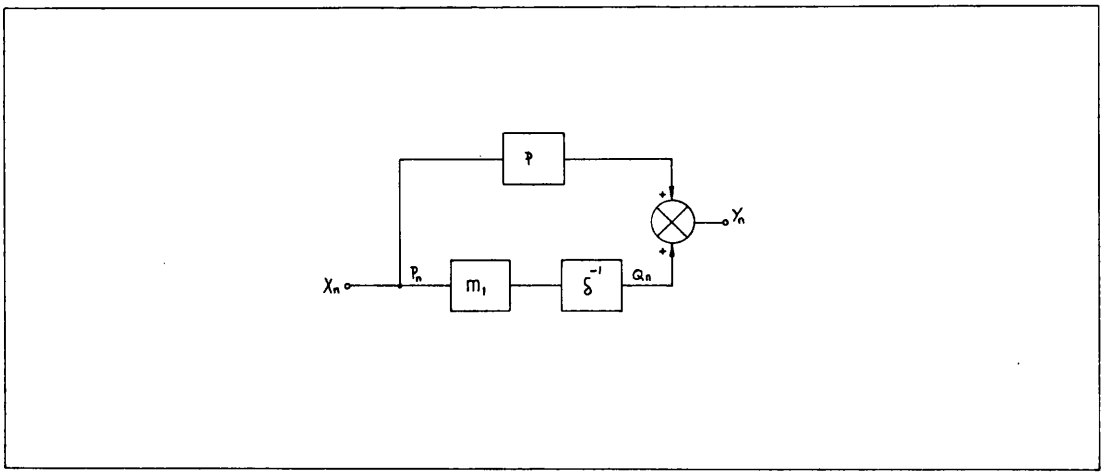

Integrator filter structure Figure 3.3

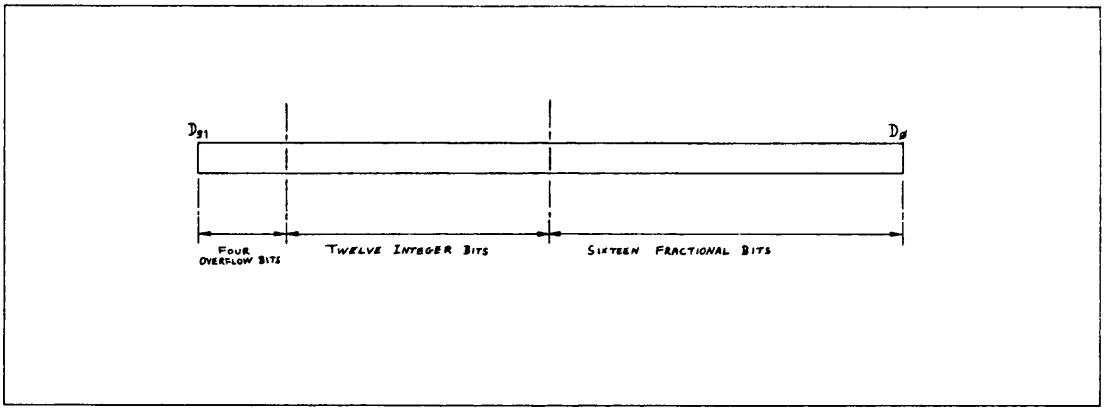

The number format used for filter variables Figure 3.4

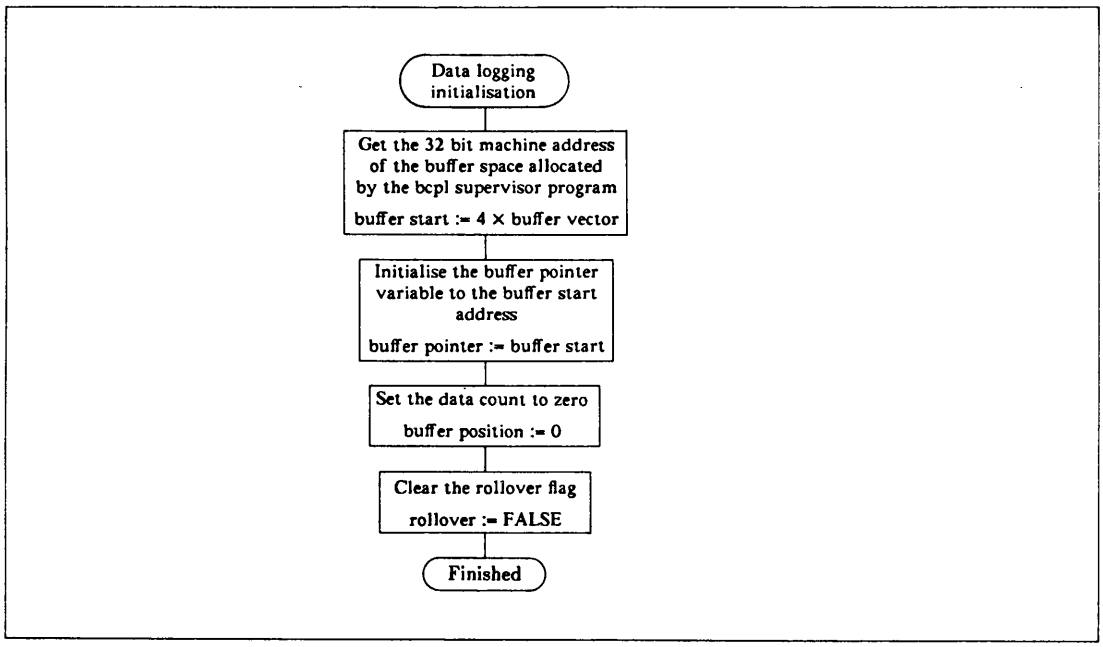

Flowchart of data logger initialisation Figure 3.5

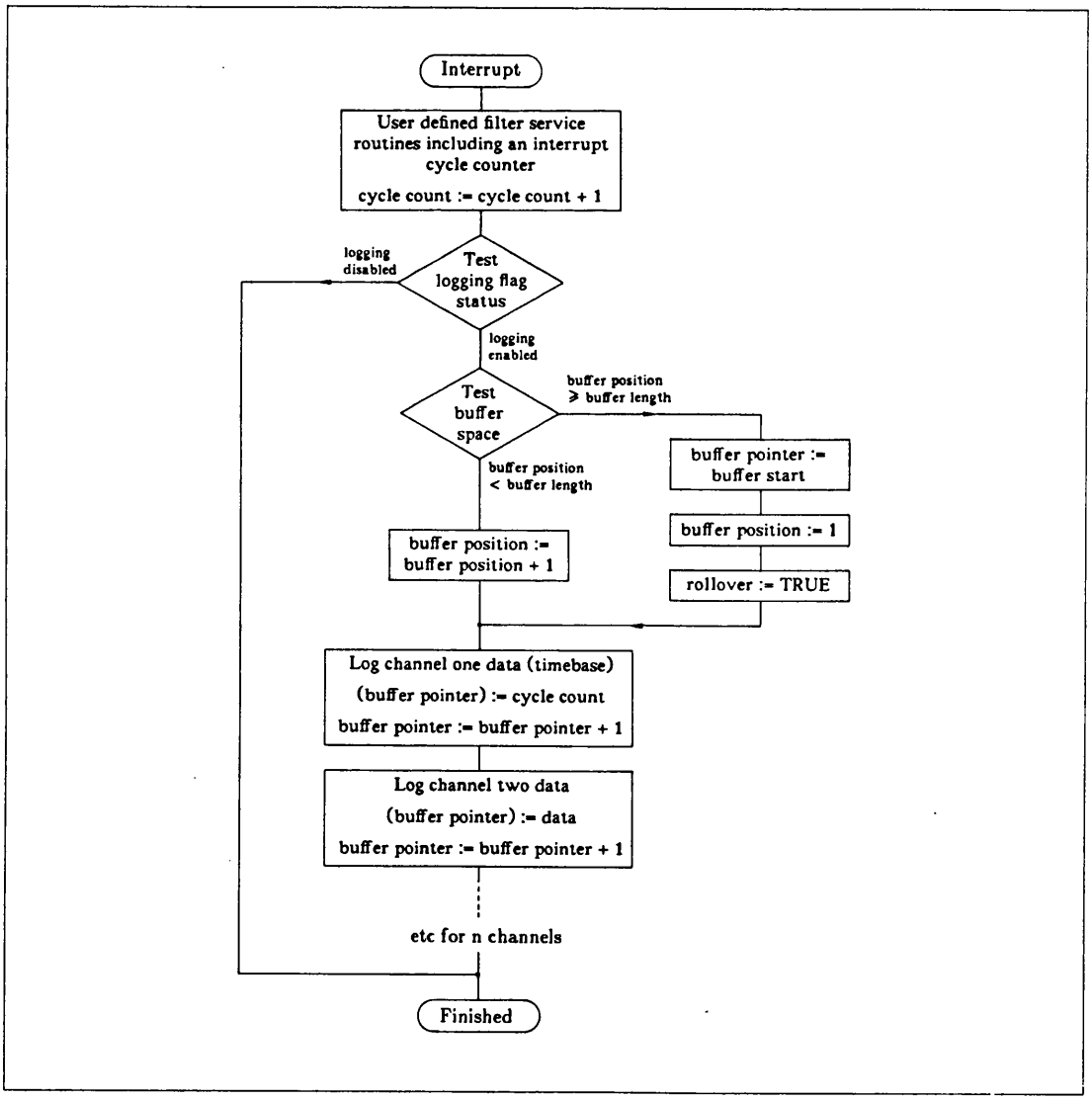

Flowchart of data logger Figure 3.6

4. Derivation of a linearised vehicle model

The digital control scheme for the vehicle was to be implemented on the multiprocessor computer system by using the standard filter structures described in the previous chapter. Because these structures were based on linear design techniques, it was necessary to produce a set of linearised mathematical models representing the vehicle dynamics in response to applied force for each of the degrees of freedom of the vehicle.

Additionally, to convert transducer information from each corner of the vehicle into the required coordinate system for each degree of vehicle freedom, a set of coordinate translation equations were derived. These equations would be required at the input to the vehicle controller and would be used in inverse form at the controller output to provide individual demand signals for the magnets.

4.1 Degrees of vehicle freedom

With the vehicle chassis as defined in chapter 2, seven degrees of vehicle freedom were identified (hereafter called modes) as defined in figure 4.1 and listed below.

1. Heave
2. Roll
3. Pitch
4. Twist
5. Lateral
6. Yaw
7. Traction

Note that with the simple motor/chassis arrangement previously discussed the centre of mass of the vehicle is coplanar with its linear synchronous motors. Because the axis of each mode passes through this central point, interaction between modes is kept to a minimum. For example, a step demand in tractive effort will cause the vehicle to accelerate but will not cause any significant pitch component.

The above seven modes were divided into three categories according to the vehicle hardware used for their control.

4.1.1 Levitation modes The heave, roll, pitch and twist modes were controlled using the magnetic field produced by the d.c. field winding of the linear synchronous motors

mounted at each corner of the vehicle. The control requirement is for a steady ride height of 7 mm (heave) with zero roll, pitch or twist. The twist mode was required because any vehicle twist would not be observable by the heave, roll or pitch controllers and hence would be uncontrolled. In the worst case, two diagonally opposing levitation motors would clamp up to the track, due either to vehicle flexing or to a severe track discontinuity.

One solution to this problem has been to produce a sufficiently rigid vehicle chassis which the levitation motors could not twist significantly[24]. This solution has the disadvantage that the degree of chassis stiffness required is very great since any twist component must not influence any of the magnet gaps by more than one or two millimetres. Also the track would have to be flat to within the tolerance of the motor gaps throughout the length of the vehicle.

Hence by defining and controlling a twist mode the vehicle chassis need be no more than a light framework and significant reductions in vehicle cost could be made. The type of twist control employed would depend on the transducer used to derive the twist signal,

1. Using a chassis twist transducer (e.g. strain gauges) the vehicle could be kept flat independent of the track.
2. Using the existing track referenced corner gap transducers a flexible vehicle (or vehicle bogie) could be made to follow a twisted track.

The latter method of twist measurement was chosen since it could be implemented using the existing vehicle hardware.

4.1.2 Side modes Control of the lateral and yaw modes is carried out using side magnets mounted on each corner of the vehicle. By controlling these modes for zero lateral and yaw error the correct alignment of the linear synchronous motors beneath the secondary track members is ensured.

4.1.3 Tractive mode Provided that the levitation and side mode controllers have lifted and aligned the vehicle and have established a steady state d.c. magnetic field in each of the linear synchronous motors, the tractive effort is then provided by controlling the current in the three phase armature windings of these motors. Throughout this thesis, the levitative and tractive modes of the LSM are considered to be fully decoupled (see section 2.1.1).

4.2 Coordinate translation

In the levitation and side control modes all measurements are taken from transducers positioned at each corner of the vehicle. Hence it was necessary to translate the transducer outputs into the chosen coordinate system. Controller outputs would similarly have to be translated to derive the individual magnet demand signals.

4.2.1 Notation The following notation was used throughout the study,

x displacement

$\ddot{x}$ acceleration

F force

Subscripts 1, 2, 3 and 4 denote corner quantities for the levitation modes, whilst 5, 6, 7 and 8 denote the corresponding side quantities. Subscripts H, R, P, T, L and Y denote, respectively, heave, roll, pitch, twist, lateral and yaw quantities as indicated by using the first letter of the appropriate parameter. Where small signal quantities are referred to, the prefix δ is also used.

4.2.2 Levitation modes With reference to figure 4.1 the following coordinate translation matrices were written down,

$$\begin{bmatrix} \delta x_H \\ \delta x_R \\ \delta x_P \\ \delta x_T \end{bmatrix} = \frac{1}{4} \begin{bmatrix} 1 & 1 & 1 & 1 \\ -1 & 1 & 1 & -1 \\ 1 & 1 & -1 & -1 \\ -1 & 1 & -1 & 1 \end{bmatrix} \begin{bmatrix} \delta x_1 \\ \delta x_2 \\ \delta x_3 \\ \delta x_4 \end{bmatrix} \qquad \text{equation 4.1}$$

$$\begin{bmatrix} \delta\ddot{x}_H \\ \delta\ddot{x}_R \\ \delta\ddot{x}_P \\ \delta\ddot{x}_T \end{bmatrix} = \frac{1}{4}\begin{bmatrix} 1 & 1 & 1 & 1 \\ -1 & 1 & 1 & -1 \\ 1 & 1 & -1 & -1 \\ -1 & 1 & -1 & 1 \end{bmatrix}\begin{bmatrix} \delta\ddot{x}_1 \\ \delta\ddot{x}_2 \\ \delta\ddot{x}_3 \\ \delta\ddot{x}_4 \end{bmatrix} \qquad \text{equation 4.2}$$

$$\begin{bmatrix} \delta F_H \\ \delta F_R \\ \delta F_P \\ \delta F_T \end{bmatrix} = \begin{bmatrix} 1 & 1 & 1 & 1 \\ -1 & 1 & 1 & -1 \\ 1 & 1 & -1 & -1 \\ -1 & 1 & -1 & 1 \end{bmatrix}\begin{bmatrix} \delta F_1 \\ \delta F_2 \\ \delta F_3 \\ \delta F_4 \end{bmatrix} \qquad \text{equation 4.3}$$

Note, for example, that the heave displacement δx_H is given by the average corner displacement, whereas the heave force δF_H is given by summing the four corner forces.

The controller outputs in turn are converted to corner quantities using the inverse of equation 4.3.

$$\begin{bmatrix} \delta F_1 \\ \delta F_2 \\ \delta F_3 \\ \delta F_4 \end{bmatrix} = \frac{1}{4}\begin{bmatrix} 1 & -1 & 1 & -1 \\ 1 & 1 & 1 & 1 \\ 1 & 1 & -1 & -1 \\ 1 & -1 & -1 & 1 \end{bmatrix}\begin{bmatrix} \delta F_H \\ \delta F_R \\ \delta F_P \\ \delta F_T \end{bmatrix} \qquad \text{equation 4.4}$$

At this stage, for simplicity, the controller outputs have been assumed to be force demands to idealised force actuators. In practice however, the controller outputs will be either current or flux demands (depending on the type of chopper used) which are then translated to appropriate corner quantites using the translation matrix of equation 4.4.

4.2.3 Side modes With reference to figure 4.1 the coordinate translation matrices for the side modes were written down as follows.

$$\begin{bmatrix} \delta x_L \\ \delta x_Y \end{bmatrix} = \frac{1}{4}\begin{bmatrix} 1 & -1 & -1 & 1 \\ -1 & 1 & -1 & 1 \end{bmatrix}\begin{bmatrix} \delta x_5 \\ \delta x_6 \\ \delta x_7 \\ \delta x_8 \end{bmatrix} \qquad \text{equation 4.5}$$

$$\begin{bmatrix} \delta F_L \\ \delta F_Y \end{bmatrix} = \begin{bmatrix} 1 & -1 & -1 & 1 \\ -1 & 1 & -1 & 1 \end{bmatrix} \begin{bmatrix} \delta F_5 \\ \delta F_6 \\ \delta F_7 \\ \delta F_8 \end{bmatrix} \qquad \text{equation 4.6}$$

Note that acceleration signals were not available to the side mode controllers.

Controller outputs were converted to corner quantities using the inverse of equation 4.6.

$$\begin{bmatrix} \delta F_5 \\ \delta F_6 \\ \delta F_7 \\ \delta F_8 \end{bmatrix} = \frac{1}{4} \begin{bmatrix} 1 & -1 \\ -1 & 1 \\ -1 & -1 \\ 1 & 1 \end{bmatrix} \begin{bmatrix} \delta F_L \\ \delta F_Y \end{bmatrix} \qquad \text{equation 4.7}$$

4.3 Modelling of the levitation modes

A linearised model representing each of the vehicle modes is required to provide the basis for the design of the vehicle controllers. In each case the vehicle dynamics are to be described in terms of applied force in that mode.

4.3.1 Heave model The total force δF_H acting on the vehicle mass M produces a gap acceleration $\delta \ddot{x}_H$ as given by equation 4.8 below,

$$\delta F_H = -M\, \delta \ddot{x}_H \qquad \text{equation 4.8}$$

The negative sign is required because an increase in applied force acts to reduce the heave gap. Using the translation matrix of equation 4.3 the total force δF_H can be seen to be the total of the four corner magnet forces,

$$\delta F_H = \delta F_1 + \delta F_2 + \delta F_3 + \delta F_4$$

As mentioned earlier, each force actuator will be a chopper/magnet combination using either current or flux feedback choppers, for which the linearised models will be derived in later chapters.

4.3.2 Roll model In the roll mode, the total force δF_R acts on the roll inertia I_R at a radius r_R from the roll axis to produce an angular roll acceleration $\delta \ddot{\theta}_R$.

$$\delta F_R r_R = -I_R \delta\ddot{\theta}_R \qquad \text{equation 4.9}$$

The angular displacement in turn is related to the linear displacement (derived from the gap transducers) according to equation 4.10 below,

$$\delta x_R = \delta\theta_R r_R' \qquad \text{equation 4.10}$$

Where r_R' is the distance from the roll axis to the gap transducers and accelerometers, and is slightly greater than r_R.

4.3.3 Pitch model In the pitch mode, the total force δF_P acts on the pitch inertia I_P at a radius r_P from the pitch axis to produce an angular pitch acceleration $\delta\ddot{\theta}_P$,

$$\delta F_P r_P = -I_P \delta\ddot{\theta}_P \qquad \text{equation 4.11}$$

And

$$\delta x_P = \delta\theta_P r_P \qquad \text{equation 4.12}$$

Note that for the pitch mode the distance from the pitch axis to the force actuators, r_P, also applies to the gap transducers and accelerometers.

4.3.4 Twist model For modelling vehicle twist $\delta\theta_T$ in response to applied twist force δF_T it was necessary to take account of the twist inertia , velocity damping and torsional stiffness components of the vehicle chassis. In general, the twist model would take the form given in equation 4.13 below,

$$\delta F_T r_T = -\delta\theta_T (s^2 I_T + sK_v + K_\theta) \qquad \text{equation 4.13}$$

where

K_θ is the torsional stiffness

K_v is the velocity damping factor

I_T is the twist inertia

Experimental values for K_θ, K_v and I_T were then obtained by carrying out steady state and dynamic tests on the vehicle chassis. To perform these two tests one end of the vehicle was clamped rigidly whilst the other end was left free to roll about a central pivot as shown in figure 4.2.

Results were taken using a simple data logging program (listings 4.1 through 4.5 inclusive) which would log the twist θ_T every millisecond for up to five second periods. Logged data was then written to hard disc using a format suitable for the GKS graph plotting utility discussed previously in section 2.5.5.

Steady state test The torsional stiffness value, K_θ, was obtained by measuring the twist θ_T for a given steady applied force at a radius r_T. From equation 4.13,

$$F_T r_T = -K_\theta \theta_T \qquad \text{equation 4.14}$$

Results from this test are presented below in table 4.1 and plotted as graph 4.1.

T (Nm)	140	175	320	375	420	460
θ_T (mrad)	0.36	0.4	0.7	0.9	1.0	1.0

TABLE 4.1. Torsional stiffness test results

From the graph,

$$K_\theta = 420\times10^3 \ Nm/rad \qquad \text{equation 4.15}$$

Dynamic testing To identify the remaining twist parameters an impulse response test was carried out. Re-arranging equation 4.13,

$$\frac{\delta\theta_T}{\delta F_T r_T} = \frac{-1/I_T}{s^2 + \frac{K_v}{I_T}s + \frac{K_\theta}{I_T}} \qquad \text{equation 4.16}$$

This has a standard form given by,

$$\frac{y}{x}(s) = \frac{1}{s^2 + 2\zeta\omega_n s + \omega_n^2} \qquad \text{equation 4.17}$$

where

$$2\zeta\omega_n = \frac{K_v}{I_T} \qquad \text{equation 4.18}$$

$$\omega_n^2 = \frac{K_\theta}{I_T} \qquad \text{equation 4.19}$$

The impulse time response of equation 4.17 is that of a decaying sinusoid as described by equation 4.20 below,

$$y(t) = \frac{1}{\omega} e^{-t/\tau} \sin(\omega t) \qquad \text{equation 4.20}$$

where

$$\omega = \omega_n \sqrt{1 - \zeta^2} \qquad \text{equation 4.21}$$

$$\tau = \frac{1}{\zeta \omega_n} \qquad \text{equation 4.22}$$

The values ω and τ are the damped natural frequency and time constant of the decaying sinusoid respectively and hence can be readily identified from an impulse time response plot. Corresponding values of undamped natural frequency ω_n and damping ratio ζ may then be obtained using equations 4.23 and 4.24 below (re-arranged from 4.21 and 4.22).

$$\omega_n = \frac{\sqrt{\omega^2 \tau^2 + 1}}{\tau} \qquad \text{equation 4.23}$$

$$\zeta = \frac{1}{\sqrt{\omega^2 \tau^2 + 1}} \qquad \text{equation 4.24}$$

Plant parameters I_T and K_v may then be obtained by re-arranging equations 4.18 and 4.19.

$$I_T = \frac{K_\theta}{\omega_n^2} \qquad \text{equation 4.25}$$

$$K_v = 2\zeta \frac{K_\theta}{\omega_n} \qquad \text{equation 4.26}$$

Dynamic testing results Graph 4.2 shows the impulse time response of the clamped vehicle, which was obtained by bouncing a large mass ($\approx 40\ kg$) from one corner of the pivoted end of the vehicle. As expected the response was clearly that of a decaying sinusoid and the values of damped natural frequency ω and time constant τ were readily identified.

$\omega = 89\ rad.s^{-1}$

$\tau = 2.0\ seconds$

Using equations 4.23 and 4.24 it follows that

$\omega_n = 89.0$

$$\zeta = 5.6\times10^{-3}$$

The twist model parameters were then obtained using equations 4.25, 4.26 and 4.15.

$$I_T = \frac{K_\theta}{\omega_n^2}$$

$$= \frac{420\times10^3}{89^2}$$

$$= 53\ kgm^2 \qquad \text{equation 4.27}$$

And

$$K_v = 2\zeta\frac{K_\theta}{\omega_n}$$

$$= 2 \times 5.6\times10^{-3} \times \frac{420\times10^3}{89}$$

$$= 53\ rad.s^{-1}/Nm \qquad \text{equation 4.28}$$

The complete twist model could then be written down by combining equations 4.13, 4.15, 4.27 and 4.28.

$$\delta F_T r_T = -\delta\theta_T(53s^2 + 53s + 420\times10^3)$$

$$= -53\delta\theta_T(s^2 + s + 7925) \qquad \text{equation 4.29}$$

And

$$\delta x_T = \delta\theta_T r_T' \qquad \text{equation 4.30}$$

As with the roll model, the radius r_T' from the twist axis to the gap transducers and accelerometers was slightly greater than r_T.

4.4 Modelling of the side modes

Derivation of the linearised model for each of the side modes was carried out as for the levitation modes.

4.4.1 Lateral model The total lateral force δF_L acts on the vehicle mass M to produce a gap acceleration $\delta\ddot{x}_L$ as given by equation 4.31 below.

$$\delta F_L = -M\,\delta\ddot{x}_L \qquad \text{equation 4.31}$$

4.4.2 Yaw model In the yaw mode, the total yaw force δF_Y acts on the inertia I_Y in a direction normal to the yaw axis and at a radius r_Y from that axis. This produces an angular acceleration $\delta\ddot{\theta}_Y$,

$$\delta F_Y r_Y = -I_Y \delta\ddot{\theta}_Y \qquad \text{equation 4.32}$$

The angular displacement in turn is related to the linear displacement (derived from the gap transducers) according to equation 4.33 below,

$$\delta x_Y = \delta\theta_Y r_Y \qquad \text{equation 4.33}$$

4.5 Chopper linearisation

Chopper linearisation was required because the output waveform of the chopper would become distorted when the rate of change of demand exceeded that which the chopper could generate. This problem is best illustrated by figure 4.3 which shows the chopper current into a magnet load (having inductance L and resistance R) following a step input demand of 40 A. Note that the modulation is completely inhibited until the 40 A demand is reached.

Starting with zero initial conditions, the instantaneous load current $i_L(t)$ when the chopper is switched on is given by equation 4.34 below,

$$i_L(t) = \frac{V_s}{R}(1 - e^{-t/\tau}) \qquad \text{equation 4.34}$$

where

V_s = 48 volts, the chopper supply voltage

$\tau = L/R$, the magnet load time constant

R is the magnet load resistance

To avoid chopper distortion, the rate of rise of input demand should not exceed the maximum rate of rise of load current. From equation 4.34,

$$\frac{d}{dt} i_L(t) = \frac{V_s}{R\tau} e^{-t/\tau} \qquad \text{equation 4.35}$$

Now to slow down the reference input, a first order lag was placed between the demand signal i_d and the chopper reference input i_r as given by equation 4.36 below.

$$i_r(s) = \frac{i_d(s)}{1 + s\tau_L} \qquad \text{equation 4.36}$$

The time constant τ_L was to be chosen to limit the worst case rate of rise of $i_r(t)$ during the hypothetical worst case 40 A step demand signal. Now for a step input demand I_d the time response of the chopper reference input $i_r(t)$ would be given by,

$$i_r(t) = I_d(1 - e^{-t/\tau_L})$$

giving

$$\frac{d}{dt} i_r(t) = \frac{I_d}{\tau_L} e^{-t/\tau_L}$$

and

$$\left.\frac{d}{dt} i_r(t)\right|_{\max} = \frac{I_d}{\tau_L} \qquad \text{equation 4.37}$$

Equation 4.37 gives the maximum rate of rise of the chopper reference input in terms of the time constant τ_L. The corresponding maximum rate of rise of load current is given by equation 4.35 with $t = 0$,

$$\left.\frac{d}{dt} i_L(t)\right|_{t=0} = \frac{V_s}{R\tau} \qquad \text{equation 4.38}$$

The value of τ_L was then chosen such that equations 4.37 and 4.38 were equal,

$$\frac{I_d}{\tau_L} = \frac{V_s}{R\tau}$$

Re-arranging,

$$\tau_L = \frac{I_d R \tau}{V_s} \qquad \text{equation 4.39}$$

4.5.1 Levitation choppers Experimental values of R and τ for the LSM d.c. windings are given in appendix A. Using the worst case or largest τ value, the linearisation time constant τ_L was calculated using equation 4.39 as follows,

$$\tau_L = \frac{40 \times 0.46 \times 0.116}{48}$$

$$= 0.0445 \; seconds$$

With this value of τ_L and the worst case step input demand of 40 A, the rate of rise of the chopper reference input would be equal to the maximum rate of rise capabilities of the chopper. Figure 4.4 illustrates how the chopper linearisation pole works for the levitation choppers. The corresponding first order lag transfer function is described by equation 4.40 below,

$$T(s) = \frac{1}{1 + 0.0445s}$$

$$= \frac{1}{1 + \frac{s}{22}} \qquad \text{equation 4.40}$$

4.5.2 Side choppers Using experimental values of R and τ for the side magnets given in appendix A,

$$\tau_L = \frac{40 \times 0.3 \times 0.046}{48}$$

$$= 0.0115 \; seconds$$

This corresponds to a lag network given by,

$$T(s) = \frac{1}{1 + \frac{s}{86}} \qquad \text{equation 4.41}$$

4.5.3 Summary of chopper linearisation To linearise the chopper response a first order lag network as described by equation 4.40 or 4.41 must precede the reference inputs of the levitation or side control choppers respectively. This will prevent loss of modulation during large current excursions such as would be encountered, for example, when initially lifting the vehicle.

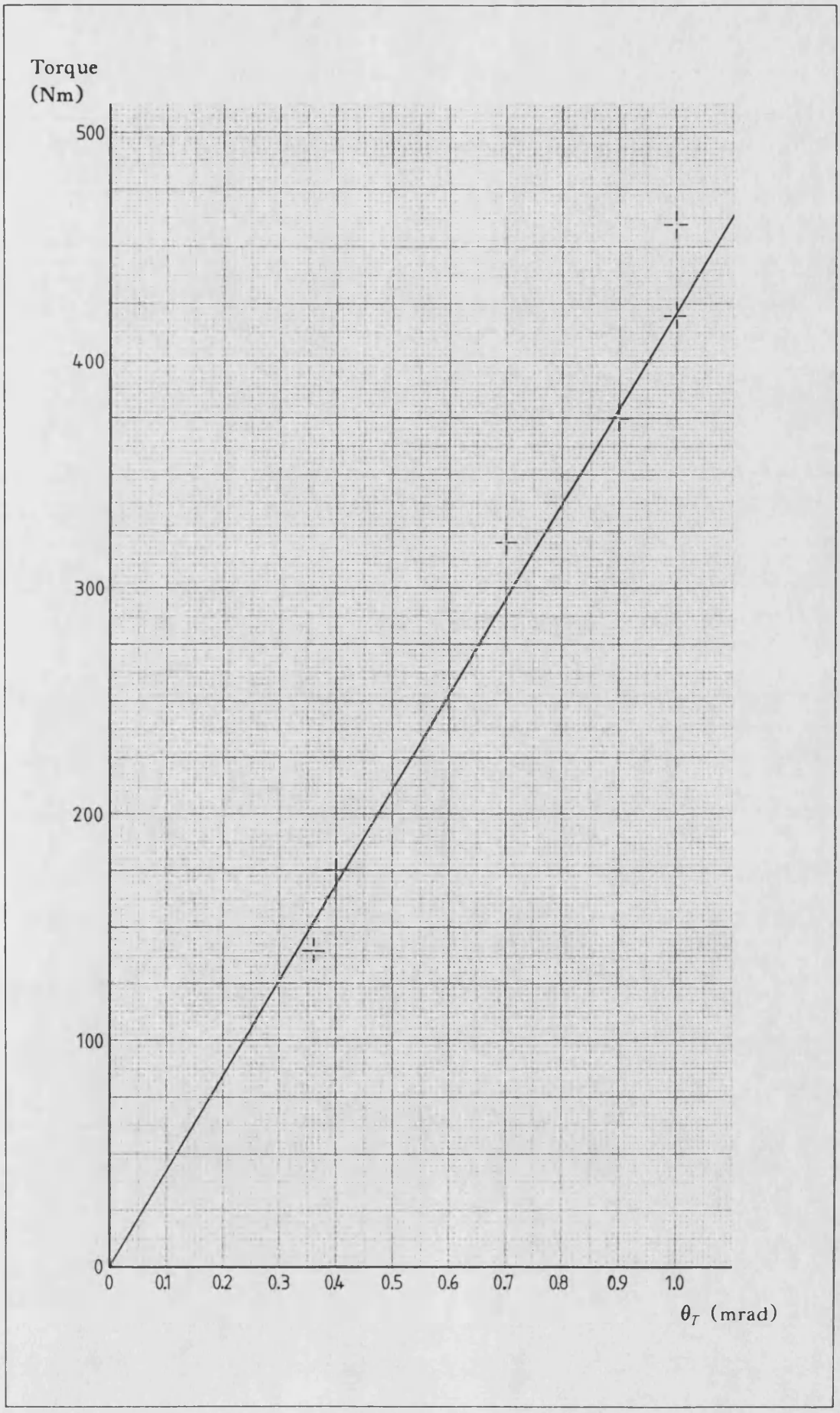

Torsional stiffness test Graph 4.1

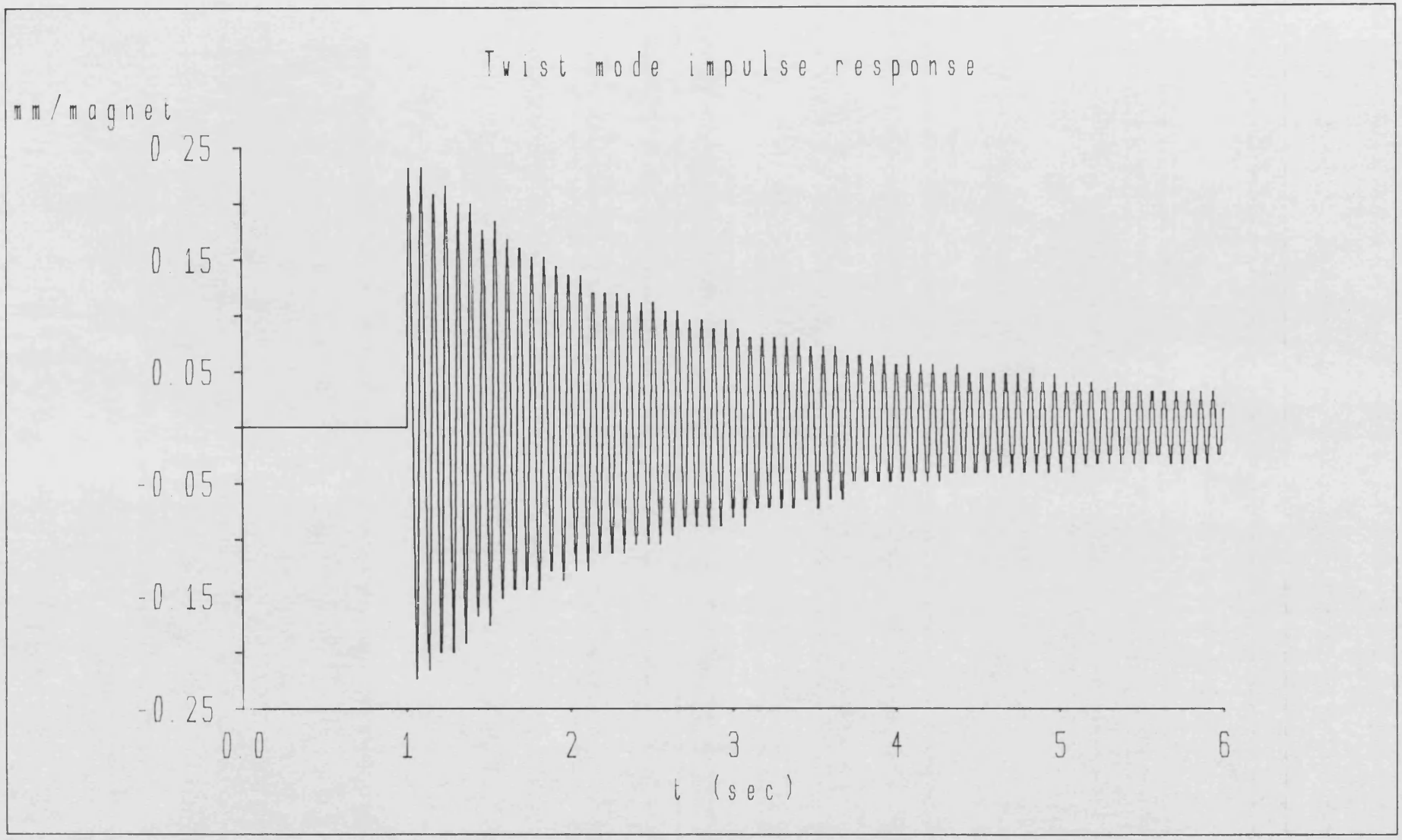

Twist mode impulse response Graph 4.2

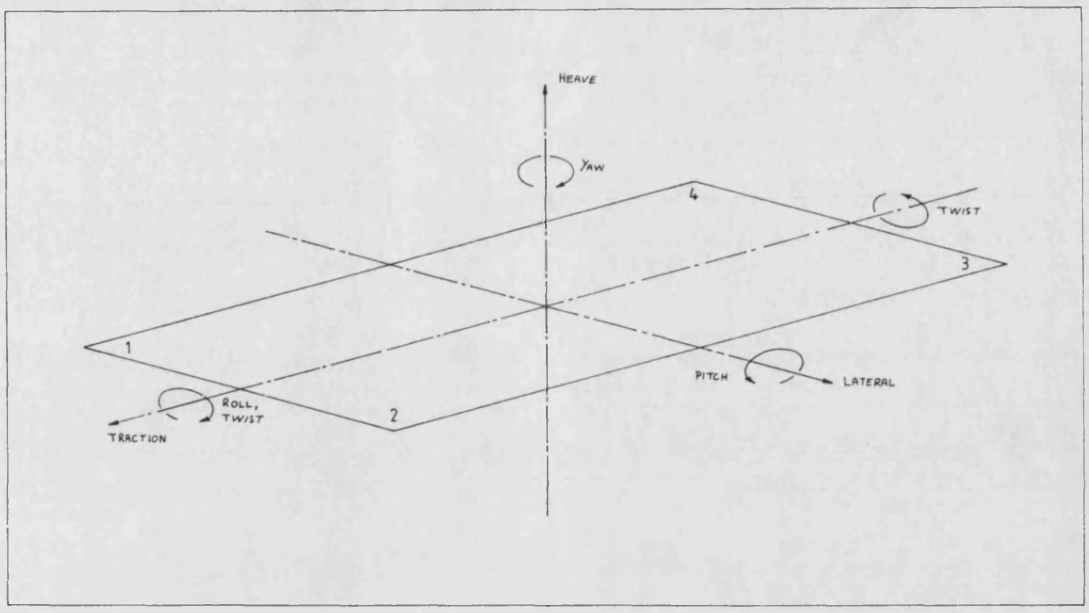

Definition of vehicle modes Figure 4.1

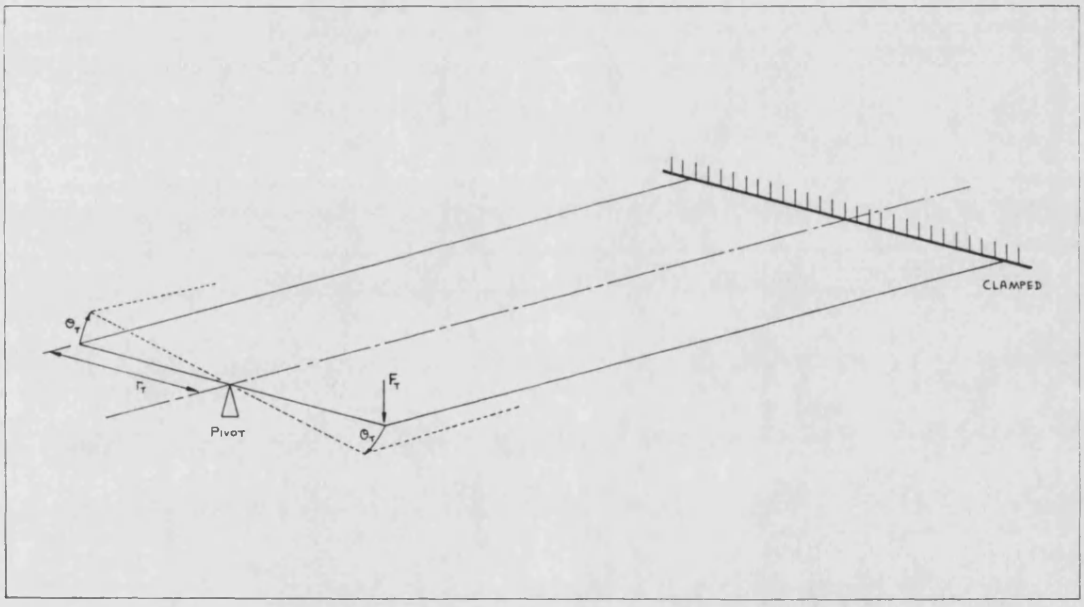

Clamped vehicle used for the derivation of the twist model Figure 4.2

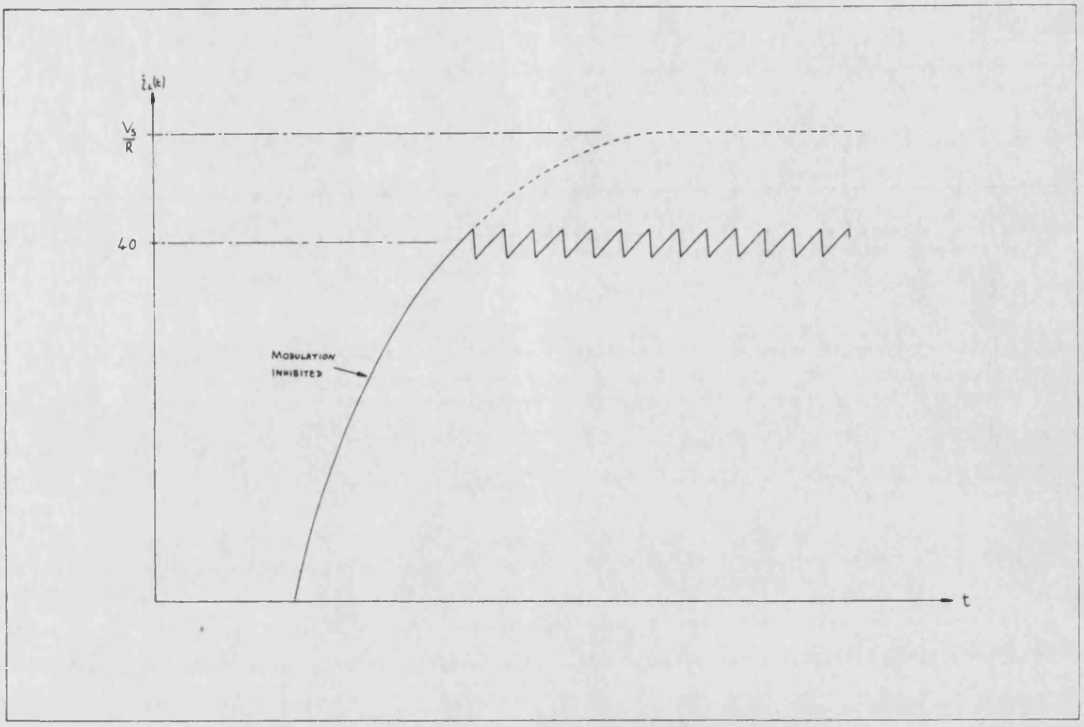

Non-linear chopper step response Figure 4.3

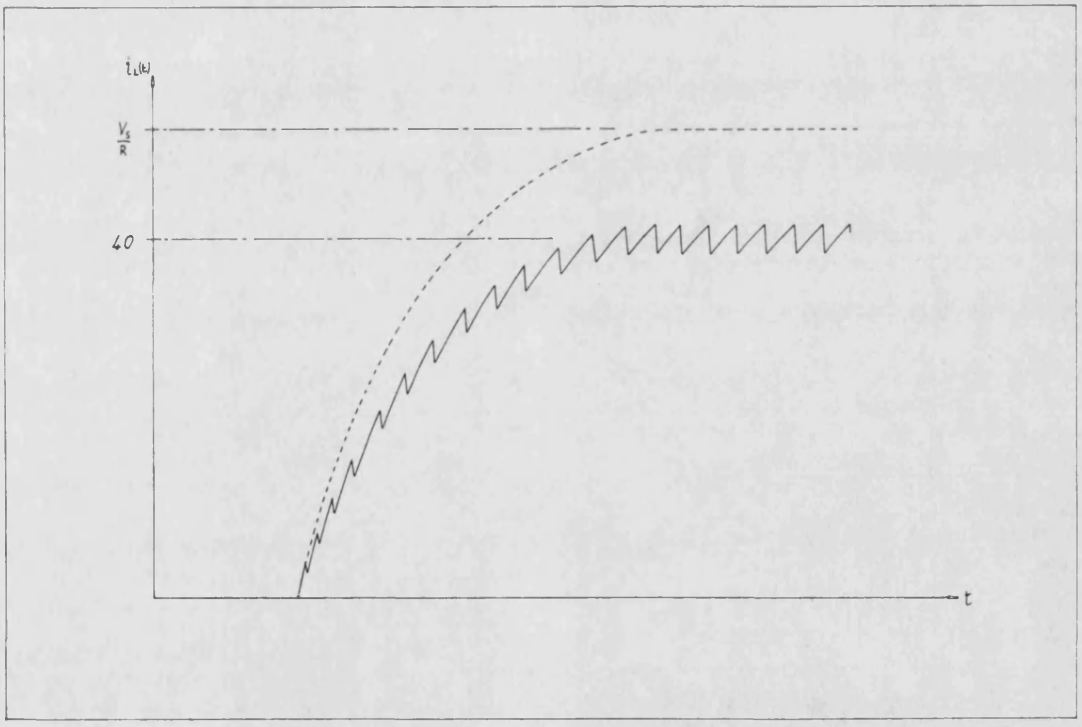

Linearised chopper step response Figure 4.4

5. Controller design and implementation

An existing control strategy proposed by Dunn[2] for levitating the pivoted vehicle was adapted and expanded for control of the whole vehicle using a high speed digital controller based on the standard digital filter structures developed in chapter 3. Control of the tractive mode will be considered in a later chapter.

5.1 Control strategy

The control strategy which had proven successful when applied to the simplified pivoted vehicle is shown in figure 5.1, where the block labelled *magnet and vehicle* represents the linearised mathematical model of a specific vehicle mode combined with the appropriate magnet model for either the levitation or side magnets. It will be shown that the magnet and vehicle model combined with the chopper linearisation pole gives a third order plant, hence there are three states available for feedback - position, velocity and acceleration. Note that the outer control loop contains an integrator in the forward path to force a type one system and hence eliminate any steady state positional errors.

In the lateral and the yaw modes the acceleration signal was not available. However, by relaxing the control requirements it was possible to derive a stable second order dominated side mode controller using just displacement and velocity feedback, deriving the velocity signal from differentiation of the displacement signal.

5.2 Transducer gains and vehicle constants

5.2.1 Gap transducers The gain of the individual gap transducers was given by,

$$K = \frac{1}{resolution}$$

$$= \frac{1}{16\times10^{-6}}$$

$$= 62500$$

This states that for a gap of 1 metre the transducer reading would be 62500. The

coordinate translation matrices as defined in chapter 4 would preserve this gain value but could be simplified by removing the factor of 1/4 from equations 4.1 and 4.5. The gain at the output of the translation matrices would then be specified as four times the individual transducer gains as follows.

$$K_g = 4 \times 62500$$

$$= 250000 \qquad \text{equation 5.1}$$

By making this simplification a software multiplication at the output of each coordinate translation matrix was eliminated.

5.2.2 Accelerometers and choppers As with the gap transducers, the accelerometer gain K_a was specified as four times the gain of the individual accelerometers (equation 2.6), allowing the factor of 1/4 to be removed from the corresponding translation matrix (equation 4.2).

$$K_a = 4 \times \frac{1}{0.08}$$

$$= 50 \qquad \text{equation 5.2}$$

The chopper gain K_c was defined in section 2.8 (equation 2.7),

$$K_c = 0.2 \qquad \text{equation 5.3}$$

5.2.3 Vehicle constants Mass and inertia figures for substitution into the vehicle models developed in chapter 4 are derived analytically in appendix D. Radius values from the various axes to the force actuators, gap transducers and accelerometers are given below,

$$r_T = r_R = 0.5\ m$$

$$r_T' = r_R' = 0.62\ m$$

$$r_P = r_Y = 1.0\ m$$

5.3 Force actuator models

Using the current feedback choppers described in chapter 2, the controller outputs would be required in the form of a current demand signal δi for each mode. A small

signal linearised model was then required to relate the motor force δF to the motor winding current and gap variations.

5.3.1 General model Now with a winding current of I amperes and a gap of x metres the force F produced by an electromagnet is given by,

$$F = K_m \frac{I^2}{x^2} \qquad \text{equation 5.4}$$

where

$$K_m = \frac{1}{2}\mu_0 N^2 A \qquad \text{equation 5.5}$$

Equations 5.4 and 5.5 are derived from first principles in appendix E. Because the force expression was non-linear, it was necessary to linearise expression 5.4 about a working point I_0, X_0 (appendix E),

$$\delta F = 2K_m \frac{I_0}{X_0^2}\left\{\delta i - \frac{I_0}{X_0}\delta x\right\}$$

Now in each of the levitation and side modes the total force δF_{mode} is derived from four motors or magnets such that,

$$\delta F_{mode} = 4\delta F$$

$$= 8K_m \frac{I_0}{X_0^2}\left\{\delta i - \frac{I_0}{X_0}\delta x\right\} \qquad \text{equation 5.6}$$

where the δi and δx are the small signal current and gap excursions, respectively, per motor. Values of K_m, I_0 and X_0 are constants specific to either the levitation motors or side control magnets.

5.3.2 Levitation motor model The levitation motor constant K_m was derived using the motor parameters outlined in appendix A,

$$K_m = \frac{1}{2}\mu_0 N^2 A$$

$$= \frac{1}{2} \times 4\pi\times10^{-7} \times 91^2 \times 11.28\times10^{-3}$$

$$= 5.869\times10^{-5} \qquad \text{equation 5.7}$$

The working gap X_0 was set by the vehicles nominal ride height of 7 mm, which would be the gap per motor limb.

$$X_0 = 7\ mm \qquad \text{equation 5.8}$$

The standing current I_0 was then set according to the steady state force exerted by the motors to maintain the total vehicle mass at the nominal ride height.

$$F_0 = \frac{Mg}{4} \quad per\ motor \qquad \text{equation 5.9}$$

Re-arranging equation 5.4 and using equations 5.8 and 5.9 it follows that,

$$I_0 = \left\{ F_0 \frac{X_0^2}{K_m} \right\}^{1/2}$$

$$= \left\{ \frac{Mg}{4} \cdot \frac{X_0^2}{K_m} \right\}^{1/2}$$

$$= \left\{ \frac{390 \times 9.81}{4} \cdot \frac{0.007^2}{5.869 \times 10^{-5}} \right\}^{1/2}$$

$$= 28.25\ A \qquad \text{equation 5.10}$$

Substituting equations 5.7, 5.8 and 5.10 into equation 5.6 the small signal force actuator model for each of the levitation modes was written down as follows.

$$\delta F_{H,R,P,T} = 270.7(\delta i - 4036.2\delta x) \qquad \text{equation 5.11}$$

5.3.3 Side magnet model Substituting the side magnet parameters given in appendix A into equation 5.5,

$$K_m = \frac{1}{2} \times 4\pi \times 10^{-7} \times 107^2 \times 3 \times 10^{-3}$$

$$= 2.158 \times 10^{-5} \qquad \text{equation 5.12}$$

As with the levitation motors, the working gap X_0 between the side magnets and the lateral guidance rails was 7 mm. The standing current I_0 was set at an arbitrary practical level of 15 A to give the force actuator finite gain for design purposes. It can be shown however[2] that the controllers would remain stable even if I_0 were set to zero.

Substituting the above values into equation 5.6 the small signal force actuator model for the side modes was written down as follows.

$$\delta F_{L,Y} = 52.85(\delta i - 2142.9\delta x) \qquad \text{equation 5.13}$$

Once the controller and vehicle models had been proven the standing current in the side magnets would be set to zero to conserve energy.

5.4 The heave mode controller

To illustrate the design procedure used for each of the vehicle modes the heave controller will now be considered in detail.

5.4.1 Magnet and vehicle in the heave mode The force actuator (equation 5.11) and vehicle heave model were combined as shown in figure 5.2a. The transfer function for the overall magnet and vehicle combination was then derived as follows.

$$\frac{\delta x_H}{\delta i} = \frac{\dfrac{-270.7}{390s^2}}{1 - \dfrac{270.7}{390s^2} \times 4036.2}$$

$$= \frac{-0.6942}{s^2 - 2802} \qquad \text{equation 5.14}$$

5.4.2 Heave controller design Equation 5.14 was substituted into the controller block diagram discussed in section 5.1 to give figure 5.2b. The characteristic equation of figure 5.2b was shown to be,

$$s^4 + s^3P(1 + 0.6942K_a h_2) + s^2(0.6942K_a h_1 P - 2802) +$$
$$sP(0.6942K_g h_0 - 2802) + 0.6942KK_g P = 0 \qquad \text{equation 5.15}$$

Controller gains K, h_0, h_1 and h_2 were then set by comparing the coefficients of this characteristic equation with the standard fourth order form given below,

$$(s^2 + 2\zeta_1\omega_{n_1}s + \omega_{n_1}^2)(s^2 + 2\zeta_2\omega_{n_2}s + \omega_{n_2}^2) = 0$$

Expanding,

$$s^4 + s^3(2\zeta_1\omega_{n_1} + 2\zeta_2\omega_{n_2}) + s^2(\omega_{n_1}^2 + \omega_{n_2}^2 + 4\zeta_1\zeta_2\omega_{n_1}\omega_{n_2}) +$$

$$s(2\zeta_1\omega_{n_1}\omega_{n_2}^2 + 2\zeta_2\omega_{n_2}\omega_{n_1}^2) + \omega_{n_1}^2\omega_{n_2}^2 = 0 \quad \text{equation 5.16}$$

Equating coefficients.

$$2\zeta_1\omega_{n_1} + 2\zeta_2\omega_{n_2} = P(1 + 0.6942K_a h_2) \quad \text{equation 5.17}$$

$$\omega_{n_1}^2 + \omega_{n_2}^2 + 4\zeta_1\zeta_2\omega_{n_1}\omega_{n_2} = 0.6942K_a h_1 P - 2802 \quad \text{equation 5.18}$$

$$2\zeta_1\omega_{n_1}\omega_{n_2}^2 + 2\zeta_2\omega_{n_2}\omega_{n_1}^2 = P(0.6942K_g h_0 - 2802) \quad \text{equation 5.19}$$

$$\omega_{n_1}^2\omega_{n_2}^2 = 0.6942KK_g P \quad \text{equation 5.20}$$

where

$K_a = 50$

$K_g = 250000$

$P = 22$

and

$\zeta_1 = 0.5, \quad \omega_{n_1} = 15$

$\zeta_2 = 1.0, \quad \omega_{n_2} = 100$

The criteria on which the values of ζ and ω_n were based are discussed in detail in the controller design study[2], although the simple guideline that $\zeta_2\omega_{n_2} \geqslant 5\zeta_1\omega_{n_1}$ for second order dominance has clearly been satisfied. Substituting the above values into equations 5.17 through 5.20.

$215 = 22(1 + 34.71h_2)$

$13225 = 763.6h_1 - 2802$

$195000 = 22(173.55\times10^3 h_0 - 2802)$

$2.25\times10^6 = 3.818\times10^6 K$

giving.

$h_0 = 0.0672$

$h_1 = 21.0$

$h_2 = 0.2527$

$K = 0.5893$

5.5 Roll, pitch and twist mode controllers

The control parameters for the remaining levitation modes will now be derived using the same procedure as for the heave controller. The values of ζ and ω_n used were the same as for the heave controller because experimental results[2] had suggested that interaction effects were minimised if all the control loops had similar design responses.

5.5.1 The roll mode controller The magnet and vehicle model for the roll mode is illustrated in figure 5.3a, for which the transfer function was shown to be,

$$\frac{\delta x_R}{\delta i} = \frac{-1.017}{s^2 - 3311}$$

The roll mode controller using this model is shown in figure 5.3b, from which the following characteristic equation was written down,

$$s^4 + s^3P(1 + 1.017K_a h_2) + s^2(1.017K_a h_1 P - 3311) +$$
$$sP(1.017K_g h_0 - 3311) + 1.017KK_g P = 0$$

Substituting values of P, K_a and K_g and comparing coefficients with the standard form,

$$215 = 22(1 + 50.86h_2)$$

$$13225 = 1119.03h_1 - 3311$$

$$195000 = 22(254.3\times10^3 h_0 - 3311)$$

$$2.25\times10^6 = 5.595\times10^6 K$$

giving,

$$h_0 = 0.048$$

$$h_1 = 14.8$$

$$h_2 = 0.172$$

$$K = 0.402$$

5.5.2 The pitch mode controller The magnet and vehicle model in the pitch mode is illustrated in figure 5.4a, for which the transfer function was shown to be,

$$\frac{\delta x_P}{\delta i} = \frac{-0.7648}{s^2 - 3086.8}$$

The pitch mode controller using this model is shown in figure 5.4b, from which the following characteristic equation was written down.

$$s^4 + s^3P(1 + 0.7648K_a h_2) + s^2(0.7648K_a h_1 P - 3086.8) +$$
$$sP(0.7648K_g h_0 - 3086.8) + 0.7648KK_g P = 0$$

Substituting values of P, K_a and K_g and comparing coefficients with the standard form,

$$215 = 22(1 + 38.24h_2)$$

$$13225 = 841.26h_1 - 3086.8$$

$$195000 = 22(191.2\times10^3 h_0 - 3086.8)$$

$$2.25\times10^6 = 4.21\times10^6 K$$

giving,

$$h_0 = 0.0625$$

$$h_1 = 19.39$$

$$h_2 = 0.229$$

$$K = 0.5349$$

5.5.3 The twist mode controller The magnet and vehicle model in the twist mode is illustrated in figure 5.5a, for which the transfer function was written down as follows,

$$\frac{\delta x_T}{\delta i} = \frac{-1.5835}{s^2 + s + 2770.6}$$

The twist mode controller using this model is shown in figure 5.5b, from which the following characteristic equation was written down,

$$s^4 + s^3(P + 1 + 1.5835K_a h_2 P) + s^2(P + 2770.6 + 1.5835K_a h_1 P) +$$
$$sP(2770.6 + 1.5835K_g h_0) + 1.5835KK_g P = 0$$

Substituting values of P, K_a and K_g and comparing coefficients with the standard form,

$$215 = 23 + 1741.9h_2$$

$$13225 = 22 + 2770.6 + 1741.9h_1$$

$$195000 = 22(2770.6 + 395.9\times10^3 h_0)$$

$$2.25\times10^6 = 8.71\times10^6 K$$

giving,

$$h_0 = 0.0154$$

$$h_1 = 6.0$$

$$h_2 = 0.1102$$

$$K = 0.2583$$

5.6 Side mode controllers

The method used for designing the side controllers was identical to that applied above in the design of the levitation controllers. Acceleration signals, however, were not available and it was necessary to relax the specification on the dominant second order response.

5.6.1 The lateral mode controller The magnet and vehicle model in the lateral mode is illustrated in figure 5.6a. The transfer function for this model was shown to be,

$$\frac{\delta x_L}{\delta i} = \frac{-0.1355}{s^2 - 290.4}$$

Figure 5.6b shows the lateral mode controller using the above magnet/vehicle model. From figure 5.6b the following characteristic equation was written down,

$$s^4 + s^3P + s^2(0.1355K_g h_1 P - 290.4) + sP(0.1355K_g h_0 - 290.4) + 0.1355KK_g P = 0$$

Comparing this with the standard form of equation 5.16 it follows that,

$$2\zeta_1\omega_{n_1} + 2\zeta_2\omega_{n_2} = P \qquad \text{equation 5.21}$$

$$\omega_{n_1}^2 + \omega_{n_2}^2 + 4\zeta_1\zeta_2\omega_{n_1}\omega_{n_2} = (0.1355K_g h_1 P - 290.4) \qquad \text{equation 5.22}$$

$$2\zeta_1\omega_{n_1}\omega_{n_2}^2 + 2\zeta_2\omega_{n_2}\omega_{n_1}^2 = P(0.1355K_g h_0 - 290.4) \qquad \text{equation 5.23}$$

$$\omega_{n_1}^2\omega_{n_2}^2 = 0.1355KK_g P \qquad \text{equation 5.24}$$

Equation 5.21 illustrates that without acceleration feedback the values of the closed loop paramaters ζ and ω_n could no longer be chosen independently but were constrained by the value of the chopper linearisation pole, P. To fix the closed loop paramaters the second order dominance criterion given below was used.

$$\zeta_2\omega_{n_2} \geqslant 5\zeta_1\omega_{n_1} \qquad \text{equation 5.25}$$

With the value of the chopper pole fixed at $P = 86$ (section 4.5.2) and using equations 5.21 and 5.25 the following values of ζ and ω_n were chosen.

$$\zeta_1 = 0.5, \quad \omega_{n_1} = 10.0$$

$$\zeta_2 = 0.5, \quad \omega_{n_2} = 76.0$$

Substituting the above values into equations 5.22 through 5.24, and using equation 5.1 for the transducer gain K_g.

$$6636 = 2.9136\times10^6 h_1 - 290.4$$

$$65360 = 86(33.89\times10^3 h_0 - 290.4)$$

$$577.6\times10^3 = 2.9136\times10^6 K$$

giving,

$$h_0 = 0.031$$

$$h_1 = 2.38\times10^{-3}$$

$$K = 0.198$$

5.6.2 The yaw mode controller The magnet and vehicle model in the yaw mode is illustrated in figure 5.7a. The transfer function for this model was shown to be.

$$\frac{\delta x_Y}{\delta i} = \frac{-0.1193}{s^2 - 255.6}$$

The yaw mode controller using this magnet/vehicle model is shown in figure 5.7b from which the following characteristic equation was written down.

$$s^4 + s^3P + s^2(0.1193K_g h_1 P - 255.6) +$$

$$sP(0.1193K_g h_0 - 255.6) + 0.1193KK_g P = 0$$

Substituting values of P and K_g and comparing coefficients with the standard form,

$$6636 = 2.565\times10^{6}h_1 - 255.6$$

$$65360 = 86(29.8\times10^{3}h_0 - 255.6)$$

$$577.6\times10^{3} = 2.565\times10^{6}K$$

giving,

$$h_0 = 0.034$$

$$h_1 = 2.69\times10^{-3}$$

$$K = 0.2252$$

5.7 Software

The software for the controllers was based on the filter test software developed in chapter 3, which provided routines to perform the following,

1. Generating timebase interrupts for an interrupt driven control service routine
2. Providing reference inputs to the controllers from the bcpl supervisory program
3. Performing n channel data logging every sample interval

However, to implement in real time the full six degree of freedom controller it was necessary to make use of a second processor, with the control task then being partitioned between the two processors running in parallel. To facilitate the use of a second parallel processor additional software was written to provide high speed inter-processor communications and to ensure synchronisation of the two processors.

5.7.1 Inter-processor communication The bcpl supervisory program (listing 5.1), which would run on the master processor, was extended to include a call to *getcomvec* as follows,

```
comms.vec := getcomvec(n)
```

This routine allocates a vector of n contiguous long words from the global backplane memory, placing the vectors start address in the global variable *comms.vec*. This address is then communicated using sendpkt* to a simple packet controlled bcpl

supervisory program running on the remote processor (listing 5.2). This program expects one of the following two packet types,

act.init instructs the remote supervisor program to initialise and run the control code. The first argument of this packet includes a bcpl address to the communication vector described above.

act.selfimm instructs the remote supervisor program to unload itself from the processor (self immolate). This is used at the end of the control run.

Once both processors have the address of the communication vector, inter-processor communications is then simply a matter of reading from or writing to agreed locations within that vector. It is important, however, that data communicated in this way does not overlap two sample intervals. Hence to ensure that the communications vector cannot be updated whilst a second processor is partway through reading a set of data, the *test and set* semaphore was introduced.

5.7.2 Test and set semaphore One of the long words in the communication vector was allocated as a semaphore flag for controlling the use of that vector by two or more processors. Any processor wishing to access the vector must first interrogate the semaphore flag using the 68000 *test and set* (TAS) instruction. If the vector is busy, the semaphore flag will already be set and the processor must wait until the vector is free and the semaphore flag cleared by whichever processor was using the vector. When the TAS instruction finds the semaphore flag clear, the instruction will automatically set the semaphore flag during the same indivisible read-modify-write memory cycle. The processor may then freely access the vector, clearing the semaphore flag when finished.

A flowchart showing the use of the communication vector in this way is given in figure 5.8.

---

* The use of sendpkt is described in the Tripos Programming guide[14].

5.7.3 Processor partitioning and synchronisation To provide synchronisation of the two processors one of the long words in the communication vector was allocated as a ready flag. Use of this flag for synchronisation is somewhat dependent on the way the control algorithm is partitioned between the two processors. Throughout this thesis all controllers were partitioned approximately as follows,

Remote processor -	Reads all the vehicle transducers
	Performs coordinate translation
	Calculates controller feedback values
Master processor -	Calculates forward path quantities
	Implements chopper linearisation poles
	Performs reverse coordinate translation
	Outputs current demands
	Performs data logging

Figure 5.9 illustrates how this partitioning would be applied, for example, to the typical full state feedback controller of figure 5.1.

Assuming that the remote program has already calculated the first set of feedback values and set the ready flag, synchronisation is then achieved by forcing the remote processor to wait for the flag to be cleared. Then at some time during the interrupt service routine on the master processor (usually the beginning) the control program on the master processor must read the feedback data and clear the ready flag, whereupon the remote processor will proceed to calculate the feedback values for the next sample interval. On completion of these feedback calculations the remote processor sets the ready flag to indicate that new data is available in the communication vector. Assuming that the control program on the remote processor is not longer than the interrupt period, then by the time the control program on the master processor is ready for new data the ready flag should already have been set, allowing the program to read the new data and proceed.

If at any time the control program on the master processor finds that no new data is available (indicated by finding the ready flag unset), then a synchronisation fault is flagged and the levitation will be aborted by the bcpl supervisory program. This

situation could arise, for example, if the remote program was inadvertently extended, making it too long for one sample interval. Processor synchronisation using the ready flag is illustrated in figure 5.10.

Finally, some additional software was required to process the transducer readings.

5.7.4 Gap, velocity and acceleration signals

Gap signals Height and side gaps were obtained by byte accessing the appropriate channel address of the gap transducer interface board detailed in section 2.6.4. This board autonomously updates all eight gap measurements every $50\,\mu s$ and always presents the most recent value, hence avoiding the need for software polling or waiting on a result.

Because the gap transducer resolution was $16\,\mu m$, the maximum eight bit relative displacement that could be read directly was only 4 mm. In order to cope with greater gap variations it was necessary to derive the higher order bits using a software routine. Upon rollover of the eight bit value, these high order bits would then be incremented or decremented in software according to whether the eight bit gap reading was increasing or decreasing respectively between sample intervals.

Gap reading algorithm The flowchart of figure 5.11 illustrates the basic principle used to generate the high order gap bits. The eight bit gap reading is first categorised into one of four quadrants (hex),

q_1	$00 \rightarrow 3F$
q_2	$40 \rightarrow 7F$
q_3	$80 \rightarrow BF$
q_4	$C0 \rightarrow FF$

The algorithm is based on the assumption that the vehicle gaps cannot physically move between more than two of these quadrants in one sample interval which, given an interval of 1 ms, would correspond to a vehicle gap speed in excess of 2 m/s.* Hence a

change from quadrant q_1 to quadrant q_4 in one sample interval is assumed to be a boundary crossing due to a reducing gap. Similarly a change from quadrant q_4 to quadrant q_1 in one sample interval is taken as a boundary crossing due to an increasing gap.

RD_GAP macro With eight gap measurements to take every sample interval it was necessary to use a highly optimised gap reading program in order to avoid swamping the processors with gap calculations. This program was implemented as a 68000 macro assembler definition called RD_GAP (see listing 5.4) for which the flowchart of figure 5.12 was included to clarify its operation. Note that absolute gap values were obtained by adding the relative value to the rest gap value as obtained directly from vehicle measurements. These rest gap values are required to be set up using the IN_GAP macro (see listing 5.4).

Acceleration signals Although directly available through byte accessing the appropriate channel of the A/D board described in section 2.7, it was necessary to first filter the 8 bit value so obtained to remove any cumulative d.c. offset. This was because past results obtained from the vehicle[2] had shown that a d.c. offset could develop in the transducer readings over a period of several seconds, and that ultimately this would cause loss of stability. The digitally implemented filter used to remove d.c. offset from the accelerometer readings is given by equation 5.26 below,

$$a.c.\ acceleration = acceleration\ reading \times \frac{s}{s+1} \qquad \text{equation 5.26}$$

Velocity signals To avoid cumulative errors, pure integration of the acceleration signals was avoided in favour of the digitally implemented transfer function given below,

---

* Results obtained in later sections will show that gap speeds during the levitation procedure or step response tests are below the suggested transducer limit of 2 m/s.

$$velocity = a.c.\ acceleration \times \frac{0.5}{1 + 0.5s} \qquad \text{equation 5.27}$$

Equations 5.26 and 5.27 were originally proposed by Dunn[2] and have sufficiently long time constants as to avoid significantly effecting dynamic acceleration or velocity measurements.

Acceleration signals were not available for the side mode controllers, and velocity signals were derived by differentiation as follows,

$$velocity = (new\ displacement - old\ displacement) \times \frac{1}{period} \qquad \text{equation 5.28}$$

A full set of listings showing the controller implementation using the standard filter blocks developed in chapter 3 within the above described structure are included as listings 5.1 through 5.9 inclusive.

5.8 Results

Experimental results obtained with the vehicle controller described in this chapter are discussed below.

5.8.1 Graph notation The notation mm/magnet (mm per magnet) used on the position-time graphs indicates that the position data has been scaled in terms of individual magnet displacements in millimetres. As an example, consider a roll step response indicating a mm/magnet increase of 1 mm. This means that the magnet gaps at corners 2 and 3 of the vehicle have *increased* by 1 mm, whereas the gaps at corners 1 and 4 have *decreased* by 1 mm, resulting in an overall positive roll (sign conventions are defined in section 4.1).

It was felt that scaling the position axes in this way was more meaningful than, for example, scaling the data in terms of an actual roll angle in degrees or radians.

5.8.2 Levitation response test Graphs 5.1 and 5.2 show position-time responses of the six controlled modes during levitation of the vehicle. The levitation procedure represents the worst conditions likely to be encountered by the controllers since the

levitation magnets are initially working well away from their 7 mm design working point.

The roll, pitch, lateral and yaw responses illustrate how quickly the vehicle is levelled out and correctly aligned beneath the track despite large disturbances of these modes during the levitation procedure. The twist controller, however, exhibited a slow first order dominant response requiring the best part of the 1.2 second logging period to untwist the vehicle. After carrying out further tests, it was found that the twist mode would always exhibit a slow first order response, and was largely invariant of changes made to the control parameters.

A possible explanation for this twist controller characteristic was given in a simulation study performed by Dunn[2] on a rigid vehicle. This study had shown that an offset between the vehicles centre of geometry and centre of mass, causing interaction between all of the modes, could give rise to very slow first order dominated responses from some of the controllers due to conflict between the interacting modes. Since it was likely that the vehicles true centre of geometry was not precisely at the centre of mass as previously assumed, it was concluded that the twist loop response was manifesting the above problem.

5.8.3 Step response tests

Levitation modes Graphs 5.3 through 5.6 inclusive show the step responses of the heave, roll, pitch and twist modes respectively. In each case the step response was centred about the 7 mm working point and was made as large as possible without causing the vehicle to go unstable or hit an end stop. Each graph shows the four levitation modes, illustrating the minimal interaction that takes place between these modes.

Side modes Graphs 5.7 and 5.8 show the step responses of the lateral and yaw mode controllers respectively.

5.8.4 Current demands Graph 5.9a shows the heave current demand (in amperes) during the heave step response test discussed above. Note that the average standing current in the levitation magnets was 28.7 A, very close to the calculated value of 28.25 A.

Graphs 5.9b and 5.9c show, respectively, the current demands in the roll and pitch loops during the above step response tests of the respective controllers. These graphs were included to illustrate the small steady state current offsets required to cope with minor parameter variations between the motors.

5.8.5 Side control with zero standing current Graphs 5.10a and 5.10b show the step response of the lateral and yaw mode controllers respectively with zero standing current in the side magnets. As expected the controllers maintained stability, but in each case the response was far more oscillatory than that obtained with the 15 A standing current. It was also noted that there was a small delay before the controller could properly react to a physical disturbance. This latter problem gave the outward impression of a controller deadband, suggesting to critical observers that the vehicle side modes had poor controllers.

Consequently, future controllers should make use of a standing current in the side magnets, although this could be significantly less than 15 A. For example, graph 5.11 shows the step responses of the previously designed lateral and yaw controllers using a standing current of 7.5 A. These controllers did not exhibit the deadband problem discussed above.

5.9 Conclusions

The main aim of this chapter was to test the validity of the linearised vehicle model and also the digital filter algorithms developed in chapter 3. With the exception of the twist loop, all of the vehicle mode controllers exhibited a good second order dominated response, showing that the vehicle model developed in this chapter was sufficiently accurate and would respond well to the linear design techniques applied.

Further investigation of the twist mode controller would be required to determine the cause of the control problem encountered. Because the vehicle model for the twist mode was derived experimentally (section 4.3.4) it was considered unlikely that this model would be significantly inaccurate, and it was decided therefore that the most likely cause of the poor twist response was interaction between various vehicle modes, which would require a multivariable solution.

Timings To obtain an estimate of processor workload, the total number of processor cycles required for the control routines of both the master and the remote processors were evaluated (recall that standard times had been derived for the macro defined routines). These results are given below as a percentage of the 8000 available processor cycles per sample interval,

master processor	82.9%
remote processor	91.8%

Whereas these figures show some useable spare capacity, it should be noted that the master processor also runs a low priority bcpl supervisory routine. Hence any increase in master processor loading will reduce the spare capacity of that processor, which in turn will adversely effect the response time of the bcpl supervisory program. However it was felt that provided the bcpl supervisory program was kept simple the control routine could use as much as 90% of the master processor.

If a considerable increase in processing power was required then a third parallel processor could be accommodated using the software techniques described in this chapter. A preferable solution, however, would be to upgrade the present two processor system by using 10 or 12 MHz processors. For example, if both of the current 8 MHz processors were to be replaced with 12 MHz versions, the equivalent power increase would exceed that provided by a third 8 MHz processor.

Asynchronous processors The control software was also tested on two processors running asynchronously. This was achieved by using independent 1 ms interrupts on

the master and remote processors, with no protection against overlapping sample intervals. Under these circumstances it was found that sometimes the master processor would read the same feedback data twice, invariably causing the controller to go unstable. No further work was carried out using controllers implemented on asynchronous processors.

Tolerance to large gap variations It was found that the vehicle was likely to go unstable for steady state ride heights of 5 mm or less. This was to be expected since the force actuator gains increase dramatically with reducing magnet gap.

Because the vehicles suspension characteristics are constrained by the available magnet gap, it was considered important that the controllers should be able to make full use of the available gap range under transient conditions. Hence to produce a more viable working vehicle there was a clear requirement for making the controller less sensitive to large gap excursions.

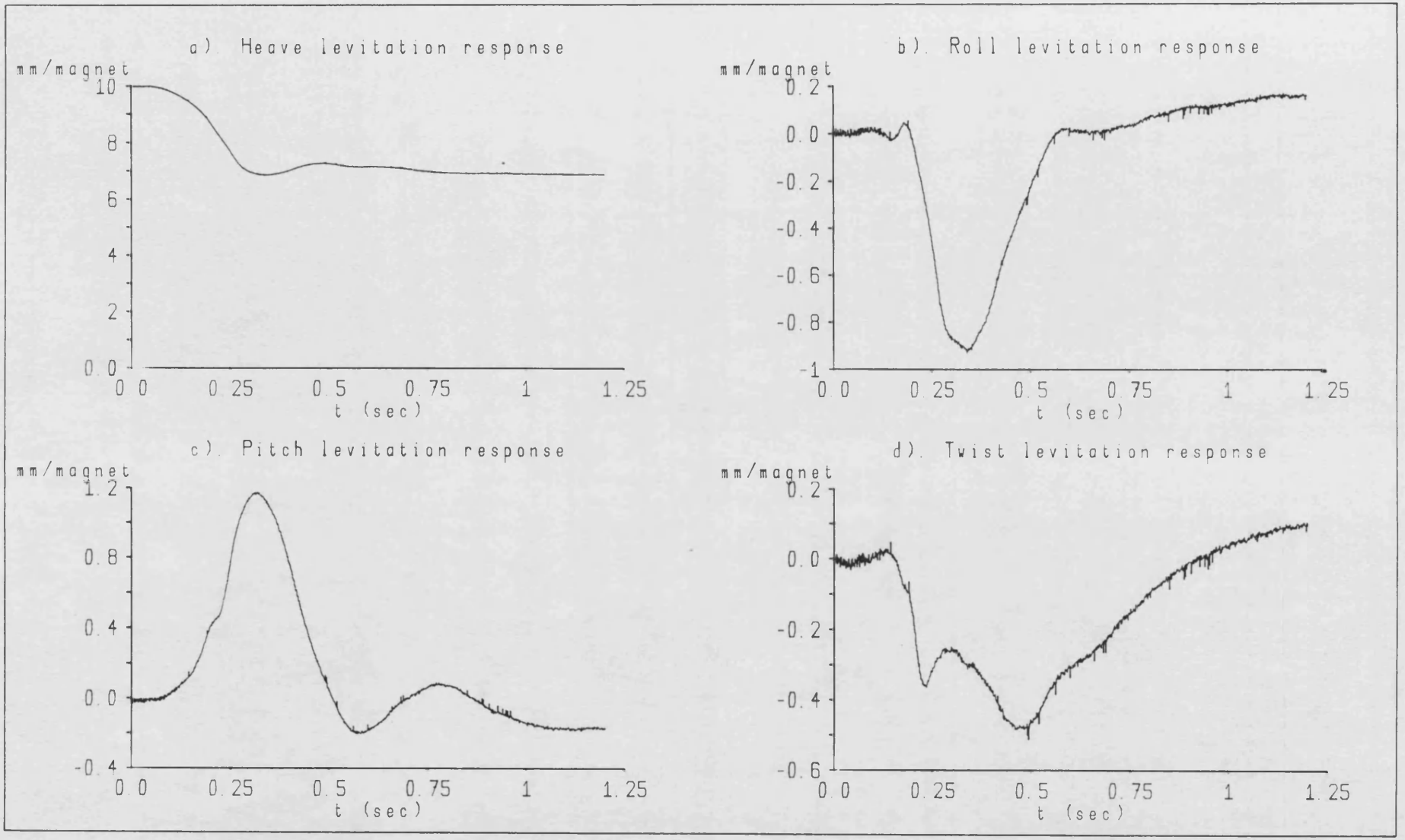

Levitation response Graph 5.1

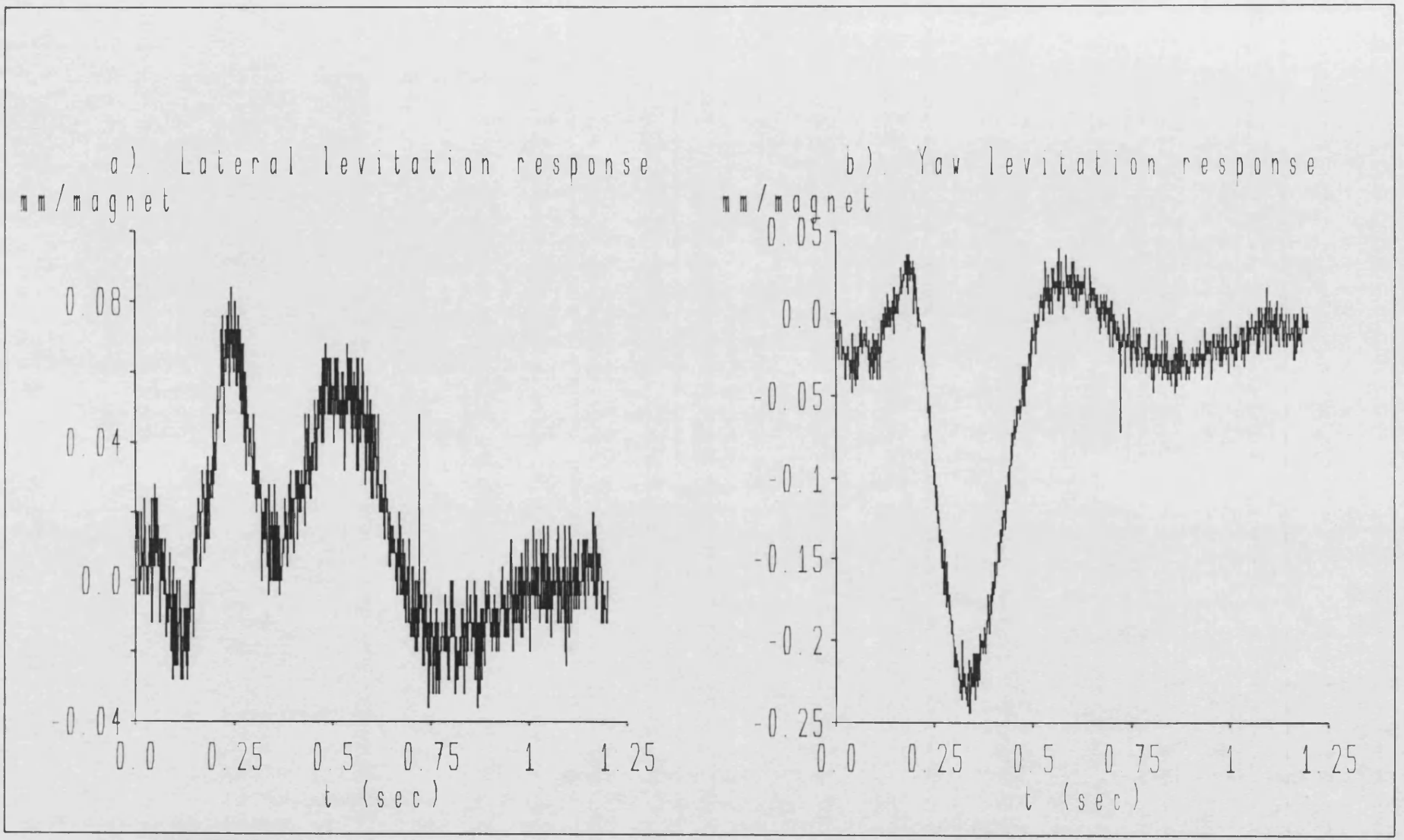

Levitation response (lateral and yaw modes) Graph 5.2

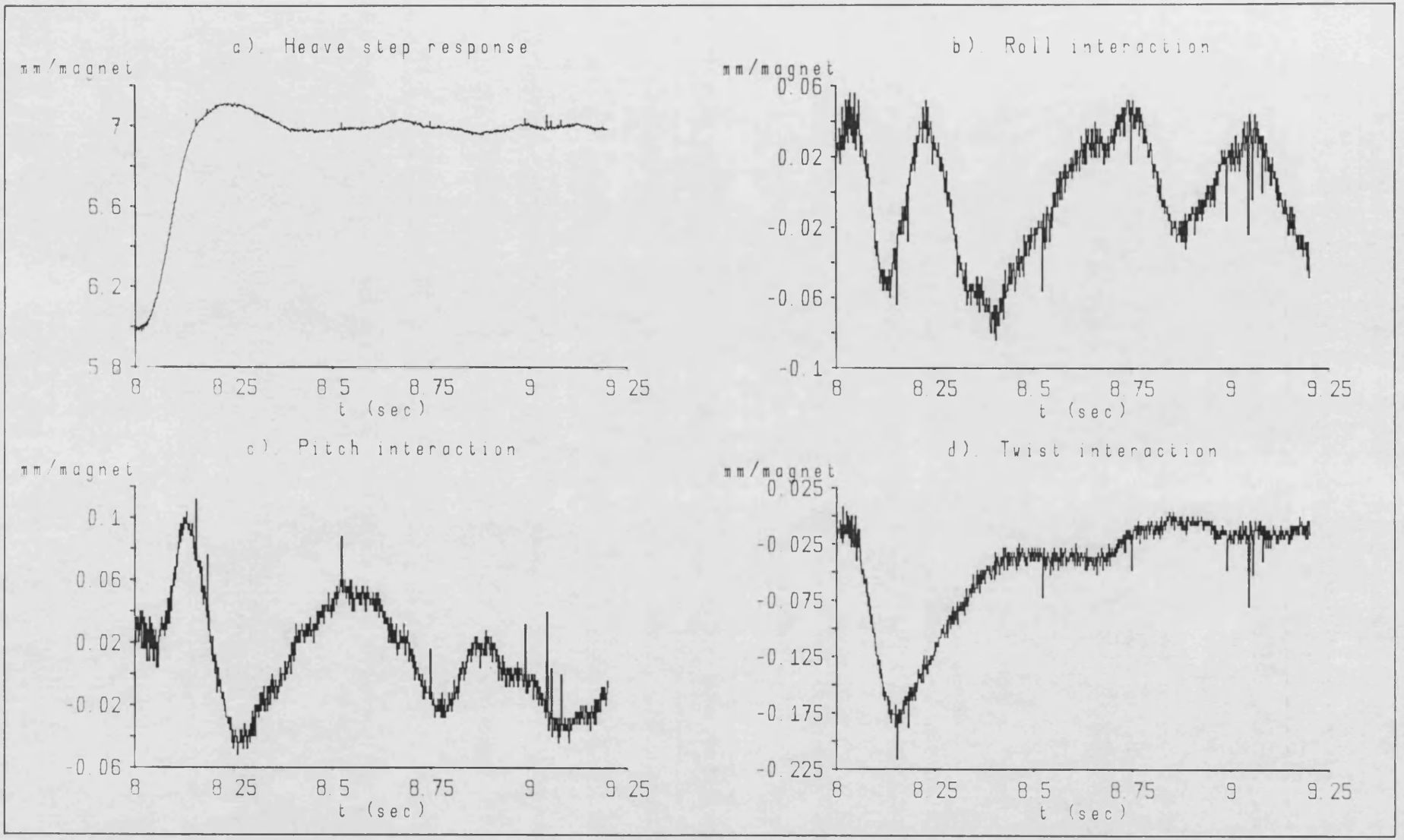

Heave step response Graph 5.3

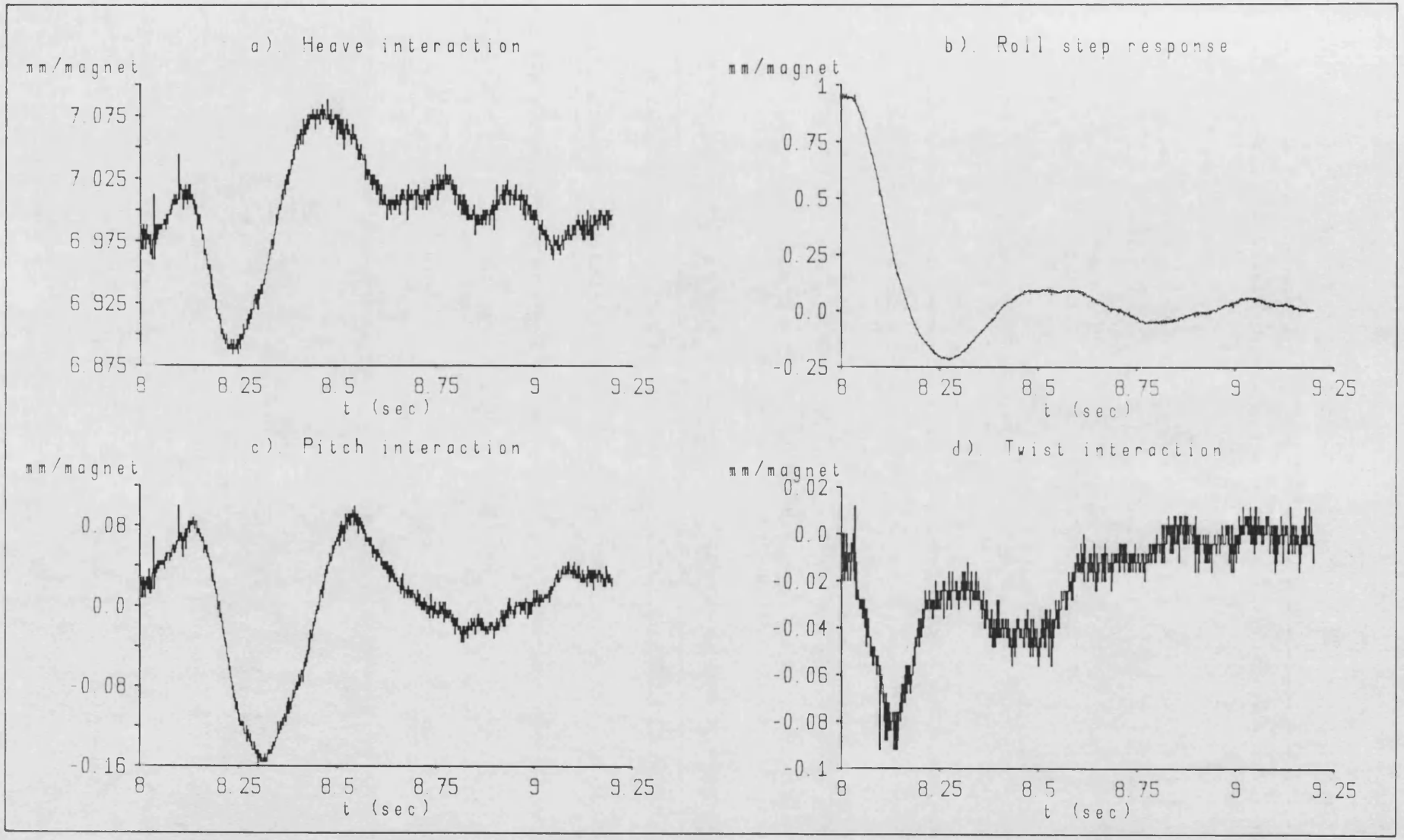

Roll step response Graph 5.4

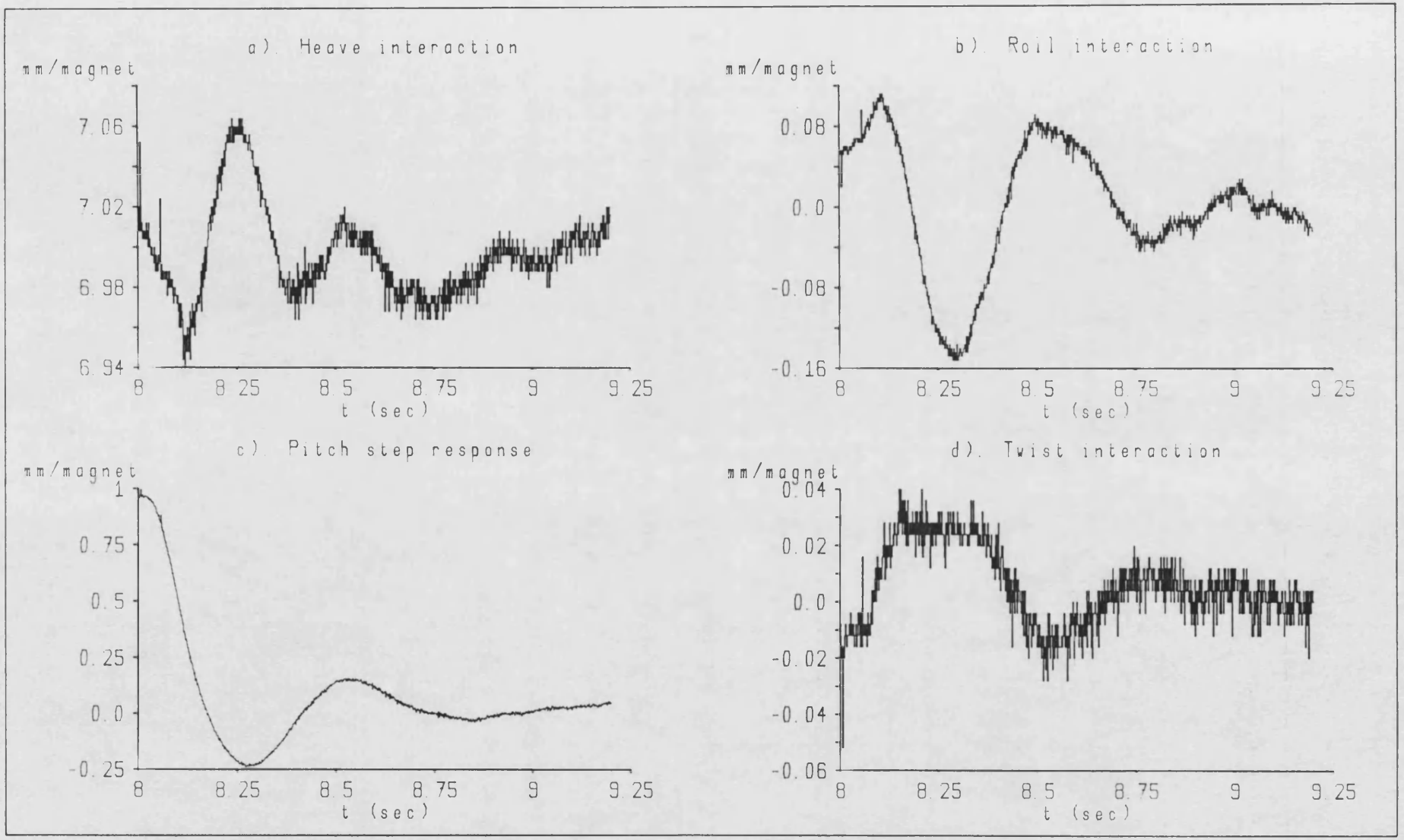

Pitch step response Graph 5.5

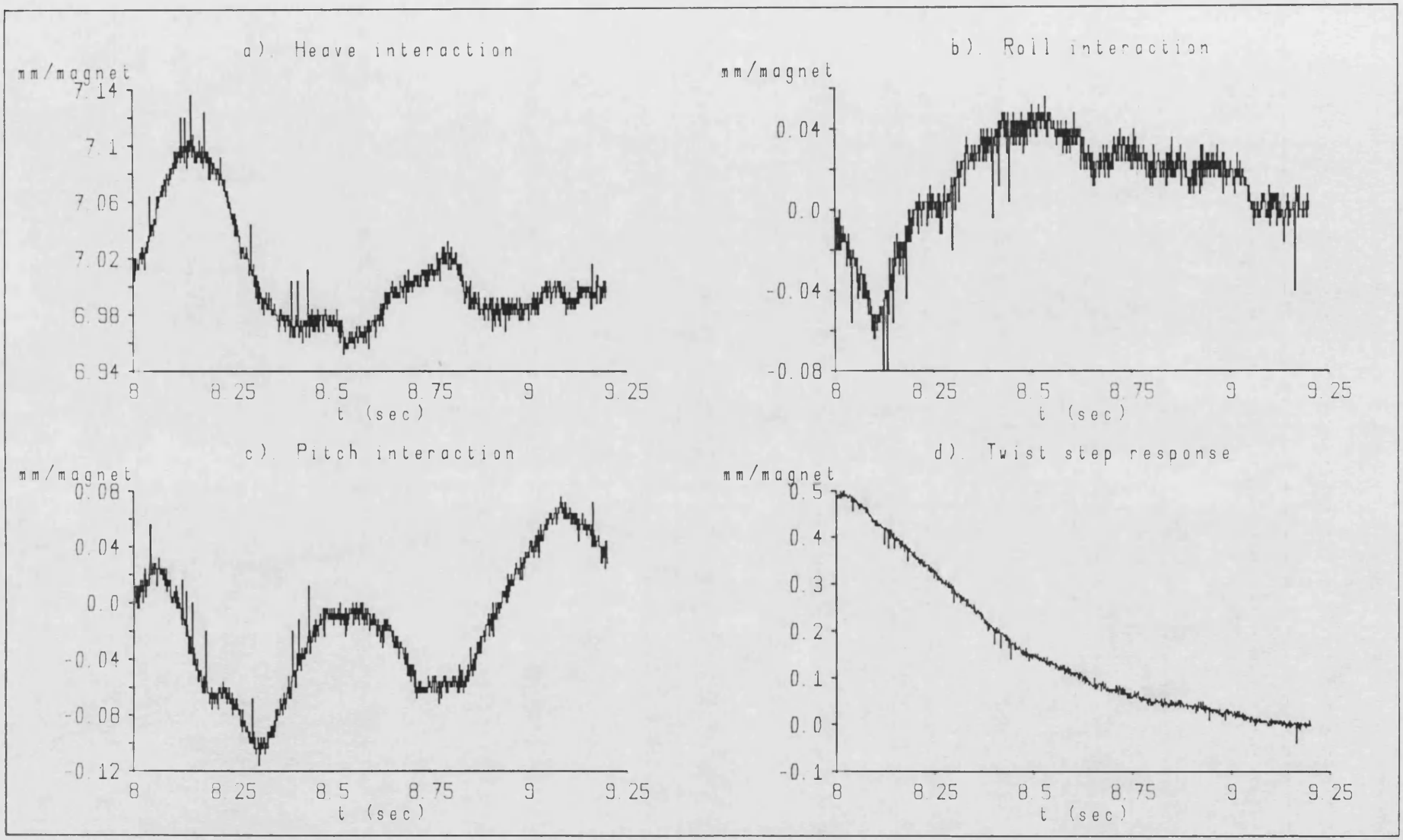

Twist step response Graph 5.6

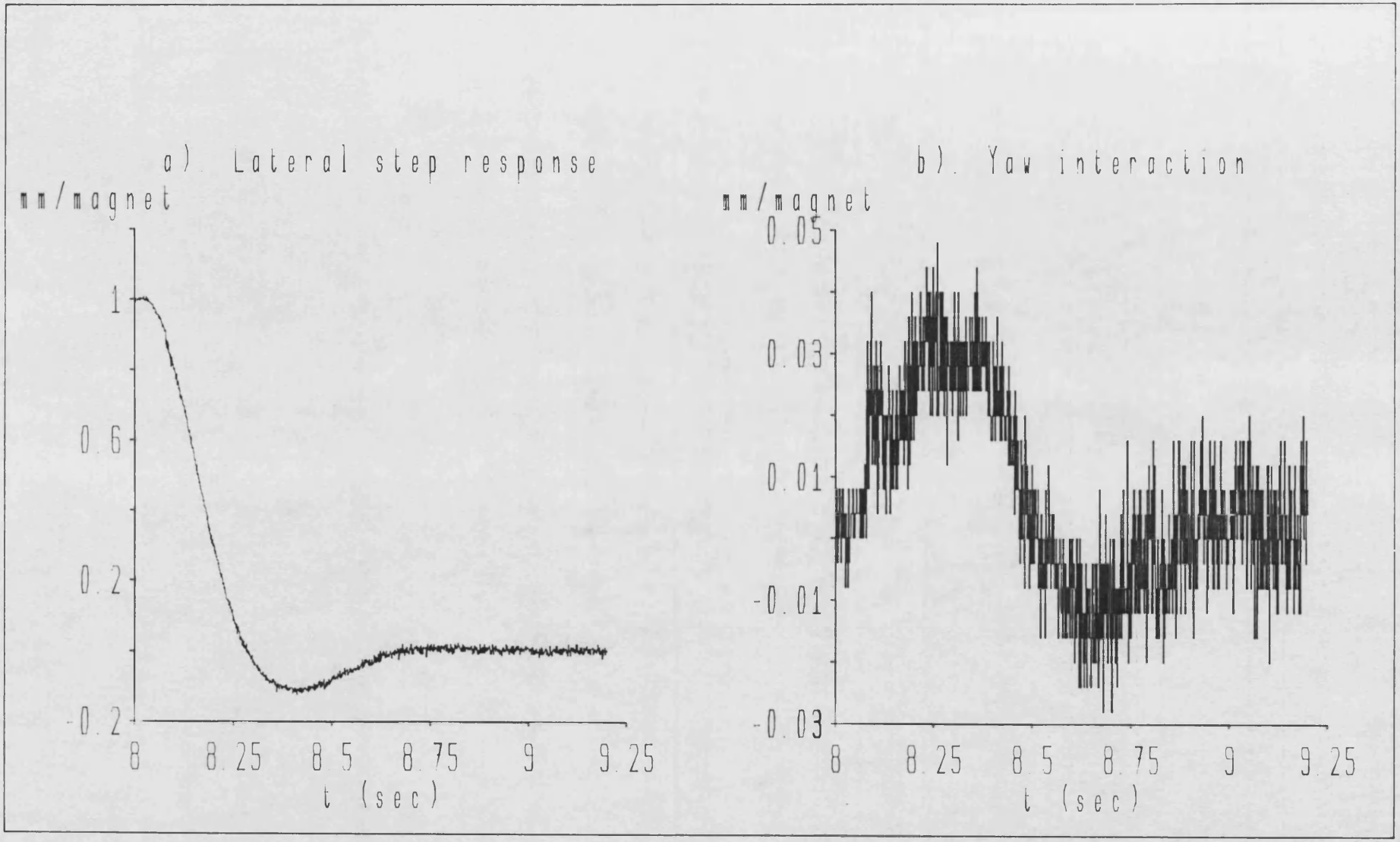

Lateral step response Graph 5.7

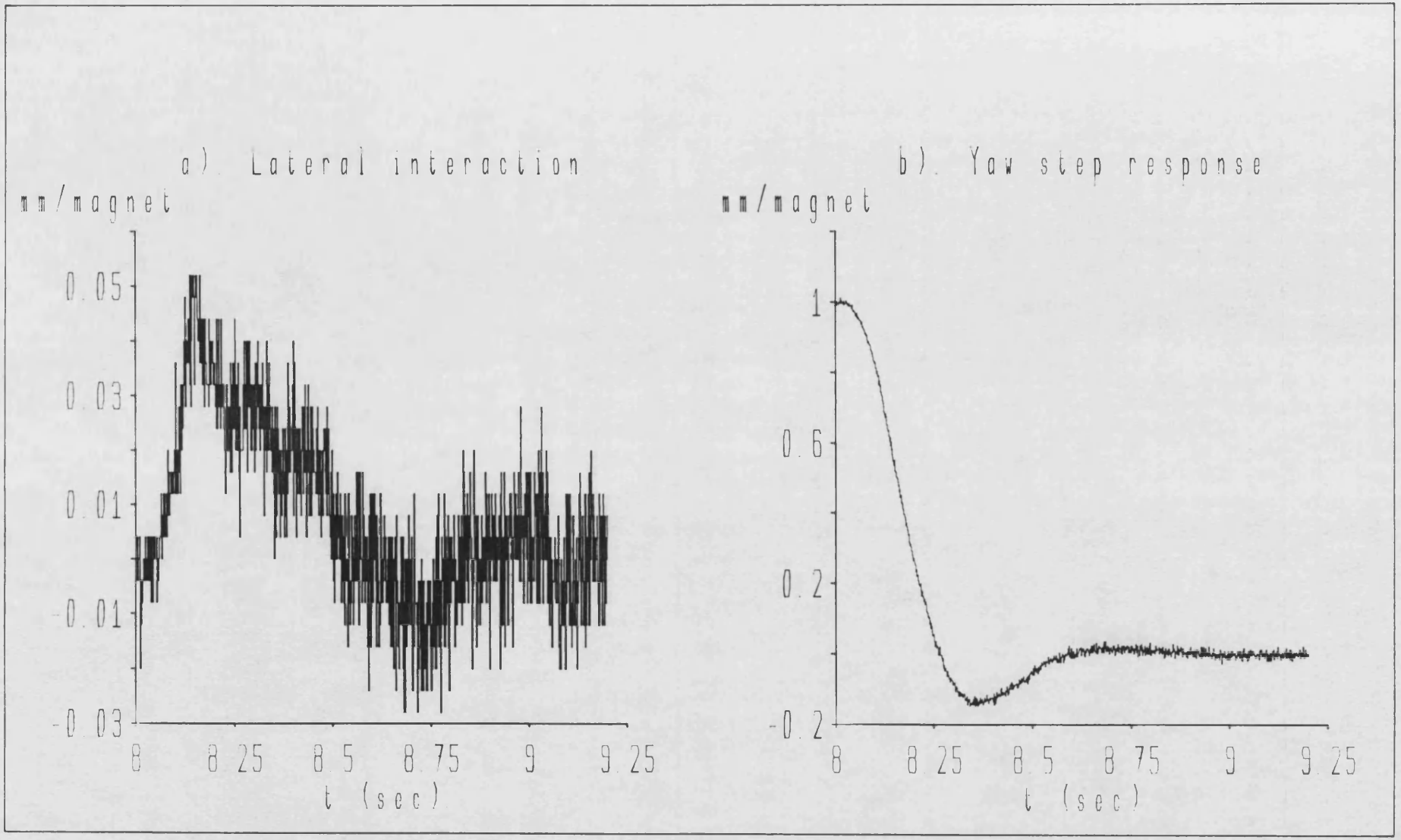

Yaw step response Graph 5.8

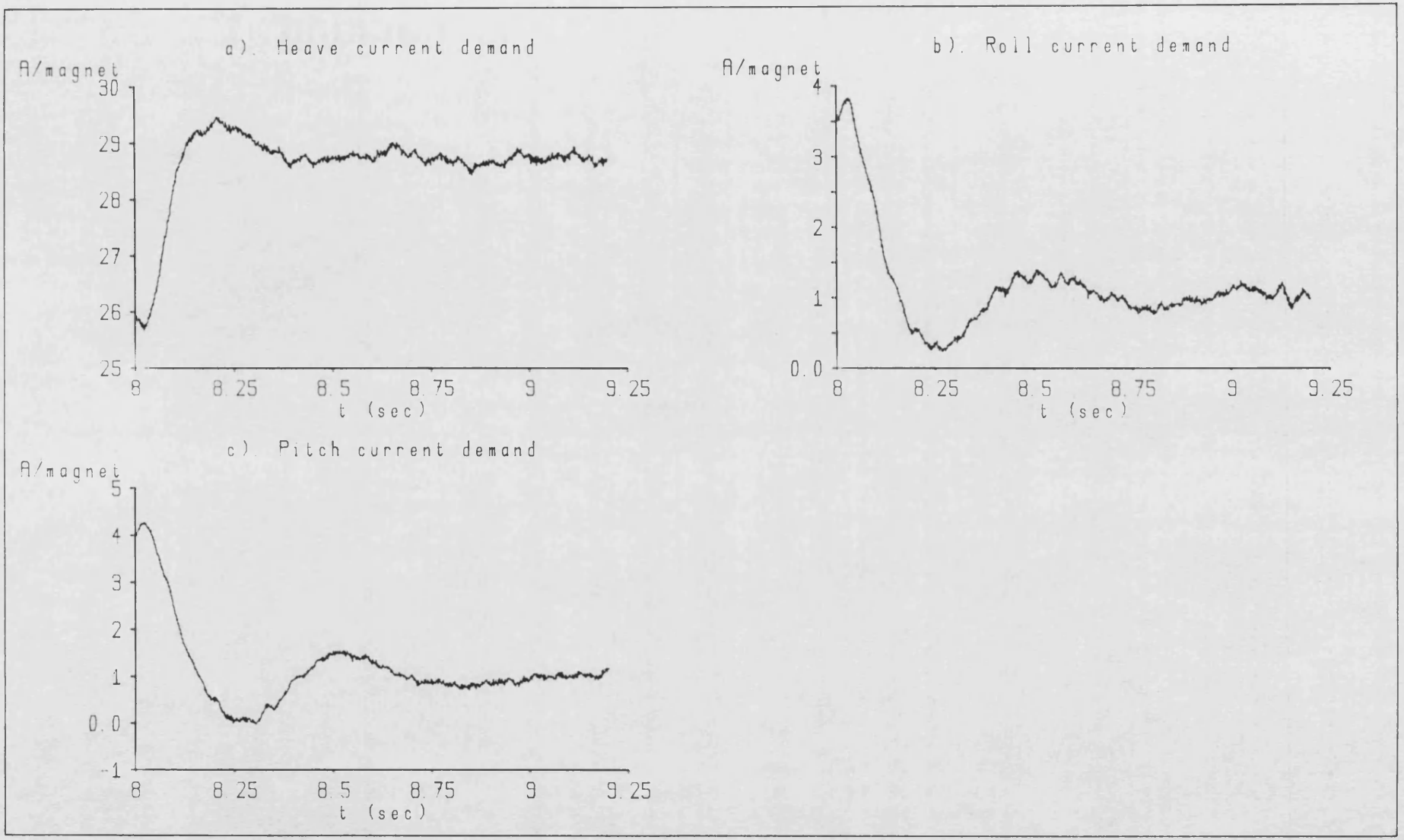

Heave, roll and pitch current demands Graph 5.9

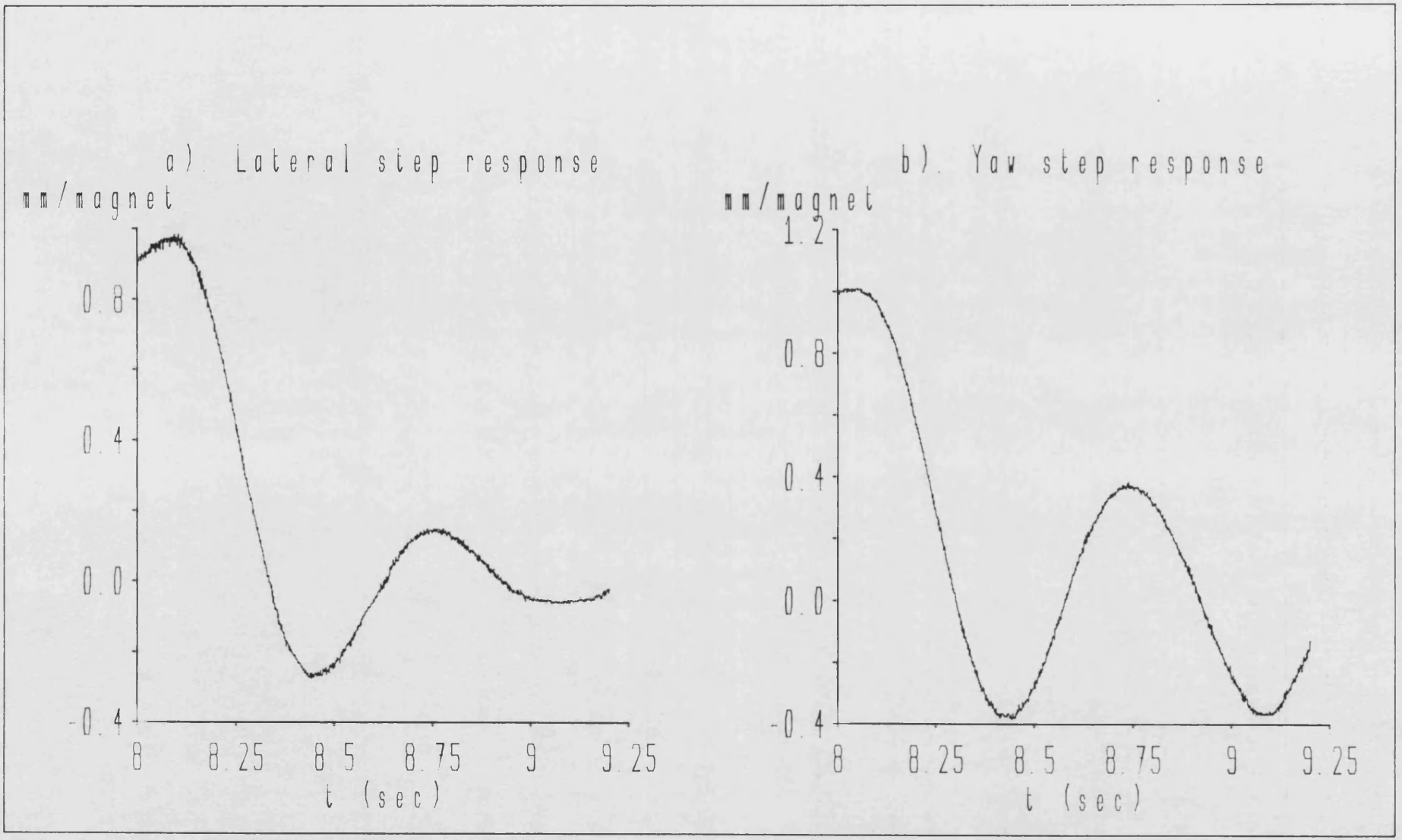

Lateral and yaw step responses (zero standing current) Graph 5.10

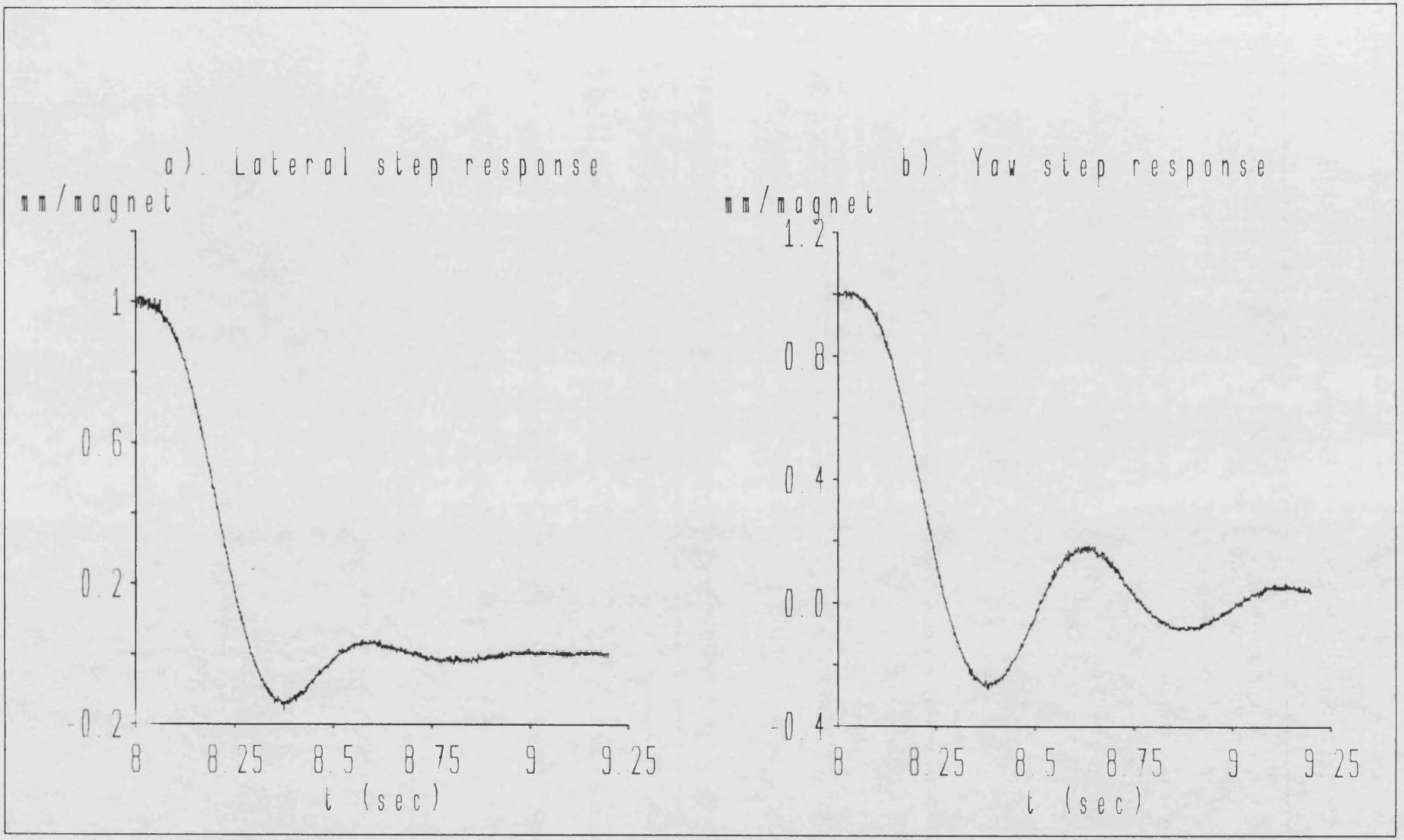

Lateral and yaw step responses (7.5 A standing current) Graph 5.11

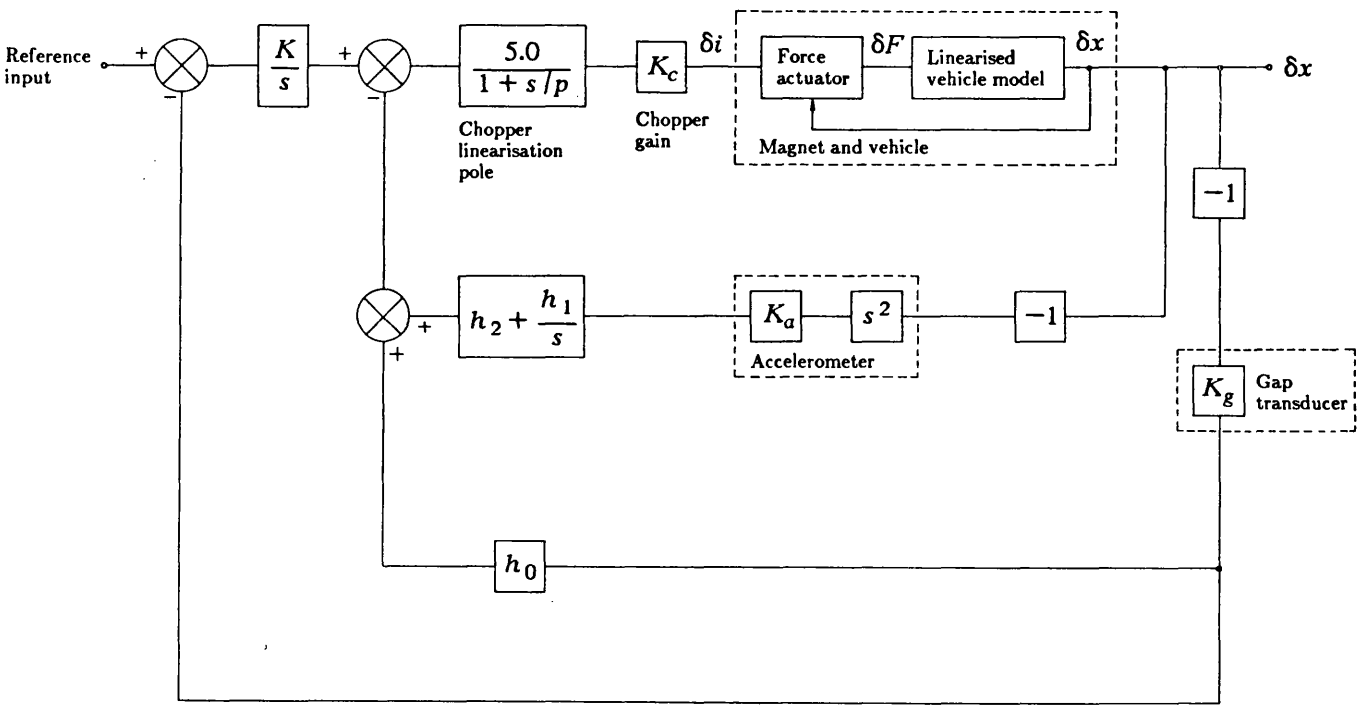

Control strategy block diagram Figure 5.1

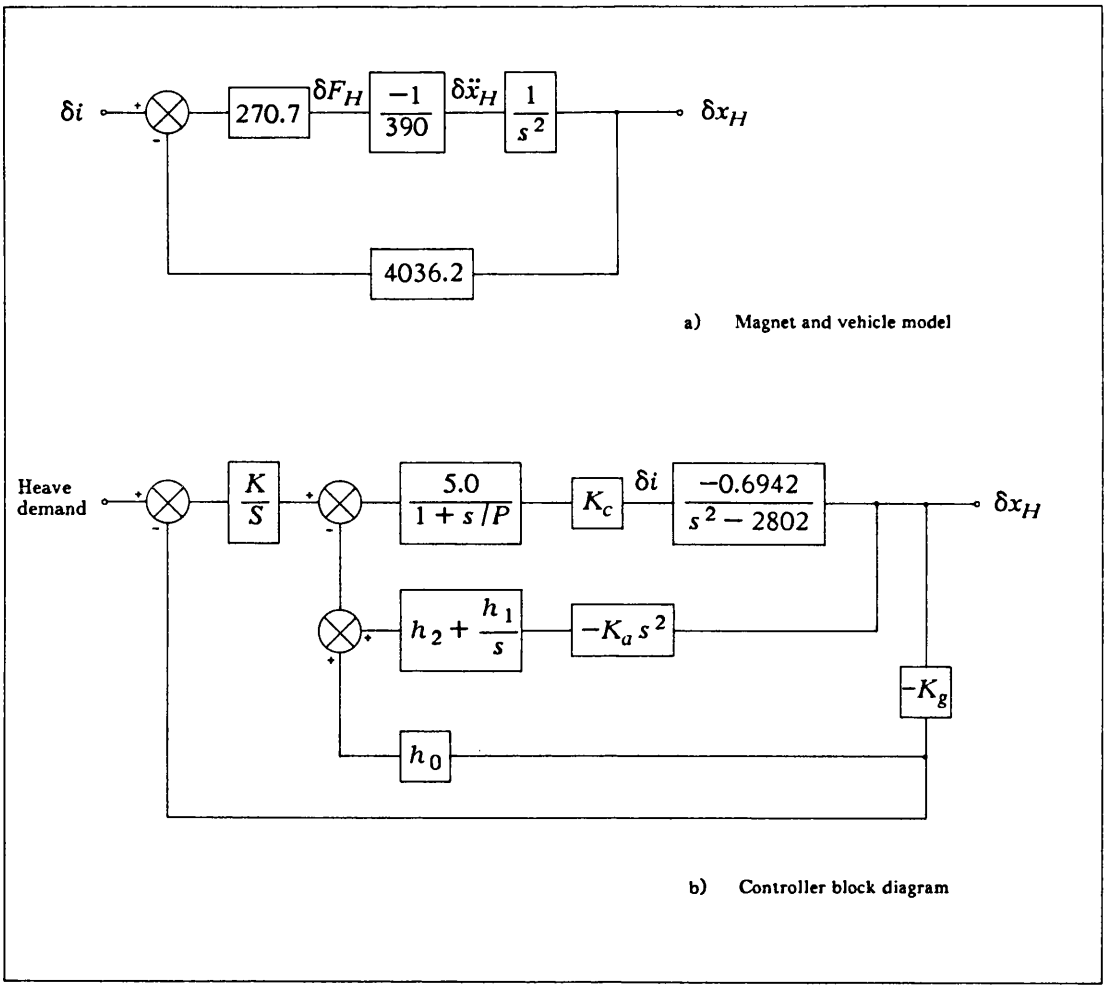

The heave mode controller Figure 5.2

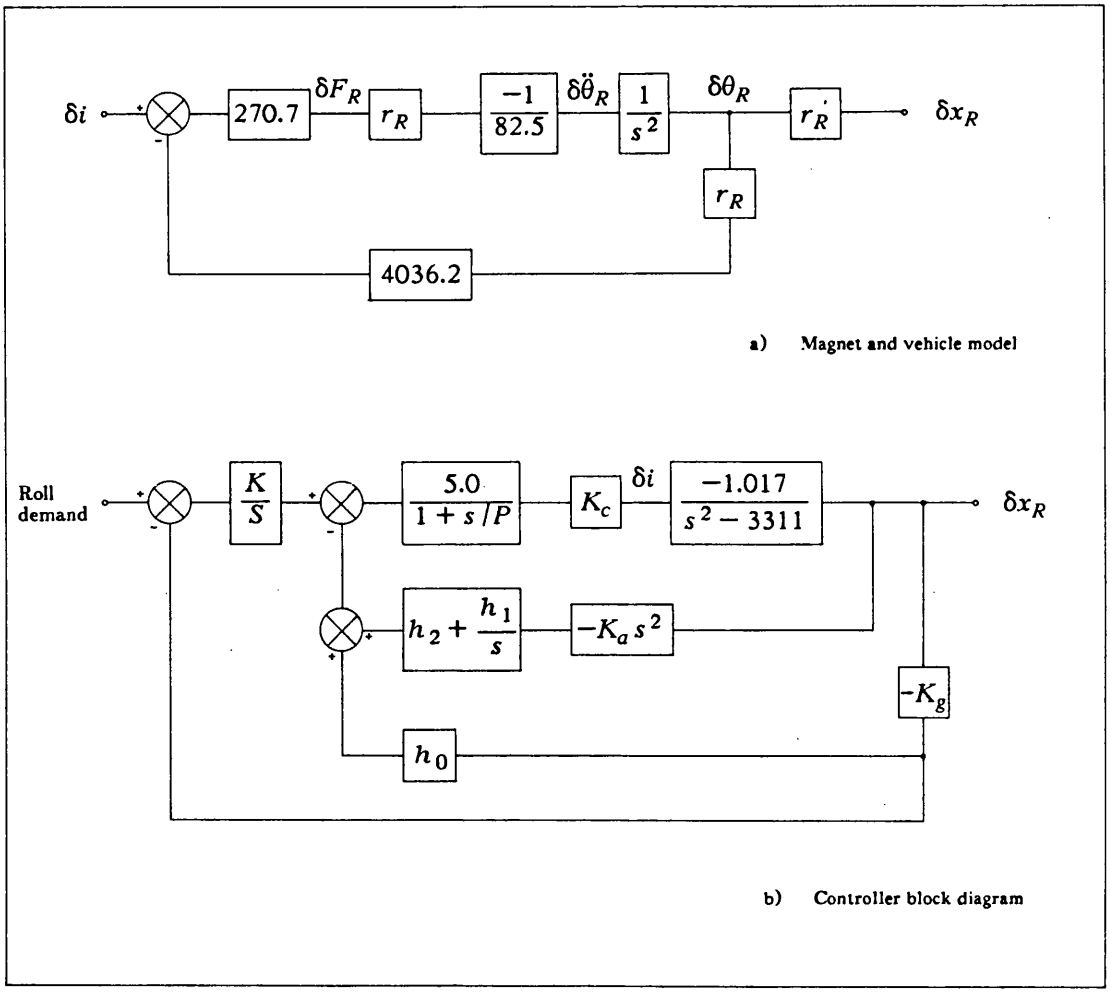

The roll mode controller Figure 5.3

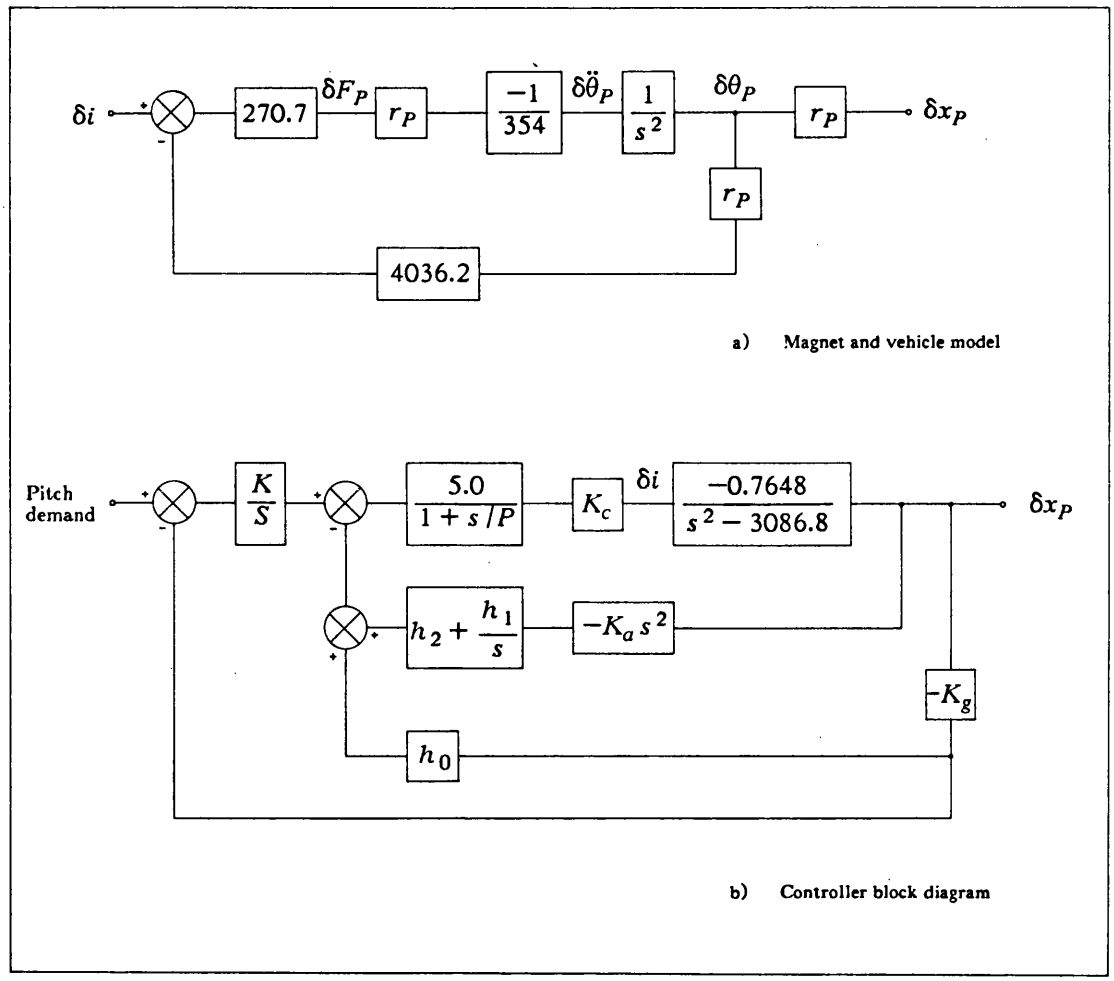

The pitch mode controller Figure 5.4

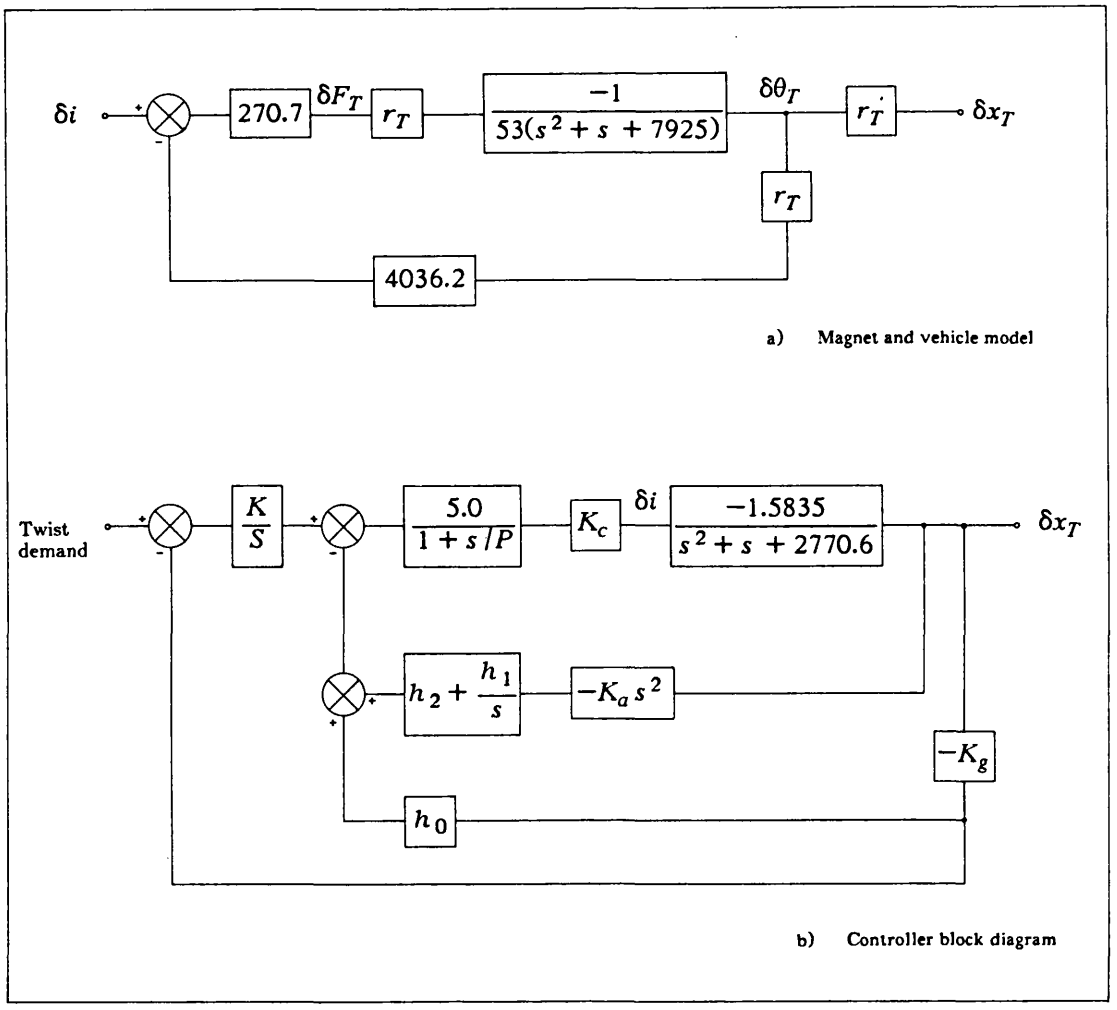

The twist mode controller Figure 5.5

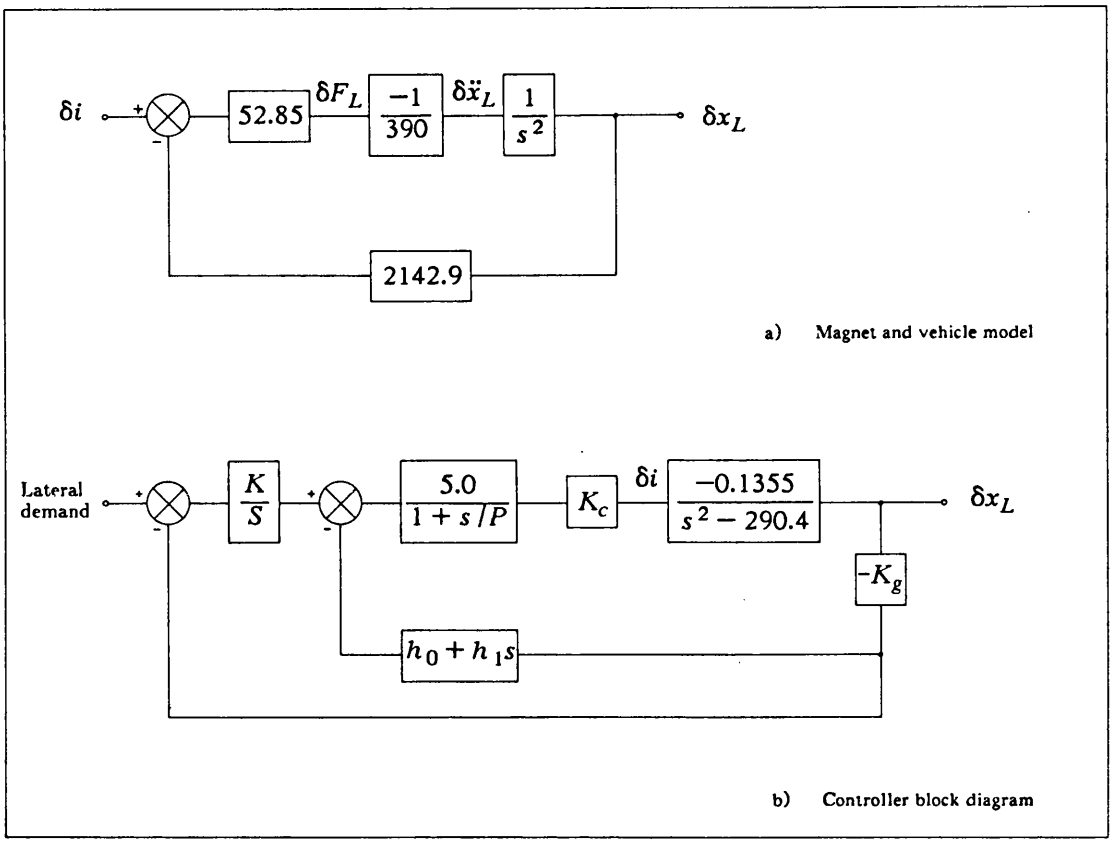

The lateral mode controller Figure 5.6

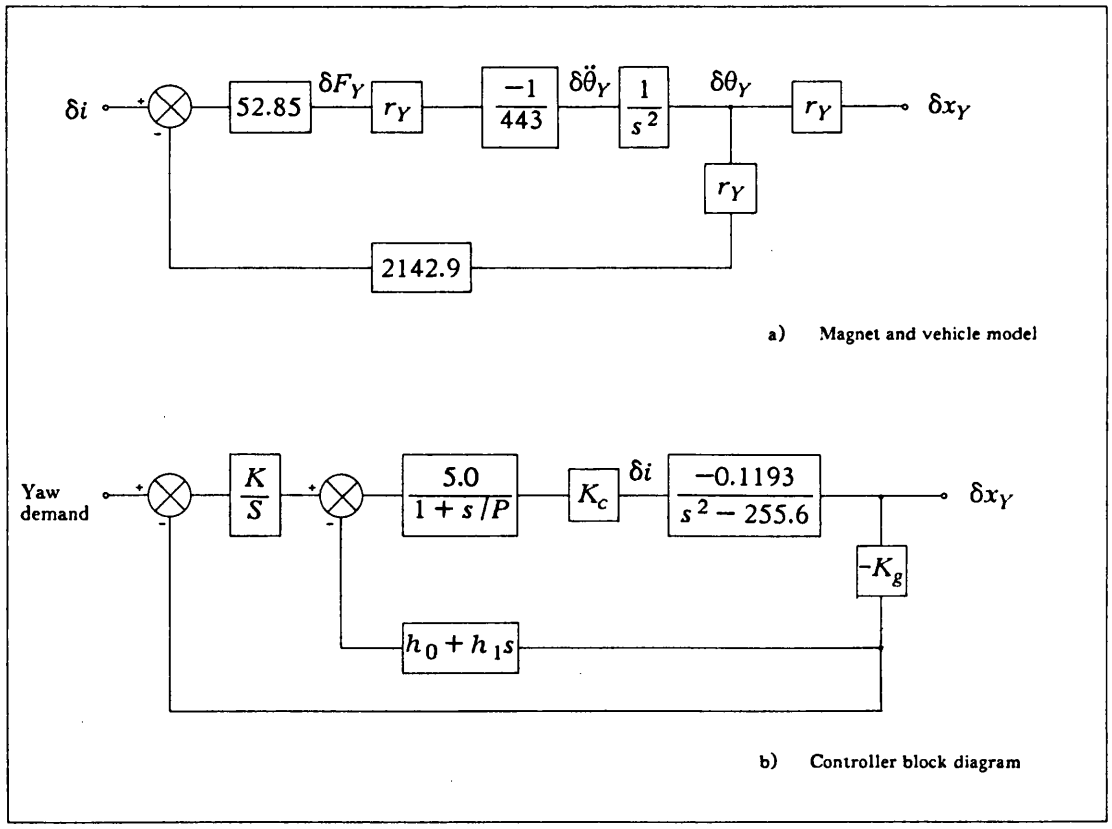

The yaw mode controller Figure 5.7

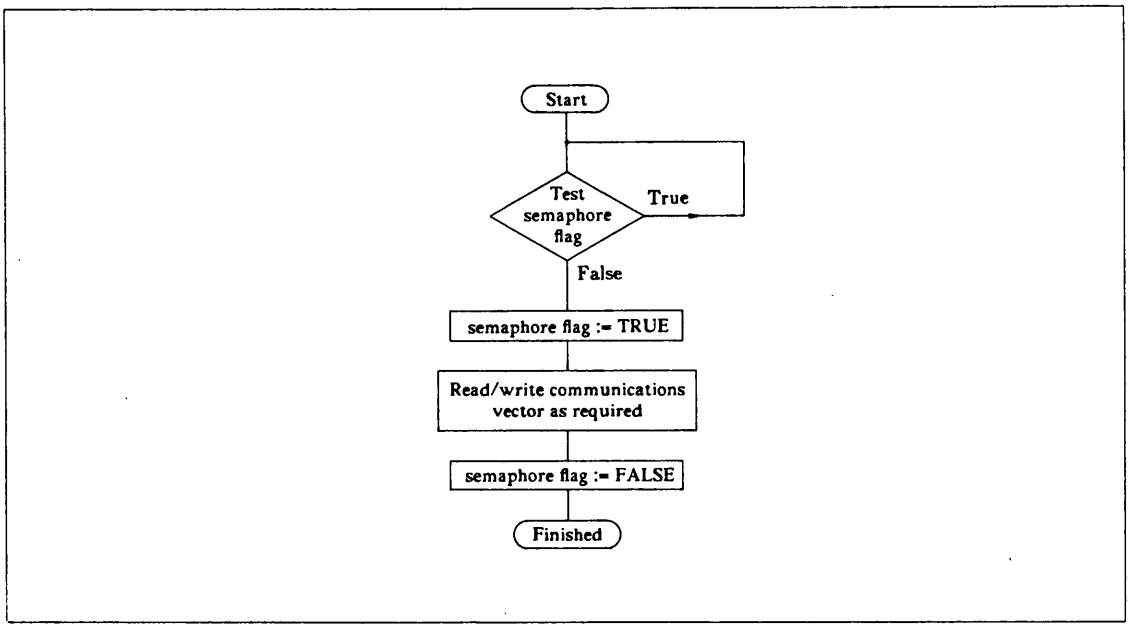

Inter-processor communication control using the semaphore flag — Figure 5.8

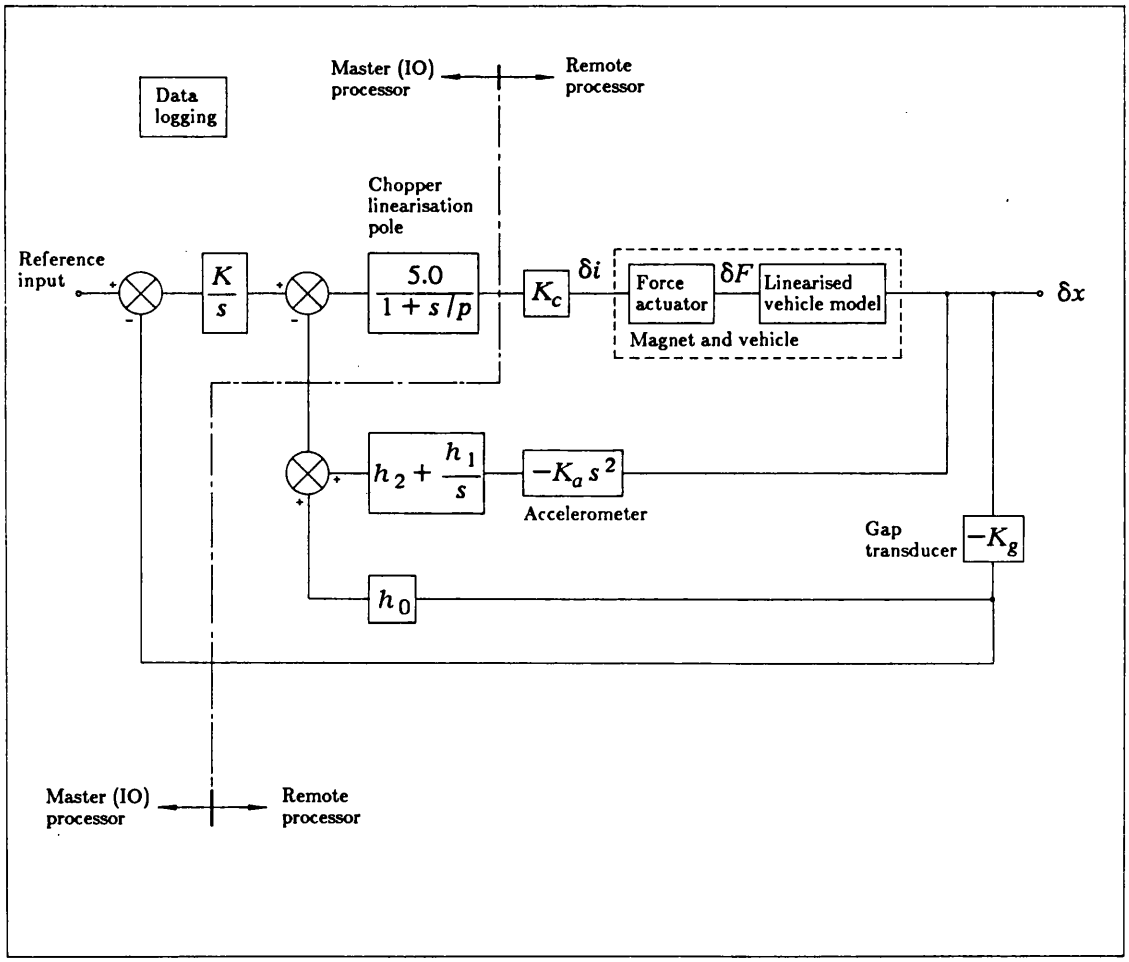

Controller partitioning between two processing nodes — Figure 5.9

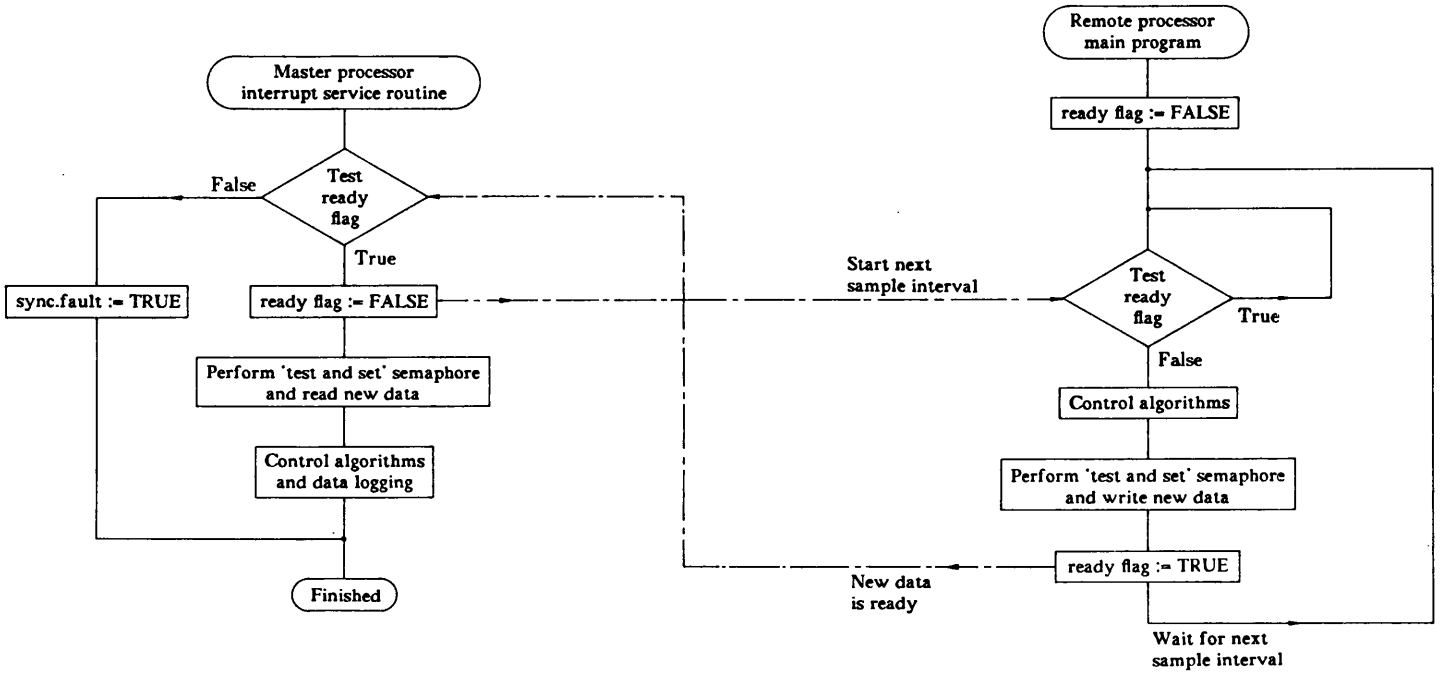

Processor synchronisation using the ready flag Figure 5.10

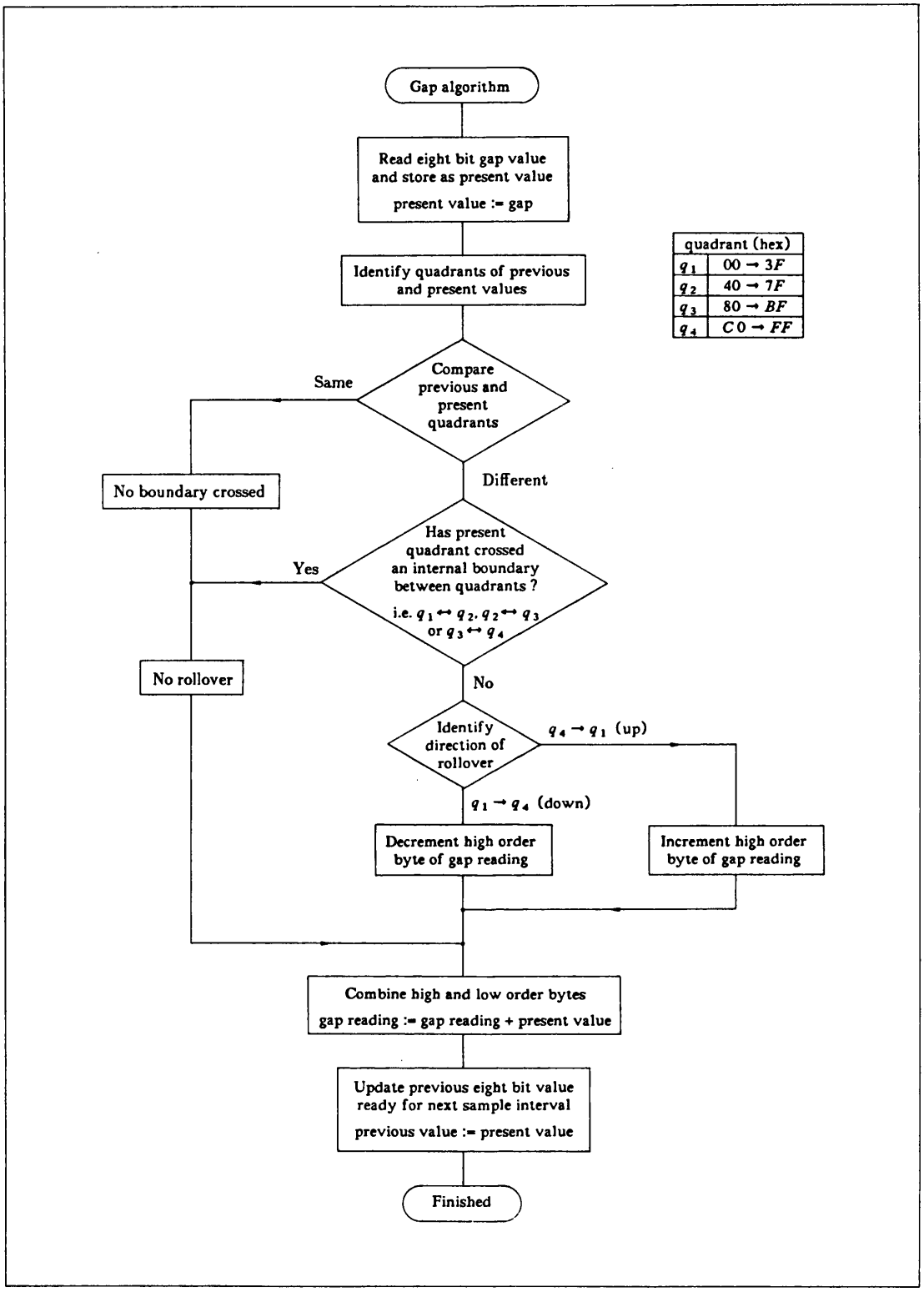

Flowchart definition of the gap reading algorithm Figure 5.11

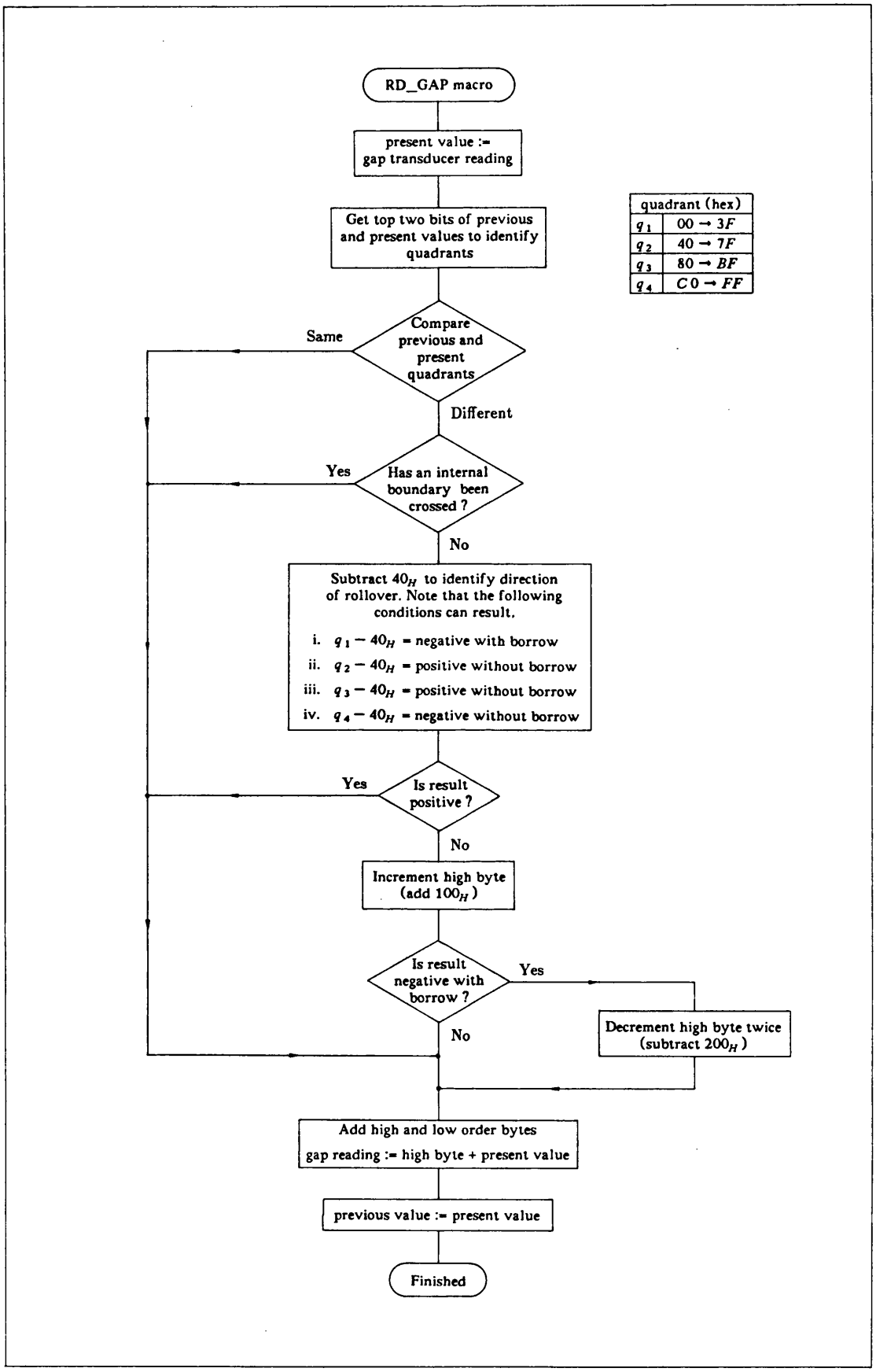

Flowchart of the RD_GAP macro Figure 5.12

6. Slitwidth modulated choppers using flux feedback

In an attempt to make the vehicle gains less sensitive to gap variations the levitation choppers were re-designed to provide flux control instead of current control. A vehicle controller would then issue flux density demands to each of the levitation motors.

The advantage of using flux control is illustrated by equations 6.1 and 6.2 below,

$$F = K_m \frac{I^2}{x^2} \quad \textit{current control} \qquad \text{equation 6.1}$$

$$F = \frac{B^2 A}{2\mu_0} \quad \textit{flux control} \qquad \text{equation 6.2}$$

Equation 6.1 illustrates how the force actuator gain based on current control is highly sensitive to gap variations, making it difficult for a controller to maintain stability after a severe gap disturbance. A much more linear force actuator is achieved by using flux control as illustrated by equation 6.2. In this latter case, the gain is independent of gap, such that a vehicle control system based on flux control should be able to cope with gap disturbances over the full range of available gap.

6.1 Flux monitoring coil

To provide flux feedback for the chopper, a flux monitoring coil was placed on the surface of one limb of the associated levitation motor as illustrated in figure 6.1. The coil length was such as to fully span the four pole motor, effectively forming a shadow winding of the levitation winding itself and also minimising any pickup of the a.c. tractive field. By using such a coil shape, any interaction between levitation and tractive flux would be observed by the flux coil and hence contained within the flux loop itself.

Now whereas the coil length must span an even number of motor poles (in this case four), the coil width was chosen to minimise the amount of leakage flux passing through the coil area (figure 6.2). With reference to figure 6.2 it can be seen that the coil should be somewhat smaller in width than the pole face to minimise the pickup of

stray flux which does not contribute towards lift force.

6.2 Equations

Figure 6.3a shows the magnetic circuit for one of the levitation motors, which has two series connected windings each of N turns forcing a flux ϕ through two gaps of length x. This arrangement was simplified to that of figure 6.3b, from which the following equation was written down,

$$2NI = l_1 H_1 + 2xH_2$$

where

$$H_1 = \frac{\phi}{A\,\mu_0\mu_r}$$

$$H_2 = \frac{\phi}{A\,\mu_0}$$

Hence

$$2NI = \frac{\phi}{A\,\mu_0}\left(\frac{l_1}{\mu_r} + 2x\right) \qquad \text{equation 6.3}$$

Provided that $\frac{l_1}{\mu_r} << 2x$ then equation 6.3 can be re-written as follows,

$$2NI = \frac{\phi}{A\,\mu_0}.2x$$

Now $\frac{\phi}{A} = B$, hence

$$2NI = B\frac{2x}{\mu_0}$$

giving

$$B = \mu_0\frac{NI}{x} \qquad \text{equation 6.4}$$

And for the flux coil, which has N_ϕ turns and area A_ϕ *beneath the secondary track members*,

$$V_\phi = N_\phi\frac{d\phi}{dt}$$

$$= N_\phi A_\phi \frac{dB}{dt}$$

$$= K_v \frac{dB}{dt} \qquad \text{equation 6.5}$$

where

$$K_v = N_\phi A_\phi \qquad \text{equation 6.6}$$

K_v is the flux coil constant and V_ϕ is the output voltage from the coil due to a flux density variation dB/dt.

6.3 Flux coil gain

The flux coil used had the following parameters,

$$N_\phi = 10$$

$$A_\phi = 2 \times 0.06 \times 0.038$$

$$= 4.56\times10^{-3} \quad m^2$$

giving

$$K_v = N_\phi A_\phi$$

$$= 0.0456 \quad V/T.s^{-1}$$

To check this value of K_v, consider the substitution of equation 6.4 in equation 6.5. For constant gap,

$$V_\phi = K_v \frac{\mu_0 N}{x} . \frac{dI}{dt} \qquad \text{equation 6.7}$$

$$= K . \frac{dI}{dt}$$

where

$$K = K_v \frac{\mu_0 N}{x} \qquad \text{equation 6.8}$$

$$= 0.0456 \times \frac{4\pi\times10^{-7} \times 91}{7\times10^{-3}}$$

$$= 0.745\times10^{-3} \qquad \text{equation 6.9}$$

The above figure represents the gain relating flux coil output voltage to a corresponding rate of change of current in the levitation winding at a gap of 7 mm. To check the

value of equation 6.9, and hence the value of K_v, a constant gap test was carried out at a gap of 7 mm using a triangular current waveform in the magnet winding to produce a square wave output voltage from the flux coil. By measuring the rate of change of current and the associated square wave peak amplitude the flux coil gain K_v was then calculated.

To produce a triangular current waveform within the levitation windings a constant current demand was issued to the corresponding current feedback chopper. Under these circumstances the action of the slitwidth modulator is such that the load voltage is switched to maintain the measured load current within a ±2 A window about the constant demand level. Because the slitwidth window is small compared with the aiming current of the chopper (see section 2.2.1), a good approximation to a triangular waveform is produced.

6.3.1 Results The results from this test are presented below in table 6.1.

	$\frac{di}{dt}$ (A/s)	V_ϕ (volts)	$K = \frac{V_\phi}{di/dt}$
1	-700	-0.75	1.07×10^{-3}
2	800	0.8	1.0×10^{-3}

TABLE 6.1. Flux coil gain test

These results would suggest that the calculated value of K was too small. To accommodate this the value of K_v was increased according to the experimental results. Using result 2 in equation 6.8,

$$K = K_v \frac{\mu_0 N}{x}$$

$$= 1.0\times10^{-3}$$

Hence

$$K_v = \frac{1.0\times10^{-3} \times 7\times10^{-3}}{4\pi\times10^{-7} \times 91}$$

$$= 0.0612 \quad V/T.s^{-1} \qquad \text{equation 6.10}$$

This was the modified value of K_v used hereafter. Note that this would suggest that the flux coil observes more flux than previously calculated. This was probably due to stray flux crossing the gap between motor limbs throughout the length of the motor, and not just beneath the secondary track members.

6.3.2 Flux coil buffer amplifier Since the above test generated almost the maximum di/dt likely to be encountered in the magnet winding, the flux coil output voltage of 0.8 volts would correspond to an approximate maximum flux coil output. Hence to bring the flux coil signals to a reasonable op-amp level a buffer amplifier with a gain of 10 was included. To derive the gap flux density, it was then necessary to integrate the flux coil output (as shown by equation 6.5).

6.4 Integrator design

To avoid possible problems with d.c. drift, an a.c. integrator with zero d.c. gain was used as shown in figure 6.4. The transfer function of this circuit is derived in appendix F and reproduced below,

$$T(s) = \frac{v_0}{v_i}(s) = \frac{-Ks}{s^2 + a_1 s + a_0} \qquad \text{equation 6.11}$$

where

$$K = \frac{1}{CR_1} \qquad \text{equation 6.12}$$

$$a_1 = \frac{2}{CR_3} \qquad \text{equation 6.13}$$

$$a_0 = \frac{(R_1 + R_2)}{C^2 R_1 R_2 R_3} \qquad \text{equation 6.14}$$

The filter coefficients were governed by the lowest cutoff frequency achievable using practical component values (i.e. $R \leqslant 1\,M\Omega$ and $C \leqslant 10.0\,\mu F$). Additionally appendix F shows that the value of K is constrained by the requirement that the values of R_1 and R_2 must be positive. With these limitations taken into account the following transfer function was derived.

$$T(s) = \frac{-0.1s}{s^2 + s + 0.213} \qquad \text{equation 6.15}$$

using

$C = 10.0\ \mu F$

$R_1 = 1\ M\ \Omega$

$R_2 = 300\ K$

$R_3 = 200\ K$

To overcome the gain constraint of the integrator and to set the overall gain of the a.c. flux measurement circuit, a third amplifier stage was added. The overall block diagram for the a.c. flux path was then as given by figure 6.5. With reference to this block diagram, the overall a.c. gain of the flux measurement circuit was written down as follows,

$$\frac{V}{B} = K_v \times K \qquad \text{equation 6.16}$$

where K is the final stage gain used to set the overall feedback gain as required.

A preliminary gain of 5.0 was set for the a.c. flux measurement circuit, such that a flux density of 1 T peak to peak would produce an output voltage of 5 V peak to peak. Using equation 6.16,

$$K = \frac{5.0}{K_v}$$

$$= \frac{5.0}{0.0612}$$

$$= 82$$

Note that the sign of the output voltage was not of any concern here since, if required, the flux coil connections could be reversed.

6.4.1 Flux coil/integrator frequency response The frequency response (gain and phase) of the a.c. flux path defined by the block diagram of figure 6.5 was calculated to produce graph 6.1. This shows a cutoff frequency of 0.14 Hz (-3 dB), above which the output voltage from the integrator would be a good representation of the gap flux

density independent of gap.

Now to provide a reasonably flat overall flux response from zero frequency a d.c. flux gain was also required, having a cutoff frequency corresponding to that of the a.c. flux gain.

6.5 Derivation of a d.c. flux signal

To provide a d.c. flux signal, equation 6.4 was considered for the given working gap of 7 mm.

$$B = \mu_0 \frac{NI}{x}$$

$$= \frac{4\pi \times 10^{-7} \times 91}{7 \times 10^{-3}} \cdot I$$

$$= 0.0164\, I$$

However a more accurate figure was obtained by using a flux density measuring instrument in the airgap, which yielded the following result.

$$B = 0.02I \qquad \text{equation 6.17}$$

Now the current I was available directly from the existing current feedback transducer which had a gain of 0.1 V/A, corresponding to an equivalent flux gain of 5.0 V/T as required. To provide the 0.14 Hz cutoff, a low pass transfer function as shown below was provisionally used, which was the low pass equivalent to that used in the a.c. flux path.

$$T(s) = \frac{0.213}{s^2 + s + 0.213} \qquad \text{equation 6.18}$$

The hardware realisation of this transfer function is described in appendix F.

6.6 Overall calculated frequency response

The frequency response of the combined a.c. and d.c. flux paths was calculated according to the block diagram of 6.6. These results are included as graph 6.2, which shows that the crossover characteristic between the a.c. and d.c. flux paths was

unacceptable due to a sharp fall in gain of approximately 28 dB at a frequency of 0.07 Hz, together with a phase flip from -90^{o} to $+90^{o}$. To overcome this discontinuity, the low pass filter in the d.c. flux path was modified to include a zero as shown below,

$$T(s) = \frac{s + 0.213}{s^2 + s + 0.213} \qquad \text{equation 6.19}$$

Using this modified low pass filter the calculated frequency response for the combined flux paths was shown to be completely flat in both gain and phase. The practical realisation of equation 6.19 is described in appendix F.

6.7 Chopper modifications for flux feedback

To provide the choppers with flux feedback the original current feedback path was simply replaced with the combined flux measurement circuitry derived above. Figure 6.7 shows the modified chopper control circuit with figures 6.8 and 6.9 providing the corresponding pcb layout details. Note that preset resistor PR1 was included to remove any d.c. offset introduced by the flux coil integrator circuitry.

The choppers using the modified control boards would operate in exactly the same way as with current feedback in that the power switching devices would be slitwidth modulated to provide minimum error in minimum time. However with flux feedback choppers this error would also be dependent on the magnet gap, so the magnet itself would behave quite differently to a magnet using one of the original current feedback choppers.

6.8 Constant gap testing

To check the operation of the choppers using flux feedback a series of constant gap frequency response tests were carried out. Of particular interest was the crossover region, where the flux feedback switches between a.c. and d.c. flux monitoring. All tests were carried out at the working gap of 7 mm. To provide reference signals the multiprocessor computer system was used to generate low frequency (0.03 to 15.0 Hz) demand sinusoids from one of the D to A channels.

Results of gap flux density were taken by noting the winding current (using the chopper load current transducer) and then using equation 6.17 to translate the measured current to an equivalent gap flux density. Recall that equation 6.17 was an experimentally derived figure relating measured winding current to actual gap flux density at a constant gap of 7 mm.

6.8.1 Flux coil/integrator frequency response To test the frequency response of the flux coil and integrator a constant flux test was carried out to check that the combined gain would fall off at 40 dB/decade at frequencies below about 0.1 Hz (in accordance with the calculated response derived in section 6.4.1). Constant gap flux at various frequencies was provided by an unmodified current feedback chopper used to set up a fixed magnitude a.c. current in the motor winding. Equation 6.17 was then used to derive the corresponding gap flux density.

Test results are given in table 6.2 and presented graphically as graph 6.3. This graph compared well with the calculated gain response given in graph 6.1. Experimental phase results were too difficult to obtain, but it was clear that no significant phase shift was present above about 2.0 Hz.

6.8.2 Overall chopper frequency response Using the modified flux feedback chopper with variable frequency constant magnitude a.c. flux demands the results presented in table 6.3 were obtained. These results show that the measured gap flux was constant for all frequencies included in the test, giving a completely flat response about the crossover frequency.

It is important to note that the flux frequency response would only be flat for a gap of 7 mm. If the gap were to be reduced or increased for a considerable length of time (i.e. seconds) then the current derived feedback would become stronger or weaker respectively. However, because the vehicle controller would be significantly faster than the d.c. flux loop it was considered reasonable to assume that any transient variations in gap would have no effect on the flux feedback gain.

To complete the flux feedback study, consideration will now be given to modelling the chopper/motor combination under non-constant gap conditions.

6.9 Flux feedback with non-constant gap

To see the effect of gap variations on the flux feedback choppers consider equation 6.4 reproduced below.

$$B = \mu_0 \frac{NI}{x}$$

giving,

$$\delta B = \frac{\partial B}{\partial i}\delta i + \frac{\partial B}{\partial x}\delta x$$

where

$$\left.\frac{\partial B}{\partial i}\right|_{I_0 X_0} = \frac{\mu_0 N}{X_0}$$

$$\left.\frac{\partial B}{\partial x}\right|_{I_0 X_0} = \frac{-\mu_0 N I_0}{X_0^2}$$

Hence

$$\delta B = \frac{\mu_0 N}{X_0}\left|\delta i - \frac{I_0}{X_0}\delta x\right| \qquad \text{equation 6.20}$$

Now gap variations δx were due to a force δF acting on a motor mass M as defined in equation 6.21 below (for a simple single motor model).

$$\delta \ddot{x} = -\frac{\delta F}{M} \qquad \text{equation 6.21}$$

The force δF was derived using equation 6.2 as follows.

$$F = \frac{B^2 A}{2\mu_0}$$

giving

$$\left.\frac{\delta F}{\delta B}\right|_{B_0} = \frac{2B_0 A}{2\mu_0}$$

$$= 2.\frac{B_0^2 A}{2\mu_0}.\frac{1}{B_0}$$

$$= \frac{2F_0}{B_0} \qquad \text{equation 6.22}$$

where F_0 is the working point motor force required to overcome gravity. For the single motor model F_0 is given by,

$$F_0 = Mg \qquad \text{equation 6.23}$$

Combining equations 6.20, 6.21 and 6.22 the block diagram of figure 6.10a was derived for the variable gap, flux feedback system. From this diagram,

$$\delta B = \frac{\mu_0 N}{X_0}\left\{\delta i + \frac{2F_0 I_0}{B_0 M s^2 X_0}\delta B\right\}$$

giving

$$\delta B\left\{1 - \frac{\mu_0 N}{X_0}\frac{2F_0 I_0}{B_0 M s^2 X_0}\right\} = \frac{\mu_0 N}{X_0}\delta i$$

But $F_0 = Mg$ and $\frac{\mu_0 N I_0}{X_0} = B_0$, giving

$$\delta B\left\{1 - \frac{2g}{s^2 X_0}\right\} = \frac{\mu_0 N}{X_0}\delta i$$

Re-arranging,

$$\frac{\delta B}{\delta i} = \frac{\mu_0 N}{X_0}.\frac{s^2}{s^2 - \frac{2g}{X_0}} \qquad \text{equation 6.24}$$

This may be represented by the block diagram of figure 6.10b, which is essentially a simplified equivalent of figure 6.10a. These figures show that the flux variations due to gap changes are contained within the flux loop, as was the original intention of the flux controlled chopper design.

Although quantitative variable gap testing was not carried out in this chapter, the effectiveness of the flux feedback could be demonstrated qualitatively by setting up the standing current in one of the magnets. Under these conditions the vehicle corner could be readily lifted with one hand and moved over the full gap range quite easily (with

$M \approx 100$ kg).

frequency (Hz)	winding current (A)	gap flux density (T) $B = 0.02 \times I$	integrator output (V)	integrator gain = $\frac{V}{B}$	integrator gain (dB)
0.03	7.6	0.152	0.113	0.74	-2.6
0.059	7.6	0.152	0.306	2.0	6.1
0.083	7.6	0.152	0.429	2.8	9.0
0.14	7.6	0.152	0.592	3.9	11.8
0.18	7.6	0.152	0.674	4.43	12.9
0.27	7.6	0.152	0.776	5.1	14.1
0.53	7.6	0.152	0.776	5.1	14.1
1.2	7.6	0.152	0.776	5.1	14.1
2.0*	7.6	0.152	0.776	5.1	14.1
4.17	7.6	0.152	0.776	5.1	14.1
7.7	7.6	0.152	0.776	5.1	14.1
10.0	7.6	0.152	0.776	5.1	14.1
15.0	7.6	0.152	0.776	5.1	14.1

* phase shift became insignificant above 2.0 Hz

TABLE 6.2. Flux coil/integrator frequency response

frequency (Hz)	winding current (A)	gap flux density (T) $B = 0.02 \times I$
0.03	13.0	0.26
0.059	13.0	0.26
0.083	13.0	0.26
0.14	13.0	0.26
0.18	13.0	0.26
0.27	13.0	0.26
0.53	13.0	0.26
1.2	13.0	0.26
2.0	13.0	0.26
4.17	13.0	0.26
7.7	13.0	0.26
10.0	13.0	0.26
15.0	13.0	0.26

TABLE 6.3. Chopper frequency response

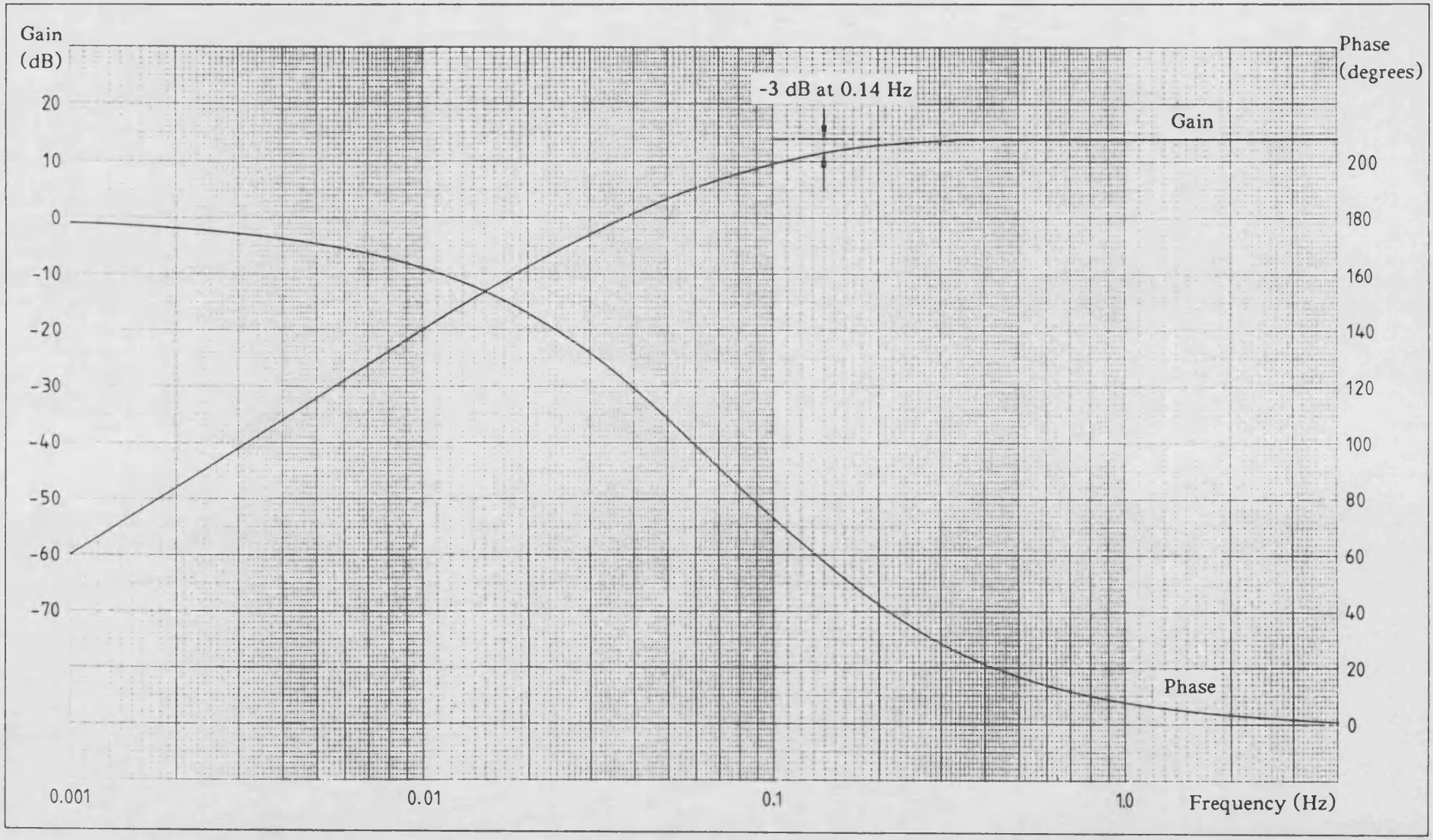

Flux coil/integrator frequency response (calculated) Graph 6.1

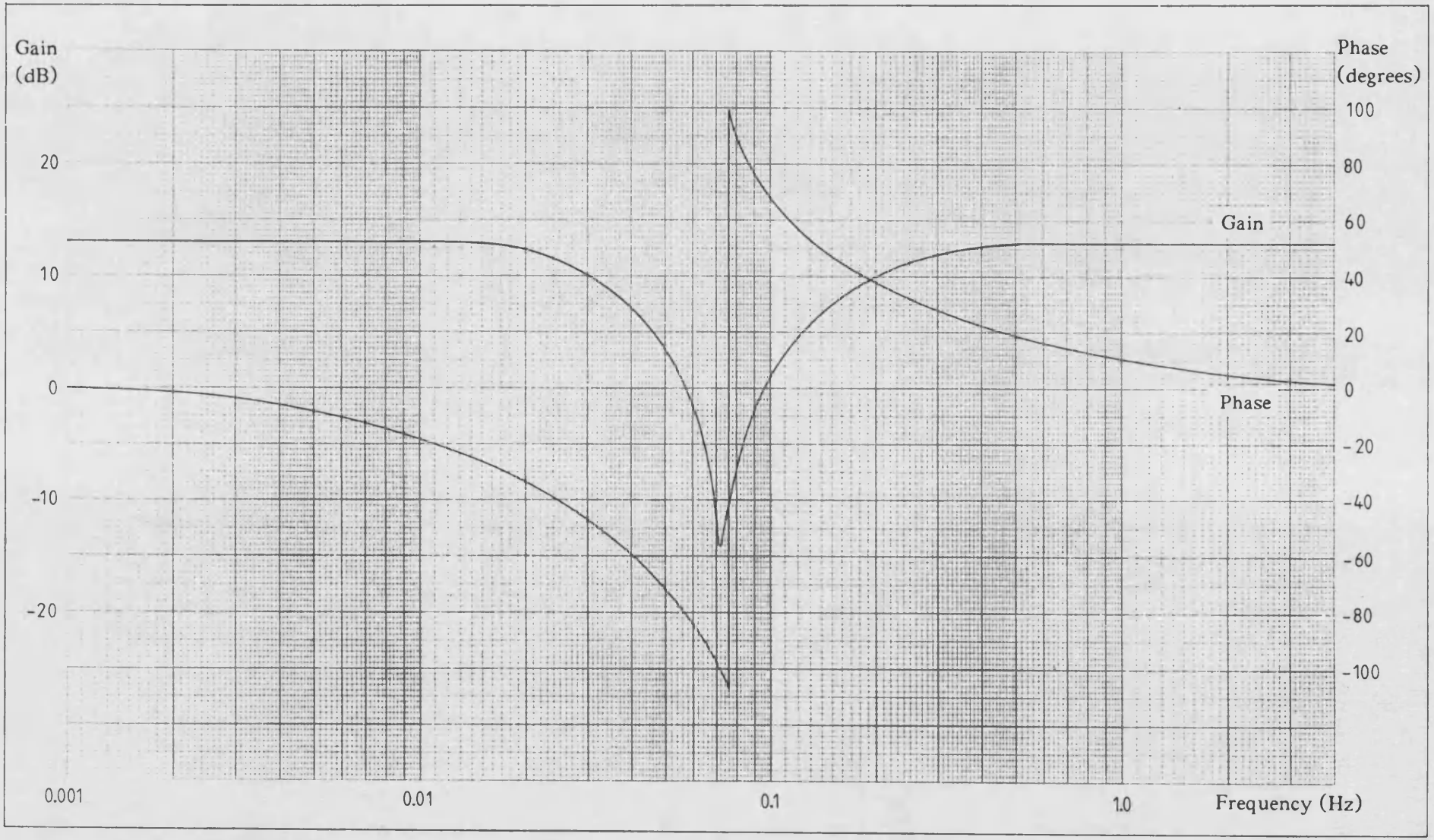

Frequency response of the combined a.c. and d.c. flux signals (calculated) Graph 6.2

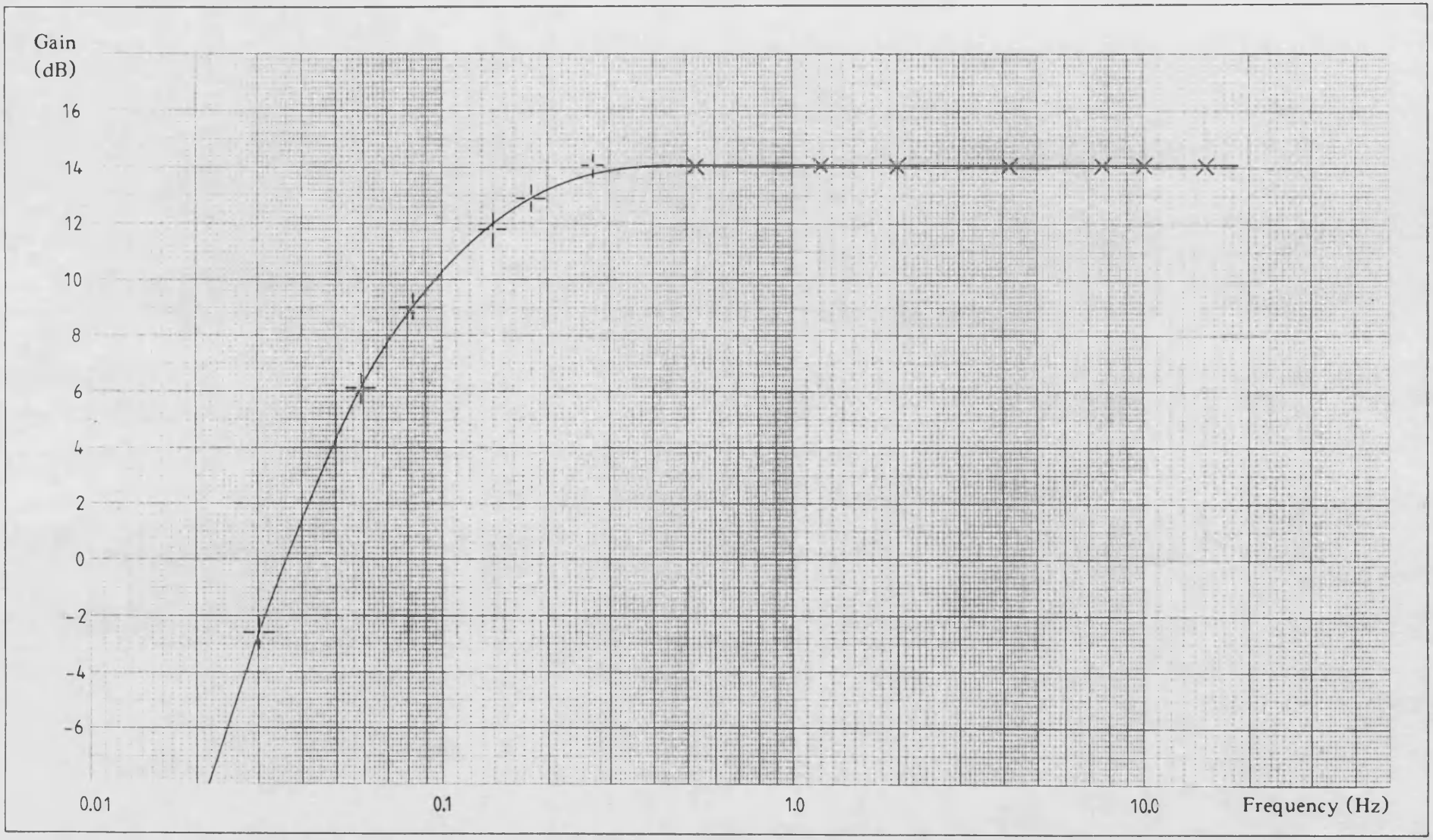

Flux coil/integrator frequency response (measured) Graph 6.3

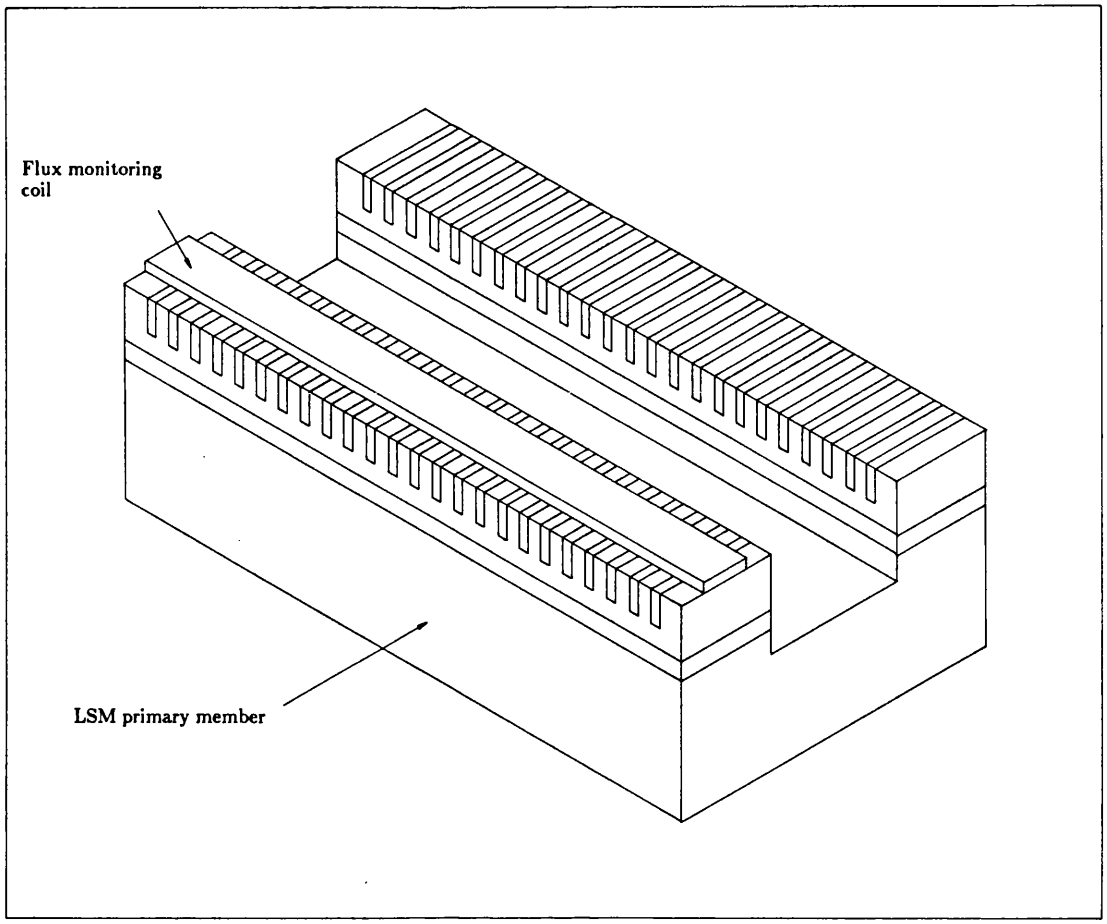

LSM incorporating a flux monitoring coil Figure 6.1

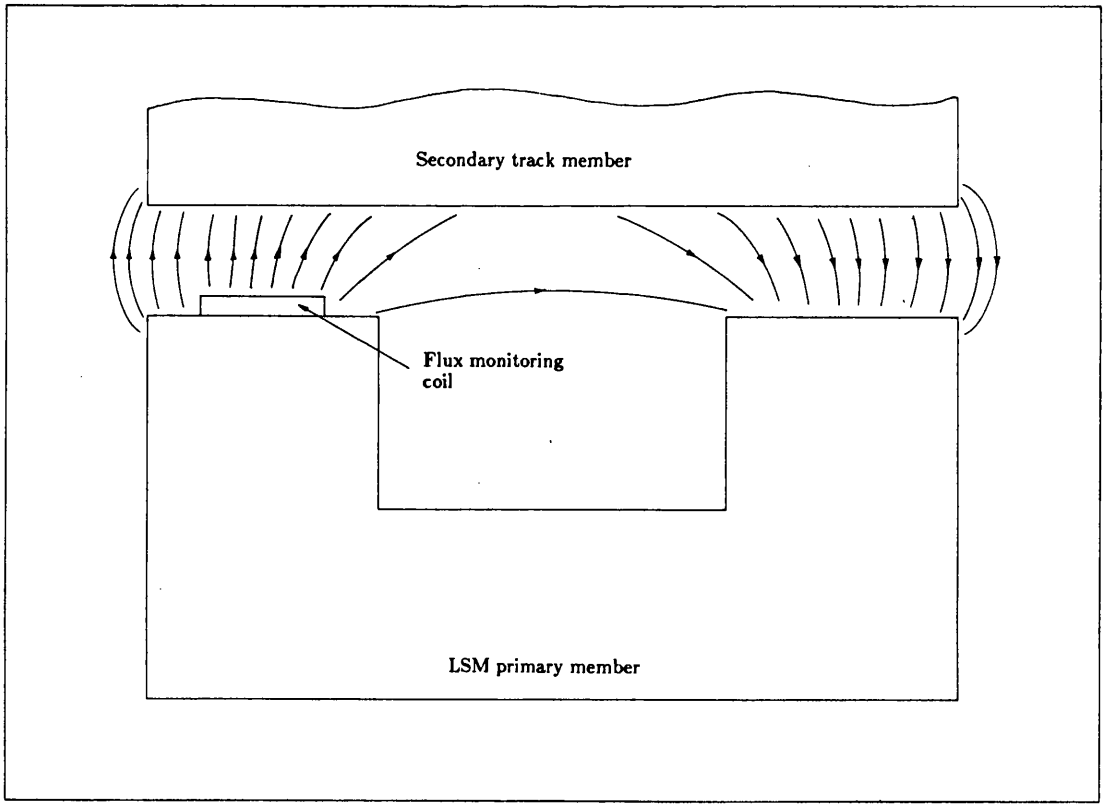

Flux path considerations governing flux coil width Figure 6.2

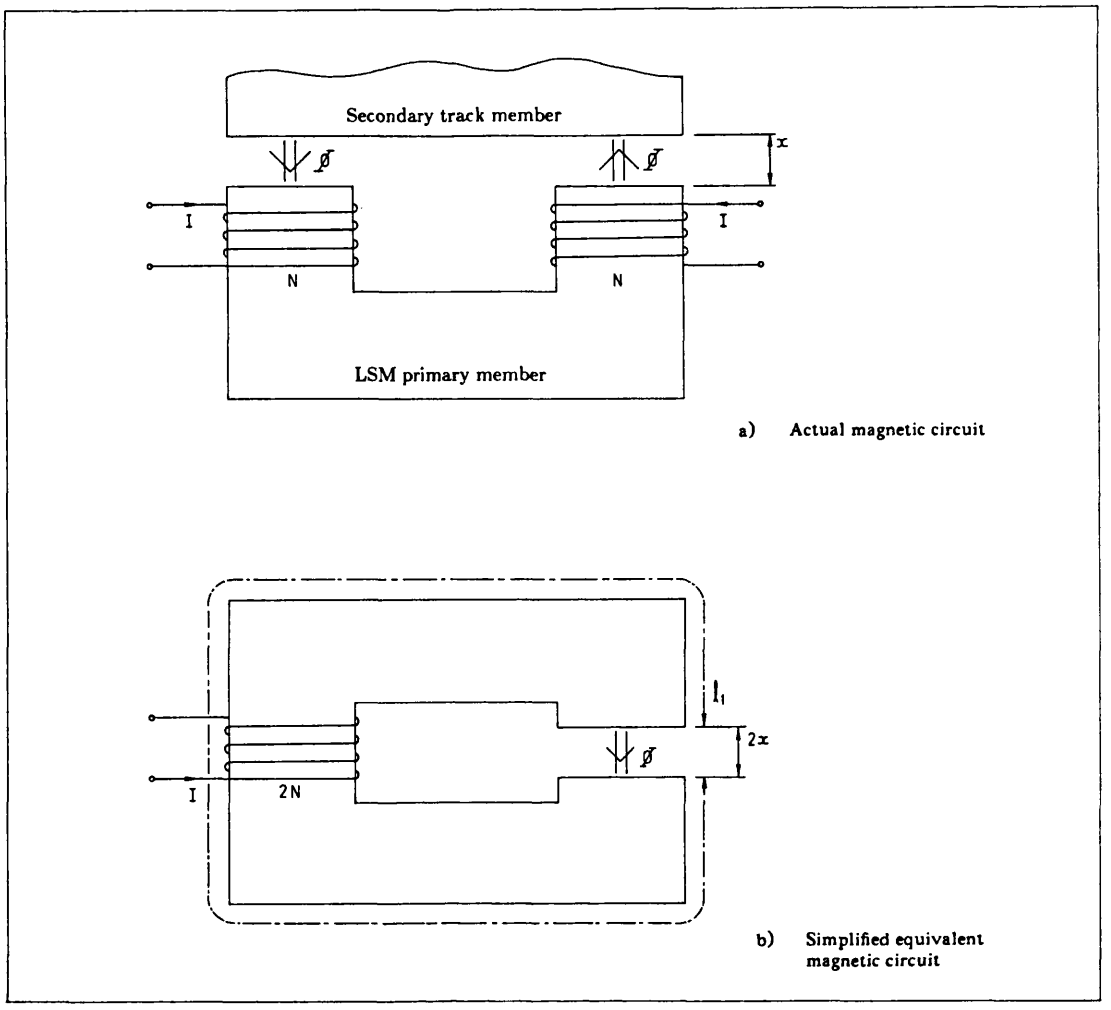

Derivation of a simplified magnetic circuit model Figure 6.3

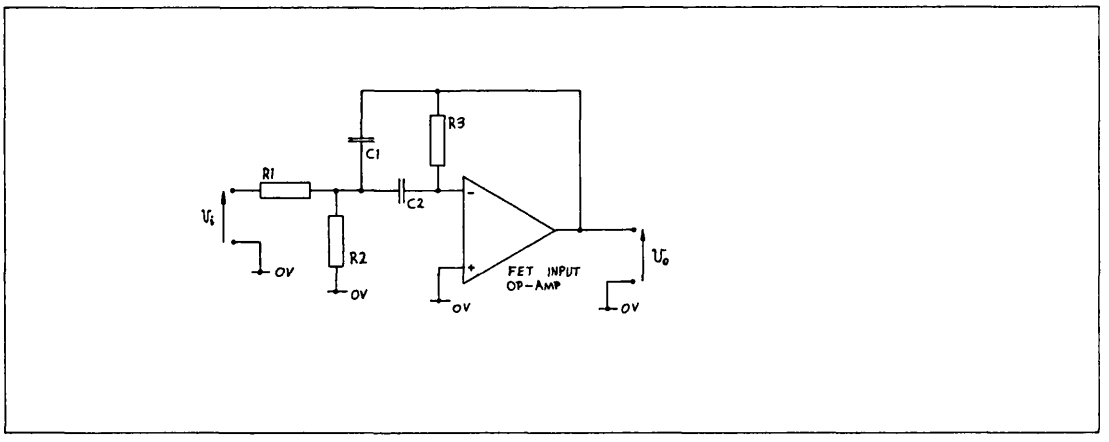

Circuit diagram of the a.c. integrator Figure 6.4

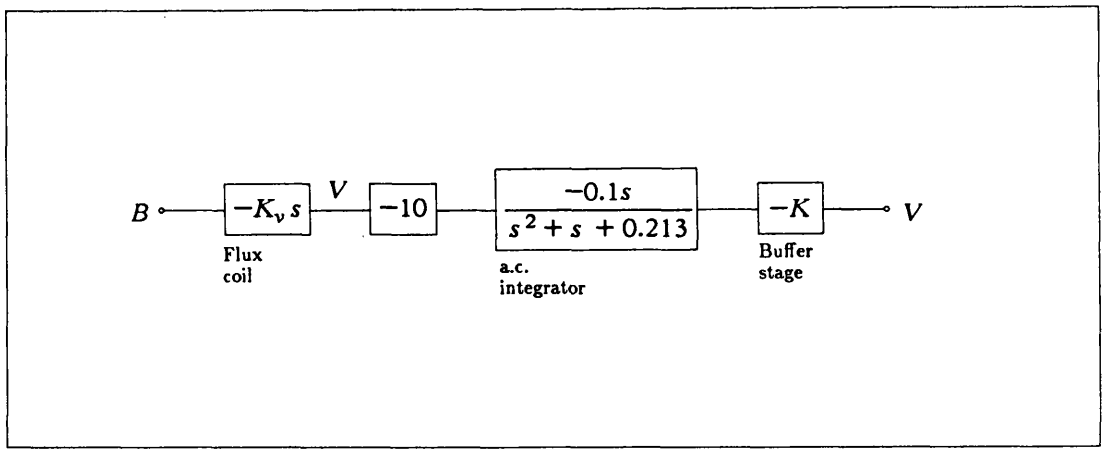

Block diagram of the a.c. flux measurement path Figure 6.5

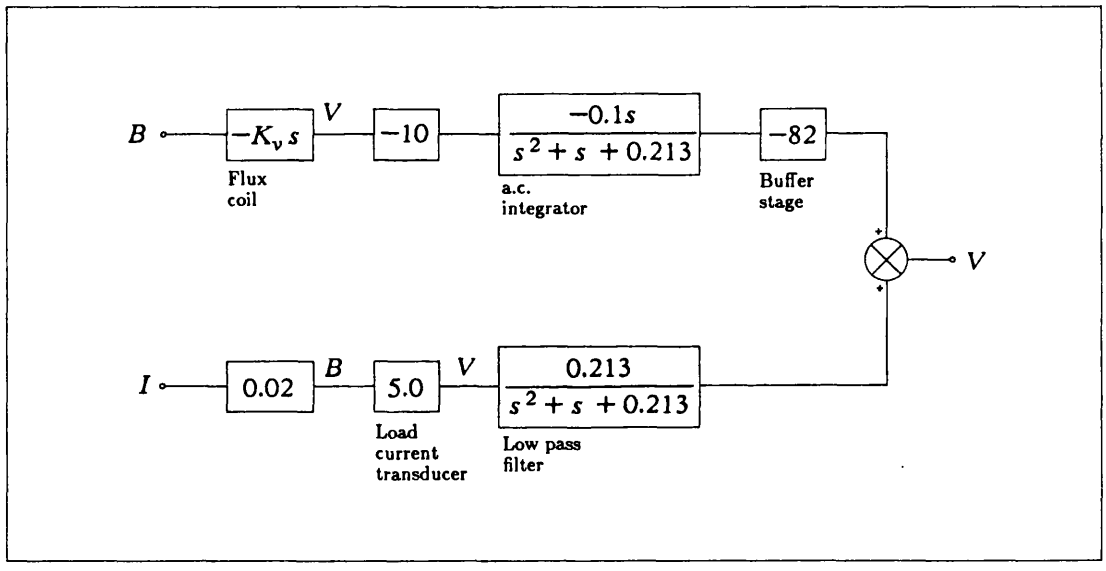

Block diagram of the combined a.c. and d.c. flux measurement paths Figure 6.6

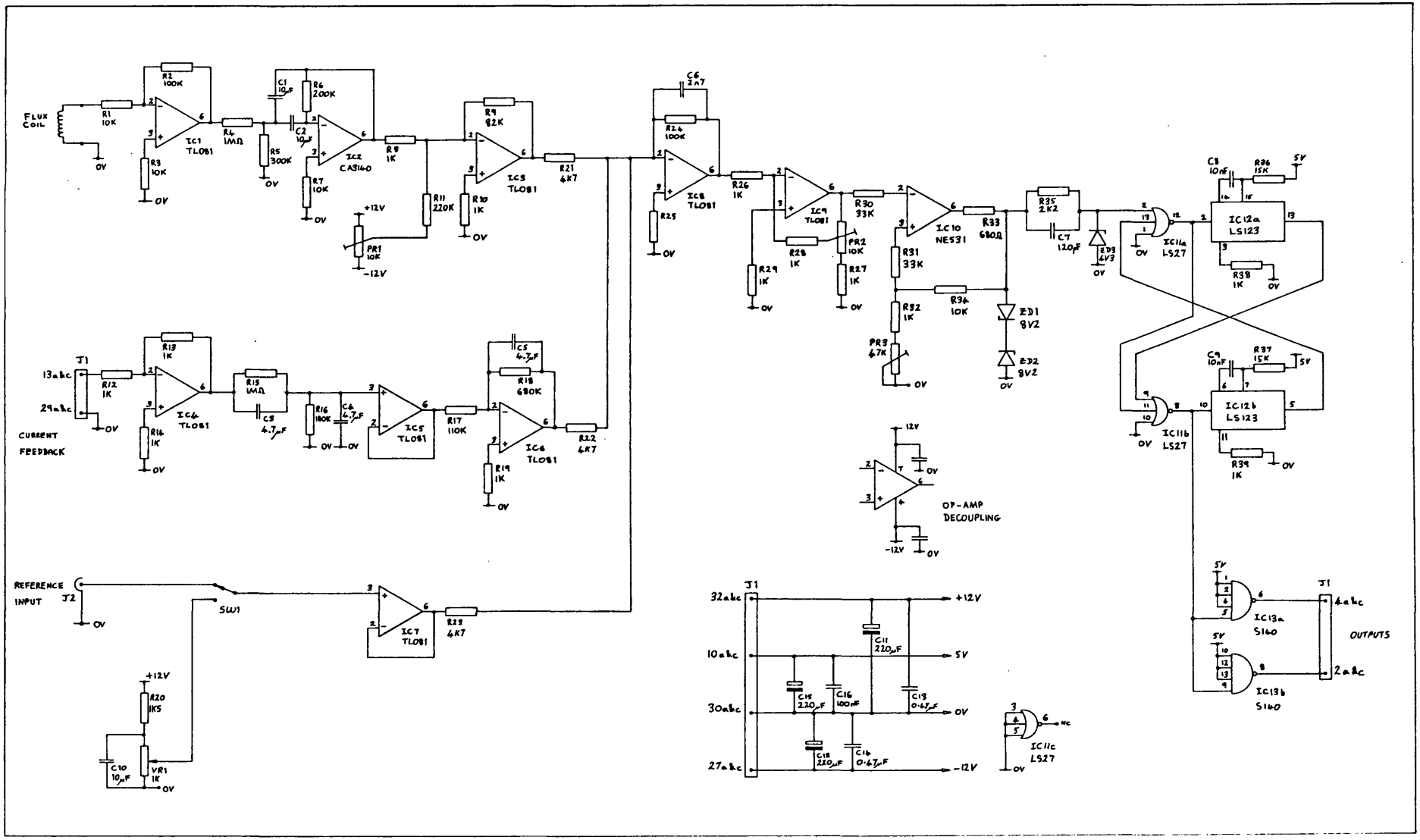

Flux feedback chopper control card circuit diagram Figure 6.7

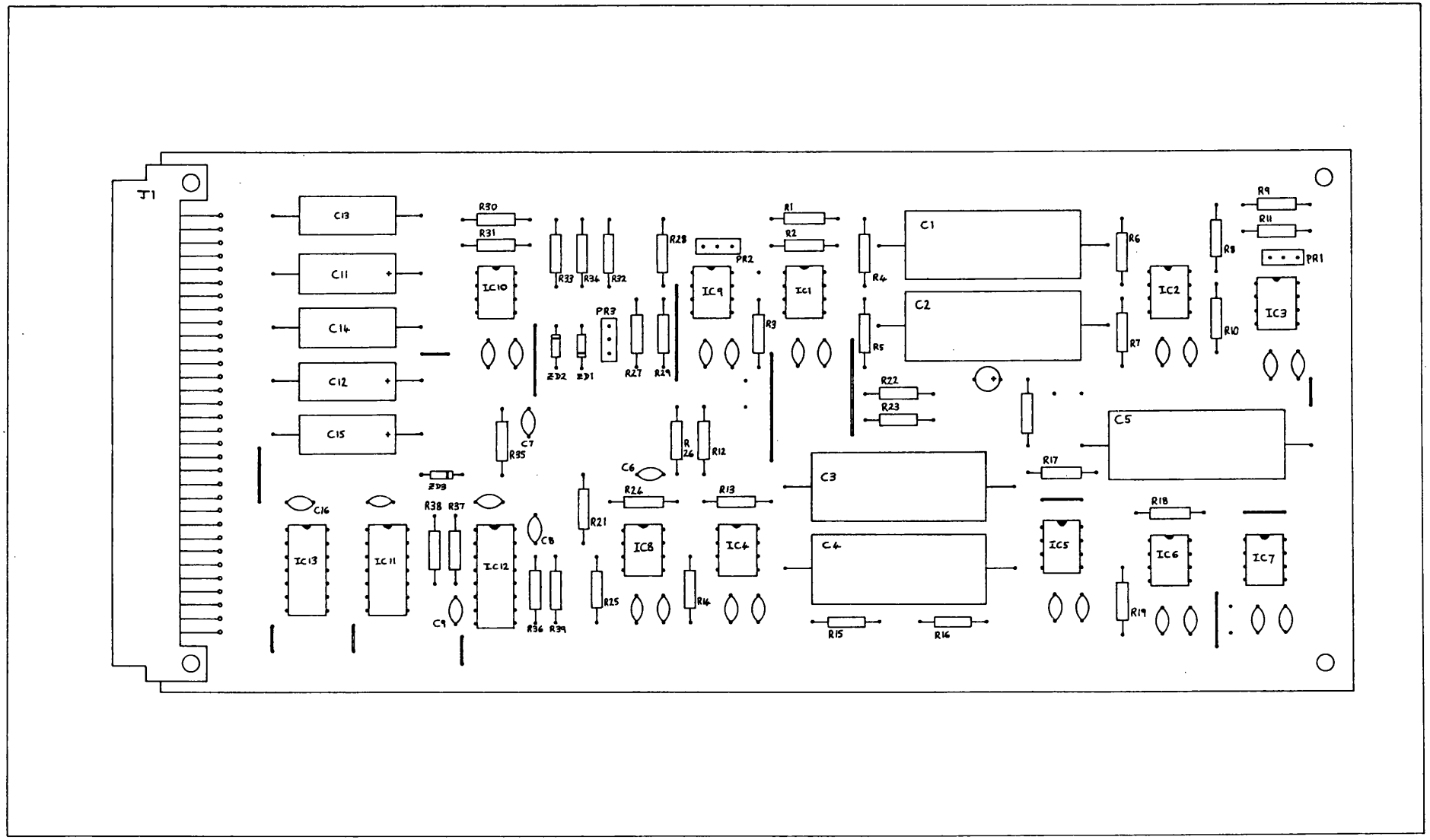

Flux feedback chopper control card component layout

Figure 6.8

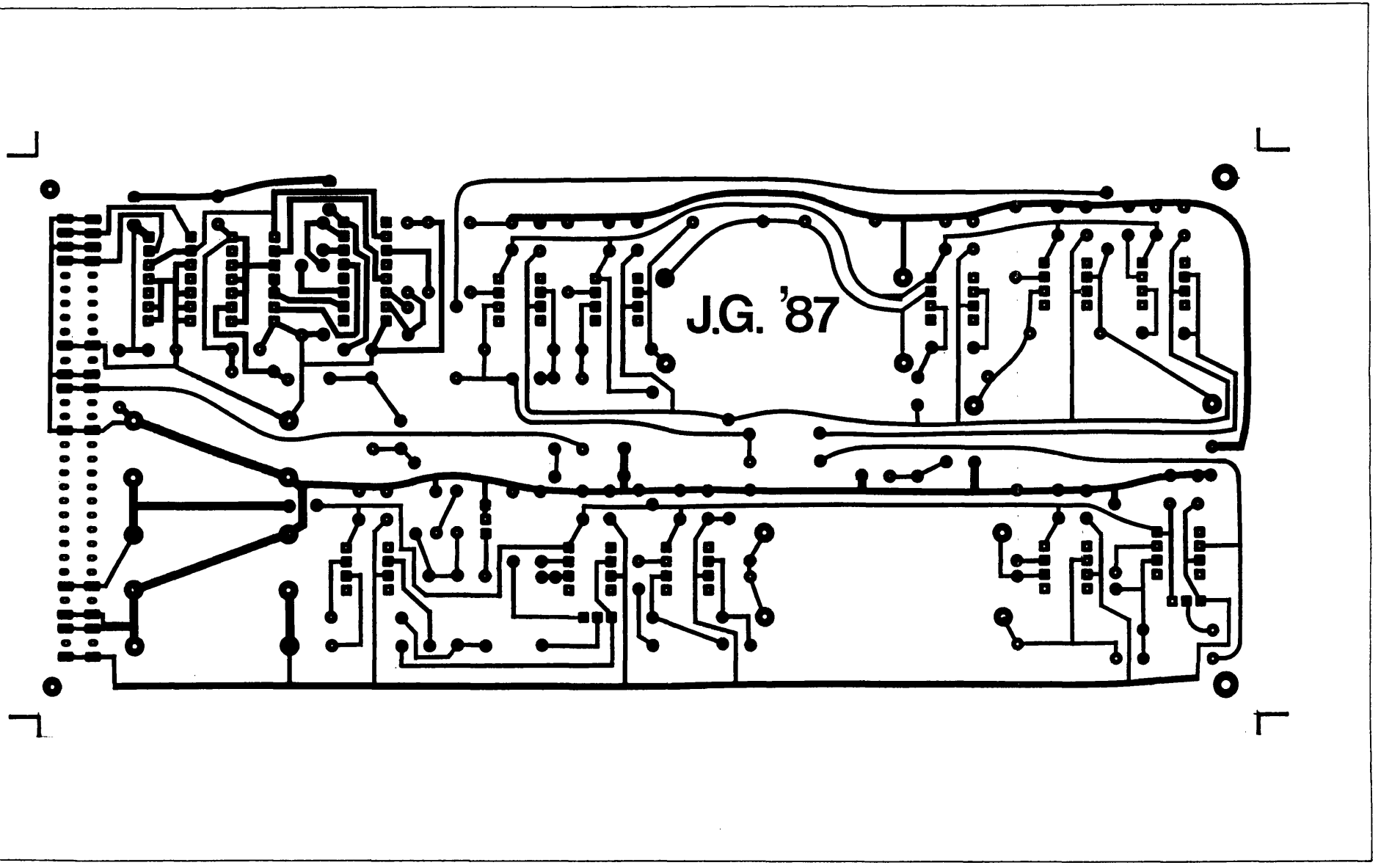

Flux feedback chopper control card pcb artwork Figure 6.9

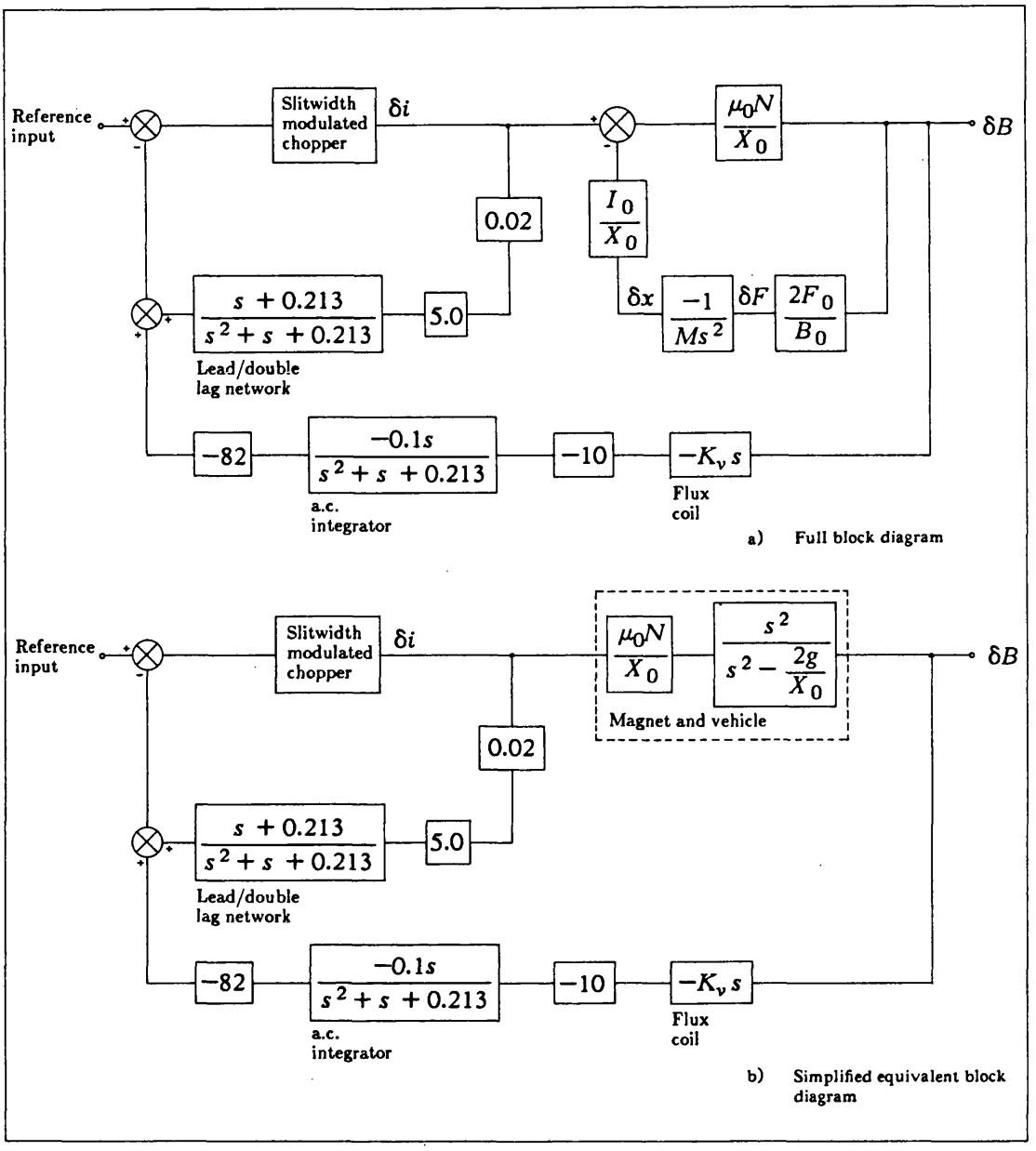

Block diagram of a flux controlled magnet Figure 6.10

7. The design and implementation of a levitation controller using flux feedback choppers

The levitation controller designed previously in chapter 5 was adapted to use the flux feedback choppers developed in chapter 6 in place of the original current feedback choppers. A detailed description of the design and implementation of this controller will now be given.

7.1 Control strategy

A block diagram of the control strategy used for each of the levitation modes is provided in figure 7.1. Although in the general form illustrated the control strategy is identical to that used in chapter 5, it will be shown that the model of the magnet and vehicle combination for each of the four levitation modes is much simplified when flux feedback choppers are used. This is because force actuators using flux controlled magnets do not exhibit the gap dependent gain characteristic of the original current controlled magnets used in chapter 5. It will also be shown that the combination of the chopper linearisation pole with the magnet and vehicle model gives a third order plant, hence there are three states available for feedback - position, velocity and acceleration.

Note that because the side modes retained the use of current controlled magnets, the lateral and yaw mode controllers of chapter 5 were used as before to provide side control for the vehicle.

7.2 Transducer gains

The values of gap transducer gain K_g and accelerometer gain K_a were derived in chapter 5 (equations 5.1 and 5.2 respectively).

7.2.1 Chopper gain The chopper gain K_c was defined previously in section 2.8 as the overall resolution of a D to A converter channel when combined with one of the original current feedback choppers. When using the flux feedback choppers, which have a nominal gain of 0.2 T/V, the new value of K_c was calculated as follows (recall that

each DAC channel has an output resolution of 0.02 V/lsb).

$$K_c = 0.2\,T/V \times 0.02\,V/lsb$$

$$= 4\times10^{-3}\,T/lsb$$

or

$$K_c = \frac{1}{250} \qquad \text{equation 7.1}$$

7.3 Force actuator model

Using the flux feedback choppers, the levitation controller outputs were required in the form of a flux density demand signal δB for each mode. Hence a small signal linearised force actuator model was required to relate variations in motor force, δF, to motor flux density variations, δB.

7.3.1 General model The general expression for the force F exerted by an electromagnet is given in equation 7.2 below,

$$F = \frac{B^2 A}{2\mu_0} \qquad \text{equation 7.2}$$

Because the relationship between force and flux density is non-linear, it was necessary to linearise equation 7.2 about a working point B_0,

$$\left.\frac{\partial F}{\partial B}\right|_{B_0} = 2\frac{B_0 A}{2\mu_0}$$

$$= \frac{2}{B_0}\frac{B_0^2 A}{2\mu_0}$$

$$= 2\frac{F_0}{B_0} \qquad \text{equation 7.3}$$

Hence

$$\delta F = K_m\,\delta B \qquad \text{equation 7.3}$$

where K_m is the motor constant,

$$K_m = 2\frac{F_0}{B_0} \qquad \text{equation 7.4}$$

The constant F_0 is the force exerted by each motor at the working point flux density, B_0.

$$F_0 = \frac{Mg}{4} \qquad \text{equation 7.5}$$

Re-arranging equation 7.2 and using equation 7.5 a general expression for the motor constant K_m was derived as follows.

$$\begin{aligned} K_m &= 2\frac{F_0}{B_0} \\ &= 2\frac{Mg}{4}\left\{\frac{4A}{2\mu_0 Mg}\right\}^{\frac{1}{2}} \\ &= \left\{\frac{MgA}{2\mu_0}\right\}^{\frac{1}{2}} \end{aligned} \qquad \text{equation 7.6}$$

7.3.2 Levitation motor model The value of K_m for the levitation motors was derived using the motor parameters outlined in appendix A and the vehicle mass defined in appendix D.

$$\begin{aligned} K_m &= \left\{\frac{MgA}{2\mu_0}\right\}^{\frac{1}{2}} \\ &= \left\{\frac{390 \times 9.81 \times 11.28\times10^{-3}}{2 \times 4\pi\times10^{-7}}\right\}^{\frac{1}{2}} \\ &= 4143.8\ N/T \end{aligned} \qquad \text{equation 7.7}$$

Now in each of the levitation modes, the total force δF_{mode} is derived from four motors such that,

$$\begin{aligned} \delta F_{mode} &= 4\delta F \\ &= 4K_m\,\delta B \\ &= 16.575\times10^3\delta B \end{aligned} \qquad \text{equation 7.8}$$

Equation 7.8 is the linearised small signal force actuator model used in the design of the levitation mode controllers. To illustrate the design procedure, the heave mode controller will now be considered in detail.

7.4 The heave mode controller

7.4.1 Magnet and vehicle in the heave mode The force actuator (equation 7.8) and vehicle heave model were combined as shown in figure 7.2a. The transfer function of the overall magnet and vehicle combination in the heave mode was then written down as follows.

$$\frac{\delta x_H}{\delta B} = \frac{-42.5}{s^2} \qquad \text{equation 7.9}$$

7.4.2 Heave controller design Equation 7.9 was substituted into the general controller block diagram discussed in section 7.1 to produce the heave controller block diagram of figure 7.2b. The characteristic equation of the heave controller was then shown to be.

$$s^4 + s^3P(1 + 0.85K_a h_2) + 0.85K_a h_1 Ps^2 + 0.85K_g h_0 Ps + 0.85KK_g P = 0 \qquad \text{equation 7.10}$$

The controller gains K, h_0, h_1 and h_2 were then set by comparing the coefficients of this characteristic equation with the standard fourth order form given below.

$$(s^2 + 2\zeta_1\omega_{n_1}s + \omega_{n_1}^2)(s^2 + 2\zeta_2\omega_{n_2}s + \omega_{n_2}^2) = 0$$

Expanding.

$$s^4 + s^3(2\zeta_1\omega_{n_1} + 2\zeta_2\omega_{n_2}) + s^2(\omega_{n_1}^2 + \omega_{n_2}^2 + 4\zeta_1\zeta_2\omega_{n_1}\omega_{n_2}) + s(2\zeta_1\omega_{n_1}\omega_{n_2}^2 + 2\zeta_2\omega_{n_2}\omega_{n_1}^2) + \omega_{n_1}^2\omega_{n_2}^2 = 0$$

Equating coefficients.

$$2\zeta_1\omega_{n_1} + 2\zeta_2\omega_{n_2} = P(1 + 0.85K_a h_2) \qquad \text{equation 7.11}$$

$$\omega_{n_1}^2 + \omega_{n_2}^2 + 4\zeta_1\zeta_2\omega_{n_1}\omega_{n_2} = 0.85K_a h_1 P \qquad \text{equation 7.12}$$

$$2\zeta_1\omega_{n_1}\omega_{n_2}^2 + 2\zeta_2\omega_{n_2}\omega_{n_1}^2 = 0.85K_g h_0 P \qquad \text{equation 7.13}$$

$$\omega_{n_1}^2\omega_{n_2}^2 = 0.85KK_g P \qquad \text{equation 7.14}$$

where

$$K_a = 50$$

$K_g = 250000$

$P = 22$

For comparison with the controller developed in chapter 5, the same values of ω_n and ζ were used.

$\zeta_1 = 0.5, \quad \omega_{n_1} = 15$

$\zeta_2 = 1.0, \quad \omega_{n_2} = 100$

Substituting the above values into equations 7.11 through 7.14 inclusive,

$215 = 22(1 + 42.5h_2)$

$13225 = 934.9h_1$

$195000 = 4.67\times10^6 h_0$

$2.25\times10^6 = 4.67\times10^6 K$

giving

$h_0 = 0.04172$

$h_1 = 14.14$

$h_2 = 0.206$

$K = 0.4814$

7.5 Roll, pitch and twist mode controllers

7.5.1 The roll mode controller The force actuator and vehicle roll model were combined as shown in figure 7.3a. The transfer function of the overall magnet and vehicle combination in the roll mode was then written down as follows,

$$\frac{\delta x_R}{\delta B} = \frac{-62.7}{s^2}$$

The roll mode controller using this model is shown in the block diagram of figure 7.3b, from which the following characteristic equation was derived,

$$s^4 + s^3P(1 + 1.245K_a h_2) + 1.245K_a h_1 Ps^2 + 1.245K_g h_0 Ps + 1.245KK_g P = 0$$

Substituting values of P, K_a and K_g and comparing coefficients with the standard form,

$$215 = 22(1 + 62.27h_2)$$

$$13225 = 1370h_1$$

$$195000 = 6.85\times10^6 h_0$$

$$2.25\times10^6 = 6.85\times10^6 K$$

giving

$$h_0 = 0.0285$$

$$h_1 = 9.65$$

$$h_2 = 0.141$$

$$K = 0.3285$$

7.5.2 The pitch mode controller The force actuator and vehicle pitch model were combined as shown in figure 7.4a. The transfer function of the overall magnet and vehicle combination in the pitch mode was then written down as follows.

$$\frac{\delta x_P}{\delta B} = \frac{-46.8}{s^2}$$

The pitch mode controller using this model is shown in the block diagram of figure 7.4b, from which the following characteristic equation was derived.

$$s^4 + s^3P(1 + 0.936K_a h_2) + 0.936K_a h_1 Ps^2 + 0.936K_g h_0 Ps + 0.936KK_g P = 0$$

Substituting values of P, K_a and K_g and comparing coefficients with the standard form.

$$215 = 22(1 + 46.8h_2)$$

$$13225 = 1030h_1$$

$$195000 = 5.15\times10^6 h_0$$

$$2.25\times10^6 = 5.15\times10^6 K$$

giving

$$h_0 = 0.0379$$

$$h_1 = 12.84$$

$$h_2 = 0.187$$

$K = 0.4369$

7.5.3 The twist mode controller The force actuator and vehicle twist model were combined as shown in figure 7.5a. The transfer function of the overall magnet and vehicle combination in the twist mode was then written down as follows.

$$\frac{\delta x_T}{\delta B} = \frac{-96.93}{s^2 + s + 7925}$$

The twist mode controller using this model is shown in the block diagram of figure 7.5b, from which the following characteristic equation was derived.

$$s^4 + s^3(1 + P + 1.9387K_a h_2 P) + s^2(P + 7925 + 1.9387K_a h_1 P) + sP(7925 + 1.9387K_g h_0) + 1.9387KK_g P = 0$$

Substituting values of P, K_a and K_g and comparing coefficients with the standard form,

$$215 = 23 + 2132.5h_2$$

$$13225 = 7947 + 2132.5h_1$$

$$195000 = 22(7925 + 484.67\times10^3 h_0)$$

$$2.25\times10^6 = 10.66\times10^6 K$$

giving

$$h_0 = 1.94\times10^{-3}$$

$$h_1 = 2.475$$

$$h_2 = 0.09$$

$$K = 0.211$$

To implement the levitation controller using flux feedback choppers, the control parameters derived above were substituted into the appropriate levitation mode controllers of the vehicle control software introduced in chapter 5.

7.6 Results

For comparison purposes, the levitation response test and the first set of step response tests discussed below are identical to those carried out with the levitation controller

designed in chapter 5. However the main aim behind the development of the flux feedback chopper was to facilitate the development of an improved levitation controller capable of making full use of the available magnet gap under transient conditions. Hence, to fully test the new controller, a further test was included in which the heave step response was logged at various magnet gaps away from the nominal magnet gap of 7 mm.

The notation mm/magnet (mm per magnet) used on the position-time graphs indicates that the position data has been scaled in terms of individual magnet displacements in millimetres (see section 5.8.1).

7.6.1 Levitation response test Graphs 7.1a through 7.1d inclusive show the position-time responses of the four flux controlled levitation modes (heave, roll, pitch and twist respectively) during the initial vehicle levitation procedure. This procedure always represents the worst case situation likely to be encountered by the levitation controller. There are two main reasons for this,

1. The levitation magnets are initially working well away from the design working point gap of 7 mm.
2. Due to the inevitable differences in magnet parameters and magnet rest gaps, one or two magnets will initially lead or lag the other magnets during the levitation procedure. This causes the vehicle to lift unevenly, introducing significant disturbances to the roll, pitch and twist modes.

This latter point is well illustrated by the roll, pitch and twist mode responses, which also show how quickly the vehicle is levelled out beneath the track during the levitation procedure. Note however that the twist mode exhibits a predominantly first order response, similar to that obtained previously in chapter 5 when the same test was performed using a levitation controller based on current feedback choppers. A discussion regarding the possible nature of the twist mode control problem is given in section 5.8.2.

7.6.2 Step response tests Graphs 7.2 through 7.5 inclusive show the step responses of the heave, roll, pitch and twist modes respectively. Each graph shows the response of all four modes during the test, illustrating the minimal interaction that takes place between these modes.

7.6.3 Heave step response tests at various magnet gaps Graph 7.6 shows the position-time response of the heave mode during a sequence of step response tests carried out at three different magnet gaps. Starting from the nominal magnet gap of 7 mm, the vehicle is first raised by 2 mm to give a gap of 5 mm.* The vehicle is then lowered back to the nominal gap, and then lowered by a further 2 mm to give a gap of 9 mm (note that the magnet rest gap is 10 mm). Finally the vehicle is again raised to end the step response test at the nominal gap.

The graph clearly shows that the second order dominated step response characteristic of the heave mode is maintained throughout the available magnet gap. This is in contrast to the levitation controller used in chapter 5, which was unable to reliably accommodate such large gap excursions because the corresponding gain variations in the current controlled magnets would cause instability.

7.6.4 The heave mode flux density demand Graph 7.7 shows the heave mode flux density demand during the heave step response test discussed above in section 7.6.3.

This graph was included to illustrate the way in which the controller adjusts the average or d.c. level of the flux density demand signal in order to compensate for variations in the d.c. gain of the flux feedback choppers when working at a sustained magnet gap other than the nominal magnet gap of 7 mm. These variations occur because the d.c. gain of the flux feedback choppers is derived from the magnet current

---

* A lower gap limit of 5 mm was necessary because the flux monitoring coils positioned on the surface of one limb of each magnet had a depth of 3.5 mm, thus reducing the available airgap. Future versions of the LSM's would avoid this problem by incorporating the flux monitoring coil into the magnet surface at the time of manufacture.

(see section 6.5) and is only a valid representation of the flux density at the nominal magnet gap. With reference to the corresponding step response, it can be seen that the overall characteristics of the levitation controller are not influenced by this effect. There are two main reasons for this,

1. The controller can easily follow the low frequency gain variations
2. The a.c. gain of the flux feedback chopper, which is independent of absolute gap, has an extremely low cutoff frequency of 0.14 Hz (-3 dB point, see section 6.4.1).

7.7 Conclusions

The main aim of this chapter was to show that the flux feedback choppers developed in chapter 6 could be incorporated into a levitation controller design to enable the vehicle to make full use of the available magnet gap under transient conditions. The requirement for better use of the magnet gap was established in chapter 5, in which a controller based on current feedback choppers was shown to be unable to reliably accommodate large gap excursions due to the gap dependent gain of the current controlled magnets. This problem is eliminated when flux controlled magnets are used because the variations in magnet current required to cope with gap fluctuations are contained entirely within the choppers flux feedback path.

This point was reflected in the form of the linearised small signal force actuator model derived in section 7.3 (equation 7.8), which was shown to be a constant gain with no gap dependent term. The experimental results presented in section 7.6.3 clearly show that the controller design based on this force actuator model would maintain a good second order dominated response at both the upper and lower limits of the available magnet gap, in addition to the nominal magnet gap.

Now it was shown previously in chapter 6 (section 6.8) that the low frequency d.c. gain of the flux feedback choppers would be correct only at the nominal magnet gap of 7 mm, and would vary accordingly if other magnet gaps were sustained for any

appreciable length of time (i.e. seconds). The experimental results presented in section 7.6.4 show that, in practice, the levitation controller could easily track these low frequency gain variations by making minor adjustments to the average flux density demand levels.

In addition, the step response tests carried out in section 7.6.2 compare well with the corresponding results obtained from chapter 5 (see section 5.8.3), thus providing further verification of the vehicle model derived in chapter 4.

To summarise, the flux feedback chopper/magnet combination offers the control design engineer a much improved force actuator which virtually eliminates the gap dependent gain characteristic of the simpler current controlled magnet. This allows the designer to make full use of the available gap when studying the suspension characteristics of the vehicle under levitation control.

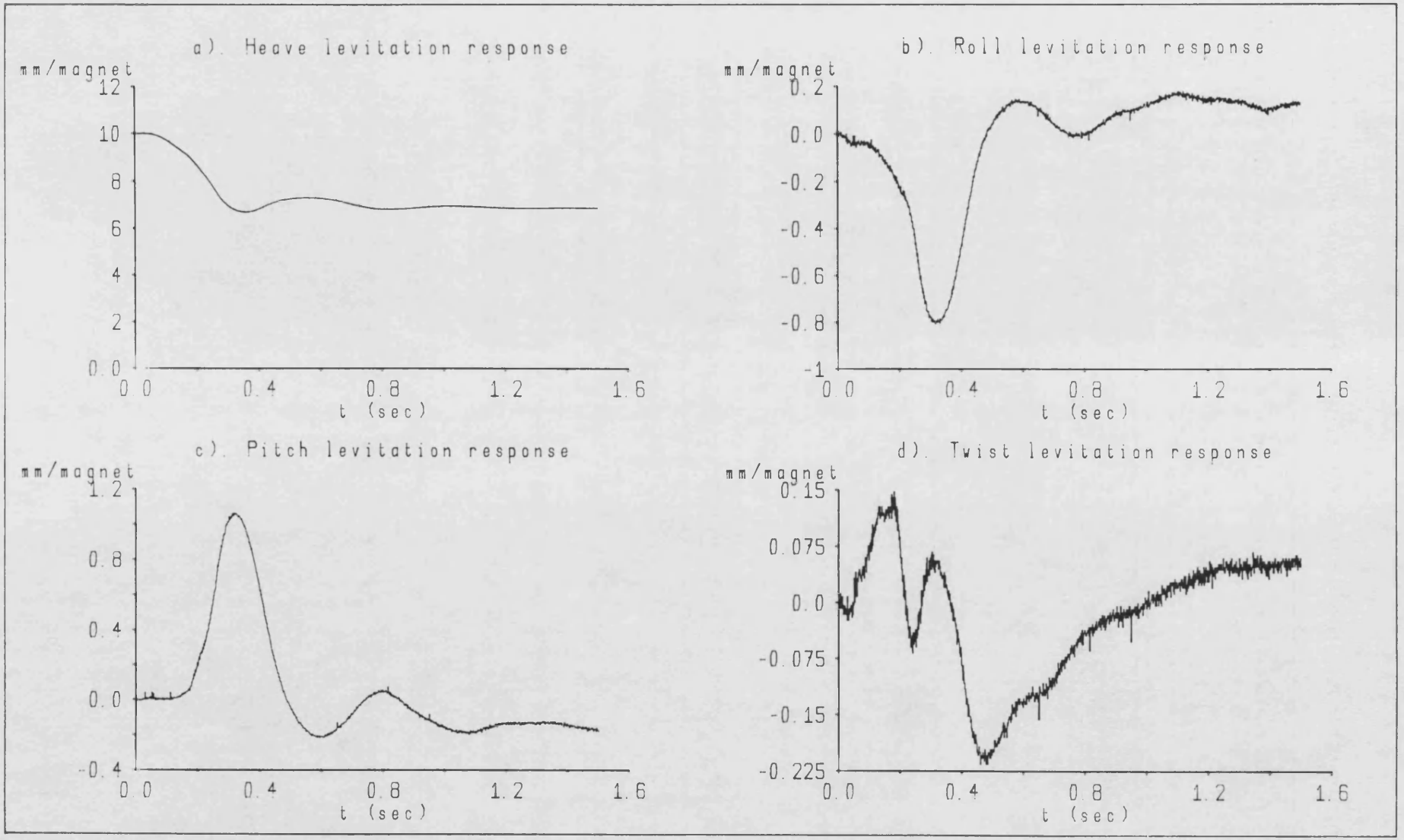

Levitation response Graph 7.1

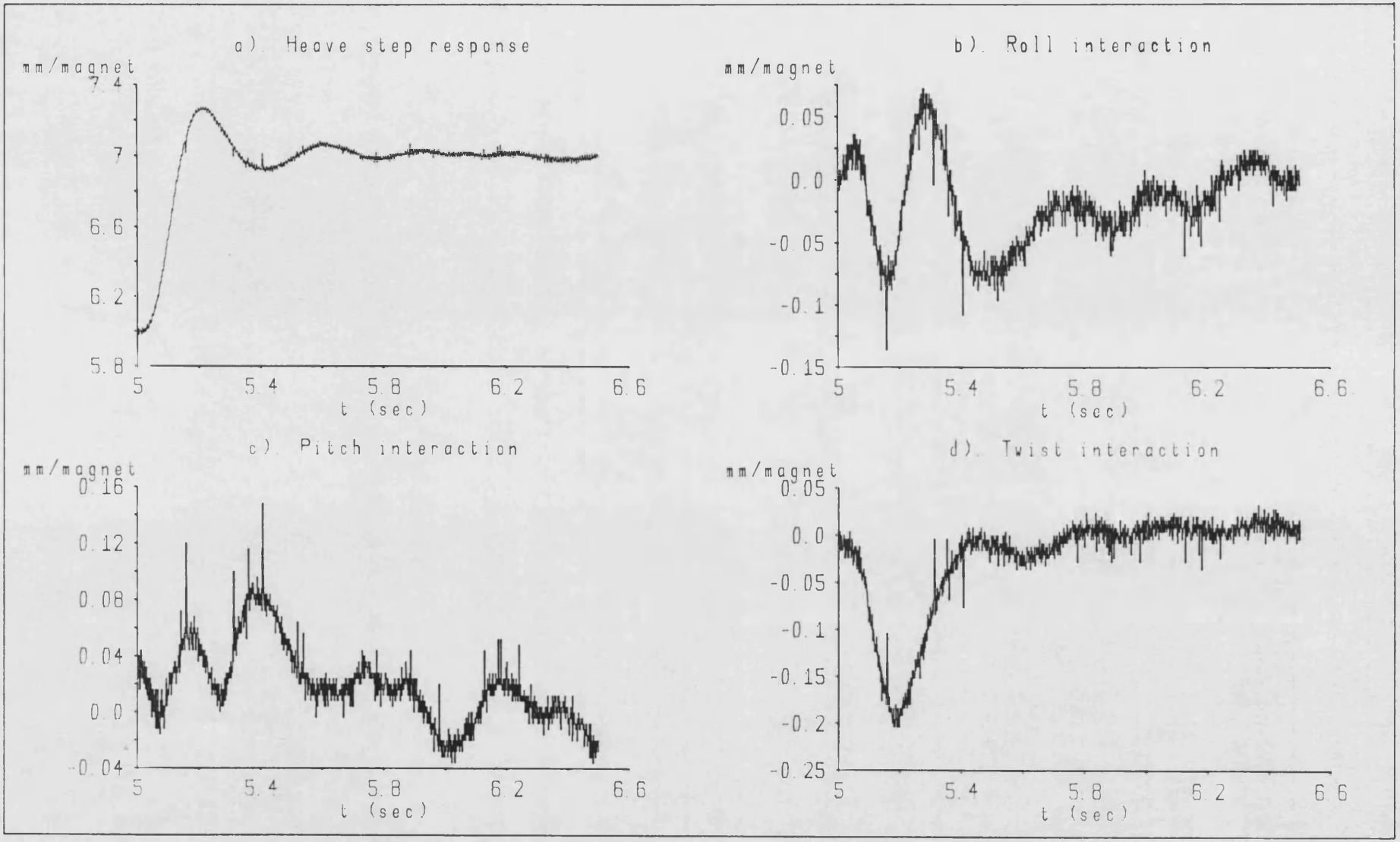

Heave step response Graph 7.2

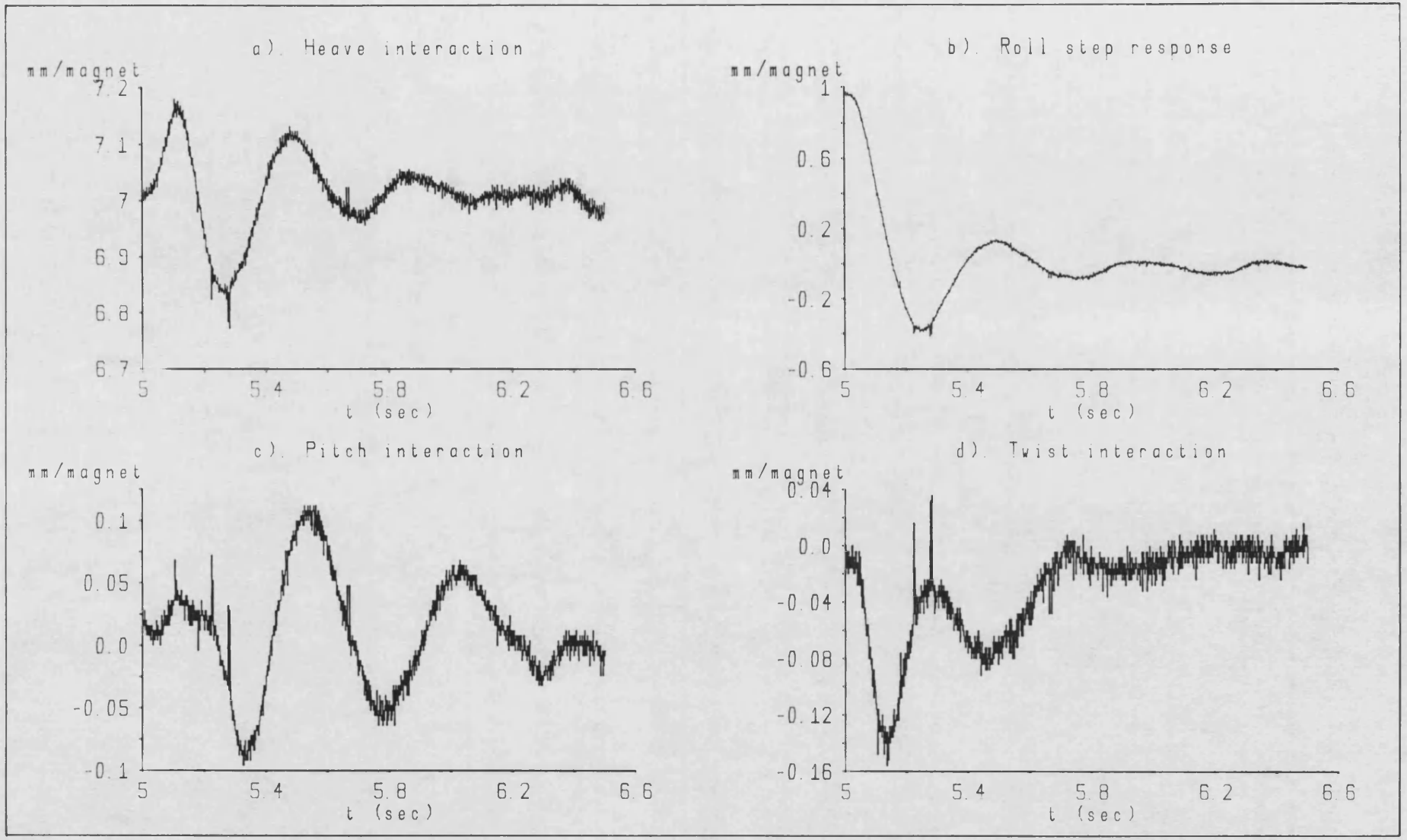

Roll step response Graph 7.3

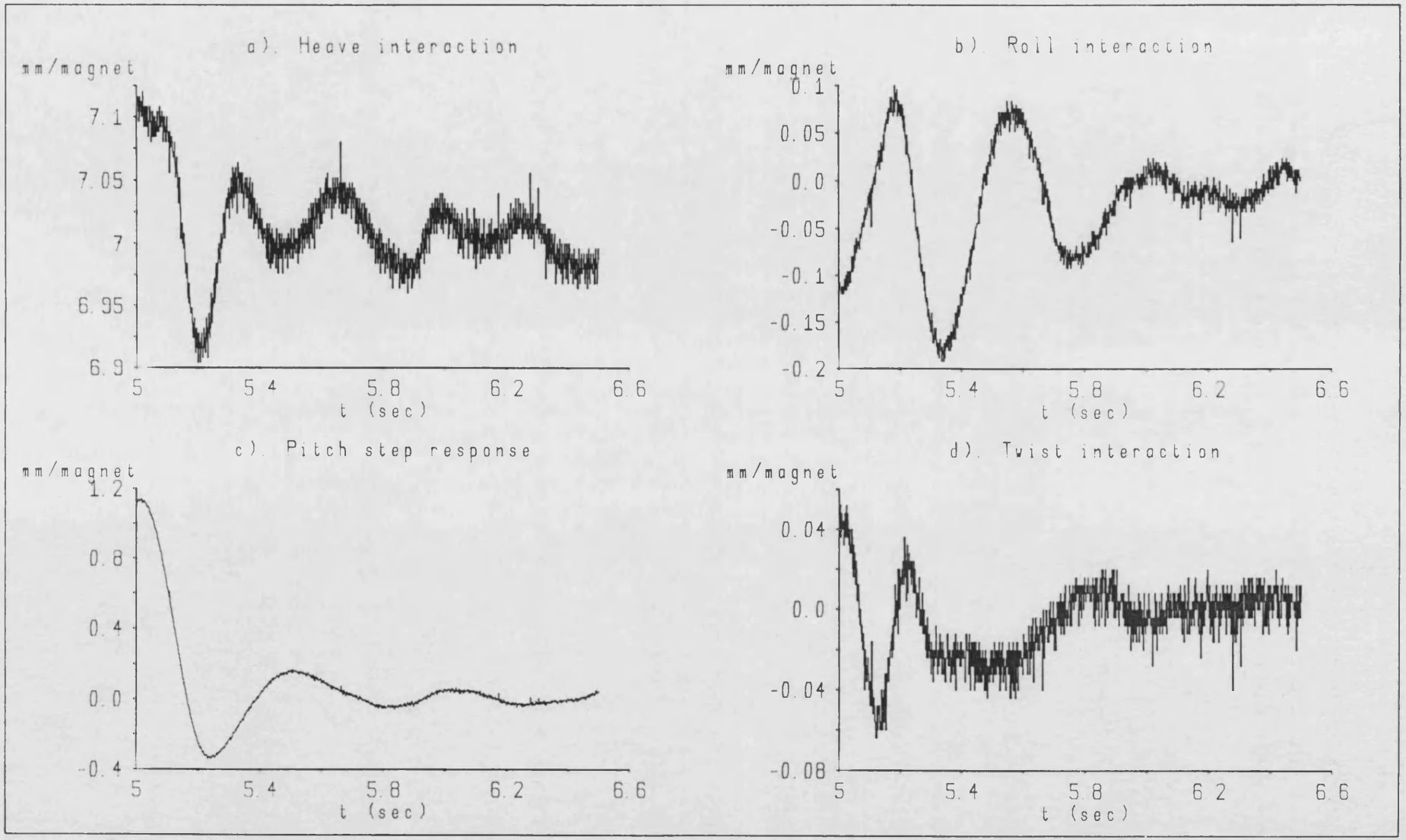

Pitch step response Graph 7.4

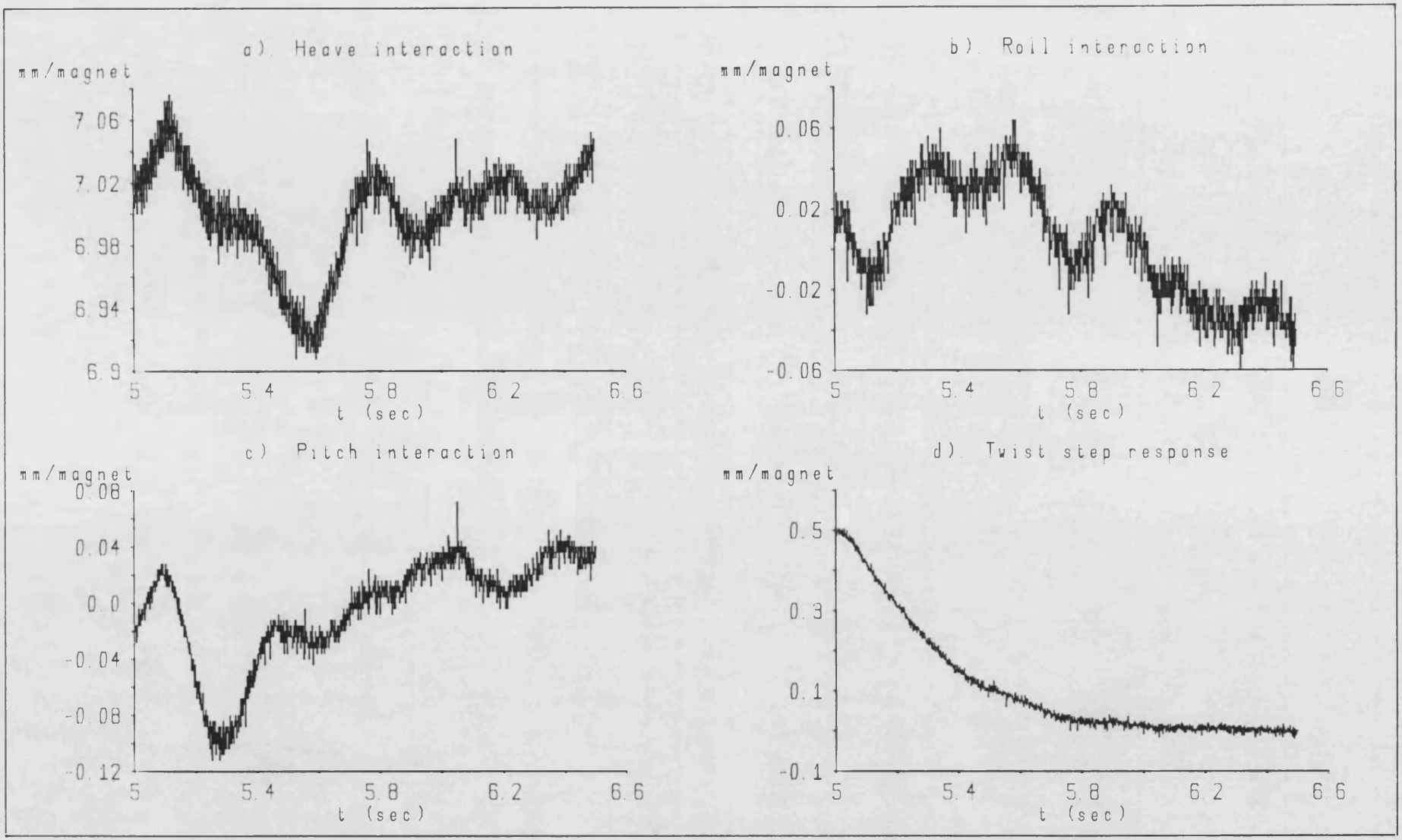

Twist step response Graph 7.5

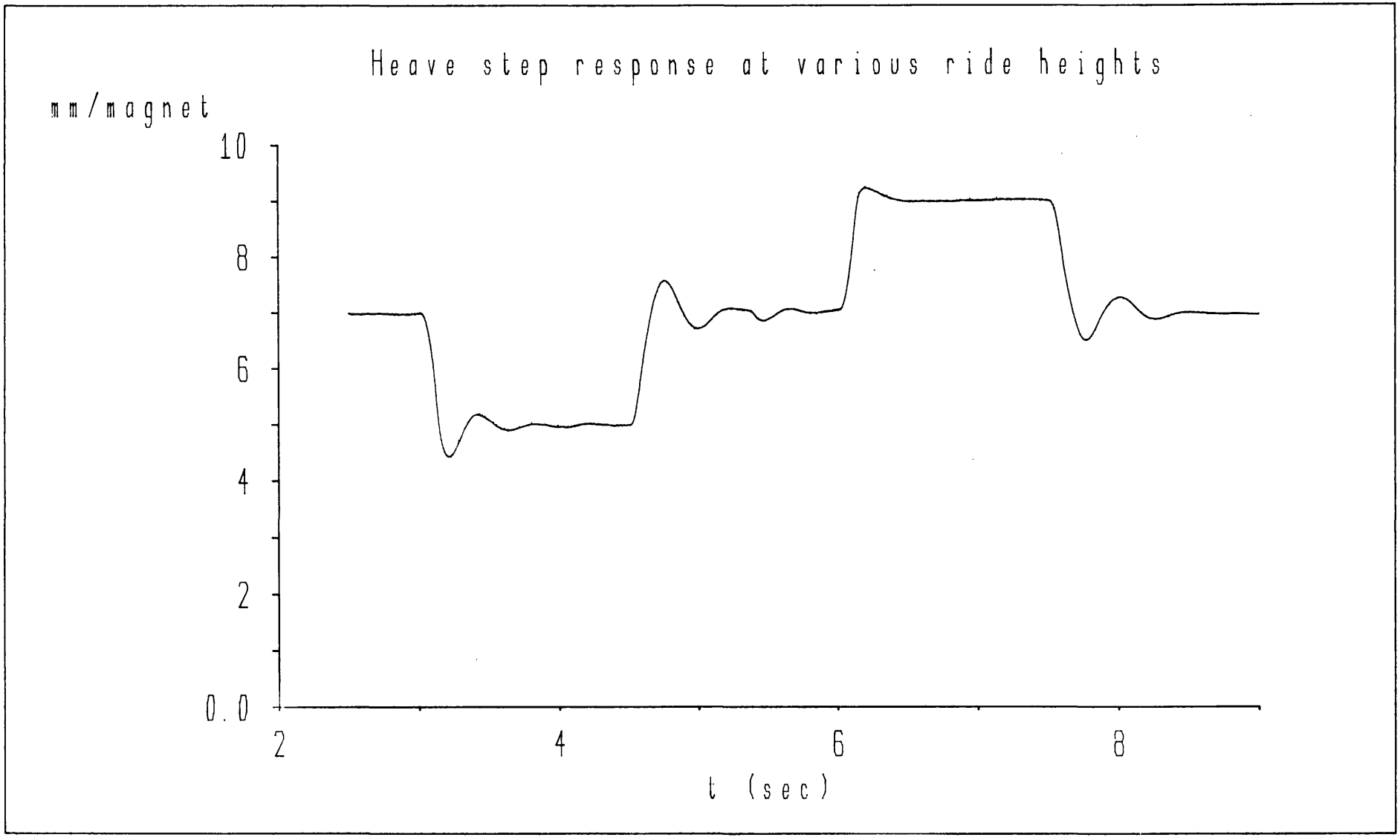

Heave step response at various ride heights Graph 7.6

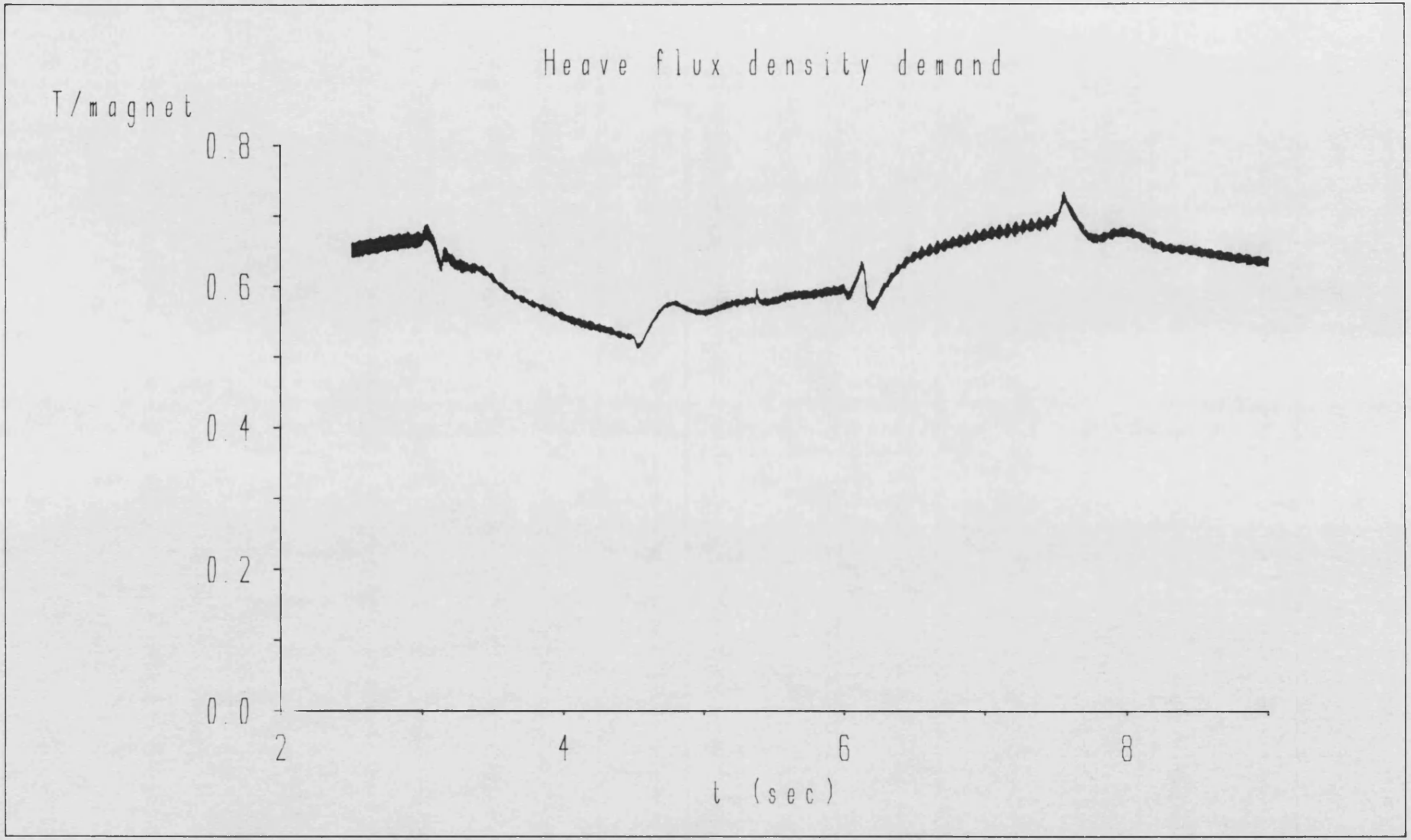

Heave flux density demand Graph 7.7

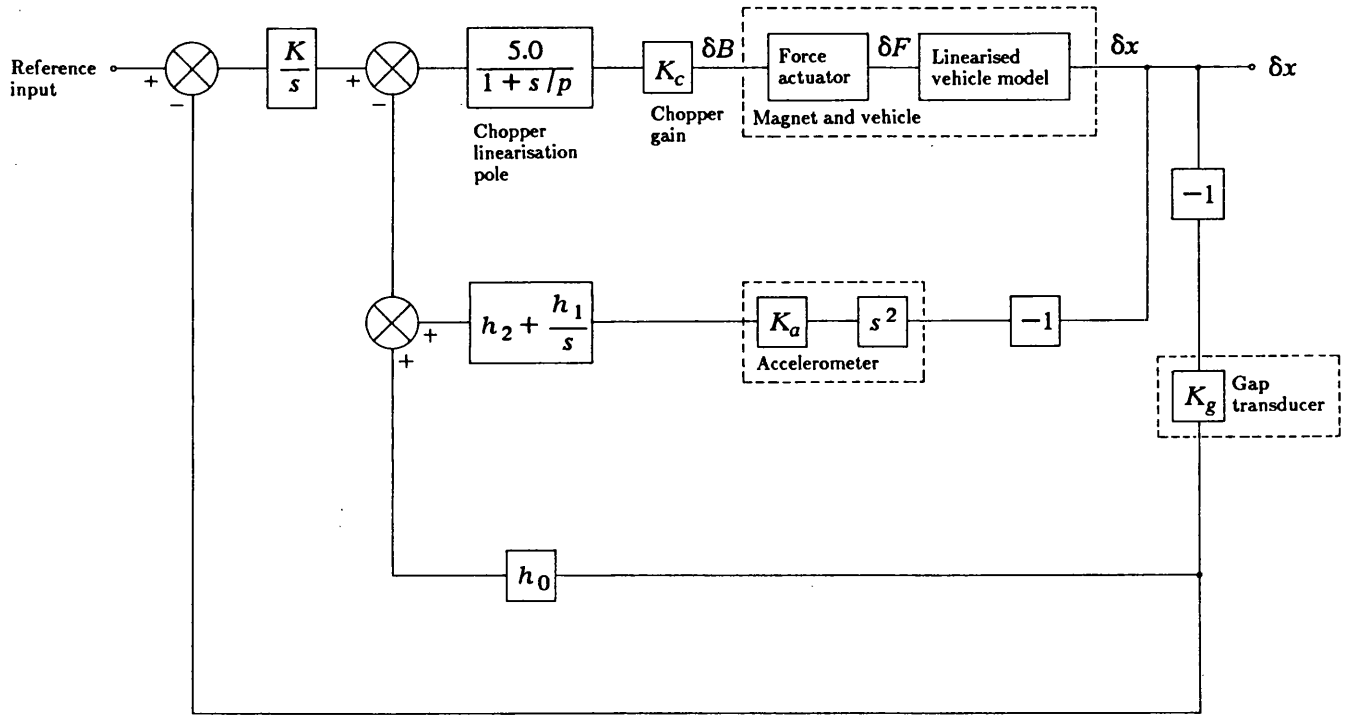

Control strategy for the levitation controller using flux feedback choppers

Figure 7.1

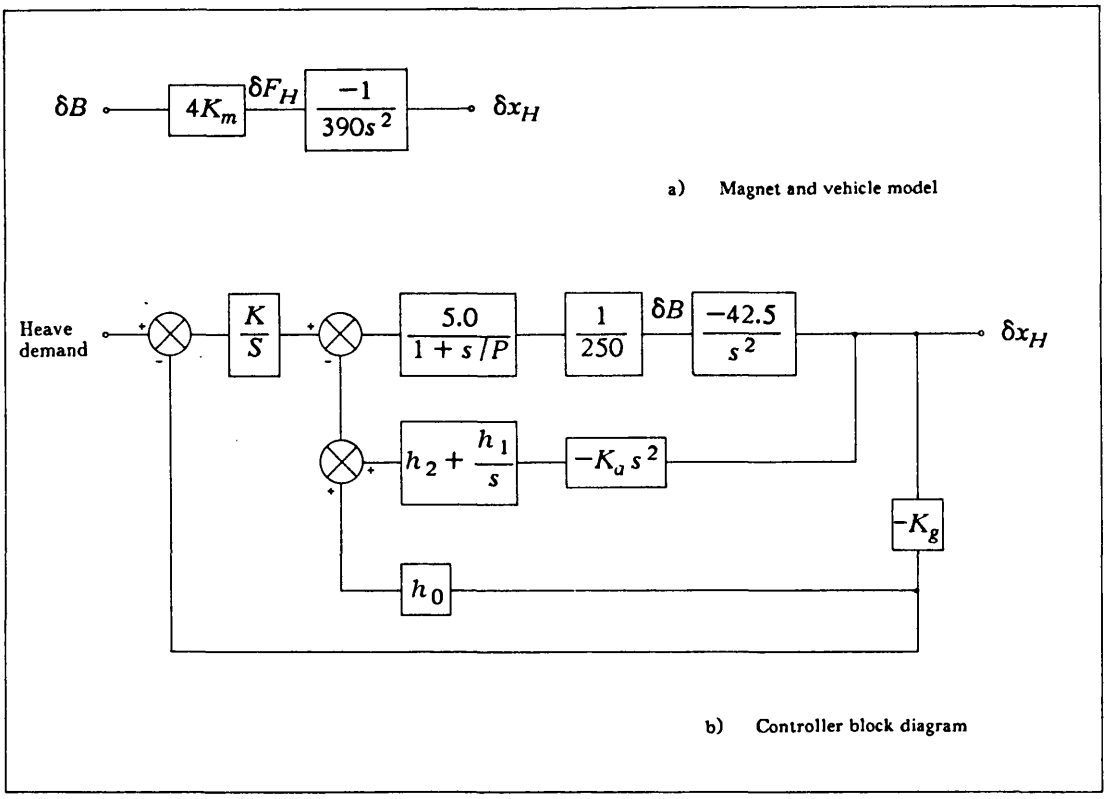

The heave mode controller Figure 7.2

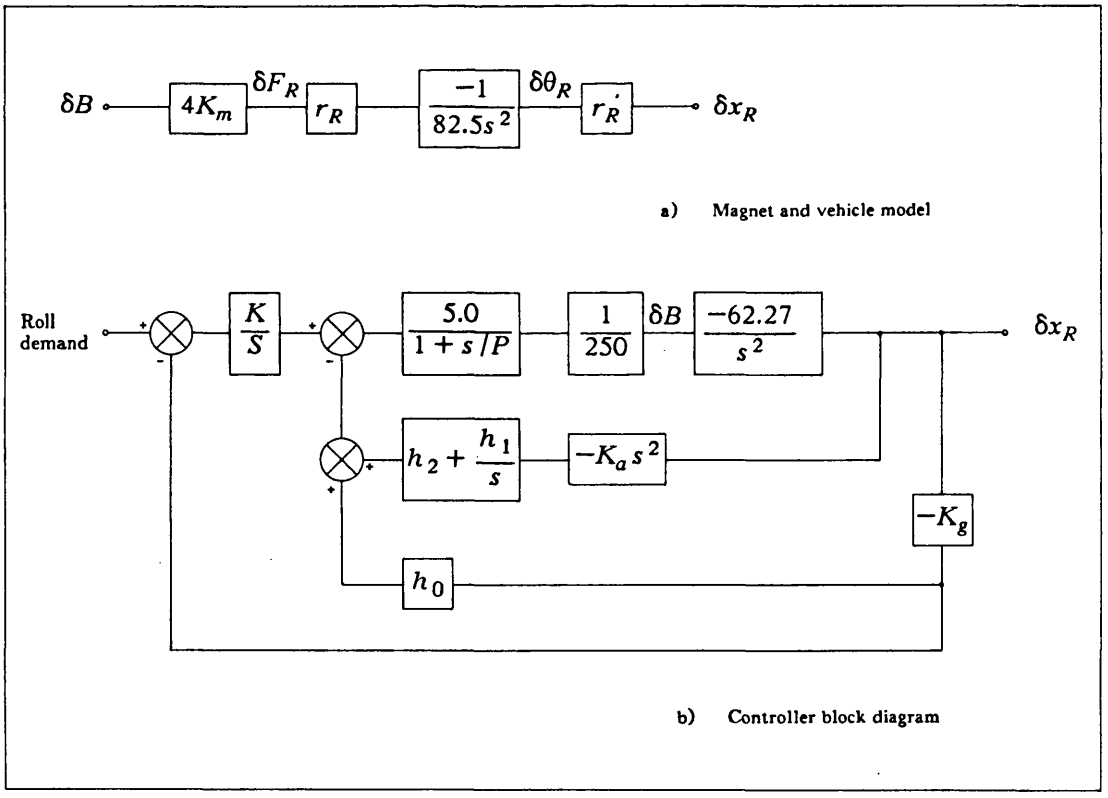

The roll mode controller Figure 7.3

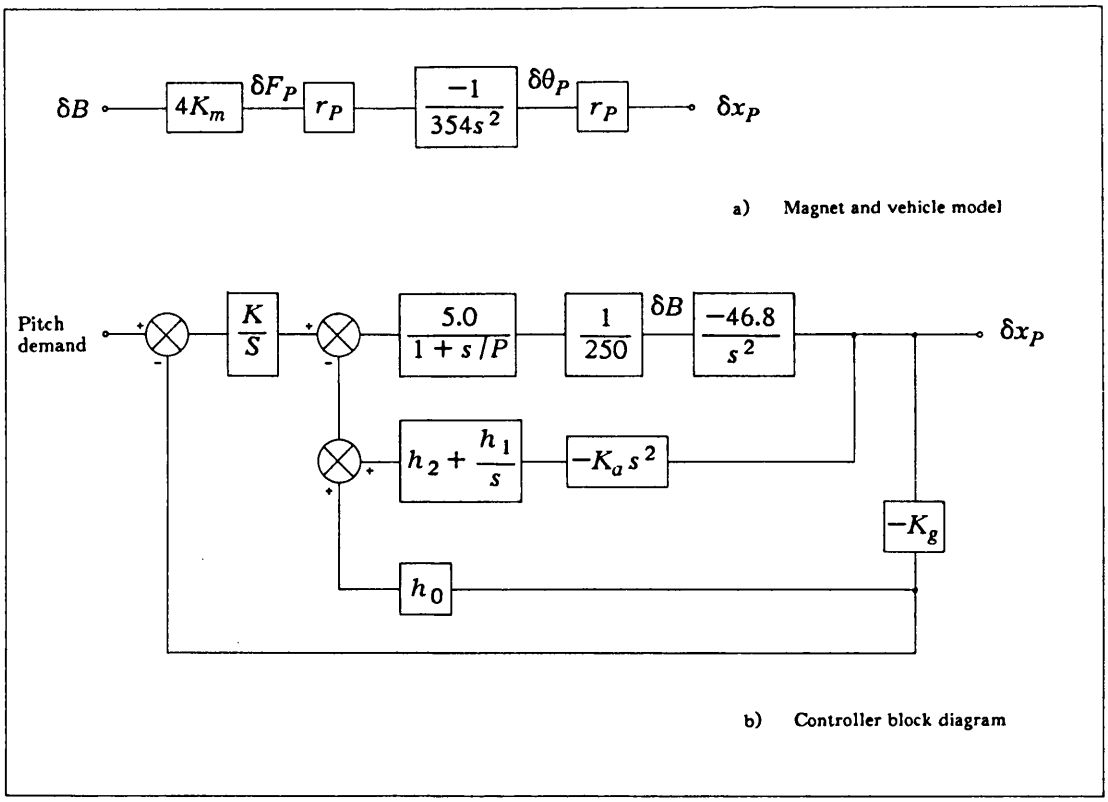

The pitch mode controller Figure 7.4

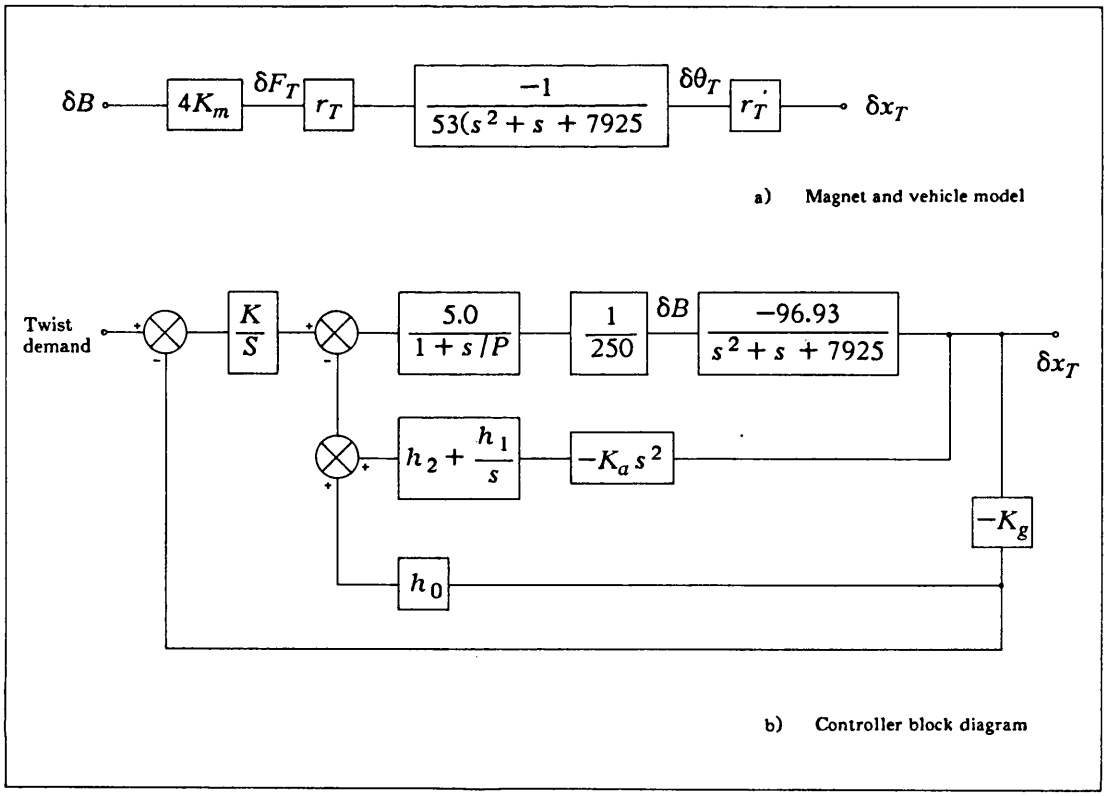

The twist mode controller Figure 7.5

8. The design and implementation of a pole position transducer system

The design of a non-contact transducer system for monitoring the position of the secondary track members will now be described. This system was primarily developed to provide a pole position feedback signal for each of the 3-phase inverter units, thus providing the mechanism for operating the linear synchronous motors at a constant torque angle of $\pm 90^{\circ}$ as discussed previously in section 2.1.1.

The transducer output can also be read by the multiprocessor system (using the interface board described in section 2.9), and hence can be used to derive relative position and velocity signals for a tractive mode controller implemented as part of a combined vehicle control program.

8.1 General description

The pole position transducer is essentially comprised of an array of twenty metal detection circuits arranged underneath the secondary track members and equally spaced at 10 mm intervals over the 0.2 m pitch of these members. A dedicated microprocessor system is then used to decode the outputs of the sensor array to generate the corresponding six bit linear pole position signal required by the 3-phase inverters (see section 2.3.5). By using a microprocessor for this decoding function, other facilities such as polarity reversal and phase offsets are easily incorporated into the transducer software.

8.2 Metal sensing technique

Each metal detection circuit uses an *induction balance* technique commonly found on some types of commercial 'treasure hunting' metal locators, but which is otherwise rarely used. The block diagram of figure 8.1 shows the main elements of an induction balanced metal detection system.

Now it can be seen from the diagram that the transmitter coil is constantly energised with an unmodulated RF carrier whilst the receiver coil, which is coplanar with the

transmitter coil, forms the front end of a tuned receiver circuit. However, the key feature of the induction balanced system, and the feature by which the system is named, lies in the arrangement of the transmitter and receiver coils with respect to one another.

By careful positioning of the transmitter coil over the receiver coil, a balance or *null* point can be found for which there is no detectable pickup of the transmitted RF in the receiver coil. To understand this effect, it should be noted that the use of an overlapping coil arrangement means that the radiated flux field from the transmitter coil passes through the receiver coil in *both* directions. It follows that the null point occurs when the total or net flux contained within the area of the receiver coil is precisely zero. Once the null point has been established, any metal introduced into the vicinity of the coil array will disturb the flux balance, thus producing a corresponding amplitude modulated RF output signal from the receiver coil.

As with other balanced measurement or detection techniques, the induction balanced metal detection system described above is inherently very sensitive. Consequently the receiver circuitry can be kept simple, which is an important consideration when twenty or more such circuits are required.

The complete pole position transducer system based on this metal detection technique is represented by the block diagram of figure 8.2. Specific details of each of the units making up the system will now be given.

8.3 Sensor coil array

The sensor coil array is comprised of twenty four identical receiver coils overlapping one limb of a common transmitter coil and equally spaced at 10 mm intervals along this limb. Figure 8.3 shows a plan view of the prototype sensor coil array used in this study and provides the essential dimensions and winding details of the transmitter and receiver coils. Note that two *dummy* receiver coils were included at each end of the

active array of twenty coils to ensure good uniformity of the transmitted source field over the full width of this array. Although these additional sense coils must also be connected to duplicate receiver circuits in order to be effective, the corresponding receiver outputs are not used by the microprocessor system in the decoding process.

8.3.1 Setting up procedure Because the precise balance point of each receiver coil is highly sensitive to coil geometry and alignment, it is necessary, but not sufficient, to employ very accurate construction techniques for manufacturing the sensor array. In practice it is also necessary for each individual sensor to be fine-tuned by energising the transmitter coil and then adjusting the alignment of each receiver coil to obtain a null indication from the corresponding receiver circuit. This alignment must then be preserved by setting the individual receiver coils in an epoxy resin such as Araldite.

Further, during the initial setting up procedure of the prototype coil array, it was found that the precise alignment required to balance any given receiver coil would be affected by any imbalance in an adjacent receiver coil. It follows that the sensor coil array must be built up one coil at a time, with each new coil being correctly aligned, balanced and set before the next coil can be placed.

8.4 Transmitter board

The transmitter coil of the coil array described above is continuously energised with an unmodulated 130 kHz carrier signal generated by an oscillator circuit on the transmitter board. This board also provides an adjustable d.c. reference signal for setting a common threshold level in each of the twenty four receiver circuits. The following circuit description is made with reference to the transmitter board circuit diagram of figure 8.4. Figure 8.5 provides the corresponding board layout details.

The transmitter coil (denoted by L1 in the diagram), in conjunction with capacitors C1 and C2, forms the tuned load circuit of a single transistor Colpitts oscillator based on transistor TR1 and associated components. In this application, where C2 >> C1, an approximation to the oscillator frequency f can be written down as follows[25],

$$f = \frac{1}{2\pi}\left\{\frac{1}{L_1 C_1}\right\}^{\frac{1}{2}}$$

$$= \frac{1}{2\pi}\left\{\frac{1}{0.47\times10^{-3} \times 3.3\times10^{-9}}\right\}^{\frac{1}{2}}$$

$$= 128\ kHz$$

The value of transmitter coil inductance L1 was determined using an inductance bridge.

When tested, using a single rail 12 V supply, the oscillator frequency was found to be 130 kHz, whilst the corresponding voltage swing on the transmitter coil L1 was 50 V peak to peak.

The remainder of the transmitter board circuitry provides an adjustable d.c. reference source derived from resistor R5, zener diode ZD1 and preset potentiometer PR1. As mentioned previously, this reference signal is used to set the threshold level in each of the receiver circuits, and does not form part of the transmitter circuitry.

8.5 Four channel receiver board

The full implementation of the pole position transducer system required twenty four separate receiver circuits to monitor the outputs of the sensor coil array described in section 8.3. This was achieved using six standard size boards (100 mm by 220 mm), with each board comprised of four identical receiver circuits together with a four channel comparator to provide the threshold detection and microprocessor interface. The following circuit description is made with reference to the four channel receiver board circuit diagram of figure 8.6. Figure 8.7 provides the corresponding board layout details.

Considering channel one, the receiver coil (denoted by L1 in the diagram), in conjunction with the series combination of capacitors C1 and C2, forms a tuned circuit at the input of a high gain voltage amplifier comprised of transistors TR1 and TR2 and

associated components. The use of a tuned input circuit ensures that the amplifier is particularly sensitive to the transmitted RF carrier signal whilst rejecting unwanted signals. Now this amplifier was originally developed as part of a metal detection system having maximum sensitivity. In practice, however, the pole position transducer application requires the detection of relatively large amounts of metal (namely the secondary track members), for which a less sensitive receiver coil must be used if saturation of the receiver amplifier is to be avoided. This was achieved by including resistor R1 in parallel with the receiver input, thus reducing the effective sensitivity of the corresponding receiver coil.

The output of the amplifier stage, which is in the form of an amplitude modulated carrier frequency, is a.c. coupled to a standard a.m. detector circuit comprised of germanium diodes D1 and D2, capacitor C5 and resistor R7. This circuit demodulates the RF carrier to derive the corresponding amplitude enevelope signal, which directly represents the level of flux imbalance in the associated receiver coil. The comparator circuit of IC1a is then used to compare the envelope signal with the fixed d.c. reference provided by the transmitter board discussed in section 8.4. The output from this comparator, which is an open collector signal, is pulled low when the amplitude of the envelope signal exceeds the d.c. reference level.

8.5.1 Receiver bandwidth The receiver bandwidth is governed primarily by the time constant of the output filter in the detector circuit, which in turn is determined by capacitor C5 and resistor R7. It is easily shown that the -3 dB frequency, f_0, of this filter is given by equation 8.1 below,

$$f_0 = \frac{1}{2\pi C_5 R_7} \qquad \text{equation 8.1}$$

Hence

$$f_0 = \frac{1}{2\pi \times 22\times10^{-9} \times 10\times10^{3}}$$

$= 723Hz$

When applied to the pole position transducer system, the receiver frequency response determines the maximum frequency at which the secondary track members can be detected passing over the sensor coil array. With a pitch of 0.2 m between these members, the corresponding vehicle speed at the -3 dB frequency derived above would be 144 m/s or 520 km/hr.

8.6 Receiver monitoring board

The receiver monitoring board includes twenty driver/LED circuits to provide a visual indication of the output status of each receiver circuit. Figure 8.8 provides the circuit diagram for this board and figure 8.9 provides the corresponding component layout details.

8.7 Z80 microprocessor board

The Z80 microprocessor board is used to decode the outputs from the twenty active receiver circuits to produce a corresponding six bit transducer output signal representing the position of a secondary track member within the 0.2 m span of the active sensor coil array. A description of the decoding algorithm implemented on the microprocessor board will be given in section 8.8. The following circuit description is made with reference to the Z80 microprocessor board circuit diagram of figure 8.10. Details of the circuit board layout and front panel assembly are provided by figures 8.11 and 8.12 respectively. Because the Z80 microprocessor board uses the Z80 series of devices in a completely standard way[26], only those features which are particularly relevant to the pole position transducer system will be described.

8.7.1 Program memory The microprocessor board includes a socket for an $8k \times 8$ or $16k \times 8$ EPROM device, IC2, which would contain the fixed program segments of the software to be implemented. Static RAM device IC3 provides a further $2k \times 8$ of read/write memory for the processor stack and system variables.

Using this arrangement, it is necessary to provide the microprocessor system with pre-programmed EPROM based software developed on another machine. The pole position transducer software used in this study was written in standard Z80 assembler[27] on a DEC microVAX computer system. Using the same system, the program was then assembled into the corresponding object code (approximately 300 bytes) and blown into an $8k \times 8$ 2764 EPROM device.

Table 8.1 below provides the addressing details of the two memory devices making up the microprocessor board program memory.

Device	Address (hex)
EPROM ($8k \times 8$)	0000 → 1FFF
EPROM ($16k \times 8$)	0000 → 3FFF
RAM ($2k \times 8$)	8000 → 87FF

TABLE 8.1. Microprocessor board memory map

8.7.2 Input ports Three 8-bit input ports are included on the microprocessor board to provide an interface to the twenty active receiver circuits described in section 8.5.

Considering input port 0, each of the eight input lines are connected to one of eight corresponding pull up resistors in resistor pack RP4, which is required because the receiver circuits provide open collector output signals. These signals are then interfaced to the microprocessor data bus using IC6, which is an inverting tri-state octal buffer device.

Table 8.2 below provides the address of each input port within the IO memory map of the microprocessor board. To read a given input port, the microprocessor simply performs an IO read cycle using the appropriate port address.

Input port	IO Address (hex)
port 0	00
port 1	10
port 2	20

TABLE 8.2. Input port addressing

8.7.3 Output ports and front panel display To output the decoded pole position value, the microprocessor board provides two latched eight bit output ports together with a two digit seven segment LED display.

The parallel eight bit data for output port 0 and output port 1 is derived from the microprocessor data bus using two eight bit latch devices, IC9 and IC10 respectively. Latched data is then presented to the two 9-way D-type sockets, J2 and J3, mounted on the front panel of the microprocessor board. In the pole position transducer application, the two output ports were used to output duplicate copies of the decoded pole position reading. In general, however, these two ports are quite separate and can be accessed independently by the microprocessor.

The two digit seven segment display is effectively decoded as a third latched eight bit output port. This is achieved by using a packed bcd (binary coded decimal) number format for the two display digits, such that the data for the most significant digit is provided by the upper four bits of the data bus, whilst the data for the least significant digit is provided by the lower four bits of the data bus. The display driver using this format is comprised of two bcd-to-decimal decoder/driver devices, IC16 and IC17, which provide direct drive to the most significant and least significant digits respectively.

Table 8.3 below provides the addressing information for the two output ports and front panel display of the microprocessor board. To update a given output port or panel display, the microprocessor performs an IO write cycle using the appropriate port

address.

Output port	IO Address (hex)
port 0	30
port 1	40
Display	60

TABLE 8.3. Output port addressing

8.7.4 Timebase interrupt facility To provide a programmable timebase interrupt facility, the microprocessor board includes a standard Z80 CTC device (counter-timer circuit), IC4. This device, which supports the Z80 vectored interrupt structure, provides four independent and fully programmable counter-timer channels. Table 8.4 below provides the IO address of each of the four channels. The corresponding programming details can be obtained from the Z80 CTC data sheet[28].

CTC channel	IO Address (hex)
channel 0	50
channel 1	51
channel 2	52
channel 3	53

TABLE 8.4. Z80 CTC addressing

8.8 Transducer software

The pole position transducer software is required to decode the outputs from the twenty active receiver circuits to produce a corresponding six bit binary coded transducer output representing the position of a secondary track member within the 0.2 m pitch of these members. A discussion regarding the derivation and software implementation of a suitable decoding algorithm will now be given.

8.8.1 Notation In the following text, the term *sensor* will be used to denote a sensor coil/receiver circuit combination. Thus an asserted or true receiver output is referred to

as an *on sensor*, whilst a negated or false receiver output is referred to as an *off sensor*. Individual sensors within the active array are numbered consecutively from 0 to 19.

8.8.2 The decoding algorithm In the simplest case, in which there is just one on sensor, it is clear that the position of the track member corresponds to the point immediately above that sensor. Further, this position can be uniquely identified by using the associated sensor number. In practice, however, six categories of sensor pattern can be identified. These patterns are represented by figures 8.13a through 8.13f inclusive, and are summarised below,

1. All sensors off
2. All sensors on
3. One group of on sensors
4. Two groups of on sensors with wraparound
5. Two groups of on sensors without wraparound
6. Three or more groups of on sensors

It can be seen that categories 3 and 4 represent valid sensor patterns, whilst categories 1, 2, 5 and 6 represent invalid sensor patterns which must be ignored. Of the two valid categories, category 3 is the simplest to decode and will be considered first.

One group of on sensors A sensor pattern comprised of just one group of on sensors corresponds to the situation in which there is a single track member above the sensor array. It follows that the corresponding position of this member, which is defined by the centre of the group of on sensors, can be written down using equation 8.2 below,

$$pole\ position = \frac{group\ end + group\ start}{2} \qquad \text{equation 8.2}$$

where *group start* and *group end* are, respectively, the sensor numbers corresponding to the first and the last on sensors in the on sensor group, as shown in figure 8.14a.

Using this equation, the position value would range from 0 to 19½ in steps of ½. A preferable integer range from 0 to 39 is obtained using equation 8.3,

$$pole\ position = group\ end + group\ start \qquad \text{equation 8.3}$$

This equation provides the algorithm for decoding a sensor pattern comprised of a single group of on sensors.

Two groups of on sensors with wraparound When the active sensor array is between two track members, the two members will energise one or more sensors at opposite ends of the array, thus producing a sensor wraparound pattern comprised of two groups of on sensors.

To decode this pattern, it is useful to consider the sensor array as a continuous *ring* of sensors, in which sensor 0 is effectively adjacent to sensor 19. Using this concept, it can be seen that the wraparound sensor pattern is, in fact, comprised of a single group of on sensors. It follows that the effective position of the track member can be decoded using equation 8.3 as before. To use this decoding algorithm, however, the sensor numbers across the ring boundary must be continuous. This is achieved by adding twenty to the sensor numbers in the first group of on sensors, such that sensor 0 becomes sensor 20, sensor 1 becomes sensor 21, and so on. This procedure, which effectively appends the first on sensor group onto the end of the second on sensor group, is represented graphically in figure 8.14b.

With reference to this diagram, the equation for decoding the wraparound sensor pattern can be derived from equation 8.3 as follows,

$$pole\ position = group\ end + 20 + group\ start \qquad \text{equation 8.4}$$

This equation decodes the wraparound sensor pattern by effectively extending the sensor array beyond sensor 19. As it stands, however, equation 8.4 does not maintain the transducer ring concept discussed above, and it is now possible for the decoded pole position value to exceed the range limit of 39. To overcome this problem, and restore the ring concept, it is necessary to subtract 40 from the decoded pole position value whenever this value exceeds the range limit.

The flowchart of figure 8.15 illustrates the complete decoding algorithm incorporating equations 8.3 and 8.4 derived above. This flowchart shows that the majority of the algorithm is concerned with sequentially scanning each sensor in the active sensor array to determine the sensor positions corresponding to the group start and group end

pointers. Provided that the sensor pattern is found to be valid, these two pointer values are then used to derive the corresponding pole position value. If, however, an invalid sensor pattern is identified, then the decoding process is aborted and the previous valid pole position value is carried over without being updated.

8.8.3 Software implementation An assembly code listing of the pole position transducer software is included as listing 8.1. In addition to implementing the decoding algorithm derived above, this software also includes conditional assembly statements which can be used to invoke optional phase reversal and phase offset routines. The phase reversal routine is used to reverse the direction of the transducer system by subtracting the decoded pole position value from 39. The phase offset routine is used to adjust the output phase of the transducer system to give a precise 90° torque angle when used in conjunction with the 3-phase inverters and linear synchronous motors.

Finally, an optimised fixed coefficient multiplication routine is used to convert the decoded position value into an equivalent six bit transducer output in the range 0 to 63. The required algorithm was derived using equation 8.5 below (recall that the decoded pole position value ranges from 0 to 39),

$$output = decoded\ pole\ position \times \frac{63}{39}$$

$$\approx decoded\ pole\ position \times (1 + 1/2 + 1/8 + 1/32) \qquad \text{equation 8.5}$$

When presented in this way, it can be seen that equation 8.5 can be implemented as an optimised series of shift/add instructions without the need to resort to a generalised multiplication routine.

8.8.4 Resolution Using an array comprised of twenty sensors, it has been shown that forty separate pole positions can be resolved. With this array spanning 0.2 m, it follows that the resolution of the pole position transducer system is given by equation 8.6 below.

$$resolution = \frac{0.2}{40}$$

$$= 5\ mm \qquad \text{equation 8.6}$$

8.9 Setting up procedure

8.9.1 Mechanical alignment The prototype sensor array was mounted on the vehicle chassis beneath one set of secondary track members as shown in figure 8.16. This diagram also shows the position of the corresponding transducer electronics, which were mounted on the vehicle chassis using a single rack system comprised of the six receiver boards, the receiver monitoring board, the transmitter board and the Z80 microprocessor board. Each receiver circuit was connected to the corresponding sensor coil using a 0.5 m length of twin screened cable.

The gap of 35 mm between the sensor array and the secondary track members corresponds to the rest gap, in which the effective ride height of the vehicle is 10 mm. It follows that when the vehicle is levitated to a ride height of 7 mm, the working gap of the sensor array will decrease to 32 mm. Hence the percentage variation in the sensor gap is less than ten percent. In practice the transducer system was shown to work equally well at any vehicle ride height within the available 10 mm working gap of the linear synchronous motors.

It is important to note that the sensor array is actually positioned to one side of the track, such that only the receiver coils pass beneath the secondary track members whilst the much larger transmitter coil is kept clear. This alignment ensures that the output-position characteristic of a given receiver circuit will exhibit a high peak when the corresponding receiver coil is directly beneath the centre of a track member.

8.9.2 Receiver calibration The remainder of the setting up procedure is concerned with the calibration of the twenty four receiver circuits. For the prototype system, this was achieved by first setting the common receiver threshold level to 3.0 V using preset potentiometer PR1 on the transmitter board. This level corresponds to

approximately half the full scale output capability of the four a.m. detector circuits on each receiver board. Starting with either one of the outermost dummy sensors, and working consecutively along the sensor array, the corresponding receiver circuits are then adjusted to give an asserted output over a ±20 mm position variation about the centre line of a track member. This corresponds to the output-position characteristic of each receiver having a width of 40 mm at the common receiver threshold level (this receiver parameter will hereafter be referred to as the *threshold width*).

With a sensor coil spacing of 10 mm, it follows that at any one time the active sensor pattern will be comprised of approximately four on sensors. These will be arranged either as a single continuous group or as two groups in a wraparound pattern. This can be verified by moving the vehicle along the track whilst observing the LED indicators on the receiver monitoring board. Finally, to complete the setting up procedure, the decoded position value displayed on the Z80 microprocessor board should be verified for various valid and invalid sensor patterns.

8.9.3 Receiver characteristics The receiver calibration procedure described above ensures that each of the twenty active receiver circuits has a similar output-position characteristic at the given sensor gap of 35 mm. This characteristic, which has a threshold width of 40 mm, ensures that the sensor pattern is always comprised of approximately four on sensors arranged symmetrically about the centre line of a track member.

In practice, however, each receiver characteristic is dependent on the sensor gap, which in turn will vary according to the vehicle ride height. Hence, in order to assess the performance of the transducer system at various vehicle ride heights, a series of tests were carried out to determine the output-position characteristics of one of the receiver circuits at three different sensor gaps.

Results The results from these tests are included in table 8.5 and presented graphically as graphs 8.1a through 8.1c inclusive (corresponding to sensor gaps of 35 mm, 30 mm and 25 mm respectively).

These graphs demonstrate that, in general, the threshold width of a given receiver circuit will increase as the sensor gap is decreased. This has the effect of increasing the number of on sensors making up a given sensor pattern, although it can be seen that the symmetry of this pattern about the track member position is not affected. Because the decoded pole position value is calculated as the centre point of this group of on sensors (see section 8.8.2), it follows that the performance of the overall transducer system will be completely unaffected by the gap dependent variations in the receiver characteristics.

8.10 Summary

The main aim of this chapter was to present the design and implementation details of a prototype pole position transducer system for use on the levitated vehicle. This was achieved by first introducing the induction balanced metal detection techniques upon which the system was based. The inherently high sensitivity offered by this technique was used to minimise the complexity of the transducer system (by minimising the component count), whilst also simplifying the calibration procedure.

Using an array of twenty such metal detector sensors together with a dedicated microprocessor system for decoding the corresponding sensor patterns, the transducer system achieves a resolution of 5 mm and provides a six bit digital output representing the position of a track member within the 0.2 m pitch of these members.

Finally, results obtained from the prototype system demonstrate that large variations in the sensor gap can be tolerated without degrading the system performance. This ensures that the transducer system will function correctly at any vehicle ride height within the available 10 mm working gap of the linear synchronous motors.

Position (mm)	Detector output voltage (V)		
	Gap = 35 mm	Gap = 30 mm	Gap = 25 mm
0	0.0	0.0	0.2
5	0.0	0.0	0.2
10	0.0	0.0	0.2
15	0.0	0.0	0.3
20	0.0	0.0	0.4
25	0.0	0.0	0.6
30	0.0	0.0	0.8
35	0.0	0.0	1.1
40	0.0	0.2	1.6
45	0.0	0.4	2.2
50	0.0	0.9	2.9
55	0.4	1.5	3.6
60	0.8	2.2	4.2
65	1.4	2.9	4.6
70	2.1	3.6	5.0
75	2.6	4.1	5.2
80	3.2	4.4	5.4
85	3.6	4.7	5.5
90	3.8	4.8	5.6
95	4.0	4.9	5.7
100	4.1	4.9	5.7
105	4.0	4.9	5.7
110	3.8	4.8	5.6
115	3.6	4.6	5.5
120	3.2	4.3	5.4
125	2.6	3.9	5.2
130	2.1	3.4	4.9
135	1.5	2.7	4.6
140	0.9	2.0	4.1
145	0.4	1.4	3.5
150	0.1	0.8	2.8
155	0.0	0.4	2.2
160	0.0	0.1	1.6
165	0.0	0.0	1.2
170	0.0	0.0	0.8
175	0.0	0.0	0.6
180	0.0	0.0	0.5
185	0.0	0.0	0.4
190	0.0	0.0	0.3
195	0.0	0.0	0.2

TABLE 8.5. Receiver characteristics

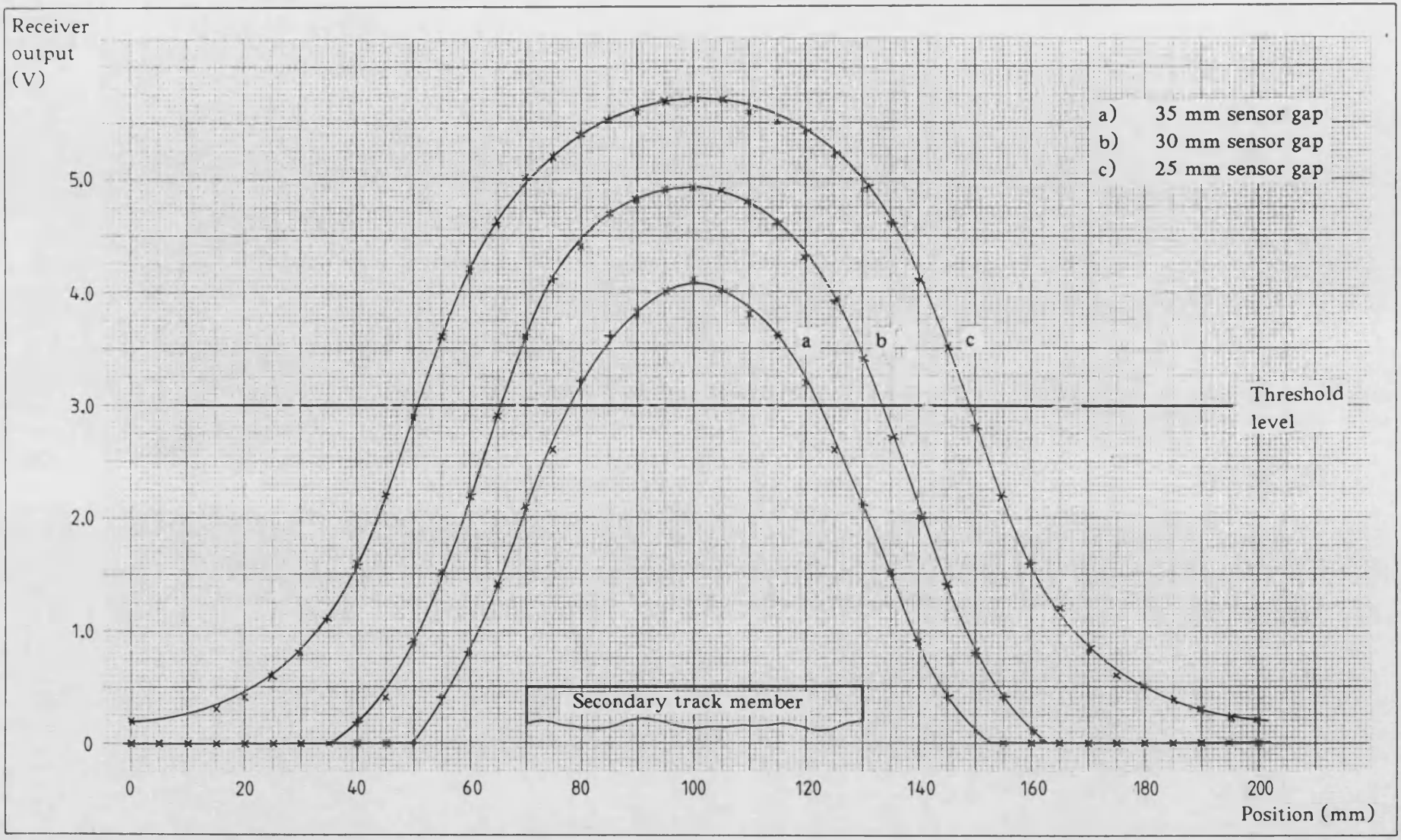

Receiver characteristics at various sensor gaps Graph 8.1

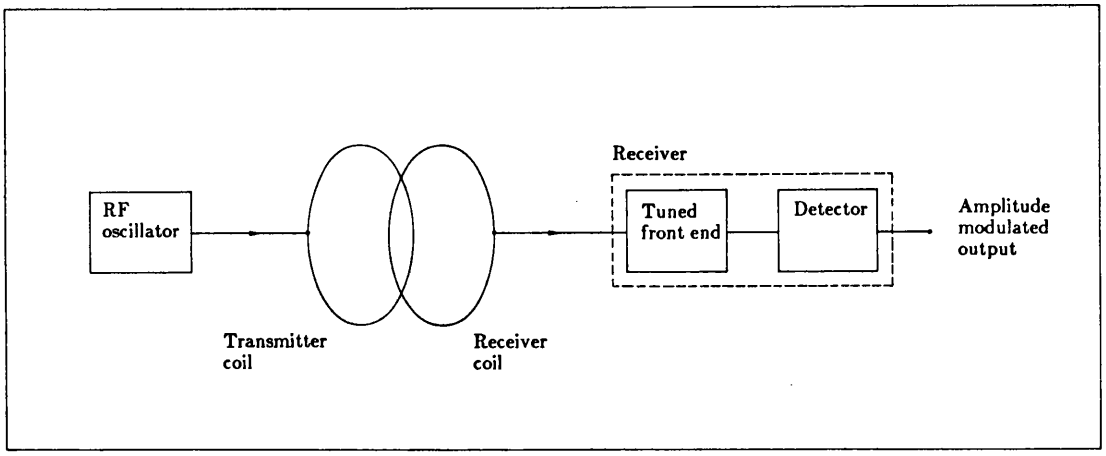

The induction balanced metal detection system Figure 8.1

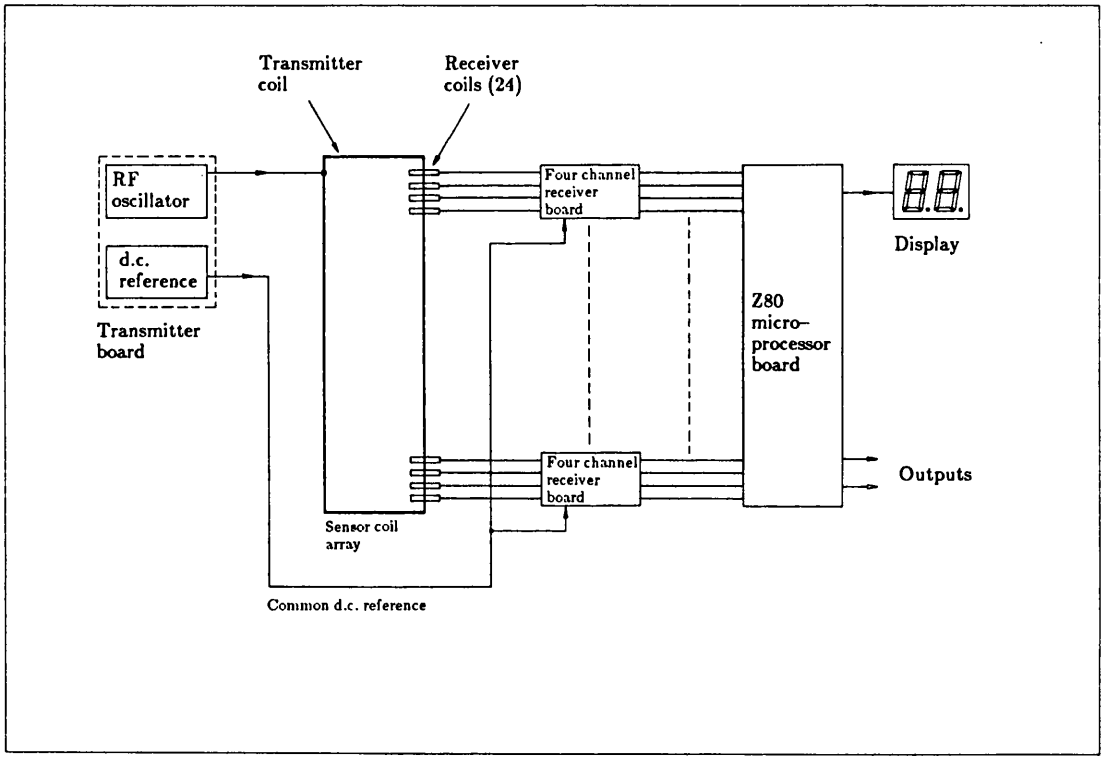

Block diagram of the pole position transducer system Figure 8.2

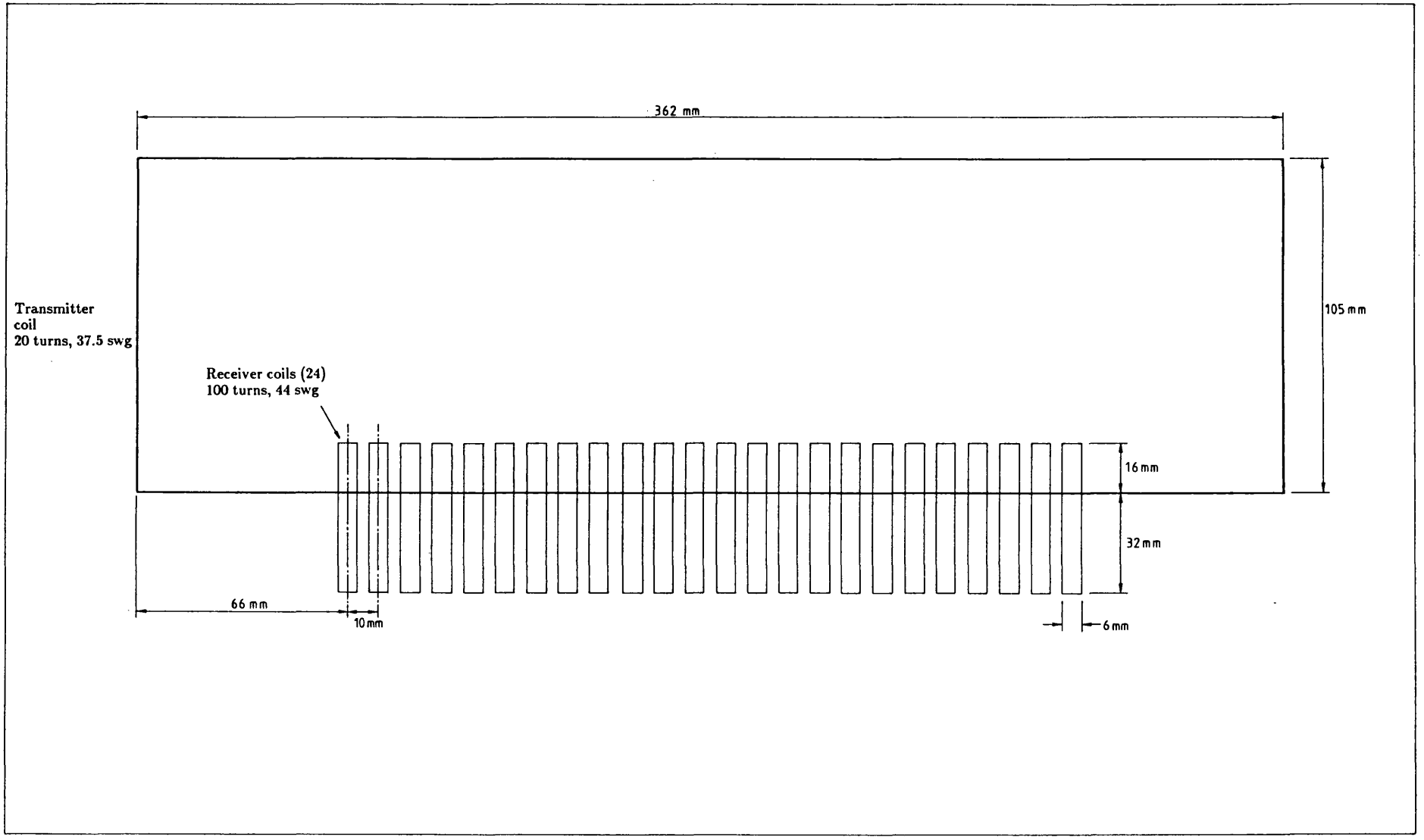

Sensor coil array Figure 8.3

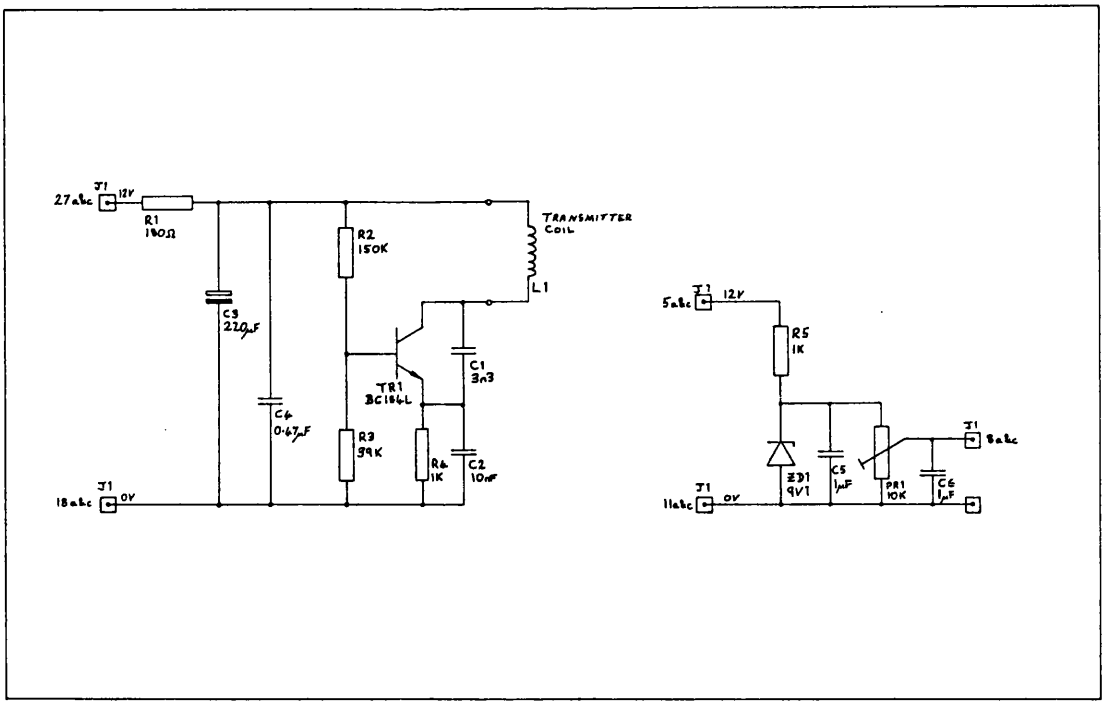

Transmitter board circuit diagram Figure 8.4

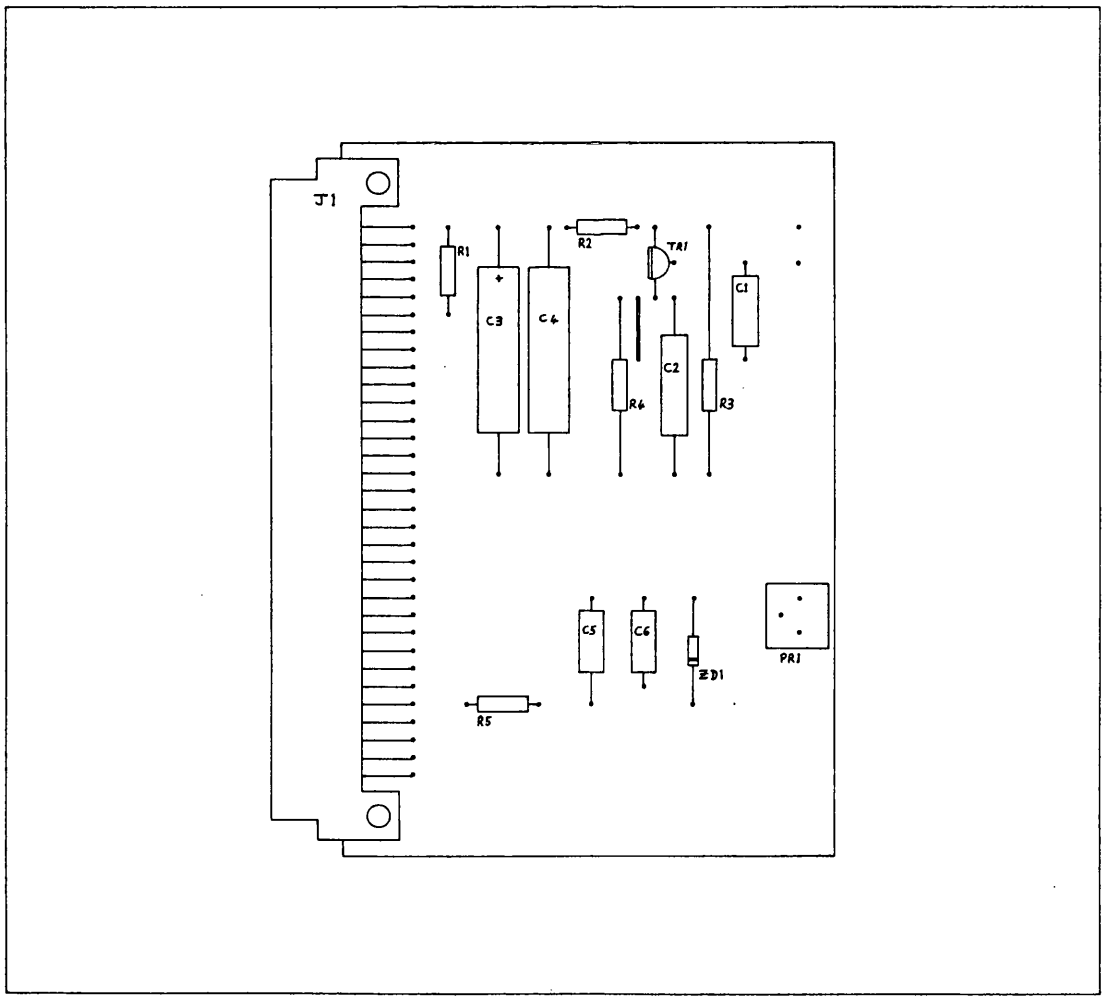

Transmitter board component layout Figure 8.5

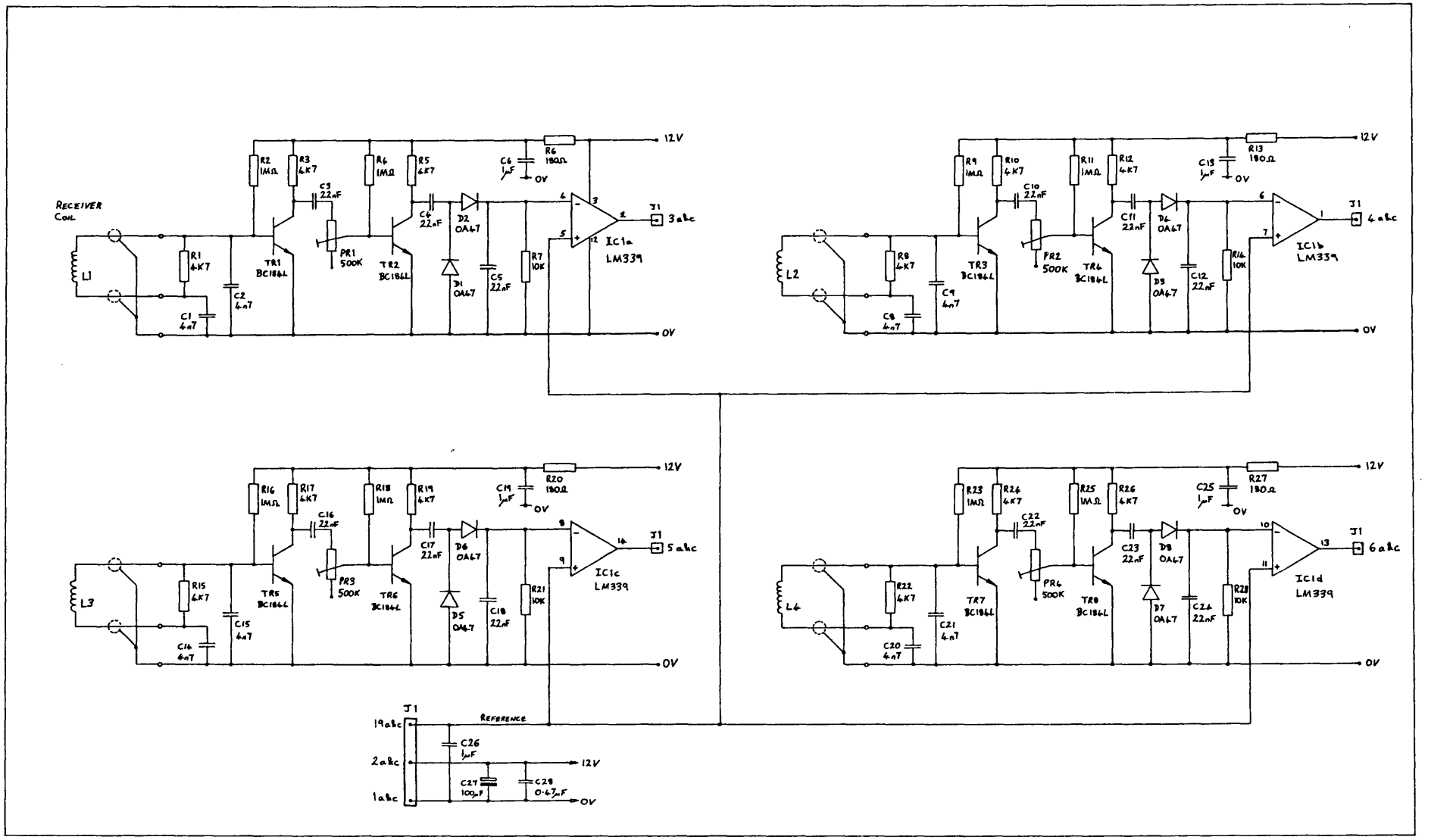

Four channel receiver board circuit diagram Figure 8.6

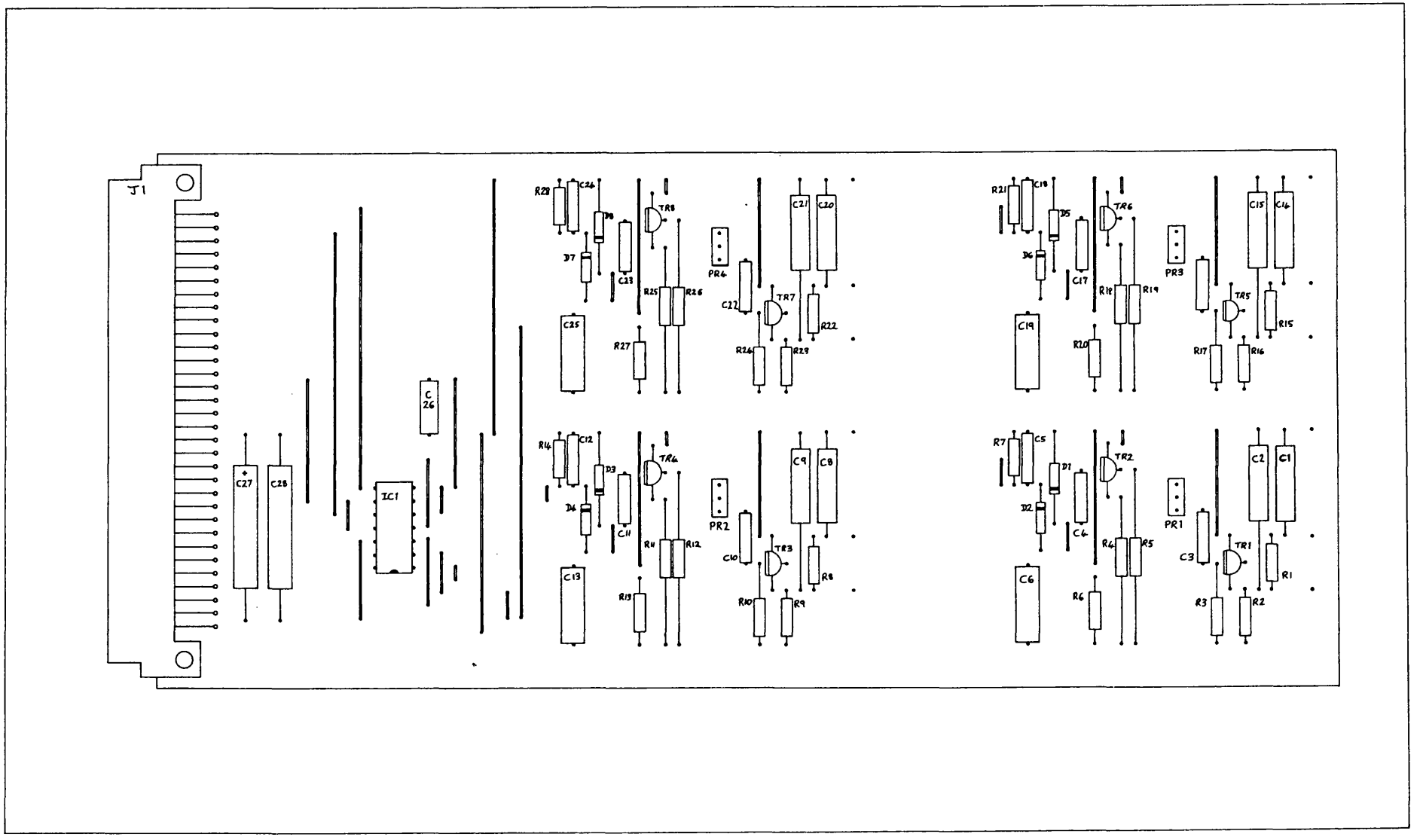

Four channel receiver board component layout Figure 8.7

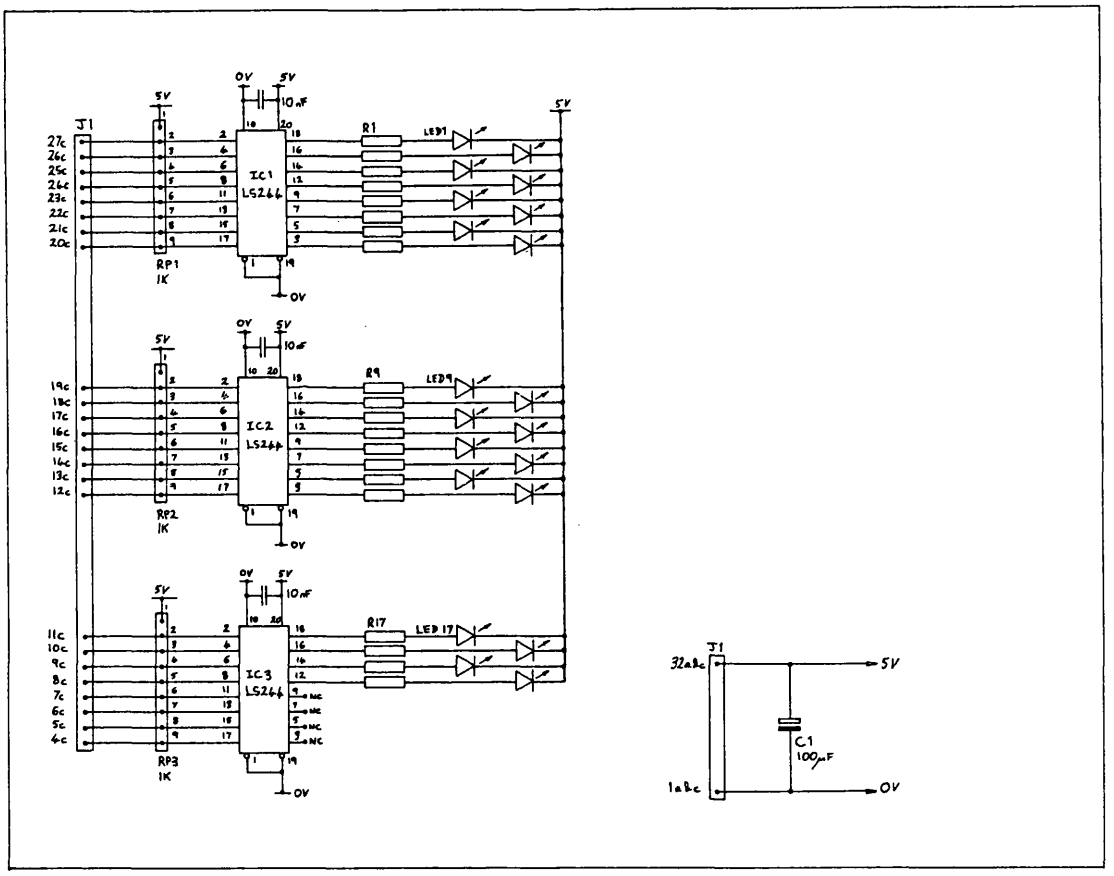

Receiver monitoring board circuit diagram Figure 8.8

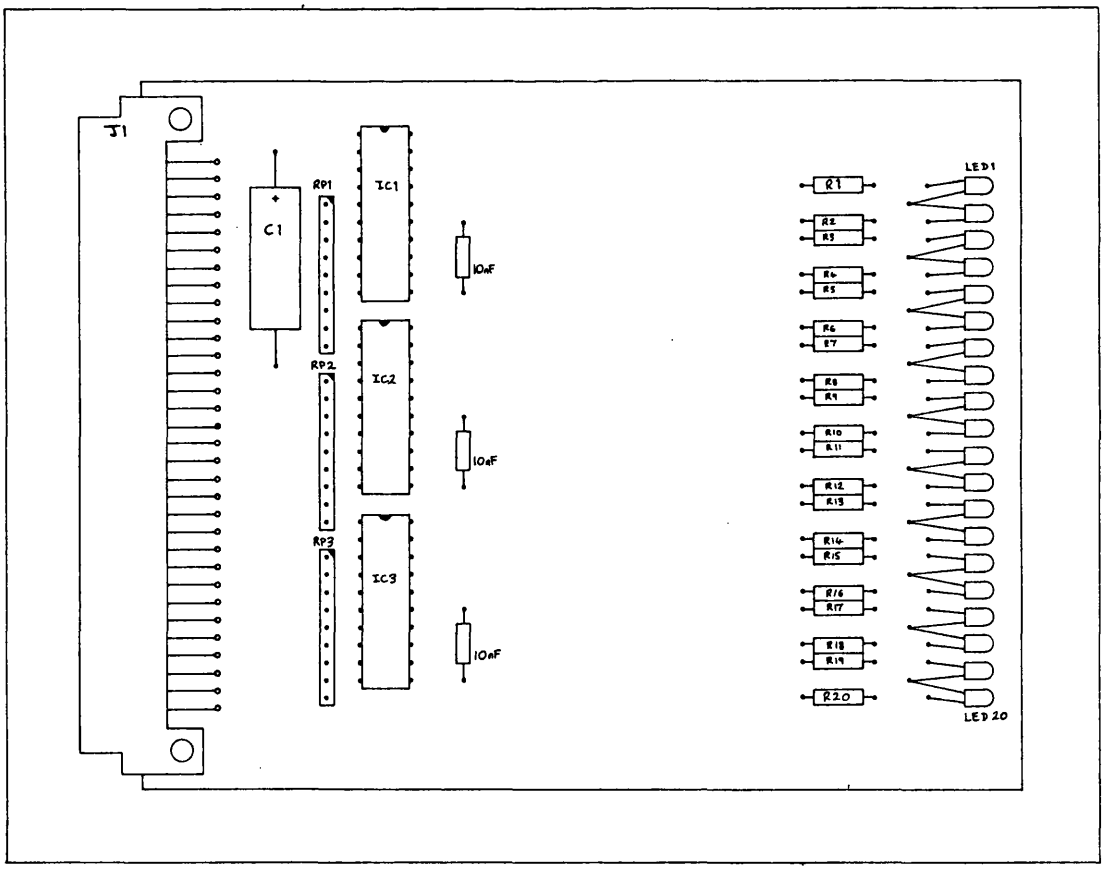

Receiver monitoring board component layout Figure 8.9

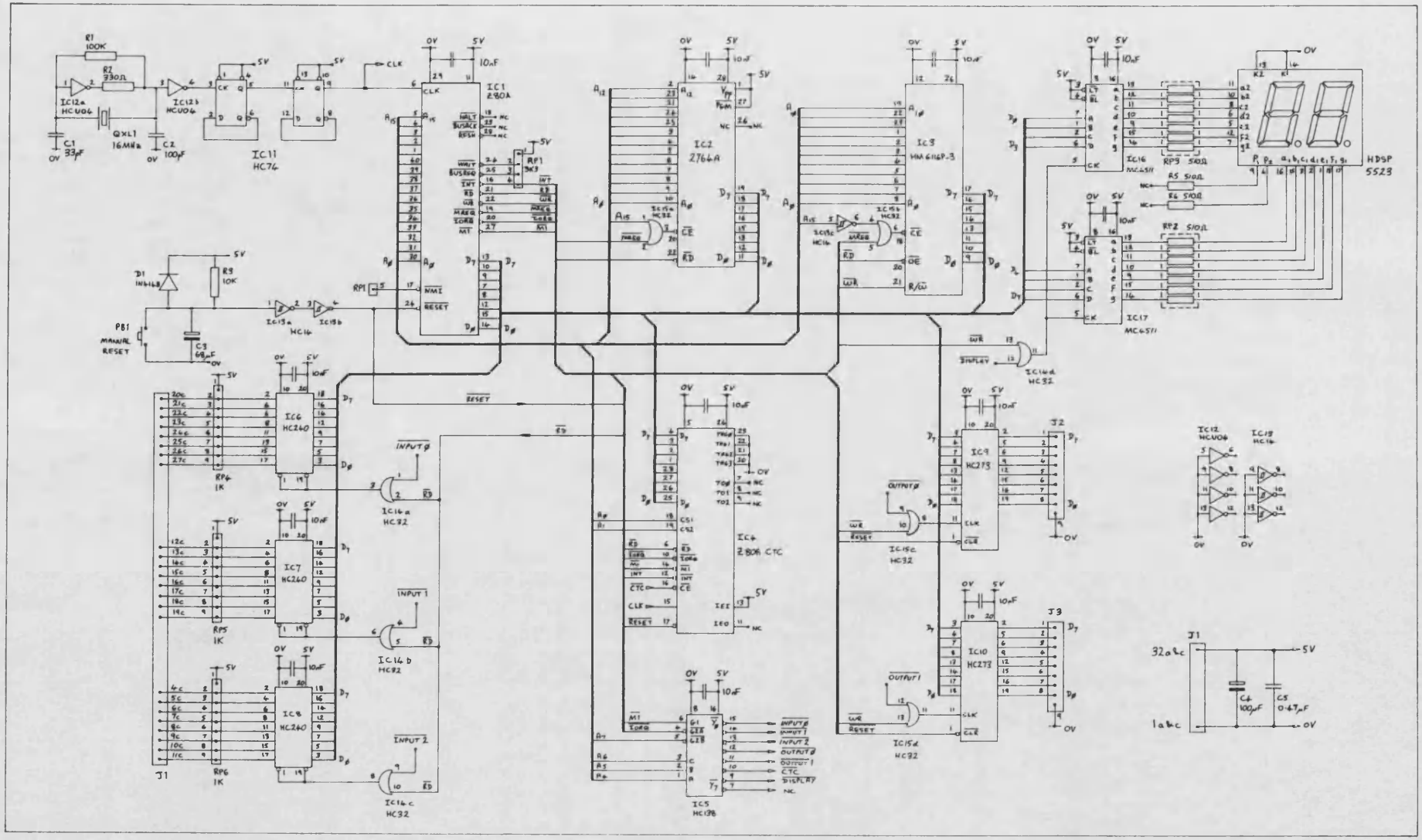

Z80 microprocessor board circuit diagram Figure 8.10

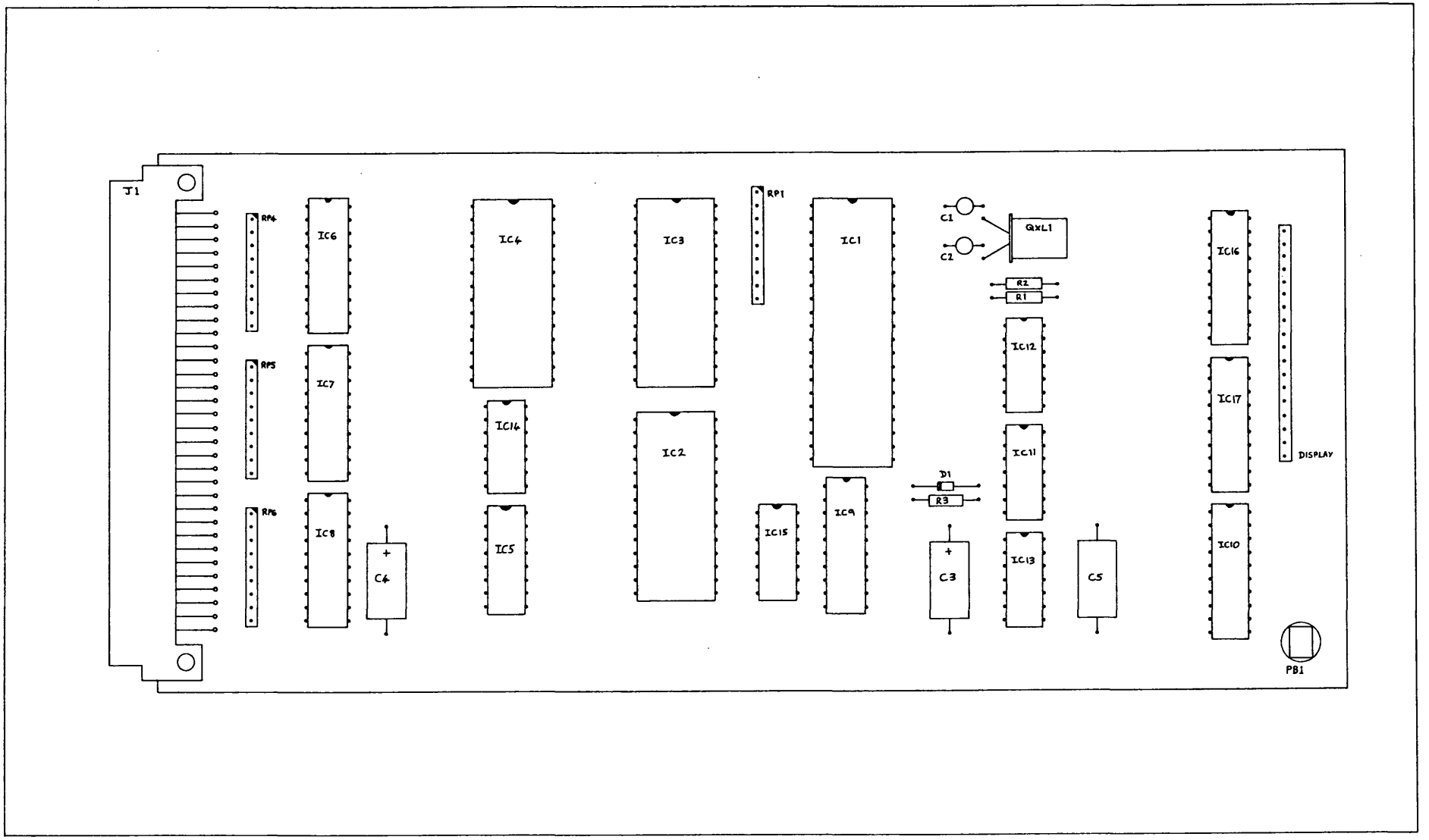

Z80 microprocessor board component layout Figure 8.11

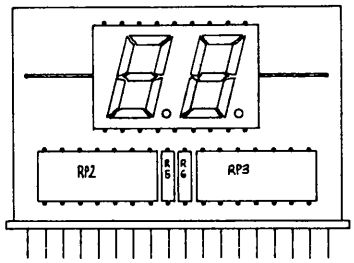

a) Display board component layout

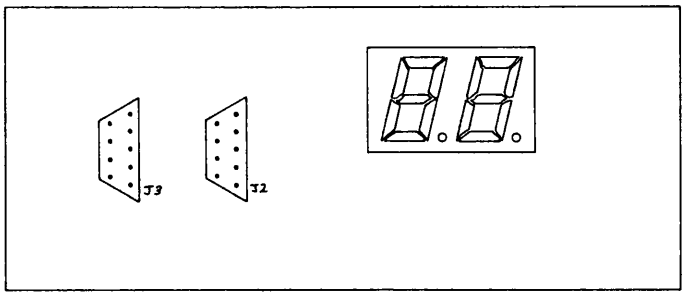

b) Front panel layout

Z80 microprocessor board front panel assembly Figure 8.12

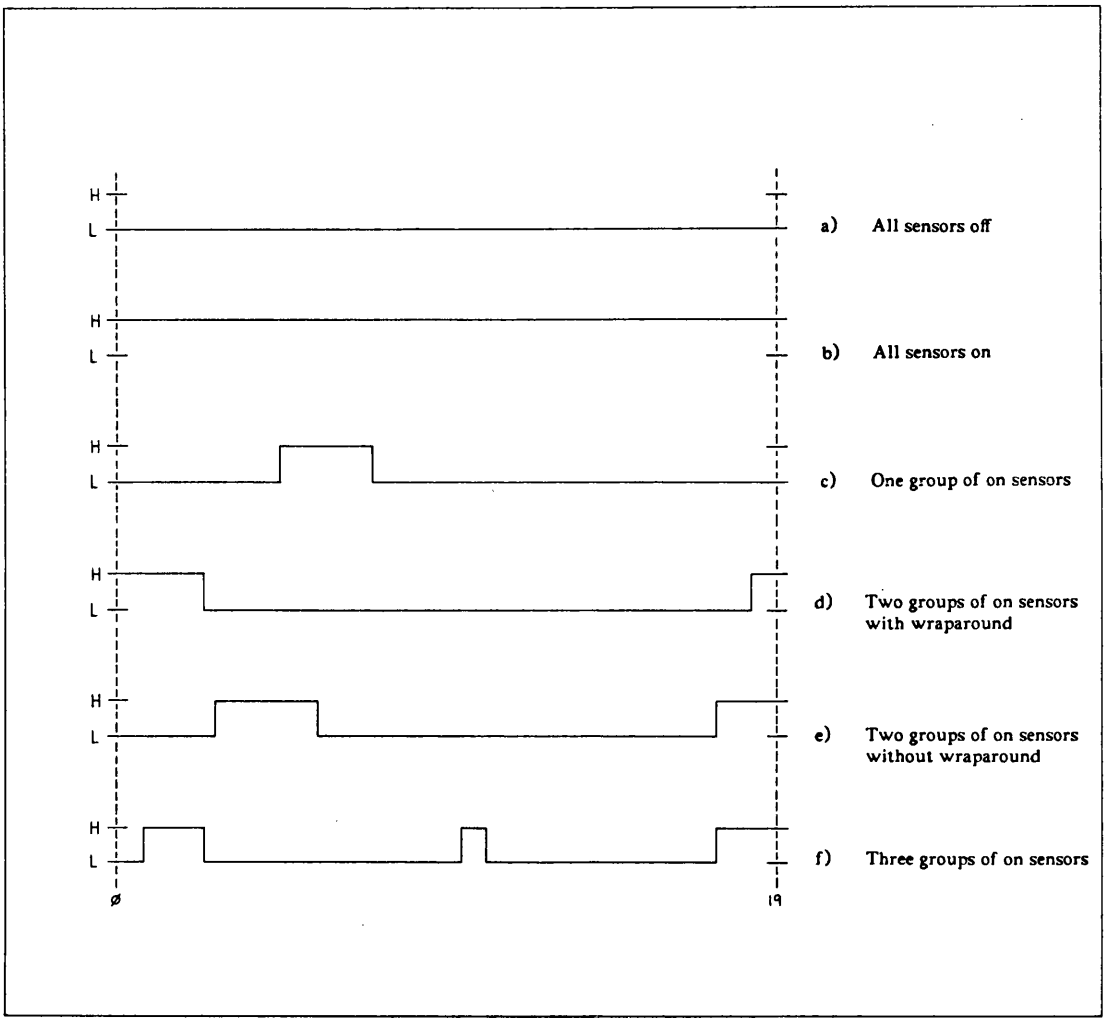

Sensor pattern categories Figure 8.13

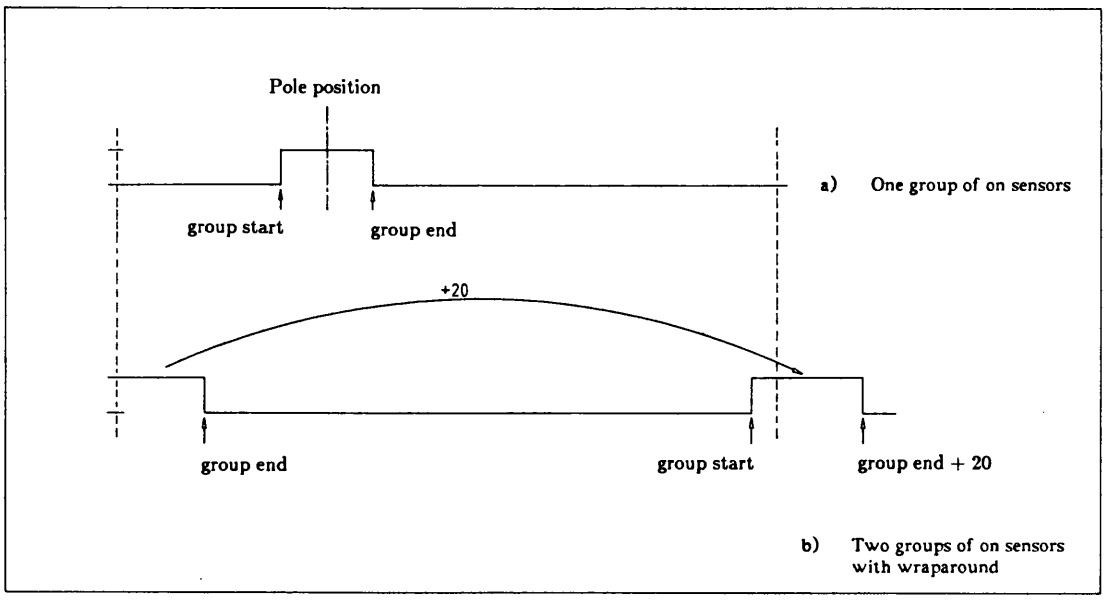

Sensor pattern decoding Figure 8.14

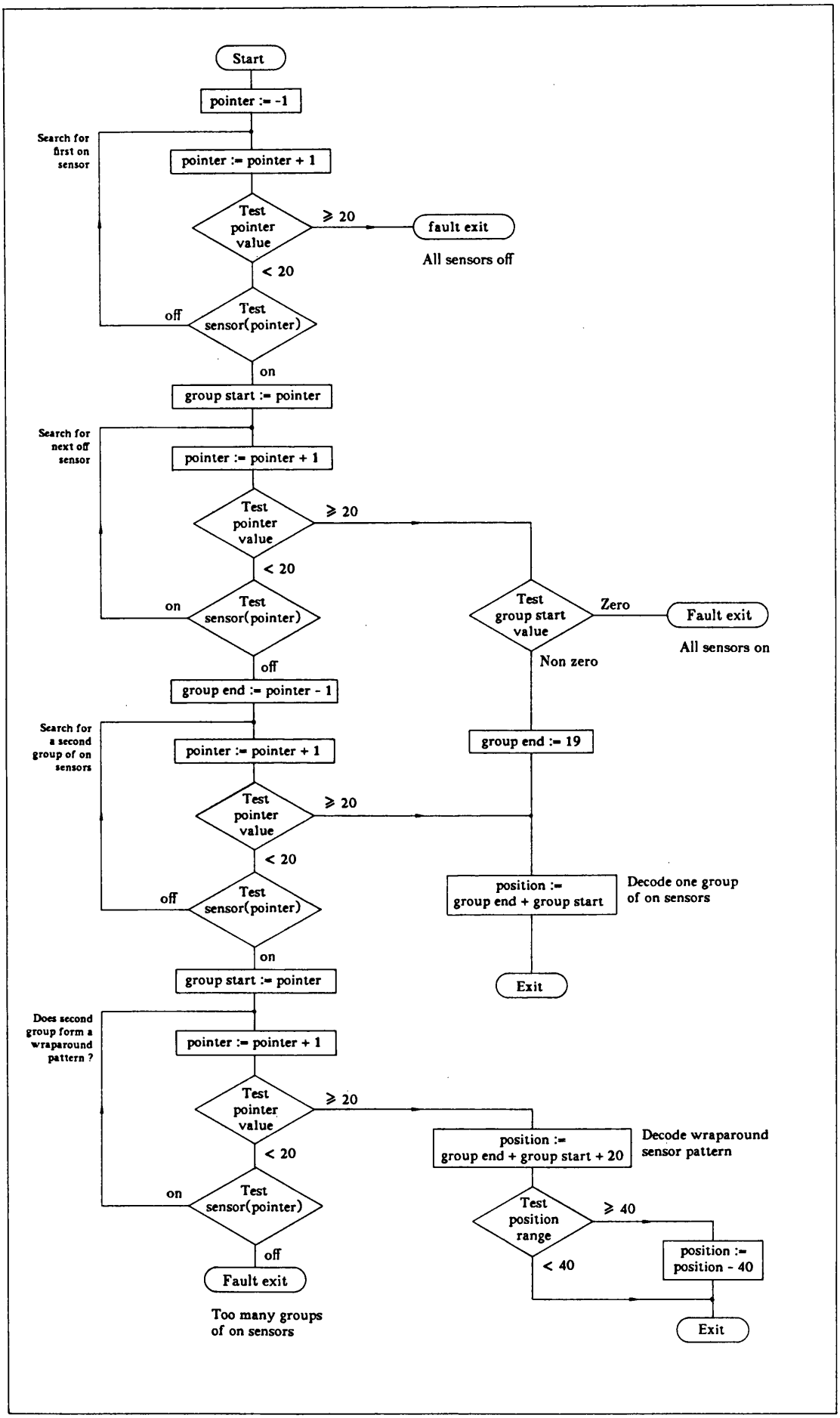

Flowchart of the position decoding algorithm Figure 8.15

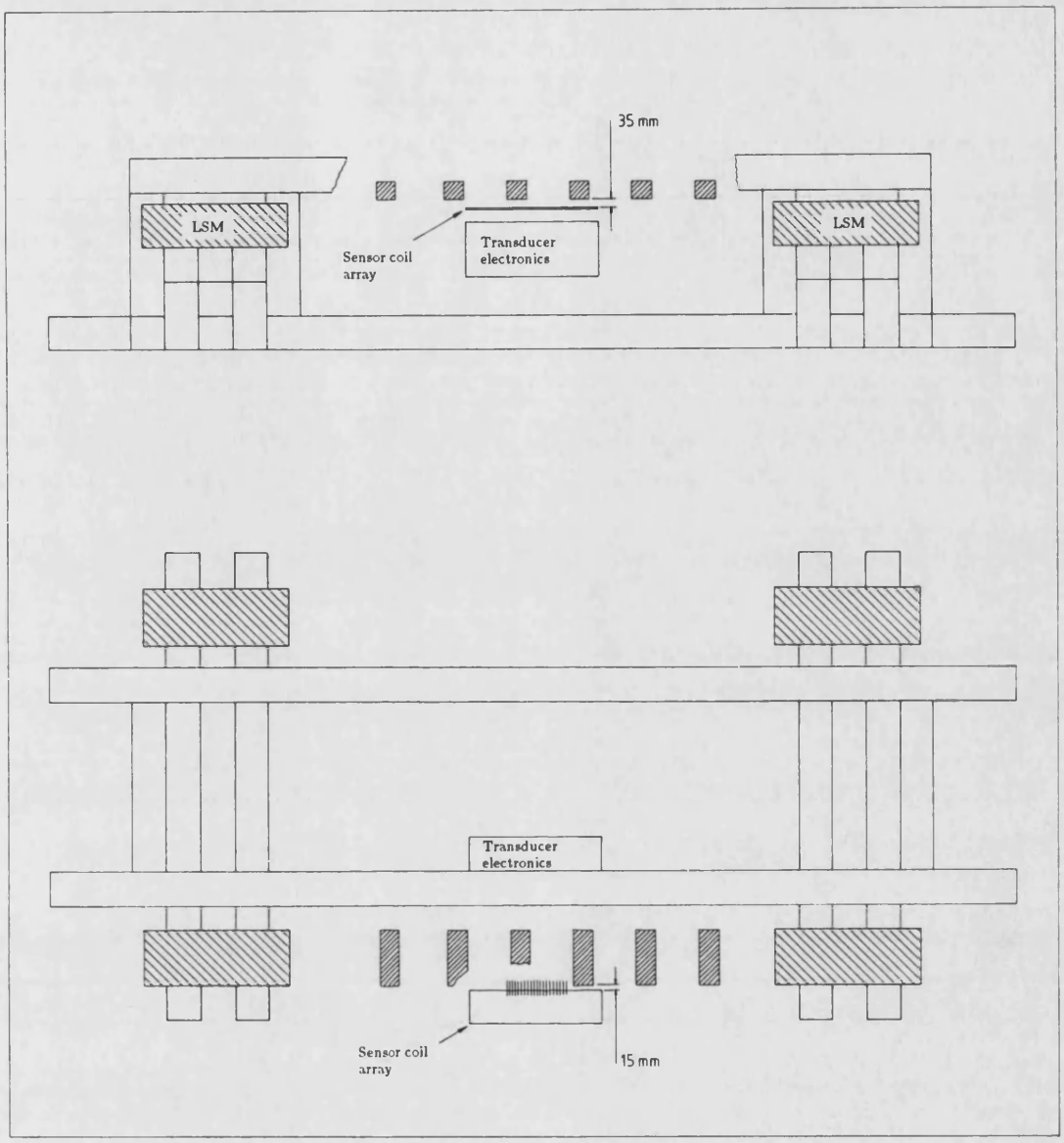

Mechanical alignment of the pole position transducer system Figure 8.16

9. Combined vehicle testing

Testing of the vehicle in combined levitative and tractive modes will now be carried out. This was achieved by combining the levitation and side mode controllers used in chapter 7 with an additional tractive mode position controller which could move the vehicle to any desired position on the track. Because only a short length of track was available, it was considered impractical to implement a velocity controller as this would not give adequate control of the rest position of the vehicle. The controller discussed will incorporate and demonstrate regenerative braking - an essential feature of any levitated vehicle in which there is no physical contact with the track.

An additional switching or *bang-bang* controller was also implemented to continuously cycle the vehicle between two track positions at constant maximum thrust. This controller would subject the vehicle to consistently high rates of acceleration, and was therefore useful when investigating any interaction effects that might exist between the levitative and tractive modes of the vehicle.

The effects of track irregularities encountered when moving the vehicle will also be demonstrated.

9.1 The LSM in the tractive mode

Provided that the pole position transducer discussed in chapter 8 is used to maintain the linear synchronous motors at a constant torque angle of $\pm 90^{o}$, then the tractive thrust from each motor is proportional to the product of the d.c. field current and the rms value of the corresponding 3-phase armature current. Hence by maintaining the d.c. field current at a reasonably constant level (consistent with steady lift), the behaviour of the LSM is similar to that of a simple d.c. motor. Additionally, by reversing the polarity of the 3-phase armature currents (*not* the phase sequence), the a.c. flux distribution of each LSM primary member will be inverted and the torque angle will toggle from $+/-90^{o}$ to $-/+90^{o}$. This has the effect of reversing the direction of thrust (see section 2.1.1 and figure 2.3), thus providing a forward/reverse facility

and regenerative braking mechanism.

It follows that, in order to maintain full control of the linear synchronous motors in the tractive mode, a controller must provide two output signals to the 3-phase inverter.

1. A proportional demand signal for setting the rms level of the 3-phase armature currents. This would provide the LSM thrust control.
2. A polarity demand signal for controlling the thrust direction.

Further, to provide closed loop control, the tractive mode controller inputs would include position and velocity feedback signals derived from the pole position transducer reading.

9.2 Position and velocity signals in the tractive mode

Relative position and velocity signals were derived from the pole position transducer signal, which has a resolution of 5 mm and provides a six bit digital output representing the position of a secondary track member within the 0.2 m pitch of these members. This output rolls through zero and repeats as each track member passes over the sensor array.

9.2.1 Relative position measurement Because of the transducer roll over described above, the maximum relative position displacement that could be read directly was only 0.2 m. In order to provide a position signal spanning more than one pitch of the track members, it was necessary to derive higher order bits using a software routine. Upon rollover of the transducer reading , these high order bits would be incremented or decremented in software according to whether the six bit position reading was increasing or decreasing respectively between sample intervals.

This requirement is identical to that encountered previously in chapter 5, in which it was necessary to derive the high order bits of the gap transducer readings by using a software routine in the form of an assembler macro definition called RD_GAP (see

section 5.7.4). By converting the six bit pole position transducer reading into an eight bit value (by multiplying by four or using two left shifts), it was possible to use the RD_GAP macro directly to provide a relative position signal in the range of 0 to ± 25 m in 5 mm steps. The gain of this position signal, K_p, was defined as follows,

$$K_p = \frac{1}{resolution}$$

where

$$resolution = \frac{0.2}{63 \times 4}$$

$$= 0.7936 \times 10^{-3}\ m/lsb$$

Hence

$$K_p = 1260 \qquad \text{equation 9.1}$$

This equation states that if the vehicle was moved one meter along the track, the position signal would indicate a relative change of 1260.

9.2.2 The velocity signal In chapter 5 a velocity signal for the side mode controllers was derived by evaluating the change in measured gap over the sample interval and then dividing this figure by the sample period T_s,

$$velocity = \frac{new\ position - old\ position}{T_s}$$

However, with a sample period of 1 ms, and because the position signal in the tractive mode is quantised into 5 mm steps, it can be seen that the position signal over one sample interval would never change by more than the quantisation level at speeds below $5\ ms^{-1}$. A more meaningful velocity signal was derived by accumulating the changes in position over fifty sample intervals and then dividing this accumulated total by the time interval of 50 ms (i.e. multiplying by 20). The velocity algorithm using this technique is illustrated by the flowchart of figure 9.1.

Note that this method of accumulating position changes over an extended time interval ensures that the velocity signal is of a high quality, having very low levels of

differentiation noise.

9.3 The LSM thrust constant

It was stated previously that the tractive mode thrust produced by each LSM when operated at a constant torque angle of $\pm 90^{o}$ would be proportional to the product of the d.c. field current and the a.c. armature current. Now for design purposes the values of d.c. field current in each of the four motors have been assumed to be equal and constant, corresponding with that required to support the total vehicle mass in steady state conditions. It follows that the tractive thrust produced by each LSM can then be related to the corresponding a.c. armature current by a thrust constant K_m.

$$F = K_m I$$

where

F is the LSM tractive thrust

I is the armature current (rms)

K_m is the LSM thrust constant when levitated

During the vehicle testing carried out in this chapter, only two of the four linear synchronous motors were used in the combined levitative and tractive modes. This arrangement was found to be more than adequate, with the combined thrust of the two motors providing good acceleration of the vehicle.

Using two motors at one end of the vehicle, the total tractive thrust F_T of the levitated vehicle can be expressed using equation 9.2 below,

$$F = 2K_m I \qquad \text{equation 9.2}$$

Now the linear synchronous motors were wired in pairs, with the a.c. armature windings of each motor pair connected in a three wire series-star configuration. This ensures that under ideal operating conditions (i.e. constant and equal field currents) the two tractive mode linear synchronous motors will operate at equal thrust levels. In practice, however, the d.c. field currents of individual motors are not constant and

will vary to cope with unbalanced vehicle loading or track irregularities. This will cause a thrust imbalance which in turn will introduce an angular turning moment tending to rotate the vehicle about the yaw axis.

To counter this problem, it has been suggested[29] that the tractive mode thrust of each LSM should be controlled separately, taking into account the individual d.c. field currents of these motors when calculating the a.c. armature currents. There were three main reasons for not implementing the tractive mode controller in this way,

1. A separate 3-phase inverter would be required for each LSM
2. Any tendency for the vehicle to rotate during a thrust imbalance situation will be prevented by the yaw mode controller
3. An increase or decrease in the d.c. field current of any one LSM must be balanced by a corresponding decrease or increase in one or more of the remaining motors. This exaggerates the thrust imbalance, but at the same time also ensures that the total vehicle thrust remains reasonably constant

The combined thrust constant for the two motors was derived experimentally by measuring the tractive mode thrust of the levitated vehicle at various armature current levels. Control of the armature current was provided by the inverter reference input, V_{ref} , which is a d.c. voltage signal in the range 0 to 5.2 volts. The results from this test are included below in table 9.1 and are presented graphically in graph 9.1.

V_{ref} (V)	Armature current (A rms)	Measured thrust (N)
0	0	0
1.0	1.0	11
2.0	2.1	20
3.0	3.0	30
4.0	4.0	40
5.2	5.0	50

TABLE 9.1. Tractive mode thrust

The graph shows a highly linear thrust/voltage characteristic for all reference voltages included in the test. From the graph,

$$\frac{F_T}{V_{ref}} = 10\ N/V$$

When combined with the 0.02 V/lsb gain of the digital to analogue converter discussed in section 2.9, the overall gain of the LSM/inverter combination was written down as follows,

$$K_i = 10\ N/V \times 0.02\ V/lsb$$

$$= 0.2\ N/lsb \qquad \text{equation 9.3}$$

9.4 A position controller for the tractive mode

9.4.1 Vehicle model The total thrust F_T acting on the vehicle mass M produces a linear acceleration $\ddot{x}_T$ as follows,

$$F_T = M\ddot{x}_T$$

or

$$x_T = \frac{F_T}{Ms^2} \qquad \text{equation 9.4}$$

Note that the vehicle model represented by equation 9.4 does not include a friction or velocity damping term. This was because the majority of vehicle friction was considered to be due to several cable harnesses trailed from the vehicle, and, whilst this friction is not insignificant, it would be difficult to determine an actual or representative figure.

To compensate for this omission, the position controller would be designed to have an underdamped second order dominant response. The vehicle friction would then provide the additional damping required to ensure a well damped overall vehicle response.

9.4.2 Control strategy A block diagram of the control strategy used for the tractive mode position controller is provided in figure 9.2. Using a linear gain to represent the inverter, it can be seen that the inverter/vehicle combination gives a second order

plant, hence there are two states available for feedback - position and velocity.

9.4.3 Controller design With reference to the controller block diagram of figure 9.2, the characteristic equation for the tractive mode position controller was written down as follows,

$$s^2 + \frac{KK_i K_p h_1}{M} s + \frac{KK_i K_p}{M} = 0 \qquad \text{equation 9.5}$$

The controller gains K and h_1 were then set by comparing the coefficients of this characteristic equation with the standard second order form given below,

$$s^2 + 2\zeta\omega_n s + \omega_n^2 = 0$$

Equating coefficients,

$$2\zeta\omega_n = \frac{KK_i K_p h_1}{M} \qquad \text{equation 9.6}$$

$$\omega_n^2 = \frac{KK_i K_p}{M} \qquad \text{equation 9.7}$$

where

$K_i = 0.2$

$K_p = 1260$

$M = 390\ kg$

Equation 9.7 suggests that the value of ω_n can be set arbitrarily by using any value of K. In practice, however, the value of K must be constrained to ensure that the maximum expected error does not exceed the maximum demand that can be accepted by the inverter (corresponding to the DAC limit of 255). Now with the short test track available it was suggested that the maximum positional error would not exceed 1 m. Hence the maximum value of K was set as follows,

$$K_{max} = \frac{255}{1 \times 1260}$$

$$= 0.2 \qquad \text{equation 9.8}$$

Using $K = K_{max}$ and substituting values of K_i, K_p and M, the corresponding maximum value of ω_n was then set according to equation 9.7.

$$\omega_n = \left\{ \frac{0.2 \times 0.2 \times 1260}{390} \right\}^{1/2}$$

$$= 0.36 \qquad \text{equation 9.9}$$

Re-arranging equation 9.6, and using $\zeta = 0.2$ to give the required underdamped response (see section 9.4.1), the remaining controller gain, h_1 was calculated as follows.

$$h_1 = \frac{2\zeta\omega_n M}{KK_i K_p}$$

$$= \frac{2 \times 0.2 \times 0.36 \times 390}{0.2 \times 0.2 \times 1260}$$

$$= 1.11 \qquad \text{equation 9.10}$$

9.4.4 Controller implementation To implement the above position controller design in software a translation routine was required to convert the bipolar controller output signal into an equivalent unipolar signal using separate forward/reverse control. The flowchart of figure 9.3 illustrates the conversion algorithm.

The tractive mode controller using this translation routine was then incorporated into the main vehicle control software used in chapter 7. The resultant combined vehicle control software provides simultaneous control of the four levitation modes (using flux feedback choppers), the two side control modes and the tractive mode. A full set of listings for the combined vehicle control software are included as listings 9.1 through 9.9 inclusive.

9.5 A switching controller using maximum thrust

A simple closed loop switching controller was also implemented in the combined vehicle software to cycle the vehicle between two track positions at maximum acceleration. This was achieved by issuing a continuous maximum thrust demand signal and then simply toggling the forward/reverse control of the inverter in accordance with two position switching boundaries. The flowchart of figure 9.4

illustrates the switching controller implementation.

9.6 Data logging

For logging the tractive mode data, it was necessary to modify the existing data logging software to provide greatly extended logging times. This was achieved by logging the required data once every ten sample intervals, thus extending the available logging time by a factor of ten whilst reducing the timebase resolution to 10 ms.

This means, for example, that the combined vehicle test software using a nine channel data logger (one timebase plus eight data channels) can record data continuously for up to 60 seconds whilst maintaining a resolution of 10 ms.

9.7 Results

Experimental results obtained from the combined vehicle presented in this chapter are discussed below.

9.7.1 Position controller step response Graph 9.2a shows the position-time response achieved by the tractive mode position controller during a series of four step response tests in which the levitated vehicle was moved by ± 0.3 m about a central point on the track.

Considering the first step input demand of +0.3 m, it can be seen that the response obtained from the vehicle is consistent with the required well damped second order dominant response specified in the controller design. The presence of a small amount of overshoot also demonstrates the action of regenerative braking, which would start when the controllers error signal changes sign at some point before the 0.3 m reference position is reached. Without this capability the tractive mode controller would be unable to oppose or reverse any vehicle overshoot, and would instead have to be re-designed to give a first order response.

When returning to the central track position the vehicle exhibited a slightly different response in that no overshoot was present. Similar differences in response were

obtained when the vehicle was moved in the other direction in response to a step input demand of - 0.3 m. Several factors should be considered when investigating the reasons for this position dependent response. These are,

1. Track irregularities such as dipped or raised sections
2. Local variations in friction due to movement of the cable harnesses trailing from the vehicle
3. Variations in the tractive thrust of individual motors as the vehicle negotiates a track irregularity

In practice, however, this minor uncertainty in the vehicle response at very low speeds would be of no consequence because the controller is still able to position the vehicle at any specified point on the track to within a few tens of millimetres.

9.7.2 Velocity signal Graph 9.2b shows the corresponding velocity-time response of the vehicle during the above step response test. This graph was included to illustrate the quality of the velocity signal that can be obtained at the relatively low velocities encountered during the test. The level of noise present in this velocity signal is directly related to the quantisation level of the pole position transducer reading from which it was derived. It follows, therefore, that this noise level will remain constant such that the overall signal quality will improve as the vehicle speed is increased.

9.7.3 Heave and pitch interaction Graphs 9.2c and 9.2d show the position-time responses of two of the levitation modes (heave and pitch respectively) during the above step response test. These graphs were included to record the level of interaction that takes place between the levitative and tractive modes whilst moving the vehicle along the track using the tractive mode position controller. The graphs illustrate, however, that no measurable interaction took place during the test.

9.7.4 Motor flux density demands Graphs 9.3a through 9.3d inclusive show the individual flux density demands issued to each of the four levitation motors during the above step response test. Note that these graphs are laid out on the paper in correct vehicle order. It is hoped that this layout will provide a better understanding of the vehicle behaviour as it negotiates the different sections of track encountered during the test.

For the first five seconds of the test the vehicle is held at the central track position and each motor maintains an approximately constant flux density of between 0.6 and 0.7 T. When the vehicle is moved to a position 0.3 m along the track, the track twist encountered is so great that the levitation controller is forced to switch off motor 1 and back off the demand to motor 3 almost to zero in an attempt to prevent the track from moving towards these two motors. To compensate for this reduction in the overall lift force, the demand in motors 2 and 4 has been increased almost to the limiting value of 1.0 T. To summarise, the vehicle ends up fully supported on just two diagonally opposite motors whilst a third motor provides the small amount of corrective force required to maintain the correct vehicle attitude. After about fifteen seconds, the vehicle returns to the central track position and the levitation controller restores the original flux density demand levels.

The effects of track twisting are also apparent when the vehicle is moved by 0.3 m in the other direction, although in this case the required changes in motor flux density are much less pronounced.

9.7.5 Switching controller test Graphs 9.4a through 9.4d inclusive show the responses of various vehicle modes (position, velocity, heave and pitch respectively) obtained from the levitated vehicle when running the maximum thrust switching controller discussed in section 9.5.

These graphs indicate that a small amount of disturbance is introduced to the heave and pitch modes of the levitated vehicle when this controller is used. Note, however,

that the disturbance only occurs as the vehicle is brought back to the center of the track from the + 0.4 m position. It has previously been shown (see section 9.7.4) that when using this section of track the vehicle is supported on only two motors. It follows, therefore, that the levitation controller would be less able to maintain the correct vehicle attitude whilst negotiating this track section at maximum thrust.

9.7.6 Flexible track test The construction of the vehicle track was such that alternate supports could be removed to make the track more flexible. Graphs 9.5a and 9.5b show the position-time responses of the heave mode during levitation of the vehicle on the standard and flexible track respectively.

The results presented in graph 9.5b clearly show that the actual levitation of the vehicle is virtually unaffected by the increased track flexibility. Once levitated, however, a high frequency resonance can be seen to build up which, whilst not shown in the graph, would invariably cause loss of vehicle stability. After running this test several times it became apparent that the unwanted resonance was confined to the track itself, although the excitation of this resonance would undoubtedly originate from the vehicle.

9.7.7 The effects of low supply voltage The power supply for the eight slitwidth modulated choppers used on the vehicle was provided by a single 48 V rechargeable lead-acid battery pack. By monitoring this battery voltage it was established that the combined vehicle would remain stable for all supply voltages down to 30 V, at which point control would be lost because the levitation choppers stop modulating. This was because the chopper aiming current of V_s/R falls below the current level required to maintain the desired flux density.

It is of perhaps greater importance to note that a decreasing chopper supply voltage causes the chopping frequency to fall considerably due to the action of the slitwidth modulator. This can become a problem if the frequency of one or more choppers falls sufficiently to excite various unwanted track or vehicle resonances, which could lead to

vehicle instability.

9.8 Conclusions

The main aim of this chapter was to provide the vehicle with a simple form of closed loop tractive mode controller which would then be combined with the existing levitation and side mode controllers to demonstrate the vehicle in a combined levitative and tractive mode.

Results obtained from the combined vehicle tests described above indicate that the present vehicle arrangement (in which the center of gravity of the vehicle is coplanar with the linear synchronous motors) exhibits no interaction between the levitative and tractive modes. Disturbances to the levitation modes do arise, however, when the vehicle negotiates a section of track which is too twisted for the vehicle to follow under full control. In this case it was demonstrated that the vehicle could end up fully supported on just two motors, with a third motor providing the small balancing force required to maintain the correct vehicle attitude. This result is of particular significance because it indicates that the levitation controller is able to maintain the correct vehicle attitude regardless of most track irregularities (provided that these irregularities can be accommodated within the available gap of 7 mm). Further, by using flux feedback choppers, the massive variations in the operating point of individual motors required to negotiate these track irregularities will not compromise vehicle stability.

Due to the short length of track available the implementation of a velocity controller for the tractive mode was considered impractical, although the availability of a suitable velocity feedback signal was adequately demonstrated. It is proposed that a vehicle operating on a less restricted track would use this signal to provide closed loop velocity control when operating between distant stopping points on the track. A position controller such as that described in this chapter could be used for accurate low speed control when the vehicle approaches a stopping point.

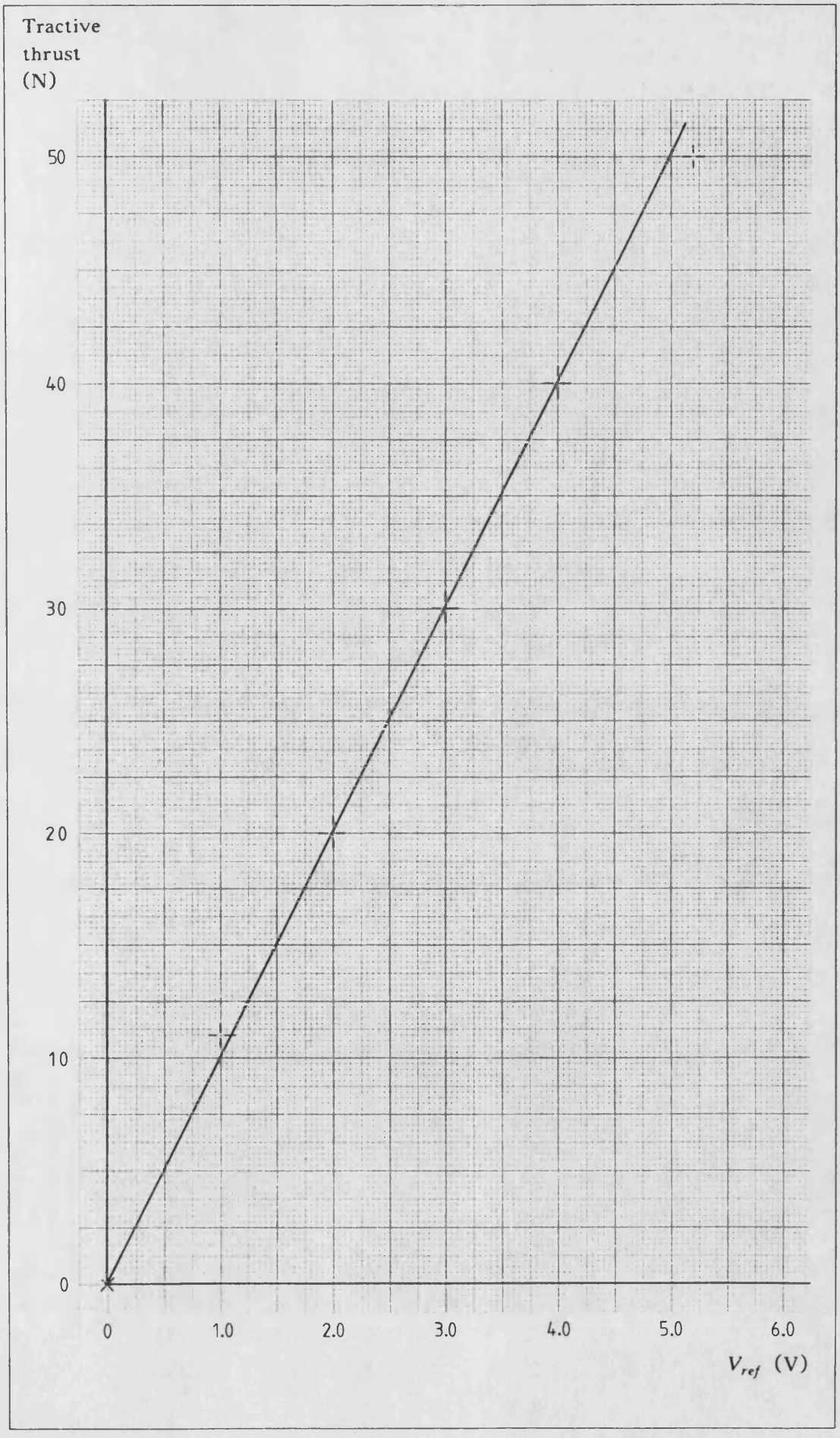

Tractive mode thrust Graph 9.1

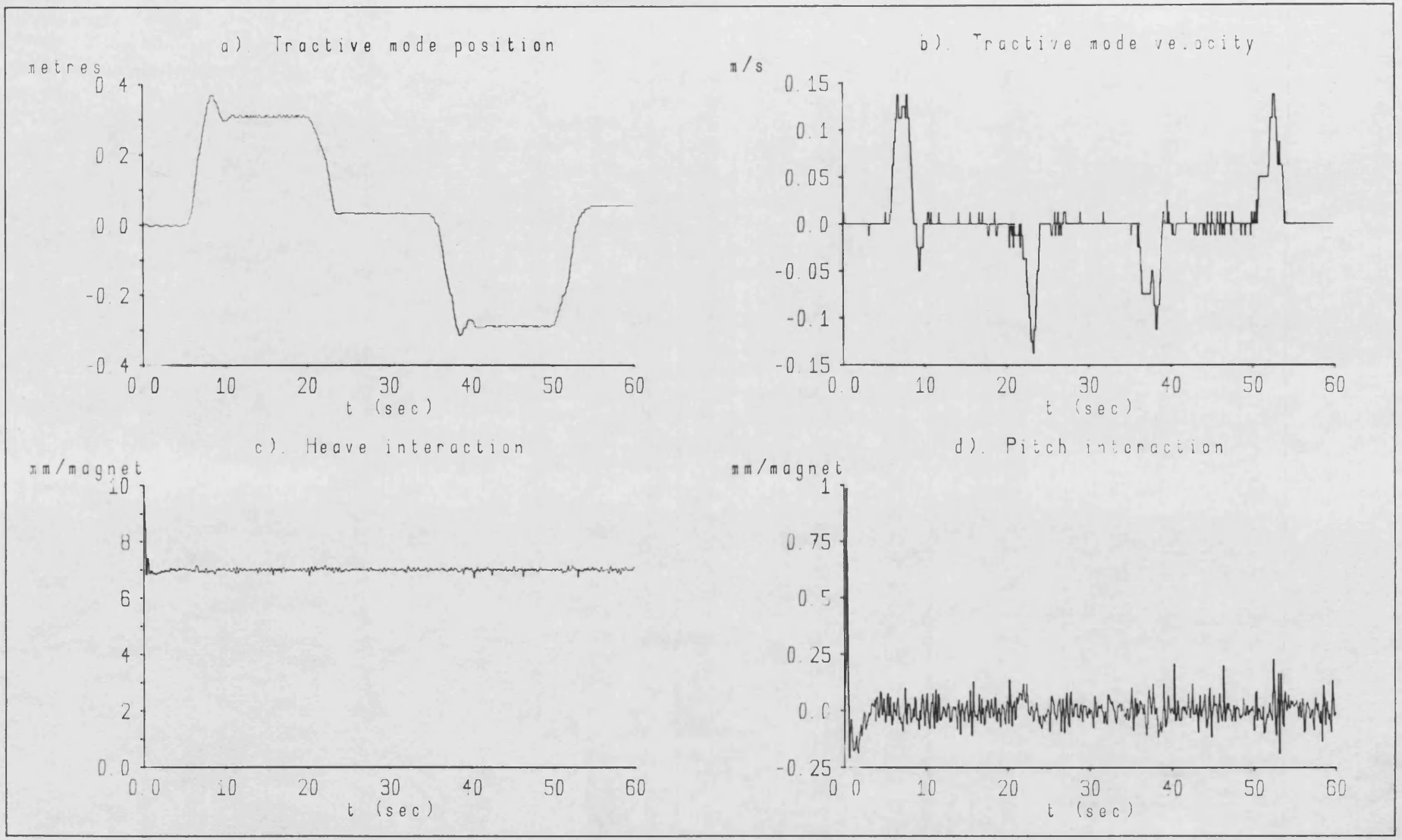

Position controller step response Graph 9.2

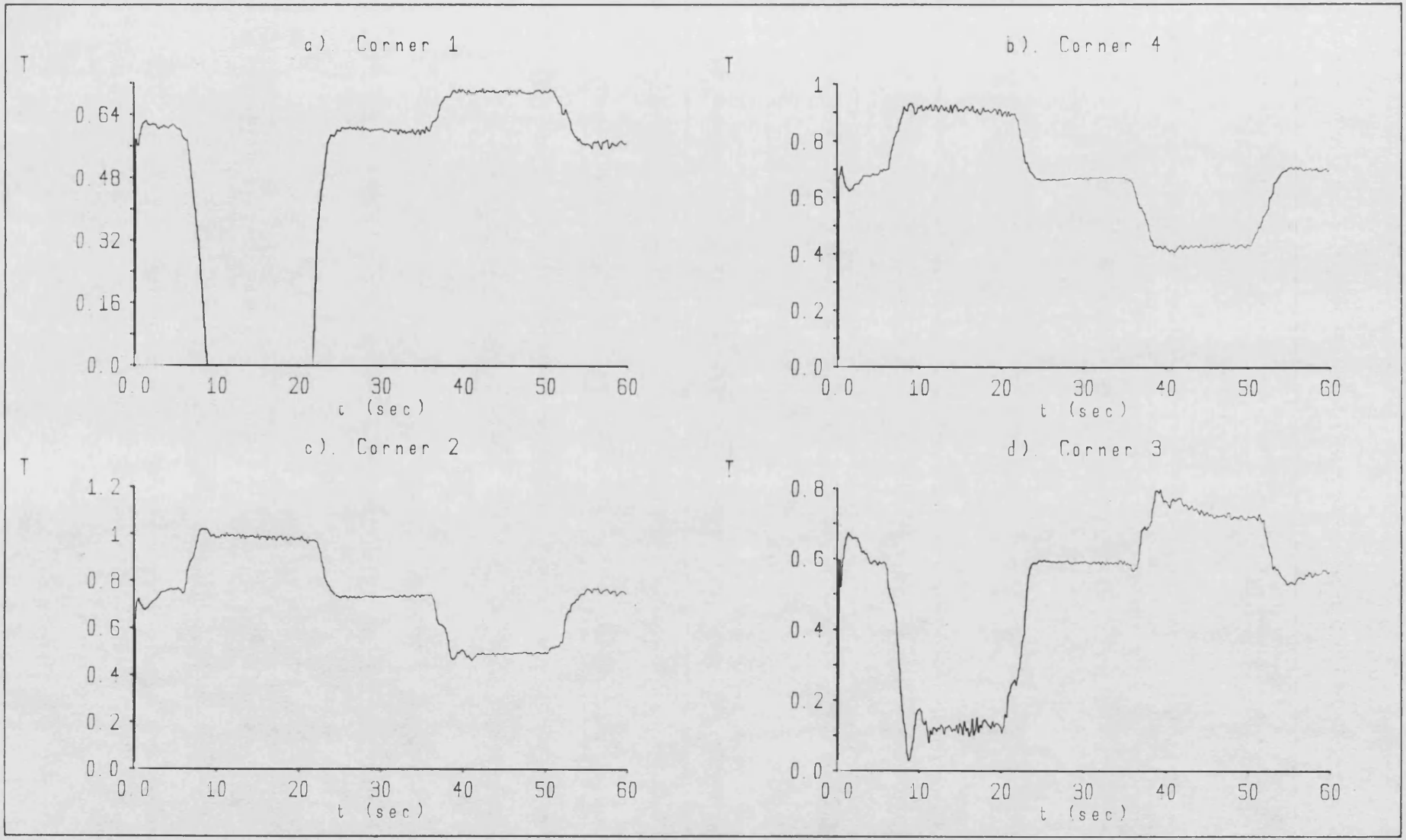

Motor flux density demands Graph 9.3

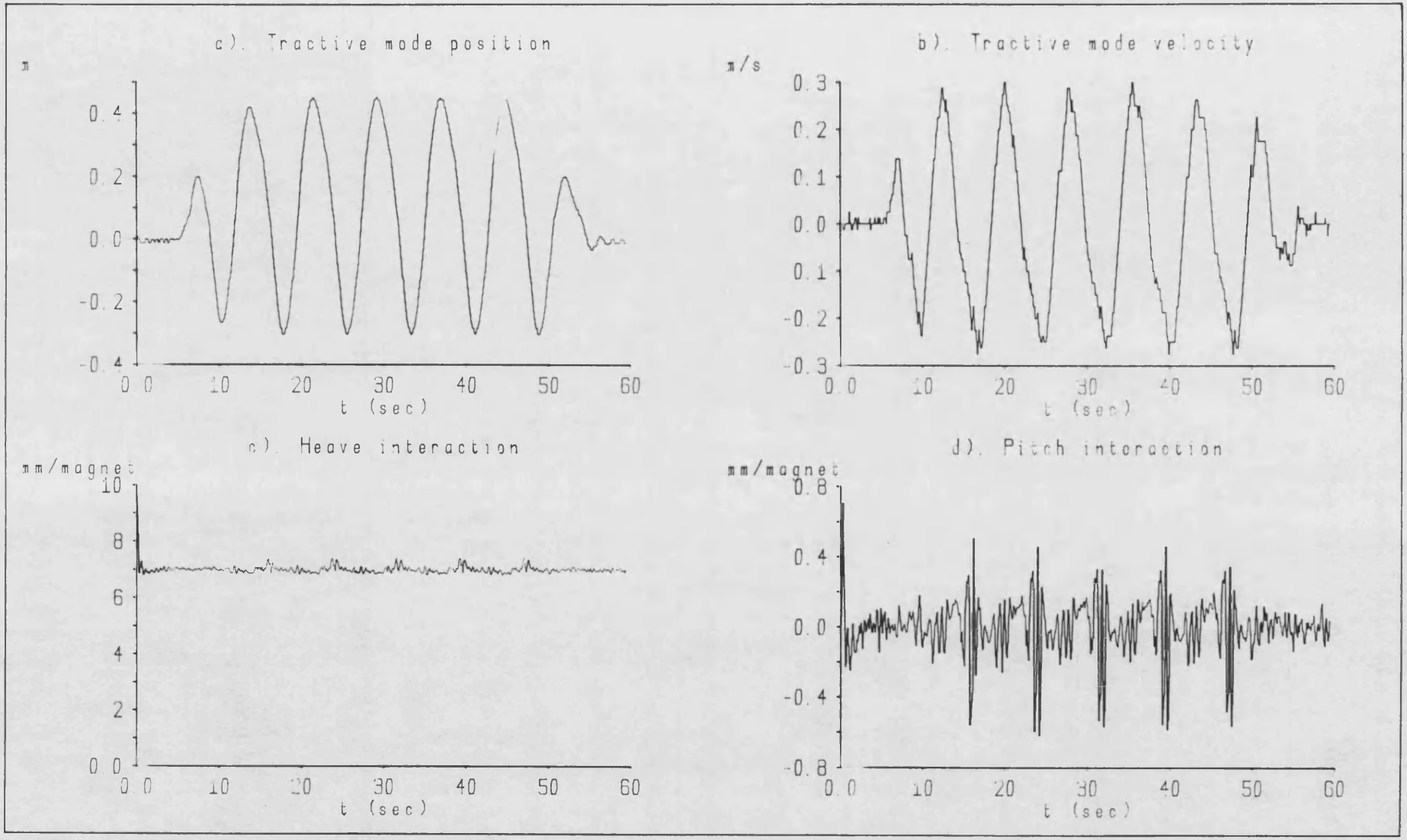

Switching controller response Graph 9.4

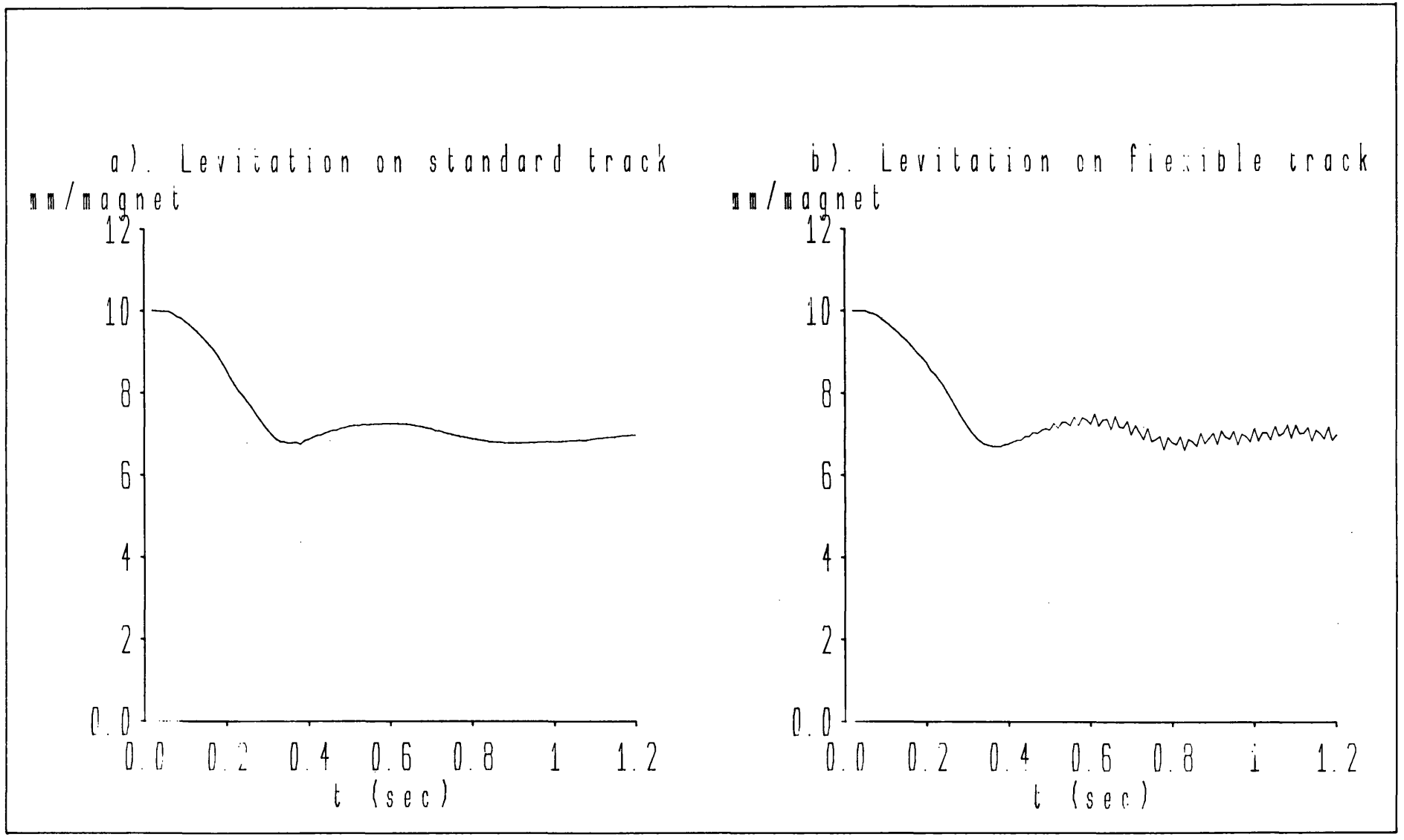

Levitation tests using standard and flexible tracks **Graph 9.5**

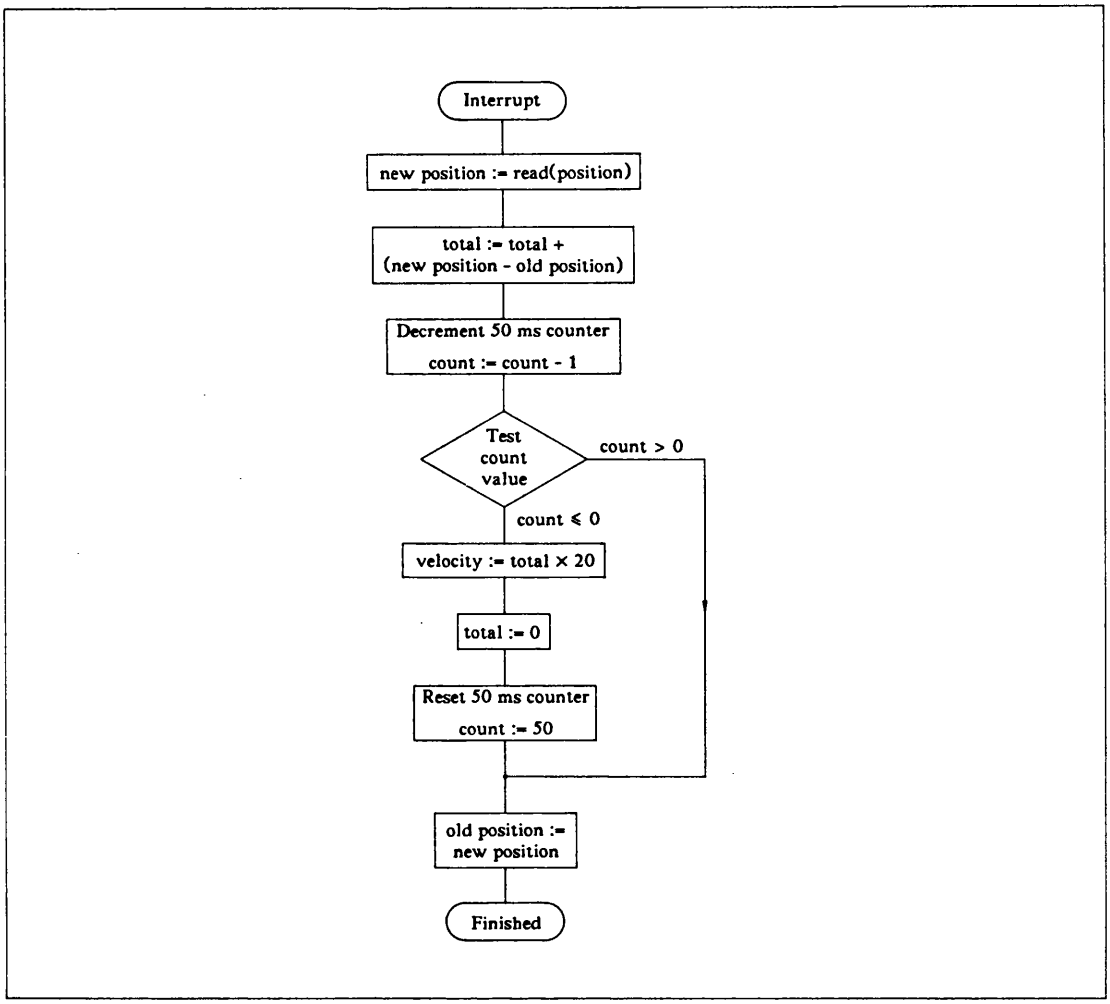

Flowchart for velocity signal derivation Figure 9.1

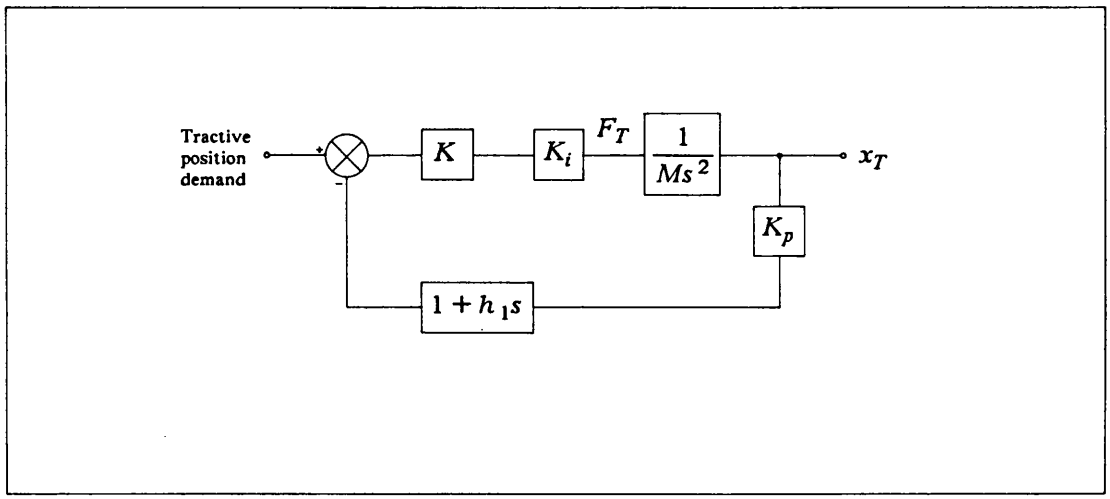

Block diagram of the tractive mode position controller Figure 9.2

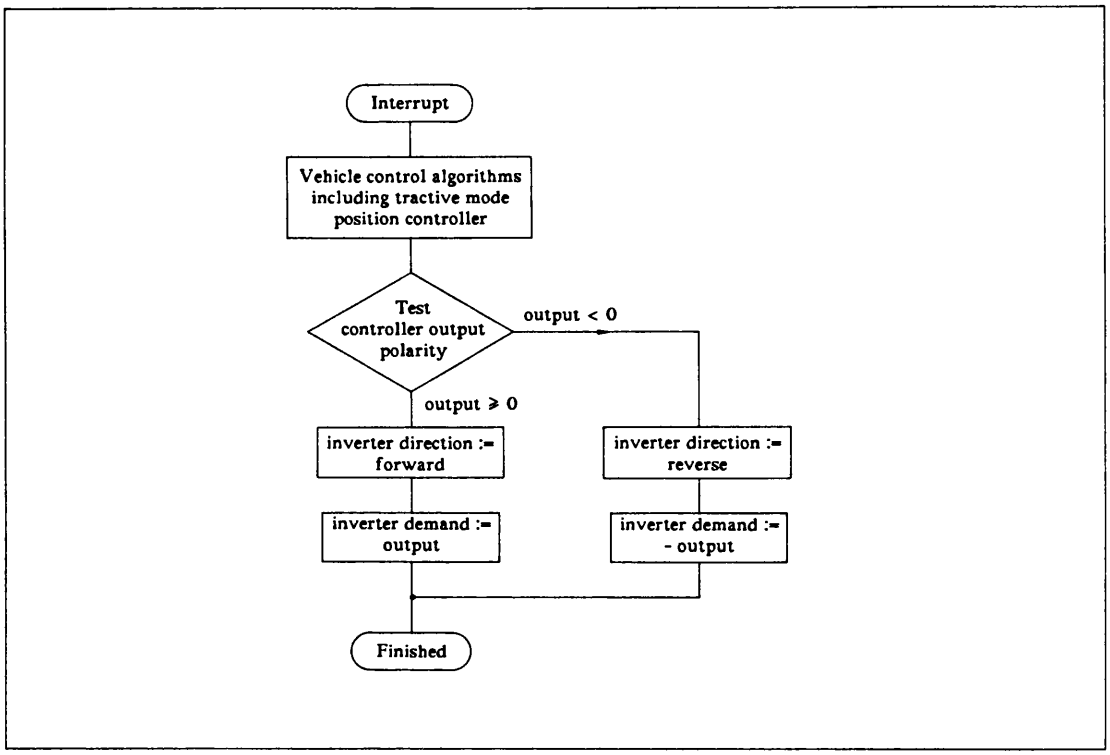

Flowchart showing forward/reverse control of the inverter Figure 9.3

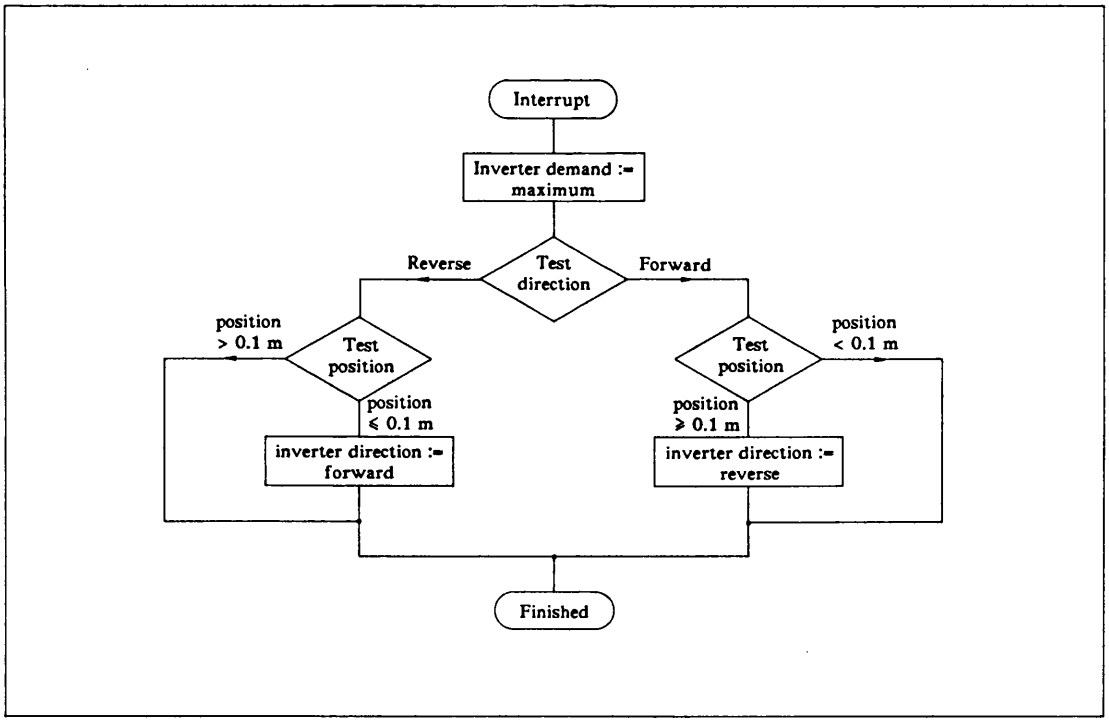

Flowchart of the switching controller Figure 9.4

10. Conclusions

This thesis has described the design of a real-time digital control system for a quarter scale magnetically levitated vehicle propelled by four linear synchronous motors. The approach to implementing the controller has proved successful and provides a fully working vehicle capable of operating in combined levitative, lateral guidance and tractive modes. It is hoped that the overall system will prove useful in the development of future digital control schemes requiring a multiprocessor implementation.

10.1 Software

One of the most important aspects of the controller design has been the development of a generalised set of structured digital filter algorithms in the form of macro definitions for a standard 68000 conditional macro assembler. These definitions make extensive use of conditional assembly facilities to generate highly optimised control code for any given controller design, thus ensuring maximum controller throughput whilst maintaining good program structure and readability. This approach has been crucial to the rapid development of the various control schemes described in this thesis and also ensures that very robust programs are produced.

The development of a multi-channel continuous data logging facility was also described, which could be incorporated into the digital control software to provide simultaneous logging of any number of internal control parameters. In addition to recording the sample results presented in this thesis, this tool has also considerably simplified the commissioning of the overall vehicle control system.

Measurements of individual processor workloads show an acceptable margin for incorporating minor software modifications on the present system. More extensive upgrading can be accommodated either by adding a third processing node or by using faster microprocessor devices in the existing nodes.

10.2 Hardware

The use of a multiprocessor system has allowed a complex digital control scheme to be performed in real-time by several low-cost general purpose microprocessors operating in parallel. Further, the completely shared memory architecture of this multiprocessor system allows data structures to be passed by reference only, thereby minimising the overheads associated with inter-processor communication. The corresponding interface hardware provides an efficient working environment for the digital control software, with many of the transducer boards incorporating a high degree of parallelism to ensure that controller input-output requirements are met.

10.2.1 Flux feedback chopper Flux feedback choppers were introduced for controlling the gap flux of the linear synchronous motors. This effectively eliminates the gap dependent gain characteristic of the chopper/motor combination and makes the corresponding levitation controller much more robust when handling large gap excursions. Another advantage is that any variations in gap flux, due to disturbances of the airgap for example, are corrected in the shortest possible time by the chopper control electronics.

It is worth noting that the vehicle has not gone unstable since the levitation control system was modified to include flux controlled motors, whereas instability was previously a recurring problem.

10.2.2 The pole position transducer system A prototype pole position transducer system specifically designed for providing closed loop torque angle control of a linear synchronous motor propelled vehicle was successfully demonstrated. The induction balanced metal detection system upon which the transducer was based has proved very satisfactory under all operating conditions thus far encountered.

11. Future work

Having established the reliability of the vehicle models and control system, some suggestions for future work will now be given. These are presented in order of importance, with the first two being considered essential if the vehicle is to be used in any practical application.

11.1 Twist mode velocity damping

The present vehicle control strategy makes use of acceleration, velocity and position feedback signals to provide stable control of the vehicle in each of the four levitation modes. This strategy was originally introduced to allow a flexible vehicle chassis to follow track irregularities by maintaining the air gaps of individual linear synchronous motors at a precise 7 mm. This was thought to present the prospect of less restrictive track tolerances and reduced civil engineering costs.

In practice, however, the vehicle has proved to be relatively inflexible. This has been shown to make the force contributions of individual motors very sensitive to the track contour and a particular case was demonstrated in which the vehicle negotiated a twisted track section supported by just two diagonally opposing motors.

A preferrable control strategy for a rigid vehicle would be to provide a stable twist mode controller incorporating some form of velocity damping. Using this technique, the vehicle chassis would be kept flat and track irregularites would then be accommodated by adjusting individual motor gaps within the available 10 mm range.

11.2 Passenger comfort

The passenger comfort provided by a magnetically levitated vehicle is determined by the suspension characteristics implemented by the corresponding levitation control scheme. Now the present vehicle uses a levitation controller comprised of four very fast second order dominant position control loops. Further, because these controllers use track referenced position feedback signals, it follows that the vehicle chassis will

observe most of the track irregularities and a very uncomfortable ride will result.

To overcome this problem, an alternative set of position feedback signals must be derived from the vehicle mounted accelerometers. Used in isolation, these would ideally provide a perfectly flat vehicle ride. In practice, however, the vehicle must be made to follow the track within the restrictions imposed by the available airgap. It follows that some form of combined position feedback signal must be used which is comprised of a track referenced d.c. component and an accelerometer derived a.c. component. This would be achieved in software by using a crossover filter between the two signals. The response of this filter would be chosen according to a given suspension characteristic.

11.3 Condition monitoring

In addition to implementing the vehicle control scheme, the multiprocessor system software could be extended to include an independent condition monitoring program running on a separate processing node. This would be used to verify the correct operation of the vehicle hardware both before and during the levitation of the vehicle. At least two fault categories should be considered.

The first category would include outright failure of a transducer essential to the vehicle control system. This would be identified, for example, by taking transducer readings from all of the interface boards and then comparing these readings with the corresponding expected values. If such a fault was detected, the condition monitoring program would block any attempt to levitate the vehicle, or, if the vehicle was already levitated, would cause the vehicle control system to abort.

The second category would include less serious faults that can be tolerated by the vehicle control system. A good example of this fault is the transducer glitch. By using separate glitch counters for each of the transducer channels provided by the interface boards, the condition monitoring program can record transducer reliability data. This

data can then be used to identify any transducer problems before they become disabling faults.

This latter fault category is particularly relevant to the gap measurement system. It has been found that the ultrasonic transmitter/receiver units used by this system will degrade after prolonged use, resulting in occasional output glitches. This degradation eventually renders the gap measurement channel useless, and the corresponding ultrasonic transmitter/receiver pair must be replaced.

11.4 Multivariable control

With seven independently controlled modes, the present vehicle control system is an obvious candidate for the application of multivariable control techniques[30,31]. These techniques can be used to decouple the interacting modes of a multivariable system by introducing appropriate cross-coupling terms between the corresponding control loops.

The vehicle arrangement discussed in this thesis, however, does not exhibit significant interaction problems and it would be difficult to assess the advantages offered by a multivariable control system.

11.5 Analogue pole position transducer system

To provide closed loop torque angle control of a linear synchronous motor, the 3-phase inverter units require two sinusoidal reference signals phase displaced by 120°. The present system achieves this by using the digital output of a microprocessor-based pole position transducer to provide the common address bus for a pair of EPROM devices containing sinewave lookup tables.

When setting up the prototype pole position transducer system, it was noted that the individual receiver circuits could be calibrated to produce an approximately sinusoidal output-position characteristic (see graph 8.1c). It follows that two receiver circuits connected to appropriately positioned sensor coils could be used to derive the two reference sinusoids required by the inverter. This presents the prospect of greatly

simplified pole position transducer and 3-phase inverter systems requiring no digital electronics.

Appendix A Principal parameters of the LSM d.c. windings and side magnets

The main parameters of the LSM d.c. windings and side magnets used in this study are listed below.

LSM d.c. windings

1. The d.c. field winding of each motor is comprised of two series connected windings (one per limb), with 91 turns per winding.

2. The main dimensions of the linear synchronous motor are provided in figure A.1. With reference to this diagram the total area of the motor face *beneath the secondary track members* was written down as follows,

$$A = 4 \times 0.047 \times 0.060$$
$$= 11.28 \times 10^{-3}\ m^2$$

Side magnets

1. Each side magnet is comprised of two series connected windings (one per limb), with 107 turns per winding.

2. The main dimensions of the side magnets are provided in figure A.2. With reference to this diagram the total cross sectional area of the magnets was written down as follows,

$$A = 0.03 \times 0.05 \times 2$$
$$= 3 \times 10^{-3}\ m^2$$

Experimentally derived values of resistance and time constant for each of the four LSM d.c. windings and four side magnets are presented below in table A.1.

Corner	LSM d.c. windings		Side magnets	
	$R(\Omega)$	$\tau\ (sec)$	$R(\Omega)$	$\tau\ (sec)$
1	0.46	0.116*	0.3	0.036
2	0.46	0.076	0.3	0.046*
3	0.43	0.102	0.3	0.039
4	0.46	0.109	0.3	0.041

* worst case τ

TABLE A.1. Winding resistances and time constants

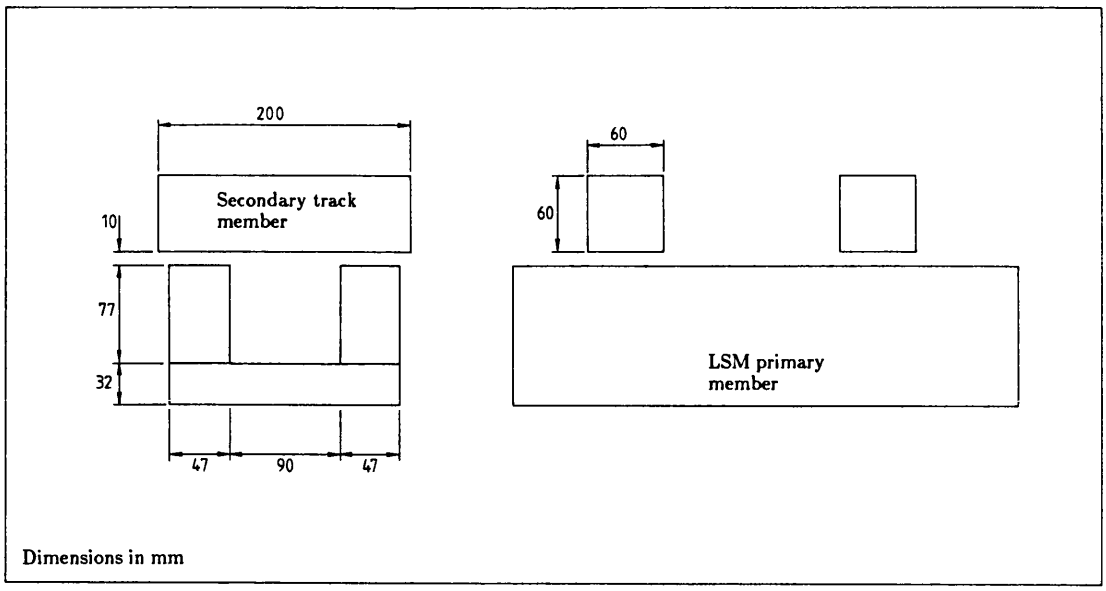

Main dimensions of the linear synchronous motors Figure A.1

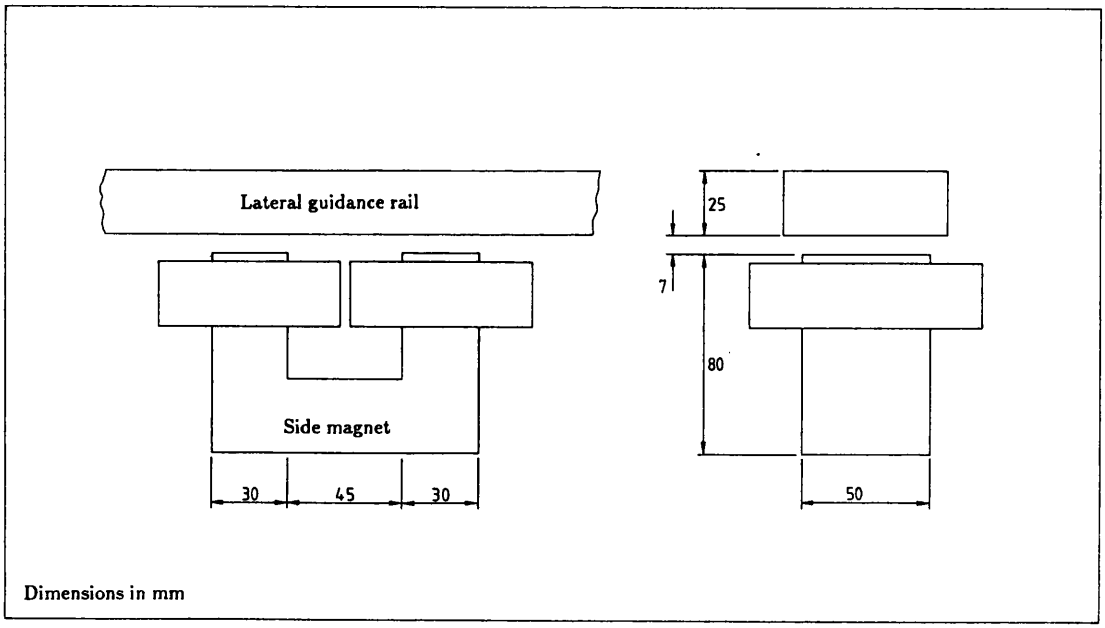

Main dimensions of the side magnets Figure A.2

Appendix B The phase measurement state machine

The phase measurement circuitry for the gap measurement board discussed in chapter 2 was implemented as a high speed synchronous state machine using the standard PROM/latch configuration[32]. The circuit was required to measure the time delay between an edge of a reference 20 kHz signal and the following edge of a second 20 kHz signal, called the return signal. This would correspond to measuring the phase difference between a reference and return pair of 40 kHz signals from which the 20 kHz signals were derived. The following general description of the state machine hardware is made with reference to the phase measurement state machine circuit diagram of figure B.1.

The 20 kHz reference and return signals provide the only two inputs to the state machine circuit, which was implemented using an octal latch, IC1, and a high speed bipolar PROM, IC2. The state machines single output line controls the clear input of an 8-bit counter, IC3, to time the delay between an edge of the reference signal and the next edge of the return signal. At the end of the timed interval an octal latch, IC4, is used to store the final count value. This is achieved by strobing the current counter value into the latch using the rising edge of the counter clear signal, which is taken high by the state machine at the end of the timed interval. Because the latch has zero set up time, there is no danger of the counter being cleared before the data can be transferred. A detailed description of the operation of the state machine hardware will now be given.

The lower three PROM data lines D_0, D_1 and D_2 are latched on every positive going transition of the 10.240 MHz clock to provide the high order PROM address lines A_5, A_6 and A_7 respectively. Hence on each active clock edge the lower three bits of data corresponding to the currently addressed PROM location are fed back to generate the new PROM address, thus selecting one of eight PROM locations. By programming appropriate data values into each of these eight locations, the state machine can be

made to follow a pre-defined sequence. In addition to the feedback generated address, the state machine can also make use of external address line inputs to select alternative pages in the PROM memory map. These pages can be programmed to contain variations in the standard state machine sequence, thus giving the state machine a conditional branch facility based on external inputs. For the phase measurement state machine, there were two external address line inputs, A_0 and A_1, corresponding to the reference and return 20 kHz signals respectively. Unused address lines A_2, A_3 and A_4 were tied low. The remaining PROM data line, D_3, was used as an output for controlling the reset line of the digital counter and strobe input of the octal latch.

The remainder of the state machine design is concerned with the procedure for generating the PROM contents to meet a given requirement. This was achieved using a formalised design procedure[32] in which the given problem is first fully specified as a timing diagram.

State machine timing diagram

The following description of the phase measurement state machine is made with reference to the timing diagram of figure B.2. This illustrates the various possible sequences of the reference and returned 20 kHz signals, which provide the two inputs to the state machine. Also shown is the required action of the state machine output, D_3.

A rising or falling edge of the reference 20 kHz input causes D_3 to go low, releasing the counter reset line and thus starting the count. The falling edge of D_3 has no effect on the positive edge triggered latch, which retains its most recent data corresponding to the final count value of the previous timed interval. Under normal operating conditions the next event would be a rising or falling edge of the return 20 kHz signal, causing D_3 to go high. The rising edge of D_3 strobes the present count value into the latch whilst simultaneously clearing the counter ready for the next timing interval. Hence the latch contains the final count value representing the time delay between an edge of the

reference signal and the following edge of the return signal. In situations where the return signal edge is coincident with the reference signal edge, no action is taken and the previous count value is retained. When no return signal edge is detected between two consecutive reference edges, a count value of zero is latched due to rollover of the eight bit counter.

The next step in the state machine design procedure is to use a state diagram to express the timing sequences described above as a corresponding set of state sequences.

State diagram

The state diagram for the phase measurement state machine is illustrated in figure B.3. Standard state machine notation[32] is used such that each of the eight possible states are uniquely identified by a circle containing the PROM address required to select that state. Transitions between states are labelled with the corresponding external input combination required to cause that transition together with the required output function.

The state diagrams symmetry is due to the similarity between the two separate state sequences required to trigger a timing interval from either edge of the reference input. States 0, 1 and 2 define the sequence for the positive edge triggered timing interval, whereas states 3, 4 and 5 define a similar sequence, but one which is triggered by the negative edge of the reference signal. Because of this similarity, only the positive edge triggered state sequence will be described in detail.

In state 1, both the reference and return inputs are low and the state machine is effectively waiting for a positive going edge on the reference input to trigger the timing interval. During this wait period the counter reset line, which corresponds to D_3 of the PROM, is held high. When the reference input goes high, the state machine selects state 2, releasing the counter reset line and starting the count. State 2 is maintained until the return input goes high, at which point state 0 is selected to indicate the end of the

timing interval. In state 0, the counter reset line is again taken high to latch the final count value and clear the counter ready for the next timing interval. State 0 is maintained until both the reference and return inputs have gone low, at which point the trigger state, state 1, is again selected.

The positive edge triggered state sequence described above is used when the reference input goes high before the return input. If, when in state 1, the return input goes high first, then the state machine switches to the equivalent negative edge triggered state sequence by selecting state 5. States 3, 4 and 5 of this sequence are directly equivalent to states 1, 2 and 0 respectively described above.

The final stage of the state machine design procedure is to construct a state table from the state diagram discussed above.

State table

The state table for the phase measurement state machine is shown in table B.1. This shows all of the possible state transitions and state outputs for each of the four possible combinations of the reference and return inputs. Because a state transition is achieved by programming the currently selected PROM location with the address of the required next state, the state table effectively provides a complete definition of the required PROM memory map. A listing of the PROM contents derived from the state table is included as listing B.1.

Present state	reference, return inputs = A_0, A_1							
	Next state = D_0, D_1, D_2				Output = D_3			
A_5, A_6, A_7	00	01	10	11	00	01	10	11
0	1	0	0	0	1	1	1	1
1	1	5	2	0	1	1	0	1
2	1	0	2	0	1	1	0	1
3	4	5	3	0	0	1	1	1
4	4	5	3	5	0	1	1	1
5	5	5	3	5	1	1	1	1
6	0	0	0	0	1	1	1	1
7	0	0	0	0	1	1	1	1

TABLE B.1. State table for the phase measurement state machine

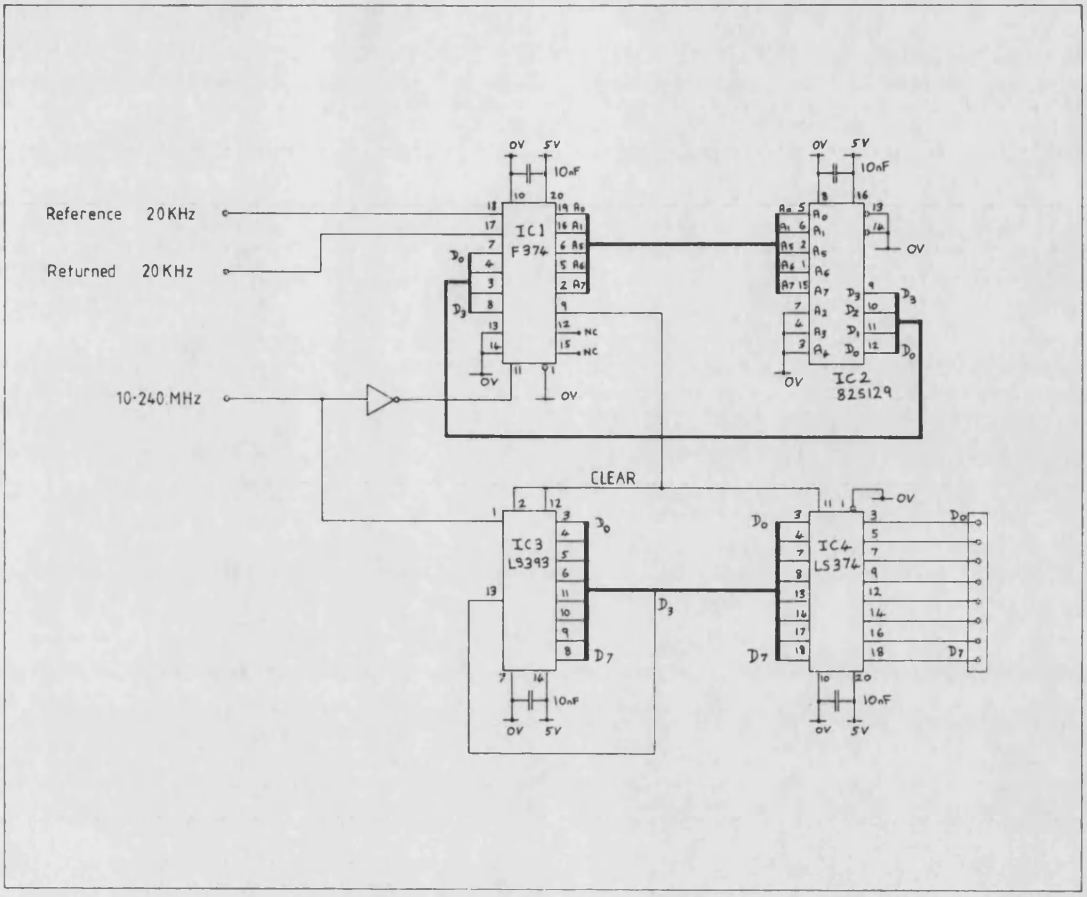

Phase measurement state machine circuit diagram Figure B.1

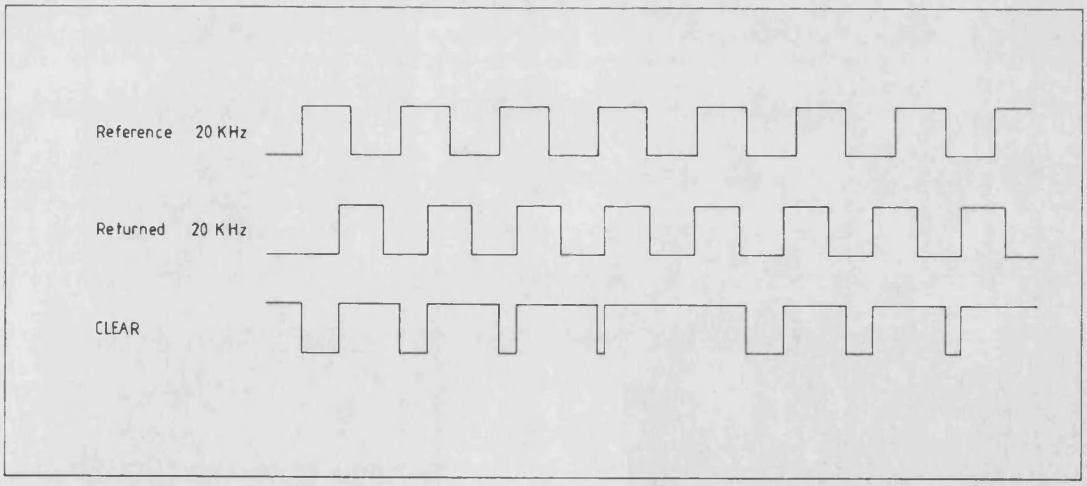

Phase measurement state machine timing diagram Figure B.2

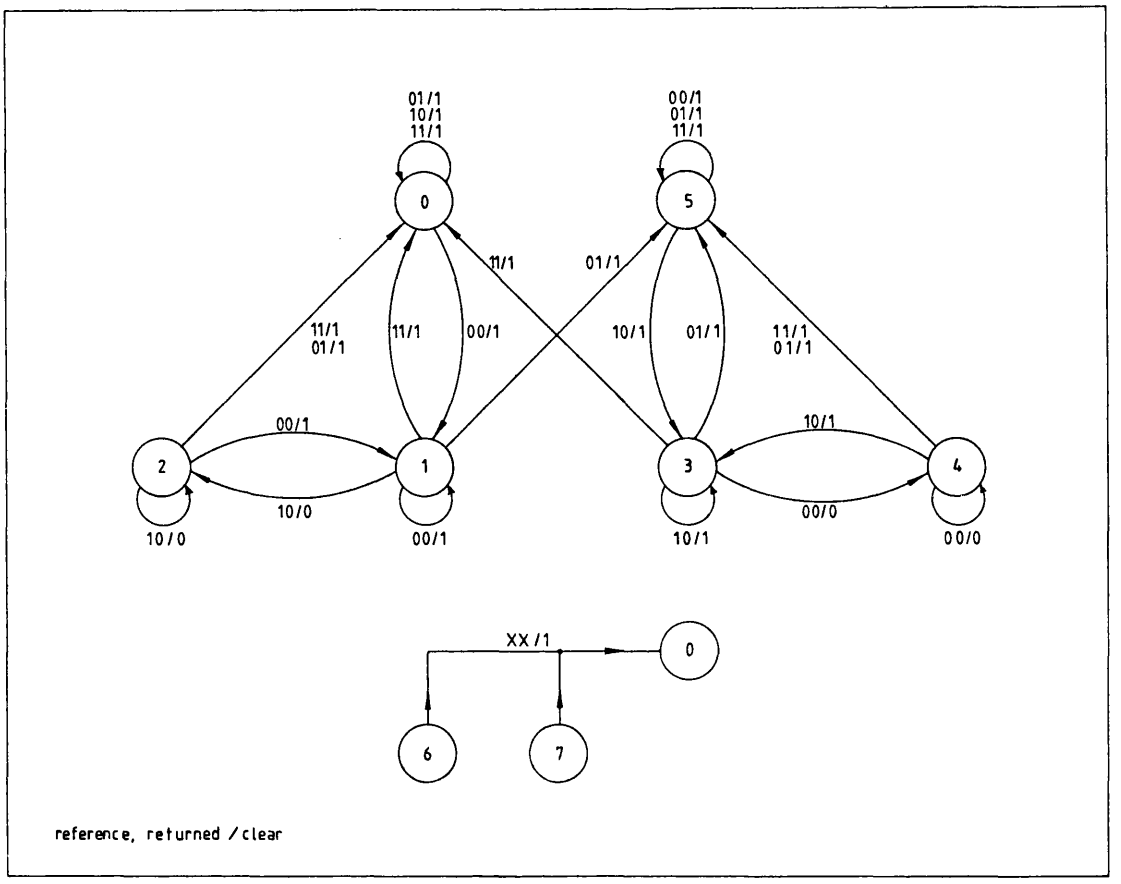

State diagram for the phase measurement state machine Figure B.3

Appendix C Filter macro summary

A summary of the high speed digital filter macros derived in chapter 3 will now be given. By combining these basic filter functions, any desired filter or controller transfer function can be realised with minimal difficulty.

Register allocation

The digital filter macros make certain assumptions about register allocation. These are,

Register D_0 must contain the filter input variable, X_n, on entry to the filter macro

Register D_1 contains the filter output, Y_n, on exit from the filter macro

Register D_2 is a general work register sometimes used by the multiply macro, MULT

Register A_3 is a pointer to the base of the storage area used by the filter variables. This is used within the filter macros to access the filter variables via the *offset* (A_3) addressing mode

Macro definitions

FILTER1 P, Q, mant1, exp1, mant2, exp2 evaluates the linear difference equations of the first order filter function,

$$P_n = X_n - Q_n$$

$$Y_n = pP_n + qQ_n$$

where

$$p = mant\,1 \times 2^{-exp\,1}$$

$$q = mant\,2 \times 2^{-exp\,2}$$

DELTA1 P, Q, mant1, exp1 updates the internal variable, Q_n, of the first order filter function,

$$Q_{n+1} = Q_n + m_1 P_n$$

where

$$m_1 = mant\ 1 \times 2^{-exp\ 1}$$

FILTER2 P, Q, R, mant1, exp1, mant2, exp2, mant3, exp3 evaluates the linear difference equations of the second order filter function.

$$P_n = X_n - Q_n - R_n$$

$$Y_n = pP_n + qQ_n + rR_n$$

where

$$p = mant\ 1 \times 2^{-exp\ 1}$$

$$q = mant\ 2 \times 2^{-exp\ 2}$$

$$r = mant\ 3 \times 2^{-exp\ 3}$$

DELTA2 P, Q, R, mant1, exp1, mant2, exp2 updates the internal variables, Q_n and R_n, of the second order filter function.

$$R_{n+1} = R_n + m_2 Q_n$$

$$Q_{n+1} = Q_n + m_1 P_n$$

where

$$m_1 = mant\ 1 \times 2^{-exp\ 1}$$

$$m_2 = mant\ 2 \times 2^{-exp\ 2}$$

FILTER3 P, Q, mant1, exp1 evaluates the linear difference equations of the integrator filter function.

$$P_n = X_n$$

$$Y_n = pP_n + Q_n$$

where

$$p = mant\ 1 \times 2^{-exp\ 1}$$

DELTA3 P, Q, mant1, exp1 updates the internal variable, Q_n, of the integrator filter function.

$$Q_{n+1} = Q_n + m_1 P_n$$

where

$m_1 = mant\ 1 \times 2^{-exp\,1}$

MULT mant, exp provides an optimised fixed coefficient multiplication routine to perform the following,

$D_1 = D_1 + (D_0 \times mant \times 2^{-exp})$

LIM_MX value is used to limit register D_1 to a maximum of *value*. This is particularly useful when sending the output of a filter to a peripheral device which cannot accept 32 bit numbers. In the case of an eight bit peripheral, for example, the limiting value on D_1 might be FF_H. A given lower limit can be ensured by using the complementary LIM_MN macro.

LIM_MN value is used to limit register D_1 to a minimum of *value*.

SLEW rate,var limits the rate of change of register D_1 between sample intervals. On entry to the macro the previous value of D_1, stored in *var*, is compared with the current value to obtain the rate of change of D_1 over one sample interval. If necessary this rate is then limited to the value defined by the *rate* argument and is then added to *var* to obtain the new slew rate limited D_1 value. Finally, this value of D_1 is used to update the value of *var*.

The slew rate limiting macro was included as a means of eliminating noise spikes received from peripheral devices.

Appendix D Mass and inertia calculations

Mass and inertia values are required for all of the vehicle control models to provide the relationship between gap acceleration and applied force or torque. For heave, lateral and tractive modes,

$$\ddot{x} = \frac{F}{M} \qquad \text{equation D.1}$$

And for roll, pitch and yaw modes,

$$\ddot{\theta} = \frac{T}{I} \qquad \text{equation D.2}$$

For the derivation of the mass and inertia values, the vehicle was considered as having a distributed mass M_d of 70 kg coplanar with four pairs of levitation motors and side control magnets, each pair having a combined mass M_m of 80 kg. Using this information, together with the relevant vehicle dimensions provided by figure D.1 the mass and inertia figures were derived for all of the free modes.

Heave, lateral and tractive modes

In each of these modes, the vehicle acceleration is related to force according to equation D.1, where the mass is given by the total vehicle mass,

$$M = 4\times80 + 70$$

$$= 390\ kg$$

Roll mode

In the roll mode, the angular acceleration of the vehicle is related to applied torque according to equation D.2. The total inertia is given by the sum of the inertia due to the point masses of the motors (I_m) and the inertia due to the distributed mass of the vehicle (I_d). For the purposes of calculation, the distributed vehicle mass will be considered as a plate of mass M_d and of width 0.65 m.

Now for a point mass M acting at a radius r from the roll axis it can be seen that[33],

$$I = Mr^2 \qquad \text{equation D.3}$$

And for a uniform plate of mass M and width l, the moment of inertia about an axis bisecting the plate along its length is given by[33].

$$I = \frac{1}{12}Ml^2 \qquad \text{equation D.4}$$

The total inertia seen by the roll mode is therefore given by,

$$I_r = I_m + I_d$$

$$= 4M_m(0.5)^2 + \frac{1}{12}M_d(0.65)^2$$

$$= 80 + 2.5$$

$$= 82.5\ kgm^2$$

Pitch mode

The total inertia seen by the pitch mode can be calculated in a similar way to the calculation for roll inertia.

$$I_p = I_m + I_d$$

$$= 4M_m\left(\frac{1.995}{2}\right)^2 + \frac{1}{12}M_d(2.495)^2$$

$$= 318 + 36$$

$$= 354\ kgm^2$$

Yaw mode

As with the roll and pitch modes, the yaw inertia is made up of two components,

$$I_y = I_m + I_d$$

where

$$I_m = 4M_m\left[0.5^2 + \left(\frac{1.995}{2}\right)^2\right]$$

$$= 398\ kgm^2$$

Previously the distributed vehicle mass has been considered as a uniform rectangular

plate of mass M_d, for which analytic expressions for inertia in roll and pitch modes may be readily derived. In the yaw mode however, the axis of rotation is perpendicular to the plate face, where the rectangular shape makes it particularly difficult to obtain an inertia figure. Hence it was decided that the simplest way to arrive at the distributed inertia figure was to use an estimated effective radius for the plate and then use the inertia formula for a disc[33].

$$I_d = M_d r_e^2$$

where r_e is the effective radius, here considered as 0.8 m.

It follows that,

$$I_d = 70 \times 0.8^2$$
$$= 45\ kgm^2$$

giving

$$I_y = 443\ kgm^2$$

Note that although the distributed inertia figure is approximate, the effect on the overall yaw inertia value is not significant.

Elsewhere within this report, reference is made to a simplified pivoted vehicle model which has only heave, lateral and roll modes. Figure D.2 illustrates the situation and shows how the pivot action forces the roll axis to an effectively lower position than in the free vehicle, requiring a re-calculation of the roll inertia.

Roll mode (pivoted)

The inertia seen by the roll mode of the pivoted vehicle was calculated as follows,

$$I_r = I_m + I_d$$
$$= 2M_m(0.35^2 + 0.5^2) + 2M_m(0.5^2) + \frac{1}{12}M_d(0.65^2)$$
$$= 100 + 2.5$$

$= 102.5\ kgm^2$

The heave and lateral modes now require an effective mass value which takes into account the angular motion of the vehicle about the pivot.

Heave and lateral modes (pivoted)

To calculate an effective mass seen by the heave and lateral modes, the inertia about the pivot is first calculated and is then translated to an equivalent mass at the point of application of the control force F. Using equation D.3 for the point masses, and with reference to figure D.2,

$$I_m = 2M_m(0.35^2 + 2.245^2) + 2M_m(0.35^2 + 0.25^2)$$

$$= 856\ kgm^2$$

For the distributed mass, it is necessary to use the parallel axis theorem[33] given below to translate the distributed inertia to the pivot axis,

$$I_{xx} = I_{yy} + Mr^2 \qquad \text{equation D.5}$$

where

I_{xx} is the moment of inertia about the x axis

I_{yy} is the moment of inertia about the y axis

r is the distance between the x and y axes

Hence

$$I_d = \frac{1}{12}M_d(2.495)^2 + M_d(0.35^2 + 1.2475^2)$$

$$= 154\ kgm^2$$

The total inertia about the pivot is therefore given by,

$$I = I_m + I_d$$

$$= 1010\ kgm^2$$

This inertia must be translated to an effective mass, M_e, distance r from the pivot. Now an angular acceleration $\ddot{\theta}$ about the pivot gives rise to an approximately linear

acceleration $\ddot{x}$ at a distance r from the pivot (provided that r is large and θ is small).

$$\ddot{x} = \ddot{\theta} r \qquad \text{equation D.6}$$

Now

$$\ddot{\theta} = \frac{Torque}{I}$$

$$= \frac{Fr}{I}$$

hence, using equation D.6,

$$\ddot{x} = \frac{Fr^2}{I} \qquad \text{equation D.7}$$

But

$$\ddot{x} = \frac{F}{M_e} \qquad \text{equation D.8}$$

Where M_e is the effective mass at radius r, due to the inertia I. Combining equations D.7 and D.8,

$$M_e = \frac{I}{r^2}$$

$$= \frac{1010}{(0.35^2 + 2.245^2)}$$

$$= 195.6\ kg$$

This is the effective mass seen by the heave and lateral modes of the pivoted vehicle.

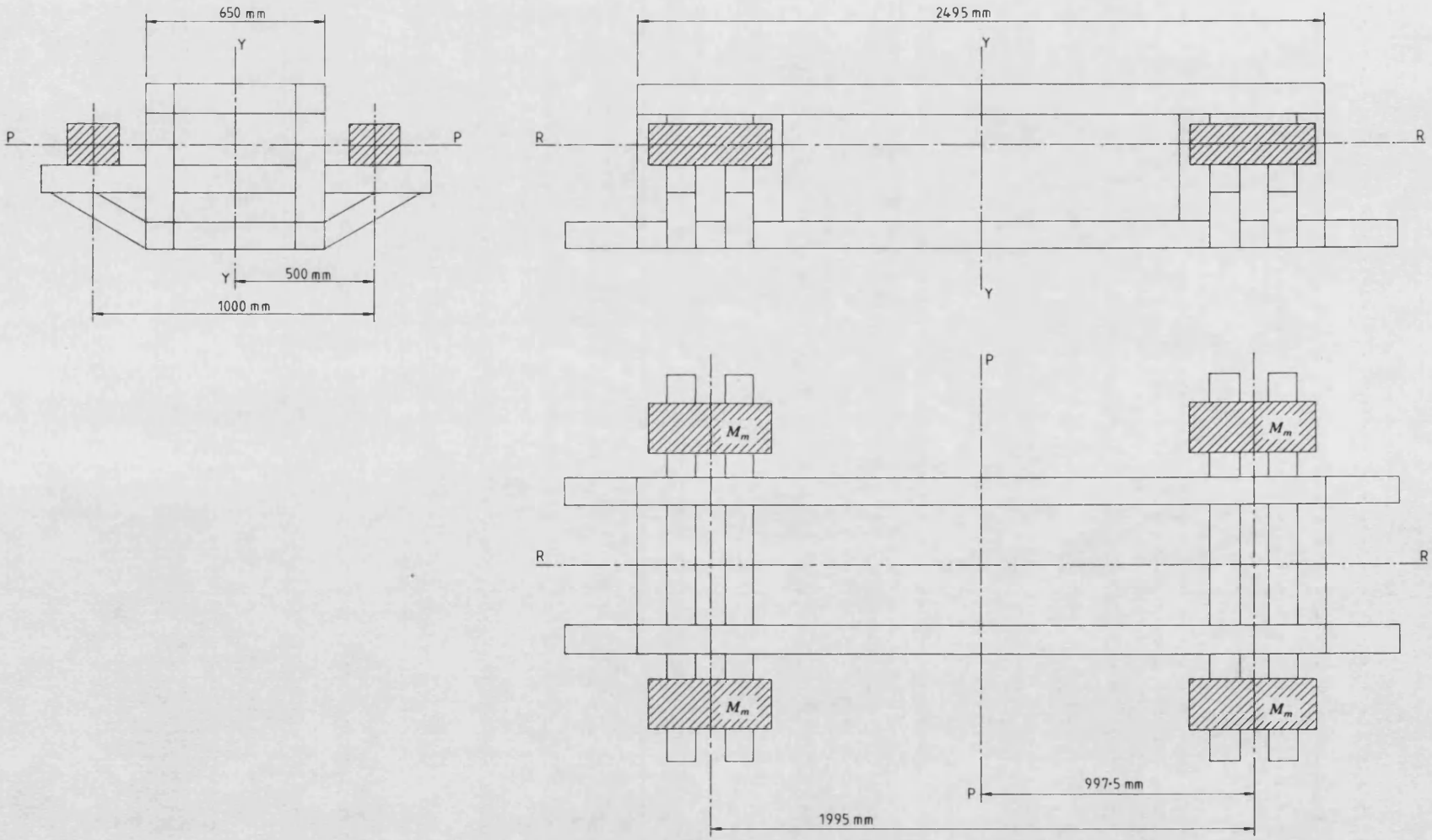

Main vehicle dimensions for inertia calculations Figure D.1

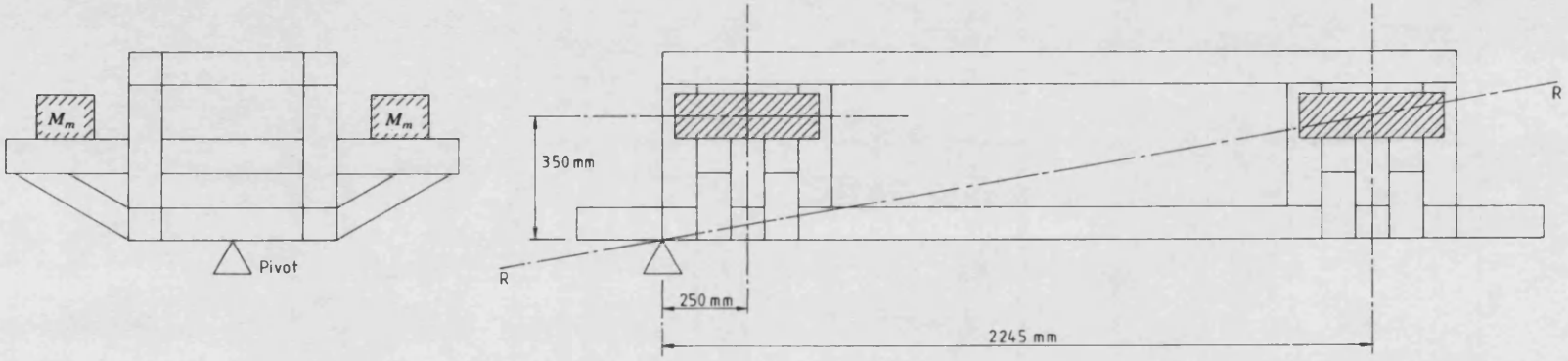

The pivoted vehicle Figure D.2

Appendix E The magnetic circuit with airgap

An expression is to be derived for the force exerted on an iron bar by an electromagnet operating at a constant current. To do this, it was first necessary to derive an expression for the inductance L of a magnetic circuit with an airgap. Consider figure E.1, which shows a toroidal magnetic circuit made from an iron with a very high permeability and which includes an airgap of length l_g. A magnetic flux ϕ is maintained within the iron and airgap by a coil of N turns carrying a constant current of I amperes.

Assuming that the length of the airgap is small compared with the cross sectional diameter of the toroid, the following equations can be written down[34].

$$B = \mu_0 \mu_r H \qquad \text{equation E.1}$$

$$NI = H_i l_i + H_g l_g \qquad \text{equation E.2}$$

$$L = \frac{N\phi}{I} \qquad \text{equation E.3}$$

where

i refers to iron related quantities

g refers to gap related quantities (i.e. air)

L is the winding inductance

Using equation E.1 in equation E.2, and using $\mu_r = 1$ for the airgap,

$$NI = \frac{Bl_i}{\mu_0 \mu_i} + \frac{Bl_g}{\mu_0} \qquad \text{equation E.4}$$

$$= \frac{B}{\mu_0}\left\{\frac{l_i}{\mu_i} + l_g\right\}$$

Provided that $\frac{l_i}{\mu_i} << l_g$, then

$$NI = \frac{Bl_g}{\mu_0} \qquad \text{equation E.5}$$

Substituting equation E.5 into equation E.3 and using $B = \frac{\phi}{A}$ it can be shown that,

$$L = \mu_0 N^2 \frac{A}{l_g} \qquad \text{equation E.6}$$

An expression for the force exerted by an electromagnet is now required. Consider the arrangement of figure E.2, where an iron bar is moved through an infinitesimally small distance δx due to a force F exerted by an electromagnet distance x from the bar. Writing down the energy balance equation for the system,

work done by the system	+	change in stored electrical energy	=	electrical input energy

or

$$\delta W_F + \delta W_E = \delta W$$

These three energy terms will now be considered separately and then combined to derive an expression for the force F in terms of the gap x and the constant current I.

Work done by the system

It can be seen that the work done by the system is qiven by equation E.7 below,

$$\delta W_F = -\delta x F \qquad \text{equation E.7}$$

where the negative sign is used to denote an energy output.

Change in stored electrical energy

The general expression for the electrical energy stored in a coil carrying a current I and having an inductance L is given by,

$$W_E = \frac{1}{2} L I^2$$

where, using equation E.6,

$$L = \mu_0 N^2 \frac{A}{x}$$

Hence, given that I is constant, the increase in stored energy due to the increase in inductance can be written down as follows,

$$\delta W_E = \frac{1}{2} I^2 \delta L \qquad \text{equation E.8}$$

Change in electrical input energy

The change in electrical input energy of the system is given by.

$$\delta W = VI\,\delta t \qquad \text{equation E.9}$$

Now.

$$V = \frac{d}{dt}(LI)$$

which, with I constant, and provided that $\delta t \rightarrow 0$, can be expressed as follows.

$$V = I\frac{\delta L}{\delta t}$$

substituting this expression into equation E.9 gives.

$$\delta W = I^2\delta L \qquad \text{equation E.10}$$

Equations E.7, E.8 and E.9 are combined to produce an expression for the force F in terms of the change δL in the inductance and the change δx in the airgap.

$$-F\,\delta x + \frac{1}{2}I^2\delta L = I^2\delta L$$

giving

$$F = -\frac{1}{2}I^2.\frac{\delta L}{\delta x}$$

For $\delta x \rightarrow 0$ and using equation E.6, it can be seen that.

$$\begin{aligned} F &= -\frac{1}{2}I^2\frac{dL}{dx} \\ &= -\frac{1}{2}I^2\left\{-\mu_0 N^2\frac{A}{x^2}\right\} \\ &= \frac{1}{2}\mu_0 N^2 A\frac{I^2}{x^2} \\ &= K_m\frac{I^2}{x^2} \qquad \text{equation E.11} \end{aligned}$$

where K_m is the motor constant.

$$K_m = \frac{1}{2}\mu_0 N^2 A \qquad \text{equation E.12}$$

To be able to design vehicle controllers using linear design techniques, it was necessary

to linearise the force expression of equation E.11 about a working point I_0, X_0.

$$\left.\frac{\partial F}{\partial i}\right|_{I_0 X_0} = 2K_m \frac{I_0}{X_0^2}$$

$$\left.\frac{\partial F}{\partial x}\right|_{I_0 X_0} = -2K_m \frac{I_0^2}{X_0^3}$$

Hence, for small perturbations about this working point,

$$\delta F = 2K_m \frac{I_0}{X_0^2}\left\{\delta i - \frac{I_0}{X_0}\delta x\right\} \qquad \text{equation E.13}$$

Equation E.13 forms the basis for designing all the vehicle levitation and side controllers using current feedback choppers.

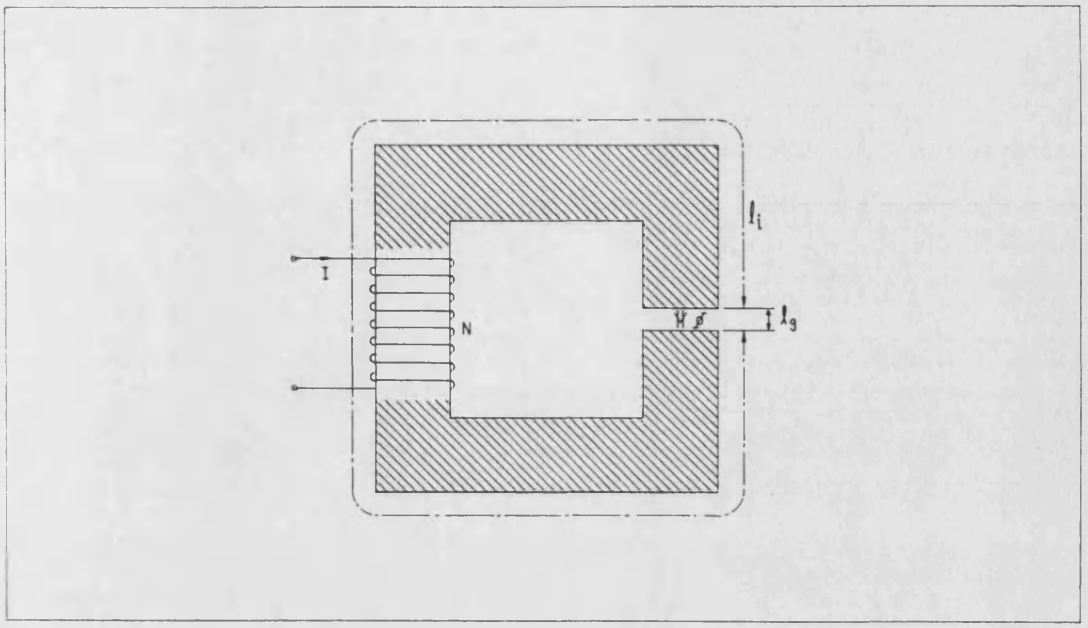

The magnetic circuit with airgap Figure E.1

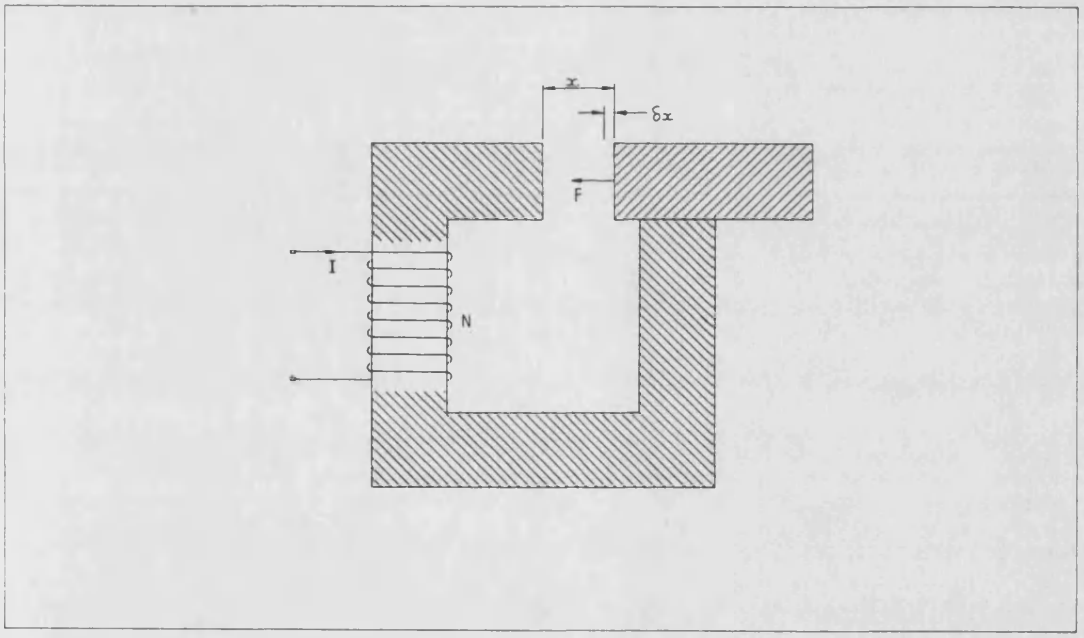

Force exerted by an electromagnet Figure E.2

Appendix F Filter realisation

The circuit realisation of the following filter transfer functions will be described.

1. $T(s) = \dfrac{-Ks}{s^2 + b_1 s + b_0}$ equation F.1

2. $T(s) = \dfrac{K}{s^2 + b_1 s + b_0}$ equation F.2

3. $T(s) = \dfrac{K(s + a_0)}{(s + b_1)(s + b_2)}$ equation F.3

The integrator

The transfer function of equation F.1 was realised using the circuit of figure F.1. With reference to this diagram the following equations were written down.

$V' = \dfrac{-i_1}{sC_2}$ *using the op−amp virtual earth concept* equation F.4

$i_1 = \dfrac{V_o}{R_3}$ equation F.5

$i_2 = (V_o - V')sC_1$ equation F.6

$i_3 = \dfrac{V'}{R_2}$ equation F.7

$i_1 + i_2 - i_3 + i_4 = 0$ equation F.8

$V_i = i_4 R_1 + i_3 R_2$ equation F.9

Combining equations F.4 and F.5.

$V' = \dfrac{-V_o}{sC_2R_3}$ equation F.10

Substituting equations F.5, F.6 and F.7 into equation F.8, and using equation F.10.

$$\begin{aligned} i_4 &= i_3 - i_1 - i_2 \\ &= \frac{-V_o}{sC_2R_3R_2} - \frac{V_o}{R_3} - V_o sC_1\left\{1 + \frac{1}{sC_2R_3}\right\} \\ &= \frac{-V_o}{sC_2R_3}\left\{\frac{1}{R_2} + sC_2 + sC_1(sC_2R_3 + 1)\right\} \end{aligned}$$ equation F.11

Finally, using equations F.7 and F.11 in equation F.9.

$$V_i = \frac{-V_o R_1}{sC_2R_3}\left\{\frac{1}{R_2} + sC_2 + sC_1(sC_2R_3 + 1)\right\} - \frac{V_o}{sC_2R_3}$$

$$= \frac{-V_o R_1}{sC_2R_3}\left\{\frac{1}{R_2} + sC_2 + sC_1(sC_2R_3 + 1) + \frac{1}{R_1}\right\}$$

which, on re-arranging gives,

$$\frac{V_o}{V_i}(s) = \frac{-s/C_1R_1}{s^2 + \frac{s}{R_3}\left\{\frac{C_1 + C_2}{C_1C_2}\right\} + \frac{1}{C_1C_2R_3R'}} \qquad \text{equation F.12}$$

where

$$R' = \frac{R_1R_2}{R_1 + R_2} \qquad \text{equation F.13}$$

Hence with reference to equation F.1 the coefficients were written down as follows,

$$K = \frac{1}{C_1R_1} \qquad \text{equation F.14}$$

$$b_0 = \frac{1}{C_1C_2R_3R'} \qquad \text{equation F.15}$$

$$b_1 = \frac{1}{R_3}.\frac{C_1 + C_2}{C_1C_2} \qquad \text{equation F.16}$$

Now if $C_1 = C_2 = C$, it is easily shown that the value of K is constrained by the requirement that R_1 and R_2 must be positive,

$$R_2 = \frac{R_1}{\left\{\frac{2b_0}{Kb_1} - 1\right\}}$$

Such that, for R_2 positive, the condition $K \leqslant \frac{2b_0}{b_1}$ must be satisfied.

Standard second order Butterworth section

The transfer function of equation F.2 was implemented using the standard second order Butterworth filter circuit of figure F.2. This is a widely used and well documented circuit[19] and will not be analysed in detail here. It can be shown that,

$$T(s) = \frac{V_o}{V_i}(s)$$

$$= \frac{A_0/C_1R_1C_2R_2}{s^2 + s\left\{\frac{C_2R_1 + C_2R_2 + C_1R_1(1 - A_0)}{C_1R_1C_2R_2}\right\} + \frac{1}{C_1R_1C_2R_2}} \qquad \text{equation F.17}$$

where A_0 is the d.c. gain.

$$A_0 = \frac{R_3 + R_4}{R_3} \qquad \text{equation F.18}$$

The transfer function coefficients in terms of the component values of figure F.2 were then written down as follows.

$$b_0 = \frac{1}{C_1R_1C_2R_2} \qquad \text{equation F.19}$$

$$b_1 = \frac{C_2R_1 + C_2R_2 + C_1R_1(1 - A_0)}{C_1R_1C_2R_2} \qquad \text{equation F.20}$$

Lead/double lag network

The transfer function of equation F.3 was implemented using a standard lead/lag network cascaded with a lag network as shown in figure F.3. Because the lead/lag network was passive, it was necessary to buffer both the input and output as shown. Figure F.4a shows the isolated lead/lag network from which the transfer function was shown to be,

$$\frac{V_o}{V_i}(s) = \frac{C_1}{C_1 + C_2} \cdot \frac{s + 1/R_1C_1}{s + \frac{R_1 + R_2}{R_1R_2(C_1 + C_2)}} \qquad \text{equation F.21}$$

Figure F.4b defines the final lag stage, from which the following transfer function was written down,

$$\frac{V_o}{V_i}(s) = \frac{-1/R_3C_3}{s + 1/C_3R_4} \qquad \text{equation F.22}$$

Hence the transfer function coefficients in terms of the component values of the combined circuits could be written down as follows.

$$a_0 = \frac{1}{R_1C_1} \qquad \text{equation F.23}$$

$$b_1 = \frac{R_1 + R_2}{R_1R_2(C_1 + C_2)} \qquad \text{equation F.24}$$

$$b_2 = \frac{1}{C_3 R_4}$$ equation F.25

$$d.c.\ gain = \frac{R_2}{R_1 + R_2} \cdot \frac{R_4}{R_3}$$ equation F.26

Component values for specific filters

The transfer function of the integrator circuit used in section 6.4 of the main text is reproduced below.

1. $$T(s) = \frac{-0.1s}{s^2 + s + 0.213}$$

With reference to figure F.1. the following component values are required to implement this transfer function (using E24 series preferred values).

$C_1 = C_2 = 10.0\ \mu F$

$R_1 = 1\ M\ \Omega$

$R_2 = 300\ K\ \Omega$

$R_3 = 200\ K\ \Omega$

The transfer function of the second order Butterworth filter circuit referred to in section 6.5 of the main text is reproduced below.

2. $$T(s) = \frac{0.213}{s^2 + s + 0.213}$$

With reference to figure F.2. the following component values are required to implement this transfer function.

$C_1 = C_2 = 4.7\ \mu F$

$R_1 = 300\ K\ \Omega$

$R_2 = 680\ K\ \Omega$

$R_3 = o/c$

$R_4 = s/c$

The transfer function of the lead/double lag circuit used in section 6.6 of the main text is reproduced below.

3. $$T(s) = \frac{s + 0.213}{s^2 + s + 0.213}$$

$$= \frac{s + 0.213}{s + 0.692} \times \frac{1}{s + 0.308}$$

With reference to figure F.3, the following component values are required to implement this transfer function.

$C_1 = C_2 = C_3 = 4.7\ \mu F$

$R_1 = 1\ M\ \Omega$

$R_2 = 180\ K\ \Omega$

$R_3 = 110\ K\ \Omega$

$R_4 = 680\ K\ \Omega$

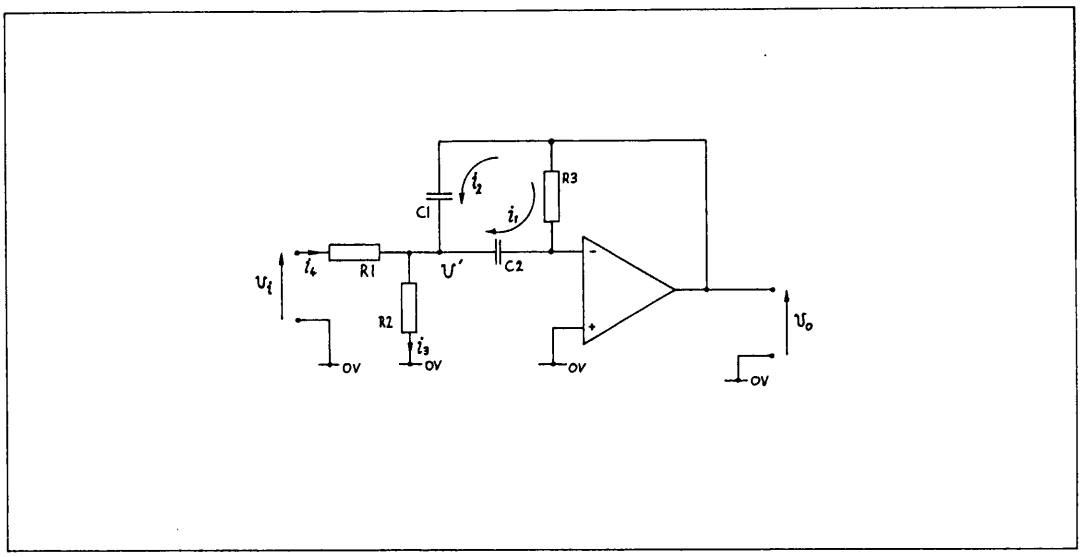

The a.c. integrator circuit diagram Figure F.1

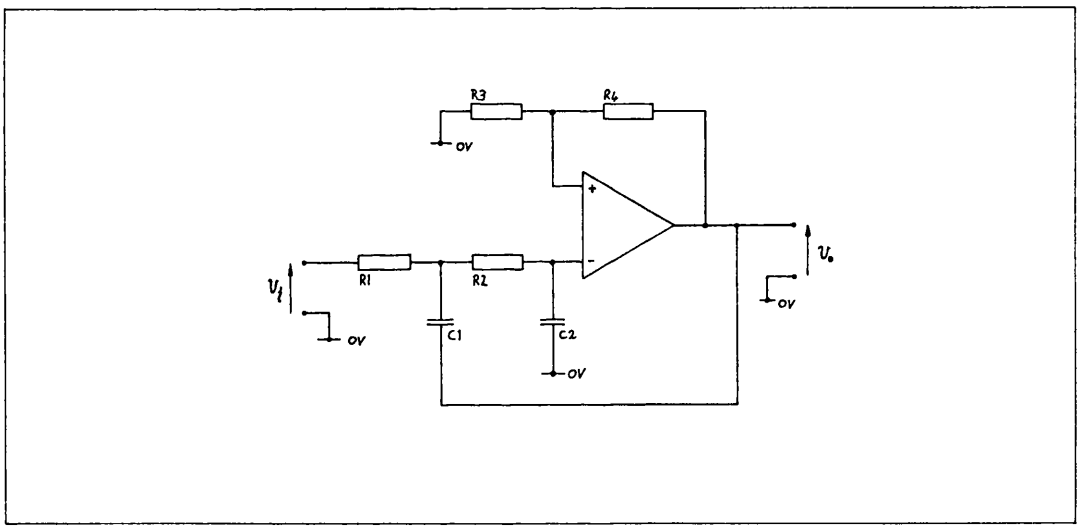

Second order low pass Butterworth filter circuit diagram Figure F.2

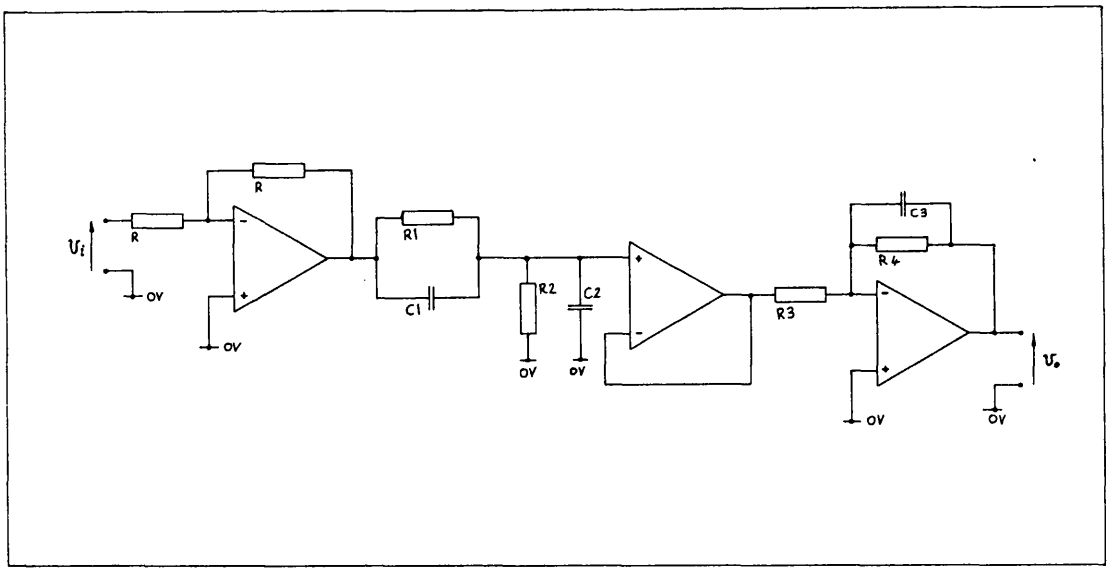

Lead/double lag filter circuit diagram Figure F.3

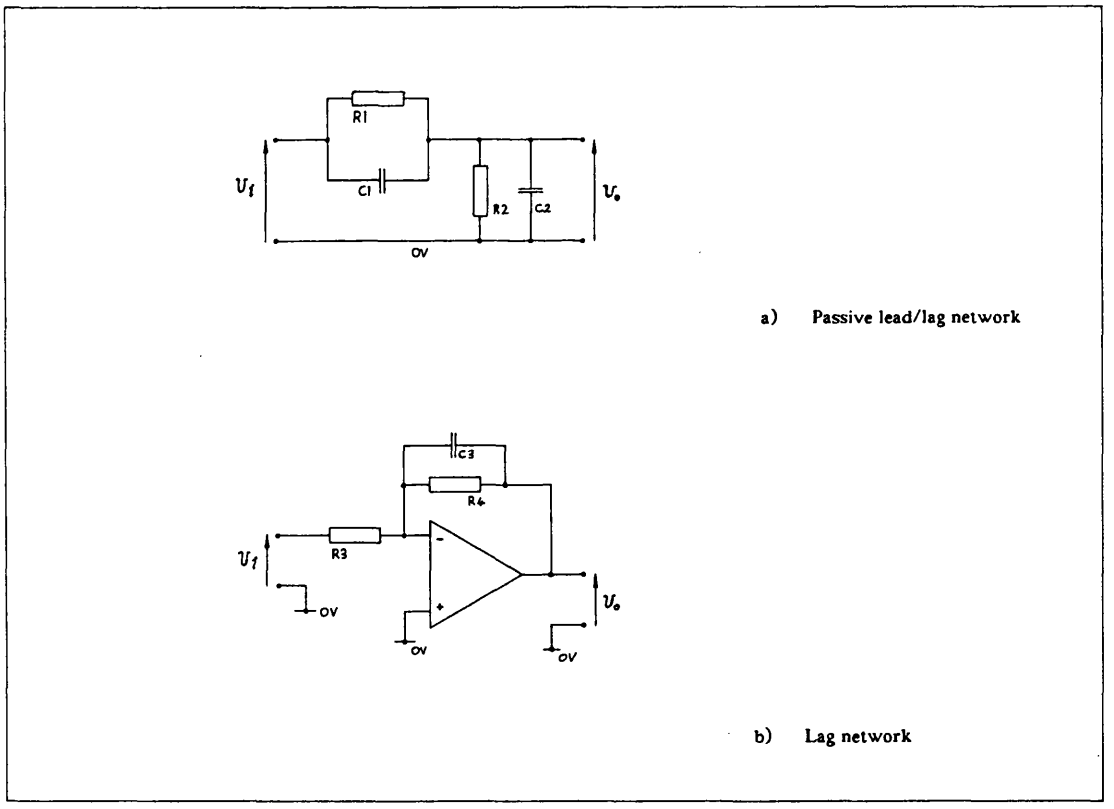

Lead/double lag circuit sections Figure F.4

Listings

All listings are stored on the dq1 hard disc partition on the levitation vehicle's multiprocessor system.

3.1 :filters.bcpl.format
3.2 :filters.asm.filter-macros
3.3 :filters.asm.timer
3.4 :filters.bcpl.runtimer
3.5 :filters.asm.filter
3.6 :filters.bcpl.supervisor
3.7 :filters.asm.filterhdr
3.8 :filters.bcpl.filterhdr
3.9 :timings.filter-macros

4.1 :twist.bcpl.twist-logger
4.2 :twist.asm.twist-log
4.3 :twist.bcpl.twisthdr
4.4 :twist.asm.twisthdr
4.5 :twist.maketwist

5.1 :train-free.bcpl.supervisor
5.2 :train-free.bcpl.remote
5.3 :train-free.asm.control-mp
5.4 :train-free.asm.process-ip
5.5 :train-free.bcpl.suphdr
5.6 :train-free.bcpl.remhdr
5.7 :train-free.asm.suphdr
5.8 :train-free.asm.remhdr
5.9 :train-free.maketrain

8.1 :Z80.asm.position-transducer

9.1 :traction.bcpl.supervisor
9.2 :traction.bcpl.remote
9.3 :traction.asm.control-mp
9.4 :traction.asm.process-ip

9.5 :traction.bcpl.suphdr

9.6 :traction.bcpl.remhdr

9.7 :traction.asm.suphdr

9.8 :traction.asm.remhdr

9.9 :traction.maketrain

B.1 :prom.gap

PROM data for the phase measurement state machine

References

1. Rumsey, A. F., Wallace, A. K. and Jeffries, A. E. H., "Propulsion and control considerations for an intermediate capacity transit system", IAS Conference, 1981

2. Dunn, R. W., "A study of linear synchronous motors in the tractive and levitative modes", PhD Thesis, University of Bath, 1988

3. Eastham, J. F., "Iron-cored linear synchronous machines", IEE Electronics and Power, March 1977, pp. 239-242

4. Balchin, M. J., Helani, M. F. and Eastham, J. F., "A comparison of the characteristics of heteropolar and homopolar linear synchronous motors", IEE Colloquium Digest, 1983/20, March 1983

5. Balchin, M. J., "Design of linear synchronous motors and guidance magnets", August 1984

6. Balchin, M. J. and Eastham, J. F., "Characteristics of a heteropolar linear synchronous machine with passive secondary", Electric Power Applications, December 1979, Vol. 2, No. 6

7. Gott, V. S., "23-Linear thyristor amplifiers", Product Design Engineering, January 1969

8. Slattery, D. T., "Power switching transistor amplifiers", PhD Thesis, University of Bath, 1975

9. Private communication with Mr. V. S. Gott, University of Bath, concerning the design and implementation of a 3-phase inverter system.

10. "HEXFET Databook - power MOSFET applications and product data", International Rectifier, 1985

11. "Piezoelectric accelerometers and vibration preamplifiers - theory and application handbook", Brüel & Kjaer, 1978

12. Dale, L. A., "Real-Time Modelling of Multimachine Power Systems", PhD Thesis, University of Bath, 1986

13. King, T. J., "TRIPOS User Guide", School of Mathematics, University of Bath, 1983

14. King, T. J., "TRIPOS Programming Guide", School of Mathematics, University of Bath, 1983

15. King, T. J., "TRIPOS Technical Guide", School of Mathematics, University of Bath, 1983

16. Tanner, D. G., "Real-time simulation of power systems", PhD Thesis, University of Bath, 1982

17. Chandler, S. R., "The development of a colour graphics workstation", PhD Thesis, University of Bath, 1987

18. Multilink Documentation, Ninetiles Computer Systems Ltd

19. Millman, J., "Microelectronics: Digital and Analogue Circuits and Systems", McGraw-Hill International Book Company, 1979

20. Goodall, R. M. and Brown, D. S., "High-speed digital controllers using an 8 bit microprocessor", Software & Microsystems, Vol. 4, Nos. 5 & 6, October/December 1985

21. Lui, B., "Effect of finite wordlength on the accuracy of digital filters - a review", IEEE Transactions, 1971, CT-18, (6), pp. 670-677

22. Agarwal, R. C. and Burrus, C. S., "New recursive digital filter having very low sensitivity and roundoff noise", IEEE Transactions, 1975, CAS-22, (12), pp. 921-927

23. Wicks, D. C., "The Numerical Solution of Differential Equations using Fortran", School of Mathematics, University of Bath, 1982

24. McGeough, P. A., "Birmingham airport maglev vehicle construction", C394/84, IMechE, 1984

25. Amos, S. W., "Principles of transistor circuits", Third edition, Iliffe Books Ltd, 1965

26. "Z80 Central processing unit technical manual", MOSTEK Z80 microcomputer devices, 1984

27. "Microtec ASMZ80 Version 4 Cross assembler and linking loader for the Z80/NSC800 Family of microprocessors", Microtec Research, 1985

28. "Z80 Counter timer circuit technical manual", MOSTEK Z80 microcomputer devices, 1984

29. Ng, H. M., "Control of heteropolar transverse-flux linear synchronous motors", PhD Thesis, University of Bath, 1981

30. Munro, N. and Patel, R. V., "Multivariable system theory and design", Pergammon, 1982

31. White, B. A. and Silson, P. M., "Application of multivariable techniques to a levitated vehicle", Application of multivariable techniques, symposium, Inst.meas.contr., 1985

32. Lewin, D., "Logical Design of Switching Circuits", Second edition, Van Nostrand Reinhold (UK) Co. Ltd., 1974

33. McLean, W. G. and Nelson, E. W., "Schaum's outline of theory and problems of engineering mechanics : statics and dynamics", Second edition, McGraw-Hill International Book Company, 1962

34. Bolton, B., "Electromagnetism and its applications", Van Nostrand Reinhold Co. Ltd., 1980